



## Aerodynamic and Mechanical System Modelling

**Jørgensen, Martin Felix**

*Publication date:*  
2013

*Document Version*  
Publisher's PDF, also known as Version of record

[Link back to DTU Orbit](#)

*Citation (APA):*  
Jørgensen, M. F. (2013). *Aerodynamic and Mechanical System Modelling*. Technical University of Denmark. Department of Mechanical Engineering. DCAMM Special Report No. S160

---

### General rights

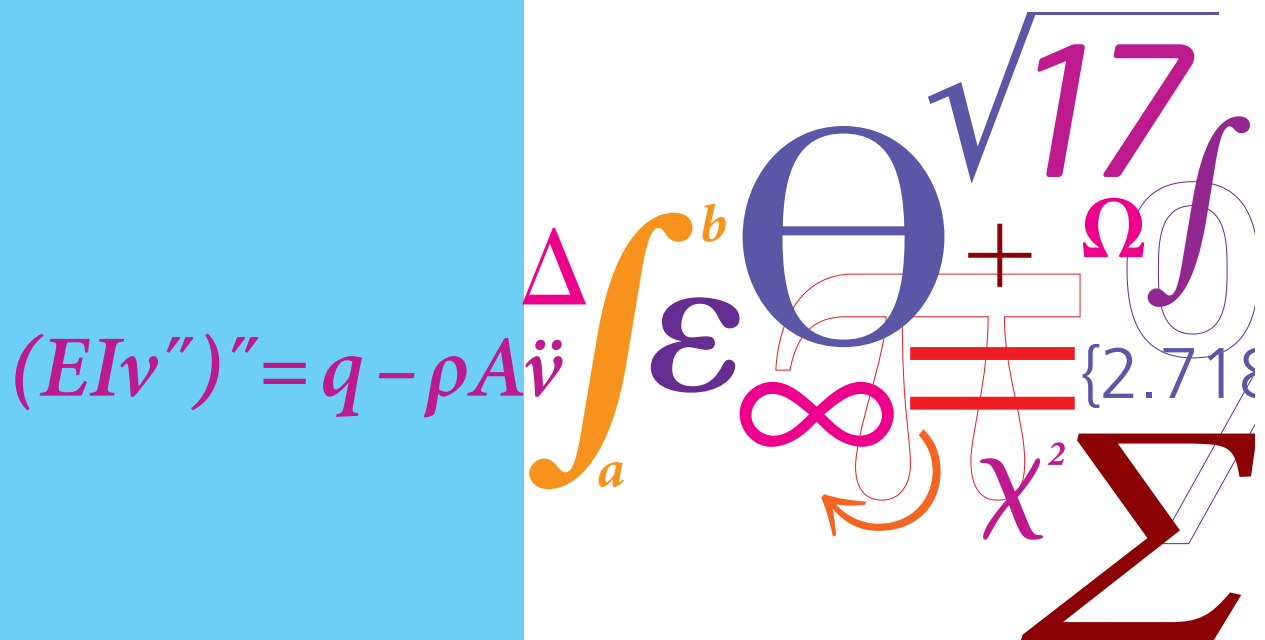
Copyright and moral rights for the publications made accessible in the public portal are retained by the authors and/or other copyright owners and it is a condition of accessing publications that users recognise and abide by the legal requirements associated with these rights.

- Users may download and print one copy of any publication from the public portal for the purpose of private study or research.
- You may not further distribute the material or use it for any profit-making activity or commercial gain
- You may freely distribute the URL identifying the publication in the public portal

If you believe that this document breaches copyright please contact us providing details, and we will remove access to the work immediately and investigate your claim.

# Aerodynamic and Mechanical System Modelling

PhD Thesis



Martin Felix Jørgensen  
DCAMM Special Report No. S160  
November 2013

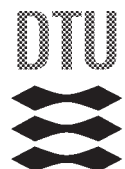


# Aerodynamic and Mechanical System Modelling

by

*Martin Felix Jørgensen*

DEPT. OF MECHANICAL ENGINEERING  
Solid Mechanics



TECHNICAL UNIVERSITY OF DENMARK



**Title of the thesis:**

Aerodynamic and Mechanical System Modelling

**Ph.D. student:**

Martin Felix Jørgensen

E-mail: mfjo@mek.dtu.dk

**Supervisors:**

Niels Leergaard Pedersen

E-mail: nlp@mek.dtu.dk

Jens Nørkær Sørensen

E-mail: jnso@dtu.dk

**Address:**

Technical University of Denmark

Department of Mechanical Engineering

Solid Mechanics

Nils Koppels Allé

Building 404

2800 Kgs. Lyngby

Denmark

Copyright © 2013 Martin Felix Jørgensen

DCAMM Special Report no. S160

ISBN 978-87-7475-370-4

## Preface

This thesis is submitted in partial fulfillment of the requirements for obtaining the Ph.D. degree in mechanical engineering at the Technical University of Denmark (DTU). The Ph.D. project was funded by DSF 09-071588 and DTU. Their financial support is gratefully acknowledged. The project was carried out at the Department of Mechanical Engineering, Solid Mechanics, DTU from December 1<sup>st</sup> 2010 - November 31<sup>st</sup> 2013. Supervisors on the project were Associate Professor, dr. techn. Niels Leergaard Pedersen from Solid Mechanics and Professor Jens Nørkær Sørensen from the Department of Wind Energy.

I am very grateful for being given this opportunity, especially to my two supervisors. I would like to thank my main supervisor, Niels Leergaard Pedersen, for his important support, help and for always being there when the modelling seemed difficult. I also wish to express my sincere thanks to co-supervisor Jens Nørkær Sørensen, who has also been a great help and support in his field of turbulence and wind modelling.

A part of this work was carried out during a 3-month stay at the University of Agder, Norway. I therefore wish to express my sincere gratitude to Associate Professor Morten Kjeld Ebbesen and Professor Michael Rygaard Hansen for hosting me and challenging me within the field of multibody dynamics. I also acknowledge the support and friendly cooperation of my project partners in the “Dynamic wind turbine model – from wind to grid”-project: Professor Zhe Chen, Institute of Energy Technology at Aalborg University and from DTU Wind Energy: Dr Scient Sven-Erik Gryning and Senior scientist Mark C. Kelly. From the Department of Wind Energy I wish to thank senior researcher Kurt Schaldermose Hansen and senior scientist Uwe Schmidt Paulsen, for their support in relation to wind turbine measurements and data collection. Senior researchers Robert Flemming Mikkelsen and Stig Øye both provided huge support regarding primarily FLEX 5, which I’m grateful of.

I would like to express my gratitude to my family for their support and encouragement. A number of friends and other people also supported me; apologies if you are not mentioned by name here. Finally, I wish to thank all colleagues at the section of Solid Mechanics for contributing to an inspiring time.

Kgs. Lyngby, November 2013.

*Martin Felix Jørgensen*

## Resume

Denne afhandling omhandler modellering af mekaniske flerlegeme-systemer anvendt på transmissionssystemet af en 500 kW vindmølle. Særligt fokus har været på gear-boks-modellering af vindmøller. Hovedparten af nærværende projekt har involveret programmering af flerlegeme systemer for at undersøge sammenhængen mellem kræfter, momenter, positioner, hastigheder og accelerationer på stive legemer.

En 500 kW vindmølle model er anvendt sammen med eksperimentelle data med henblik på at validere en model i FLEX 5, som er et anerkendt aero-elastisk værktøj der også anvendes af vindmølle industrien. Bl.a. er flerlegeme modelleringen af en planet-gearkasse både med og uden bindinger vha. fleksibilitet, et område som er undersøgt. En stiv og beregningsmæssig hurtig samt en fleksibel mere korrekt flerlegeme-model er udviklet. Den fleksible flerlegeme-model udmærker sig især ved at belastningerne internt fordeles fysisk mere korrekt. Et væsentligt problem som der er opnået en god model-beskrivelse af, er når der skiftevis er en eller to tænder i indgreb ad gangen. Dette giver en momentan og nærmest øjeblikkelig ændring af tandstivheden, hvilket er indarbejdet i den fleksible model. De involverede stivheder er fundet vha. separate beregninger foretaget med Finite Element Metoden. Effekten af denne diskontinuitet er evalueret i simuleringer hvor også dæmpning er inkluderet.

Der er foretaget en detaljeret undersøgelse og beregning af f.eks. tand normal-kræfter, spændinger og udmattelsesproblemer i tandoverfladen på gear. I udmattelses-beregningerne er der også taget hensyn til vindens turbulens for at undersøge dennes indflydelse på udmattelse på eller under tandoverfladen.

## Abstract

This thesis deals with mechanical multibody-systems applied to the drivetrain of a 500 kW wind turbine. Particular focus has been on gearbox modelling of wind turbines. The main part of the present project involved programming multibody systems to investigate the connection between forces, moments, positions, velocities and accelerations of rigid bodies.

A 500 kW wind turbine model has been used together with experimental data for validating a model in FLEX 5, which is a recognised aero-elastic tool also used by the wind turbine industry. Among other things, multibody modelling of a planetary gearbox, both including and without constraints using flexibility, is an area that has been investigated. A rigid and computationally fast together with a flexible more correct multibody-model, has been developed. The flexible multibody-model specifically excels from distributing the internal loads physically more correct. A substantial problem which a proper model description has been accomplished for, is when alternating one or two teeth is in mesh at once. This causes a momentary and almost immediate change in tooth stiffness, which is implemented in the flexible model. The stiffnesses involved have been found using separate calculations using the Finite Element Method. The effect of this discontinuity is evaluated in simulations where damping is also included.

A detailed investigation and calculation of e.g. tooth normal forces, stresses and fatigue problems in the tooth surface of gears have been conducted. In the fatigue calculations, considerations of turbulence from the wind are also included in order to investigate the fatigue effects from the latter, on or below the tooth surface.

## Publications

The following publications are part of the thesis

- [P1] M. F. Jørgensen, N. L. Pedersen, J. N. Sørensen, U. W. Paulsen, Rigid Matlab drivetrain model of a 500 kW wind turbine for predicting maximum gear tooth stresses in a planetary gearbox using multibody gear constraints, *Wind Energy*, 2013 (online version, published before inclusion in an issue).
- [P2] N. L. Pedersen and M. F. Jørgensen, On gear teeth stiffness evaluation, *Computers & Structures*, Accepted, 2013.
- [P3] M. F. Jørgensen, N. L. Pedersen and J. N. Sørensen, Comparison and implementation of a Rigid and a Flexible Multibody Planetary Gearbox Model, *Multibody System Dynamics*, Submitted, 2013.
- [P4] M. F. Jørgensen, N. L. Pedersen and J. N. Sørensen, Gear fatigue damage for a 500 kW wind turbine exposed to increasing turbulence using a flexible multibody model, *Journal of Multi-body Dynamics*, Submitted, 2013.

# Contents

<b>Preface</b>	<b>i</b>
<b>Resume</b>	<b>ii</b>
<b>Abstract</b>	<b>iii</b>
<b>Publications</b>	<b>iv</b>
<b>Contents</b>	<b>v</b>
<b>1 Introduction</b>	<b>1</b>
1.1 Definition of the problem . . . . .	1
1.2 Historical background, current development and motivation . . . .	1
1.3 Thesis layout and structure . . . . .	5
<b>2 Wind and aerodynamics</b>	<b>6</b>
2.1 The nature, statistical properties and cause of turbulence . . . . .	7
2.2 Generation of synthetic wind . . . . .	8
2.2.1 1-dimensional non-deterministic wind field . . . . .	8
2.2.2 3-dimensional non-deterministic wind field . . . . .	9
2.3 Blade forces and rotor torque . . . . .	9
2.3.1 Blade Element Momentum (BEM) theory . . . . .	12
<b>3 Rigid multibody dynamics</b>	<b>16</b>
3.1 Coordinate system transformations . . . . .	16
3.1.1 Bryant angles . . . . .	17
3.1.2 Euler parameters (quaternions) . . . . .	17
3.1.3 Vector and matrix algebra . . . . .	19
3.2 Equations of motion . . . . .	20
3.2.1 The concept of bodies, joints and force elements . . . . .	21
3.3 Rigid gear constraints . . . . .	23
3.3.1 Improved gear constraint (no rotation/fixed) . . . . .	24
3.3.2 Example of implementation – 2 bodies (no rotation/fixed) .	25
3.3.3 Example of implementation – 3 bodies (rotating) . . . . .	26
3.3.4 Differentiation of constraint equations . . . . .	29
3.3.5 Differentiation of gear constraint equations . . . . .	31

3.3.6	Post-processing . . . . .	32
3.4	Wind turbine model . . . . .	32
3.4.1	Forces and moments . . . . .	33
<b>4</b>	<b>Flexible gearbox model</b>	<b>40</b>
4.1	Mass-damper-spring system . . . . .	41
4.1.1	No damping . . . . .	42
4.1.2	Including damping . . . . .	42
4.1.3	Gear tooth stiffness evaluation . . . . .	44
4.1.4	Gear tooth damping . . . . .	45
4.2	Force element approach . . . . .	46
4.2.1	Realistic gear tooth stiffness . . . . .	48
<b>5</b>	<b>Fatigue</b>	<b>52</b>
5.1	Fatigue damage calculation . . . . .	52
5.1.1	Rainflow counting of stress cycles (linear damage hypothesis)	53
5.2	Fatigue from gear tooth surface stresses (pitting) . . . . .	54
5.2.1	Tooth surface stress details . . . . .	54
5.2.2	Results of accumulated fatigue damage . . . . .	57
<b>6</b>	<b>Conclusion</b>	<b>62</b>
<b>A</b>	<b>Example of equilibrium analysis</b>	<b>65</b>
<b>B</b>	<b>Multibody gear constraints</b>	<b>67</b>
<b>C</b>	<b>Gearbox data</b>	<b>70</b>
<b>D</b>	<b>Publications</b>	<b>71</b>
P1:	(Rigid MATLAB drivetrain model of a 500 kW wind turbine...) . . .	72
P2:	On Gear Tooth Stiffness Evaluation . . . . .	91
P3:	(A Rigid and a Flexible Multibody gearbox model) . . . . .	112
P4:	(Gear fatigue damage for increasing turbulence) . . . . .	136

# Chapter 1

## Introduction

The following chapter provides an introduction to the topics described in this thesis along with problem definition. An attempt has been made to briefly explain the challenges in a historical perspective related to past, current and expected future development within the area. Finally, an outline of the chapters in the present thesis is presented.

### 1.1 Definition of the problem

Multibody analysis computer programs are used in many places in the industry and for various research purposes. Multibody dynamics is based on classical mechanics and used to model how interconnected rigid or flexible bodies act together. Examples of a few engineering applications include: Modelling of wind turbines, satellites, robots, vehicles and other rotating machines. Each body may undergo large translational and rotational displacements. The simulation results can be coupled to CAD data in order to present realtime animations. Commercial packages tend to be very user-friendly and the commercial Multibody Dynamics (MBD) software, Adams<sup>1</sup> and SIMPACK<sup>2</sup> are perhaps among the most recognised tools in this field.

Although this thesis is a result of a “from wind to grid”-project, all the electrical aspects of e.g. voltage stability, shunt capacitor banks, power quality, induction generator models, interaction of wind farms with the power grid etc. are excluded. The focus of this work has been to develop code for analysing forces, torque and the main components, such as the gearboxes, in a wind turbine. The project and thesis involves mechanics/dynamics as well as wind engineering topics.

### 1.2 Historical background, current development and motivation

It is generally accepted among researchers that global warming is a consequence of greenhouse gases. Climate models predict changes such as rising sea levels and the consequences of nature’s complex and not fully understood ecosystem

---

<sup>1</sup><http://www.mscsoftware.com/product/adams>

<sup>2</sup><http://www.simpack.com/>



breakdowns, encouraging the development of increasingly efficient renewable energy sources. Every year now, more oil is consumed than discovered [1] and the trend is not in favour of future generations – in other words, global oil reserves are decreasing.

Wind energy causes no emissions and unlike oil, coal and gas, wind will never be depleted. Before the year 2000 the global cumulative installed wind capacity [2] was below 20.000 MW, which increased to 48.000 MW in 2004, 121.000 MW in 2008 and 283.000 MW in year 2012.

Today's tendency is to produce larger and larger wind turbines in order to increase the efficiency and to reduce the cost of energy. This problem is known as upscaling and described in e.g. [3] which also presents a simple theoretical model for upscaling according to  $m \sim s^3$  and  $P \sim s^2$ , where  $m$  is the mass,  $s$  is the scaling factor and  $P$  is power output. It can be seen that, at some point, the mass becomes too big. In the past few years, a number of wind turbines from 4-7.5 MW wind turbines have been developed. Siemens Wind Power already have the SWT-6.0-154 offshore wind turbine (also known as Turbina Sapiens) with direct drive technology ready for sales<sup>3</sup>. Vestas is expected to release the new "game changer"<sup>4</sup> V164-8.0 MW offshore wind turbine in 2015 and recently claimed<sup>5</sup> "there had been no major problems with the prototype".



Figure 1.1 500 kW Nordtank windturbine at DTU Risø, Roskilde, Denmark.



Figure 1.2 Meteorological (met) mast at DTU Risø, Roskilde, Denmark.

Using gearboxes in wind turbines is challenging because especially offshore wind turbines are subject to extreme conditions, e.g. waves, generally stronger

<sup>3</sup><http://renewables.seenews.com/news/siemens-launches-sale-of-6-mw-offshore-wind-turbine-164295>

<sup>4</sup><http://renews.biz/48963/vestas-builds-8mw-game-changer/>

<sup>5</sup><http://www.reuters.com/article/2013/08/29/vestas-offshore-idUSL6N0GT27A20130829>

and steadier wind and generally a harsh environment (e.g. corrosive action of salt water etc). Additionally, it is more difficult and expensive to do maintenance repairs offshore. Gearboxes require frequent maintenance and gearbox failures are very expensive. The direct-drive technology (used by Siemens and others) completely eliminates this component and it is therefore a mechanically simpler system with fewer moving parts. Fewer rotating components and a simpler design make maintenance cheaper (e.g. no oil change, reduced bearing-related problems). On the other hand, the direct-drive technology depends on expensive rare earth magnets<sup>6</sup>. In an interview, Vestas' head of technology research, Finn Strøm Madsen, said that they only<sup>7</sup> "require a tenth of the rare-earth metals needed to make the magnets in a direct-drive turbine of the same size". The same article states that "China controls more than 90 percent of the global market for the metals". Finn Strøm Madsen is later quoted as saying: "If you need spare parts for the direct-drive generator in five or 10 years and you cannot get them, that's a totally different risk scenario".

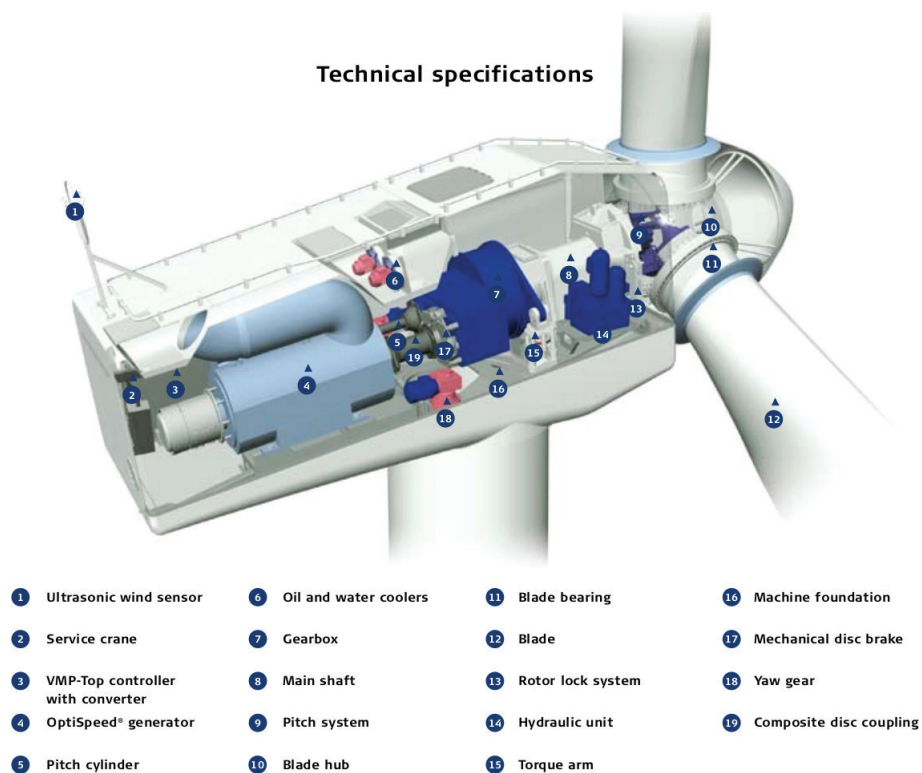


Figure 1.3 V52 wind turbine. Illustration courtesy of Vestas Wind Systems A/S.

<sup>6</sup><http://www.cleantechinvestor.com/portal/wind-energy/9552-the-giant-wind-gamble.html>

<sup>7</sup><http://www.bloomberg.com/news/2011-05-26/siemens-bets-on-new-technology-in-offshore-wind-turbine-battle-with-vestas.html>

To put everything in a larger context, the wind turbine capacity has increased by around 30-40 times in the last 3-4 decades and in the near future the wind turbine capacity can be increased up to 10-12 MW according to [4]. Another perspective to this discussion is that energy storage technologies (batteries, fly-wheels, pumped hydro, etc. also discussed in [4]) need to be further developed in order to increase power yield at times with surplus in the power production. There have been a lot of discussions about the need in the future to move further on to using intelligent/smart power grid solutions where e.g. electrical machines such as dish washers, washing machines, dryers, etc. only run in the night or when the electricity price is low<sup>8</sup>. Also a recent trend is to manufacture electrically driven cars like the Tesla Model S<sup>9</sup> with its slogan “Zero emissions. Zero compromises”. Unfortunately, the transition cannot be described as a walk in the park – a few months ago Europe’s foremost champion for electric cars, the company called Better Place, was declared bankrupt<sup>10</sup>. There is no doubt that it will be a challenge to continue to reduce the cost of electricity and to further promote renewable energy such as wind technology as a solution to global warming and the lack of fossil fuels in the future. Plenty of backup power (energy storage) is required if the wind does not blow at certain times when electricity is needed.

The gearbox is said to be the weakest link in a wind turbine and a more thorough discussion of gearbox technologies, including a historic perspective of the direct-drive approach for wind-turbines, is given in [5]. The technology battle between manufacturers using gearboxes or those using direct-drive technology is not discussed further in this thesis. Although this thesis does not address the direct-drive technology and even though Figure 1.3 shows an illustration of a Vestas wind turbine, there is no conflict of interest in relation to the research carried out. Neither Vestas, Siemens or any other wind turbine manufacturer has been involved in this project (or in funding it) so the author does not address the question of which technology is better than the other.

In this project, there was access to measurements from a 500 kW wind turbine which justifies focusing on the geared technology. The present thesis describes an approach to the modelling of wind turbines with gearboxes, but the multi-body approach could also be used for modelling a gearless wind turbine.

---

<sup>8</sup><http://www.stateofgreen.com/en/InFocus/Wind-Integration--Moving-towards-the-Smart-Grid>

<sup>9</sup><http://www.teslamotors.com/models>

<sup>10</sup><http://singularityhub.com/2013/06/09/electric-car-company-better-place-bankrupt-burns-nearly-1-billion/>

### 1.3 Thesis layout and structure

The following is a description of the chapters of this thesis:

- Chapter 1 includes general remarks, a short introduction to the field of wind turbines and the need for renewable energy, the technological aspects of using gearboxes in wind turbines, etc.
- Chapter 2 is devoted to introducing some basic concepts in relation to wind and aerodynamic modelling. This is the basis for understanding FLEX5.
- Chapter 3 introduces the concept of rigid multibody dynamics. Of particular interest will be the modelling of (planetary) gearboxes, gear teeth, obtaining gear tooth reaction forces, etc.
- Chapter 4 takes the discussion and model to a more advanced level by describing a gearbox multibody model where some bodies are connected by springs and dampers.
- Chapter 5 describes how the multibody model is used to predict fatigue in the gearbox, e.g. on the tooth surface.
- Chapter 6 summarises the work and provides suggestions for future work.

## References

- [1] W. Palz, *Wind Power for the World, The Rise of Modern Wind Energy*. Pan Stanford Publishing, 2013.
- [2] “Global wind report – annual market update 2012,” tech. rep., 2012.
- [3] G. Sieros, P. Chaviaropoulos, J. D. Sorensen, B. H. Bulder, and P. Jamieson, “Upscaling wind turbines: theoretical and practical aspects and their impact on the cost of energy,” *Wind Energy*, vol. 15, pp. 3–17, JAN 2012.
- [4] M. Islam, S. Mekhilef, and R. Saidur, “Progress and recent trends of wind energy technology,” *Renewable and Sustainable Energy Reviews*, vol. 21, pp. 456–468, 2013.
- [5] A. Ragheb and M. Ragheb, “Wind turbine gearbox technologies,” *2010 1st International Nuclear and Renewable Energy Conference, INREC’10*, 2010.

## Chapter 2

### Wind and aerodynamics

Aerodynamics is the study of the behaviour of objects and forces in an air flow. The science behind aerodynamics is comprehensive and this chapter, therefore, only describes a few fundamental basic concepts.

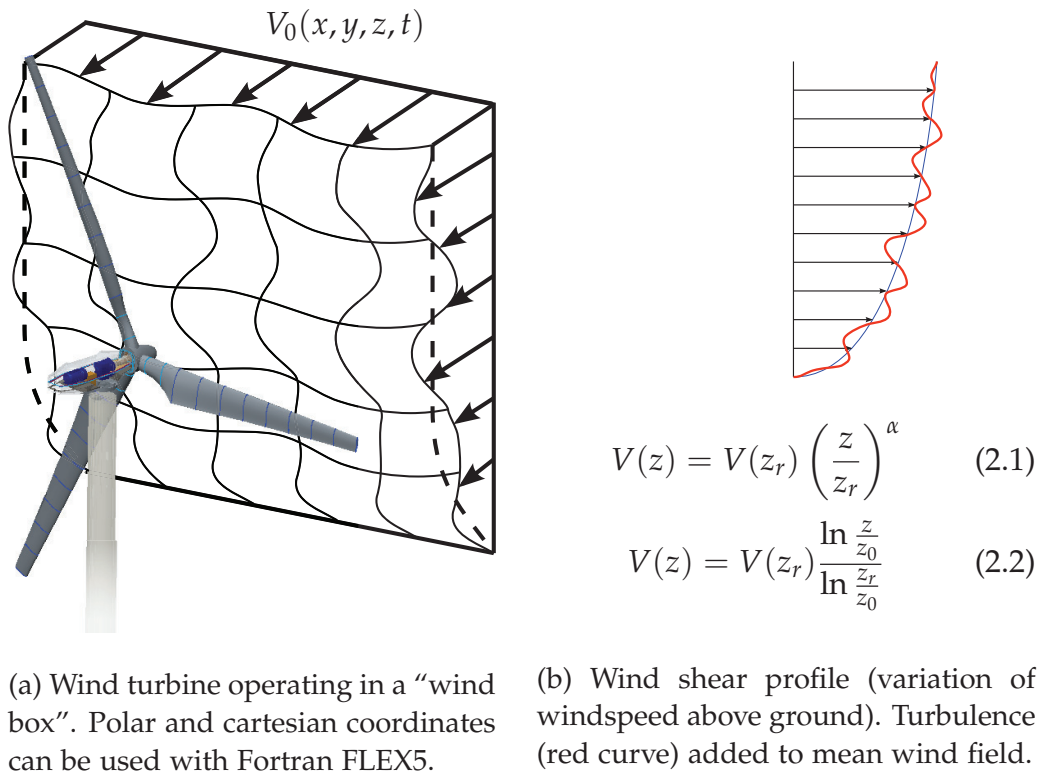


Figure 2.1 Wind turbine subject to atmospheric turbulence.

An introduction to the theory about aerodynamics of wind turbines is provided in [1]. Aerodynamic/aeroelastic codes like FLEX5 [2] are used for modelling the physics of wind turbines interacting in a turbulent wind field. The part of the atmospheric flow closest to the ground, the surface layer is of particular interest. The output from aerodynamics/aeroelastic tools consists of timeseries data of e.g. power yield, forces and torque on blades and on the tower. The quality of aerodynamic/aeroelastic model output depends on to what degree input values are realistic and e.g. the accuracy of the physically correct power spectra and spatial coherence of the wind field.



Figure 2.1 illustrates the concept of turbulence as a fluctuating and a mean wind speed part. Equations for the power law and logarithmic profiles [3] are shown in Equation (2.1) and (2.2), where  $V(z)$  is the wind speed at the height above ground  $z$ . The wind shear or power law exponent is denoted  $\alpha$ . The roughness length is  $z_0$  and it is a measure of ground disturbances and obstacles. Small roughness lengths mean only a few flow disturbances and obstacles are present, like for instance wind above calm water. Longer roughness lengths indicate buildings, trees and other obstacles that cause frictional forces and delay, local speed and direction changes such that turbulence is generally increased with larger values of  $z_0$ .

## 2.1 The nature, statistical properties and cause of turbulence

Turbulence is generated either from pressure gradients and surface roughness or from heat convection due to temperature differences between ground and air [4]. Temperature gradients can arise due to uneven solar heating. Hot air rises up above colder air and somewhere between the earth's poles and the equator, air masses meet and mix up in frontal systems [5]. But also the Coriolis force, caused by the rotation of the earth itself, has an impact. This effect creates a very complex system of both large and small-scale air flows. From weather forecasts, it is known that the weather (e.g. amount of sun, rain, air temperature, wind speed, pressure, etc) is not easily predicted even though large computing clusters with many thousands of processors are used.

A turbulent wind field is said to be stochastic using probability theory terminology and an example of this "chaotic" phenomenon is shown with the red curve in Figure 2.1. The wind shear equations (2.1) and (2.2) resemble the atmospheric boundary layer, if sufficient data are collected from e.g. meteorological masts (see Figure 1.2 on page 2 in the introduction). Turbulence makes the wind non-deterministic although computer-generated turbulence can be reproduced over and over again using the same random seed numbers. The mean (the deterministic part) and the variance of the wind speed is given by [4]

$$\bar{v} = \frac{1}{T} \int_0^T \mathbf{v}(t) dt \quad (2.3) \quad \overline{v^2} = \frac{1}{T} \int_0^T (\mathbf{v}(t) - \bar{v})^2 dt \quad (2.4)$$

The standard deviation is the square root of the variance, i.e.  $\sigma = \sqrt{\overline{v^2}}$  in [m/s]. Notice that in fluid dynamics, it is typical to decompose a signal into a mean (i.e.  $\bar{v}$ ) and a fluctuating part, i.e.  $\mathbf{v}'(t) \equiv \mathbf{v}(t) - \bar{v}$ . This decomposition process is known as Reynolds averaging. The turbulence intensity is defined

$$TI \equiv \frac{\sigma}{\bar{v}} = \frac{\sqrt{\overline{v^2}}}{\bar{v}} \quad (2.5)$$

which can also be described as the root-mean-square (RMS) of the velocity fluctuations  $\mathbf{v}'(t)$  divided by the Reynolds averaged mean velocity.

## 2.2 Generation of synthetic wind

A time series can be decomposed into a mean wind speed component added with fluctuations. For all methods, deterministic  $u_d$  and stochastic  $u_s$  wind parts are added together:  $U(x, y, z, t) = u_d(x, y, z, t) + u_s(x, y, z, t)$  and similar procedures are used in the lateral  $V(x, y, z, t)$  and vertical directions  $W(x, y, z, t)$ . To give an idea of how software packages resemble the physics of the real world, an example of how to construct a 1D wind field is given below.

### 2.2.1 1-dimensional non-deterministic wind field

The following is an example of generating a single-point stochastic wind field, calculated as the finite sum of coefficients,  $a_0$ ,  $a_n$  and  $b_n$ . Using a discrete Fourier transformation (DFT) [1]

$$a_0 = \frac{1}{N} \sum_{n=1}^N u_i \quad \text{mean wind speed} \quad (2.6)$$

$$u(t) = a_0 + \underbrace{\sum_{n=1}^{N/2} a_n \cos(\omega_n t) + b_n \sin(\omega_n t)}_{\text{fluctuating/turbulent part}}, \quad \omega_n = \frac{2\pi n}{T} \quad (2.7)$$

$$a_n = \frac{2}{N} \sum_{i=1}^N u_i \cos\left(\frac{2\pi n}{N} i\right), \quad n = 1, \dots, \frac{N}{2} - 1 \quad (2.8)$$

$$b_n = \frac{2}{N} \sum_{i=1}^N u_i \sin\left(\frac{2\pi n}{N} i\right), \quad n = 1, \dots, \frac{N}{2} - 1 \quad (2.9)$$

The stochastic wind signal can be approximated as a sum of finite-length periodic signals. But often the Fast Fourier Transform (FFT) is used for making a spectral representation of the wind by transferring a signal from time-domain into the frequency domain. The Power Spectral Density (PSD) can be found, which has dimensions  $[(\text{m/s})^2/\text{Hz}]$  or  $[\text{W/kg}]$  [4, 1] but by using an inverse DFT, a time series can also be constructed from a known power spectral density function (PSD). Typically, either a von Karman's or a Kaimal [6] spectrum is used. The latter, which better corresponds with experimental data, is shown below according to [7]

$$PSD(f) = \frac{f S_k(f)}{\sigma_k^2} = \frac{4 f L_k / V_{\text{hub}}}{(1 + 6 f L_k / V_{\text{hub}})^{\frac{5}{3}}} \quad (2.10)$$

where  $V_{\text{hub}}$  is wind speed at hub height,  $f$  is the frequency [Hz],  $k$  is an index for direction (i.e. 1=longitudinal, 2=lateral and 3=upward),  $S_k$  is a single-sided velocity component spectrum,  $\sigma_k$  is standard deviation and  $L_k$  is an integral scale parameter. A single-point time-series can then be generated according to [1]:

$$u(t) = \bar{u} + \sum_{n=1}^{N/2} \sqrt{\frac{2 \text{PSD}(\omega_n)}{T}} \cos(\omega_n t - \phi_n), \quad t = i\Delta t \text{ for } i = 1, \dots, N \quad (2.11)$$

### 2.2.2 3-dimensional non-deterministic wind field

The turbulence field generated above only describes a single point in the rotor swept area. Aeroelastic codes like FLEX5 need a turbulence box such as illustrated in Figure 2.1a with a wind speed grid defined using either polar (standard Pascal version of FLEX5) or rectangular (Fortran version) coordinates. The default FLEX5 (Pascal-version) wind field uses polar coordinates. It has 5 radial stations and 32 azimuthal stations.

For generating 3D turbulent wind fields, important stochastic wind turbulence models include methods proposed by Paul Veers [8] and Jacob Mann (see e.g. [9] and [10]). The standard wind generator in FLEX5 (Windsim7) uses the Sandia/Veers-method [11, 8]. Windsim7 generates a realistic 3D turbulent wind field. A free Matlab-program for generating a 3D wind field is also found on Matlab central<sup>1</sup>, which is an online forum or user community where Matlab users can exchange code.

## 2.3 Blade forces and rotor torque

The history of wind turbine blades (airfoils) began with using published blade profiles from wind tunnel research performed by NACA (The United States National Advisory Committee for Aeronautics) [12]. Blades are manufactured extensively using composite materials and only small blade profile changes can lead to huge power curve and noise levels [13]. Generally, a lot of knowhow from the aerospace industry is involved in the development of improved blades in terms of avoiding problems related to e.g. local buckling and fibre/matrix/interlaminar/sandwich failure (see [14]).

An example of airfoil forces (including velocity triangle) and parameters is shown in Figure 2.2, where  $\alpha$  is the angle of attack,  $W$  is induced velocity and  $V_{\text{rot}}$  is rotor plane velocity. The induced velocity  $W$  should be understood as an

<sup>1</sup><http://www.mathworks.com/matlabcentral/fileexchange/35867-3d-turbulent-wind-field-simulation-by-means-of-sandia-method-for-wind-energy-applications>



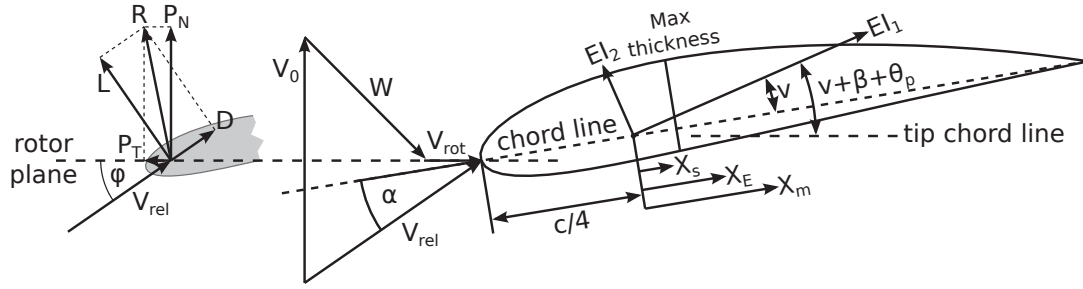


Figure 2.2 Airfoil forces ( $L$ =lift,  $D$ =drag,  $R$ =resultant force vector,  $P_N$ =normal of  $R$  and  $P_T$ =tangential of  $R$ ) for incoming wind  $V_0$ , which is seen as  $V_{rel}$  by the airfoil. Faster airflow over the top of the airfoil generates less pressure than below (Bernoulli equation). The pressure difference causes the lift force  $L$  (left illustration), which rotates the hub.

important velocity, which acts as a brake on the incoming wind, due to rotor axial pressure. The chord length is  $c$ ,  $EI_x$  denotes bending stiffness around principal axis  $x$ ,  $v$  is the angle from the chord line to the first principal axis,  $\beta$  is the twist angle and finally  $X_s$ ,  $X_E$  and  $X_m$  denotes respectively distances of shear centre, point of elasticity and mass centre measured from the reference point [1]. Information about these parameters must be obtained using e.g. wind tunnel experiments, and from the lift and drag equations, corresponding lift ( $C_l(\alpha)$ ) and drag ( $C_d(\alpha)$ ) coefficients can be obtained.

$$L = \frac{1}{2} \rho V_{rel}^2 c C_l(\alpha) \quad D = \frac{1}{2} \rho V_{rel}^2 c C_d(\alpha) \quad (2.13)$$

(2.12)

In order to calculate the rotor torque, the objective is to take a turbulent wind field (i.e.  $V_0$ ), find a method to calculate induced velocities (i.e.  $W$ ), add these vectors to the rotor plane velocity (i.e.  $V_{rot}$ ) and the result is the wind speed seen by the blade (i.e.  $V_{rel}$ ). Once the blade forces are known at each radial station, these forces are integrated along the length of each blade and for each blade, the torque from known blade forces can be found. The resulting torque is a summation of torque on all 3 blades. This torque accelerates the wind turbine from standstill and drives the main shaft on the low-speed side. The generator torque is lower but put on the high-speed side of the gearbox, meaning that the rotor does not accelerate above a pre-determined angular velocity. Two approaches [15] for determining blade forces are:

- Numerical methods based on the Euler equations (motion for inviscid fluid) or the Navier-Stokes equations (if viscosity is considered). These are becoming faster and increasingly popular in some situations (e.g. yaw or interaction of wind turbines in wind parks [15]).

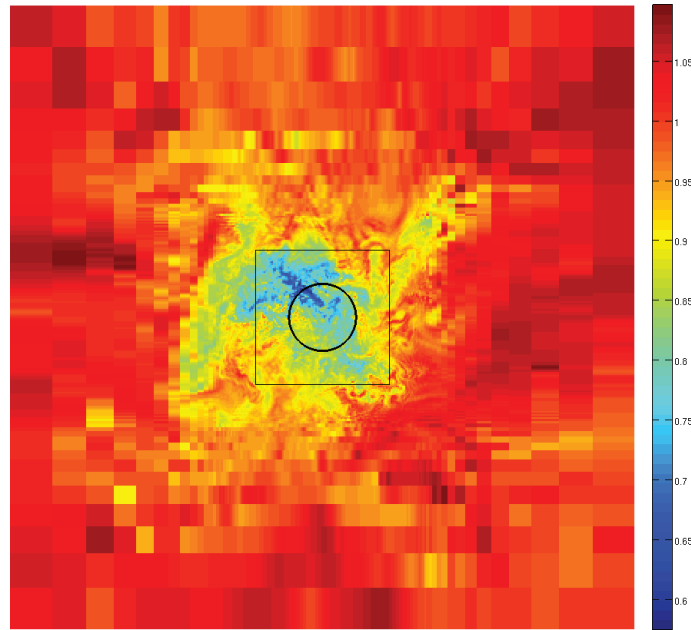


Figure 2.3 CFD (Ellipsys3D) coupled to FLEX5 with cyclic boundary conditions (infinite long row of wind turbines in a wind farm). Snapshot from work of PhD student Søren Juhl Andersen.

- The Blade Element Momentum method (BEM) from [16], which is computationally very fast/efficient and the most popular approach today. The first table in [17] shows that the 5 aero-hydro-servo-elastic modelling software packages: FAST<sup>2</sup>, BLADED<sup>3</sup>, FLEX5<sup>4</sup>, ADAMS<sup>5</sup> and HAWC2<sup>6</sup> all use the BEM-method.

An example of recent development is to couple numerical Navier-Stokes methods involving Computational Fluid Dynamics (CFD) with structural codes. The wind field snapshot in Figure 2.3 shows a wind turbine in an “infinite wind farm” simulated using cyclic domain boundary conditions and the wake effects are studied. The wind field is used with FLEX5 which rotates the blades, main shaft, deflects the blades etc. and the CFD geometry is updated and meshed until a steady solution has been found.

The 3D flow around a wind turbine is highly complex and CFD-based methods yield good insight into the details of the flow field: Investigation of streamlines, vortex phenomena/patterns, local effects of flow separation, laminar to

<sup>2</sup>National Renewable Energy Laboratory, Golden, Colorado, US

<sup>3</sup>GH Bladed: Garrad Hassan & Partners Limited, Bristol, UK

<sup>4</sup>Stig Øye, Gentofte, Denmark

<sup>5</sup>MSC Software Corporation, Santa Ana, California 92707, US

<sup>6</sup>DTU Risø, Roskilde, Denmark

turbulent transition of boundary layer, etc. However, for practical reasons (i.e. calculation time) these details are not important for this work and therefore the focus is on the BEM-method before discussing implementation of the multibody program.

### 2.3.1 Blade Element Momentum (BEM) theory

The physical properties of the nacelle, tower, blades and rotor must be taken into account (e.g. mass properties, stiffness and damping coefficients, etc.) for solving the non-linear dynamic equations of motion of the form

$$\mathbf{M}\ddot{\mathbf{x}} + \mathbf{C}\dot{\mathbf{x}} + \mathbf{K}\mathbf{x} = \mathbf{F}_g(t, \mathbf{x}, \dot{\mathbf{x}}) \quad (2.14)$$

where  $t$  is time,  $\mathbf{x}$  is the degrees of freedom (DOF)-vector,  $\mathbf{M}$  the mass matrix,  $\mathbf{C}$  the damping matrix,  $\mathbf{K}$  is the stiffness matrix and  $\mathbf{F}_g$  is the vector of external forces and torque.

Equation (2.14) must be solved in order to obtain the DOFs for positions  $\mathbf{x}$ , velocities  $\dot{\mathbf{x}}$  and accelerations  $\ddot{\mathbf{x}}$  using e.g. a Runge-Kutta Nyström (RKN) time-integration scheme (as in [1]). The BEM-method is the most commonly used method for calculating the induced velocities ( $W$  in Figure 2.2) and thus the local angles of attack ( $\alpha$  in Figure 2.2) [1]. This is done quickly by using empirical values (e.g. lift and drag coefficients) contrary to using numerical CFD-calculations. Once the local angle of attack and/or induced velocities are known, the loads on the right-hand-side (RHS) of Equation (2.14) can be calculated and the solution for the next time-step can be calculated.

The procedure for doing an unsteady BEM calculation is [1]:

- read geometry and program parameters (timestep, end time, blade data, twist angle, lift and drag coefficients as a function of angle of attack, etc.)
- initialise blade position and velocity
- discretise blades in  $N$  elements
- initialise induced velocities, for all timesteps, for all blades and for all blade elements
- Calculate the velocity relative to the blade  $\mathbf{V}_{\text{rel}}$  as the sum of  $\mathbf{V}_0$ ,  $\mathbf{V}_{\text{rot}}$ ,  $\mathbf{W}$  shown in Figure 2.2. These terms correspond to wind speed, rotor plane velocity and induced velocity respectively, where the latter is a kind of wind disturbance velocity. The following applies

$$\mathbf{V}_{\text{rel}} = \mathbf{V}_0 + \mathbf{V}_{\text{rot}} + \mathbf{W} \Rightarrow \begin{pmatrix} V_{\text{rel},y} \\ V_{\text{rel},z} \end{pmatrix} = \begin{pmatrix} V_y \\ V_z \end{pmatrix} + \begin{pmatrix} -\omega x \cos \theta_{\text{cone}} \\ 0 \end{pmatrix} + \begin{pmatrix} W_y \\ W_z \end{pmatrix} \quad (2.15)$$

where  $\omega$  is the rotational speed of the rotor,  $x$  is radial distance measured from hub and  $\theta_{\text{cone}}$  is the rotor coning angle measured from the vertical plane. The rotor coning angle is typically not aligned completely with the vertical plane, e.g. it can be changed such that the blades move even further away from the tower, to avoid the blades hitting the tower.

- The flow angle  $\phi$  and angle of attack  $\alpha$  can be calculated using

$$\tan \phi = \frac{V_{rel,y}}{V_{rel,z}}, \quad \alpha = \phi - (\beta - \theta_p) \quad (2.16)$$

where  $\beta$  is the twist angle and  $\theta_p$  is the pitch angle, both shown on Figure 2.2.

- The static lift  $C_l$  and drag  $C_d$  coefficients are determined from a table (experimental data from wind tunnel or perhaps in combination with CFD or from books when using standardised profiles).
- The dynamic airfoil data should then be determined using a dynamic stall model, which takes into account that there will be a delay when the angle of attack is changed, before the airflow properties change.
- The normal and tangential loads are

$$p_z = L \cos \phi + D \sin \phi, \quad p_y = L \sin \phi - D \cos \phi \quad (2.17)$$

where  $L$  and  $D$  can be calculated using (2.12) and (2.13).

- New equilibrium values for induced velocities  $W_z$  and  $W_y$  should then be calculated and new unsteady induced velocities, using a dynamic wake model, should be found.
- The induced velocity for each blade should be calculated, using a yaw model for calculating the azimuthal variation.

Some of the equations and more detailed aspects of this method have been excluded here, because the aeroelastic FLEX5 code has not been improved or modified in any way in this project.

## References

- [1] M. O. L. Hansen, *Aerodynamics of Wind Turbines*. Earthscan, 2nd ed, 2009.

- [2] S. Øye, *Various FLEX 5 documentation*. DTU Mechanical Engineering, 2001.
- [3] G. K. V. Ramachandran, *A numerical model for a floating TLP wind turbine*. PhD thesis, Technical University of Denmark, Department of Wind Energy.
- [4] R. Gasch and J. Tvele, *Wind power plants: fundamentals, design, construction and operation*. Springer, 2012.
- [5] J. Berg and J. Mann, *Introduction to Micro Meteorology for Wind Energy – 45701*. Risø DTU, Roskilde, 2011.
- [6] J. Kaimal, J. Wyngaard, Y. Izumi, and O. Coté, “Spectral characteristics of surface-layer turbulence,” *Quarterly Journal of the Royal Meteorological Society*, vol. 98, no. 417, pp. 563–589, 1972.
- [7] “Ds/en 61400-1:2005 – elproducerende vindmøller – del 1: Konstruktion-skrav.”
- [8] P. S. Veers, “Three-dimensional wind simulations.,” *Sandia Report, SAND-0152*, 1988.
- [9] J. Mann, “The spatial structure of neutral atmospheric surface-layer turbulence,” *J. Fluid Mech.*, vol. 273, pp. 141–168, 1994.
- [10] J. Mann, “Wind field simulation,” *Probabilistic Engineering Mechanics*, vol. 13, no. 4, pp. 269–282, 1998.
- [11] S. . Jan, “Digital simulation of random processes and its application,” *Journal of Sound and Vibration*, Vol. 25,, No. 1, 1972.
- [12] E. N. Jacobs, K. E. Ward, and R. M. Pinkerton, “The characteristics of 78 related airfoil sections from tests in the variable-density wind tunnel,” *CASI*, 1933.
- [13] H. Stiesdal, “The wind turbine components and operation,”
- [14] T. J. Kryger, W.-H. Jakob, and P. Peter, “New guidance for the development of wind turbine blades,” *Copenhagen Offshore Wind*, 2005.
- [15] M. Hansen, J. Sørensen, S. Voutsinas, N. Sørensen, and H. Madsen, “State of the art in wind turbine aerodynamics and aeroelasticity,” *Progress in Aerospace Sciences*, vol. 42, no. 4, pp. 285 – 330, 2006.
- [16] H. Glauert, “Airplane propellers,” in *Aerodynamic theory*, pp. 169–360, Springer, 1935.

- [17] J. Jonkman, S. Butterfield, P. Passon, T. Larsen, T. Camp, J. Nichols, J. Azcona, and A. Martinez, "Offshore code comparison collaboration within iea wind annex xxiii: Phase ii results regarding monopile foundation modeling," *European Offshore Wind Conference & Exhibition, 4–6 December 2007, Berlin, Germany*, p. 12.

## Chapter 3

### Rigid multibody dynamics

The history of multibody dynamics for computer simulations [1] began with Newton's laws of motion in the 17th century, when considering something simple, a free particle. Equations for rigid body motion were introduced in the 18th century by Euler who already used the free body principle with reaction forces and together these contributions are known as Newton-Euler equations. In the latter part of the 20th century, computer software programs that, for instance, allowed animations of the solution were developed. The first textbooks specifically about computer-aided analysis of multibody systems [2, 3, 4] are from around 1988-1989 and more thorough historical details of past and recent developments are described in e.g. [1, 5].

Newtonian mechanics is a type of analysis involving motion, time and forces and dynamics is a description of non-stationary systems [2]. Two categories exist: Kinematics dealing with the motion of the bodies and dynamics which deals with the forces and moments. Multibody systems are collections of rigid or flexible bodies/links. Multibody dynamics is an area widely used, especially in robotics, vehicle dynamics (e.g. bicycles, automobiles, trains), aerospace (e.g. spacecrafts, satellites/space stations) industries and wherever machines/mechanisms are used including bio-dynamical systems (e.g. human bodies, animals). Bodies are connected with constraint elements, e.g. joints, bearings, force elements (springs/dampers/actuators). The motion of bodies may undergo large translations and rotational displacements [4]. The motion of rigid bodies can be described in 2D using 3 generalised coordinates and in 3D using 6 generalised coordinates.

#### 3.1 Coordinate system transformations

Coordinate system transformations are important, not only for understanding how aeroelastic codes work and transfer the blade loads and rotor torque to other coordinate systems (or references of frame) locally inside the wind turbine. Coordinate system transformations are also important for understanding the concept of multibody joints and how bodies are assembled and fixed using constraints and references from inertial (global) references of frame into local (rotating or non-rotating) references of frame.

### 3.1.1 Bryant angles

An example of describing a wind turbine using several coordinate systems and Bryant angles with corresponding transformation matrices is given in [6]. A more general approach is presented using the following equations (from [2]), where  $\mathbf{A}$  denotes a  $3 \times 3$  transformation matrix.

$$\mathbf{A}_1 = \begin{bmatrix} 1 & 0 & 0 \\ 0 & c\phi_1 & -s\phi_1 \\ 0 & s\phi_1 & c\phi_1 \end{bmatrix} \quad \mathbf{A}_2 = \begin{bmatrix} c\phi_2 & 0 & s\phi_2 \\ 0 & 1 & 0 \\ -s\phi_2 & 0 & c\phi_2 \end{bmatrix} \quad \mathbf{A}_3 = \begin{bmatrix} c\phi_3 & -s\phi_3 & 0 \\ s\phi_3 & c\phi_3 & 0 \\ 0 & 0 & 1 \end{bmatrix} \quad (3.1)$$

where  $c\phi$  is short for  $\cos \phi$  and  $s\phi$  is short for  $\sin \phi$ . Hence the complete transformation is given by  $\mathbf{A} = \mathbf{A}_1 \mathbf{A}_2 \mathbf{A}_3$  and the nine matrix elements are known as direction cosines [2]. The column vectors of  $\mathbf{A}$  are orthogonal basis vectors (an orthonormal set), i.e. they are linearly independent and  $\mathbf{A}^T = \mathbf{A}^{-1}$  is called an orthogonal matrix. An alternative coordinate system representation is Euler angles, which is similar to Bryant angles except that the rotation axes are different (see e.g. [2]).

An attempt at showing a coordinate transformation of an object (the teapot can be considered a rigid body) is seen in Figure 3.1. The black coordinate system is the inertial reference of frame and the red coordinate system is the transformed coordinate system. Coordinate systems can be moving/rotating (e.g. wind turbine blades, rotating shafts) or fixed (wind turbine tower).

### 3.1.2 Euler parameters (quaternions)

It is generally known that despite Euler and Bryant angles are commonly used to describe the orientation of a body, these 3 parameters (Equation (3.1)) lead to singularities when rotation axes coincide (some values of  $\phi = n\pi$ ,  $n = 0, \pm 1, \pm 2, \dots$  due to the sine/cosine functions).

Euler's theorem expresses that a rotation in space can always be expressed as a rotation of some angle about some given axis. A quaternion is a vector of 4 parameters where the first is the rotational angle  $\phi$  and the last 3 is a vector in 3-dimensional space,  $\mathbf{e} = \{e_1, e_2, e_3\}^T$ . Euler parameters are a subset of quaternions, because Euler parameters are unit quaternions. Using unit vector  $\mathbf{u}$  for the rotational axis, the above-mentioned can be expressed using

$$\begin{aligned} e_0 &= \cos \frac{\phi}{2} \\ \mathbf{e} &= \mathbf{u} \sin \frac{\phi}{2} \end{aligned} \quad (3.2) \quad \begin{aligned} e_0^2 + \mathbf{e}^T \mathbf{e} &= 1 \\ e_0^2 + e_1^2 + e_2^2 + e_3^2 &= 1 \end{aligned} \quad (3.3)$$



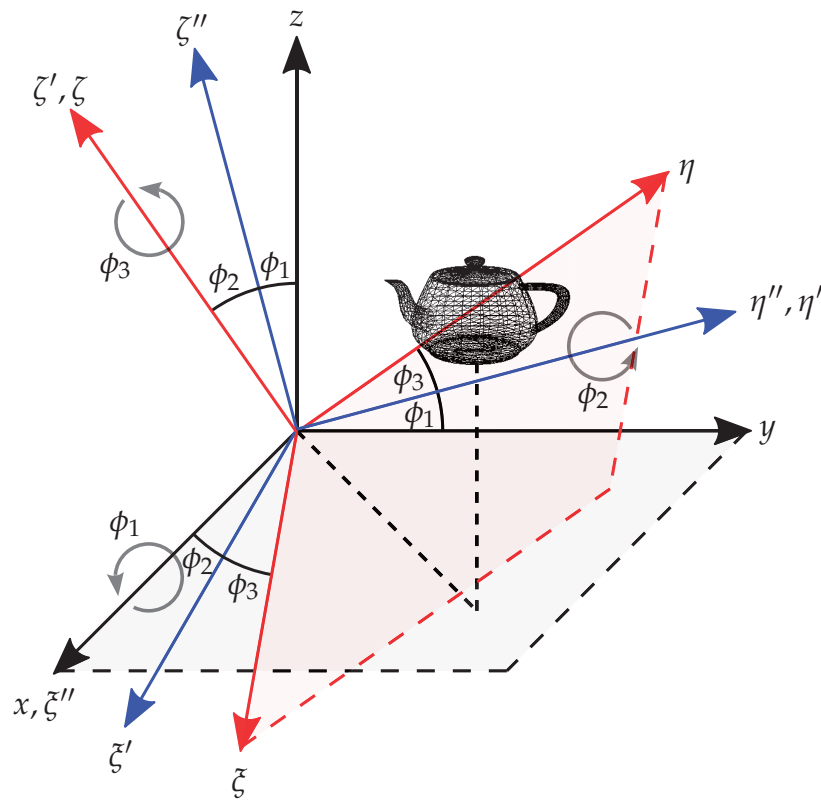


Figure 3.1 Sequential Bryant angle rotations (first  $\phi_1$  CCW about the  $x$ -axis, then  $\phi_2$  CCW about the  $\eta''$ -axis, finally  $\phi_3$  CCW about the  $\zeta'$ -axis).

and it is easy to see that the norm of the 4 Euler parameters is unity [2]. Euler parameters can be used to calculate direction cosines  $\mathbf{A}$  using

$$\mathbf{A} = 2 \begin{bmatrix} e_0^2 + e_1^2 - \frac{1}{2} & e_1 e_2 - e_0 e_3 & e_1 e_3 + e_0 e_2 \\ e_1 e_2 + e_0 e_3 & e_0^2 + e_2^2 - \frac{1}{2} & e_2 e_3 - e_0 e_1 \\ e_1 e_3 - e_0 e_2 & e_2 e_3 + e_0 e_1 & e_0^2 + e_3^2 - \frac{1}{2} \end{bmatrix} \quad (3.4)$$

To avoid singularities, Euler parameters are used in the multibody program. Another reason to use Euler parameters is that they only require 4 real numbers instead of 9 for a whole transformation matrix. Also the sine and cosines introduce round-off errors so when many  $3 \times 3$  transformation matrices are multiplied together, “drifting” can happen, meaning that after a while the resulting transformation matrix may not even be orthogonal anymore (causing distortion and arbitrary scaling). Euler parameters can also “drift” – they must be a unit quaternion and if the module is not 1 anymore, a possible solution is to re-normalise the vector of 4 Euler parameters.

### 3.1.3 Vector and matrix algebra

Generally, a prime is used to specify a vector in the local coordinate system and a vector without any prime specifies vectors in the global coordinate system. A transformation of a point in a local coordinate system  $\mathbf{s}'$  to a vector in the global coordinate system is typically written:  $\mathbf{s} = \mathbf{A}\mathbf{s}'$  (this implies  $\mathbf{s}' = \mathbf{A}^T\mathbf{s}$ ), where  $\mathbf{s}' = \{x', y', z'\}^T$ . The time-derivatives of the transformation matrix  $\mathbf{A}$  are (see e.g. [7, 2])

$$\dot{\mathbf{A}} = \tilde{\boldsymbol{\omega}}\mathbf{A} = \mathbf{A}\tilde{\boldsymbol{\omega}}' \quad (3.5) \quad \ddot{\mathbf{A}} = \dot{\tilde{\boldsymbol{\omega}}}\mathbf{A} + \tilde{\boldsymbol{\omega}}\tilde{\boldsymbol{\omega}}\mathbf{A} \quad (3.6)$$

where  $\boldsymbol{\omega} = \dot{\boldsymbol{\theta}}$  is the vector of angular velocity components and the skew-symmetric matrix of a vector  $\mathbf{s} = \{s_1, s_2, s_3\}^T$  is

$$\tilde{\mathbf{s}} = \begin{bmatrix} 0 & -s_3 & s_2 \\ s_3 & 0 & -s_1 \\ -s_2 & s_1 & 0 \end{bmatrix} \quad (3.7)$$

The time-derivatives of the transformation matrix become important when constraints are implemented. From Equation (3.5):  $\dot{\mathbf{s}} = \dot{\mathbf{A}}\mathbf{s}' = \tilde{\boldsymbol{\omega}}\mathbf{A}\mathbf{s}' = \tilde{\boldsymbol{\omega}}\mathbf{s}$  where  $\boldsymbol{\omega} = \{\omega_x, \omega_y, \omega_z\}^T$ .

Each body in space has six DOFs, three translational ( $\mathbf{s} = \{x, y, z\}^T$ ) and three rotational ( $\boldsymbol{\theta} = \{\theta_x, \theta_y, \theta_z\}^T$ ) parameters. The transformation matrix  $\mathbf{A}$  can be calculated once a sequence of rotations around each of the axes has been defined (e.g. Bryant or Euler angles or other sequences). However, when using e.g. Bryant or Euler angle parametrisation, singularities (gimbal lock) can arise.

This situation arises when one degree of freedom is lost, because two of the three planes become identically aligned. To avoid the problem with singularities, Euler parameters are used in the time-integration code (described in the next section).

Other important identities include rules for transposing a skew-symmetric matrix and calculating the cross product using the skew-symmetric matrix [7]

$$\tilde{\mathbf{s}} = -\tilde{\mathbf{s}}^T \quad \text{and} \quad \mathbf{s}_1 \times \mathbf{s}_2 = \tilde{\mathbf{s}}_1 \mathbf{s}_2 \quad (3.8)$$

Sometimes it is important to be able to re-arrange matrices such that equations can be reduced by collecting terms etc:

$$(\mathbf{A} \mathbf{B} \mathbf{C})^T = \mathbf{C}^T \mathbf{B}^T \mathbf{A}^T \quad (3.9) \quad (\mathbf{A} \mathbf{B} \mathbf{C}^T)^T = (\mathbf{C}^T)^T \mathbf{B}^T \mathbf{A}^T = \mathbf{C} \mathbf{B}^T \mathbf{A}^T \quad (3.10)$$

These identities and relations are useful when constraints are involved and a simple example will be provided in section 3.3.4 on page 29.

## 3.2 Equations of motion

The procedure is to solve  $n$  differential equations and  $m$  algebraic equations

$$\begin{cases} \mathbf{M} \ddot{\mathbf{q}} - \Phi_{\mathbf{q}}^T \boldsymbol{\lambda} = \mathbf{g}, & \Phi_{\mathbf{q}} = \frac{\partial \Phi}{\partial \mathbf{q}} \\ \Phi(\mathbf{q}, t) = 0 \end{cases} \quad (3.11)$$

where  $\mathbf{M} \in \mathbb{R}^{n \times n}$  is the mass/inertia matrix,  $\mathbf{q} \in \mathbb{R}^n$  is a vector of cartesian coordinates,  $\Phi_{\mathbf{q}} \in \mathbb{R}^{m \times n}$  is the Jacobian of the  $\Phi(\mathbf{q}, t) \in \mathbb{R}^m$  kinematic constraint equations,  $\boldsymbol{\lambda} \in \mathbb{R}^m$  are the Lagrange multipliers and  $\mathbf{g} \in \mathbb{R}^n$  are the external body forces applied in the global reference system.

Techniques for solving (3.11) are described in e.g. [2, 8, 9, 10]. Constraints are expressed at acceleration level, to form equations of motion from the DAE-system (3.11) into an ODE in the form given by [2]:

$$\begin{bmatrix} \mathbf{M} & -\Phi_{\mathbf{q}}^T \\ \Phi_{\mathbf{q}} & \mathbf{0} \end{bmatrix} \begin{Bmatrix} \ddot{\mathbf{q}} \\ \boldsymbol{\lambda} \end{Bmatrix} = \begin{Bmatrix} \mathbf{g} \\ \gamma \end{Bmatrix} \quad (3.12)$$

Sometimes the term  $\gamma$  is replaced by  $\gamma - 2\alpha\dot{\Phi} - \beta^2\Phi$ , where  $\alpha$  and  $\beta$  are positive constants [11]. This approach is known as Baumgarte stabilisation and the extra terms adjust for numerical errors (not eliminating, but typically decreasing drift in the solution – depending on chosen parameters).

Equation (3.12) is solved using initial positions/rotations and initial translational/angular velocities  $(\dot{x}, \dot{y}, \dot{z}, \omega_{\xi}, \omega_{\eta}, \omega_{\zeta})$ , where the axes  $\xi, \eta, \zeta$  (the same as

$x', y', z'$ ) are local coordinate system axes. An ODE-solver in Matlab is used to obtain positions/orientations from the previous (or initial) values using time-integration. Likewise velocities are calculated numerically from accelerations. To be more specific:

$$\mathbf{y} = \begin{Bmatrix} \mathbf{q} \\ \dot{\mathbf{q}} \end{Bmatrix} \quad \dot{\mathbf{y}} = \begin{Bmatrix} \dot{\mathbf{q}} \\ \ddot{\mathbf{q}} \end{Bmatrix} \quad (3.13)$$

or:

$$\begin{aligned} \mathbf{y} &= \{x, y, z, e_0, e_1, e_2, e_3, \dot{x}, \dot{y}, \dot{z}, \omega_\xi, \omega_\eta, \omega_\zeta\}^T \\ \dot{\mathbf{y}} &= \{\dot{x}, \dot{y}, \dot{z}, \dot{e}_0, \dot{e}_1, \dot{e}_2, \dot{e}_3, \ddot{x}, \ddot{y}, \ddot{z}, \dot{\omega}_\xi, \dot{\omega}_\eta, \dot{\omega}_\zeta\}^T \end{aligned}$$

Using  $\mathbf{y}$  (initially defined or from previous timestep), Equation (3.12) is solved to yield the accelerations  $\ddot{\mathbf{q}}$  in vector  $\dot{\mathbf{y}}$ . The new vector  $\dot{\mathbf{y}}$  should then be formed using the newly calculated accelerations and the already known translational velocities  $\{\dot{x}, \dot{y}, \dot{z}\}^T$ , together with the time derivative of Euler parameters [2]:

$$\dot{\mathbf{p}} = \frac{1}{2} \mathbf{L}^T \boldsymbol{\omega}', \quad \text{where: } \mathbf{L} = \begin{bmatrix} -e_1 & e_0 & e_3 & -e_2 \\ -e_2 & -e_3 & e_0 & e_1 \\ -e_3 & e_2 & -e_1 & e_0 \end{bmatrix} = [-\mathbf{e}, -\tilde{\mathbf{e}} + e_0 \mathbf{I}] \quad (3.14)$$

where  $\mathbf{p} = \{e_0, e_1, e_2, e_3\}^T$  and  $\boldsymbol{\omega}' = \{\omega_\xi, \omega_\eta, \omega_\zeta\}^T$ .

Time-integration routines such as ODE45 numerically integrate  $\dot{\mathbf{y}}$  in order to obtain the new positions and velocities in  $\mathbf{y}$  for the next timestep where everything is repeated. Equation (3.4) can be used to form the transformation matrix  $\mathbf{A}_i$  of rigid body  $i$ . This will then be the starting point of the next time-step calculation where coefficients are inserted into the Jacobian matrix and the term  $\gamma$  must be recalculated.

It should also be mentioned that, for the sake of simplicity and unless otherwise described, all bodies described in this thesis have local coordinate systems in their own centre of mass and angular velocities (and accelerations) are unlike translational DOFs described using local coordinate systems. When this is the case, the mass matrix becomes invariant and does not need to be recalculated in each time-step [7] and it is still easy to use matrix operations to convert to/from local/global coordinate systems.

### 3.2.1 The concept of bodies, joints and force elements

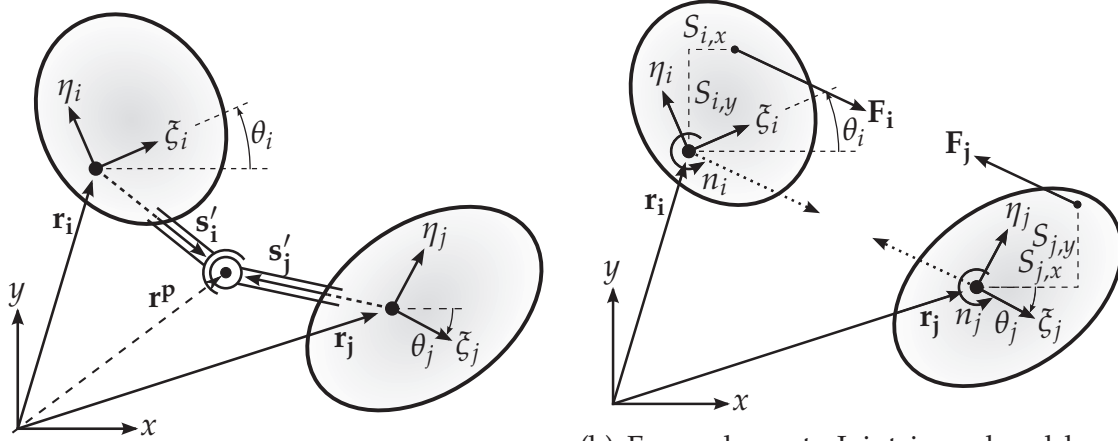
Consider a vector  $\mathbf{r}$  from the origin of the global coordinate system to the origin of a local coordinate system (Figure 3.2a). The vector  $\mathbf{s}'$  is defined from the local

coordinate system origo to e.g. a joint, connecting another body. By including the rotation of the object  $\mathbf{A}$ , the endpoint of  $\mathbf{s}'$  measured in global coordinates becomes  $\mathbf{r}^p = \mathbf{r} + \mathbf{A}\mathbf{s}'$  which is illustrated in Figure 3.2a. This figure also shows that two objects (body  $i$  and body  $j$ ) can be assembled and connected by a spherical joint using the constraint equation

$$\Phi^{(s,3)} \equiv \mathbf{r}_i^p - \mathbf{r}_j^p = \mathbf{r}_i + \mathbf{A}_i \mathbf{s}_i'^p - \mathbf{r}_j - \mathbf{A}_j \mathbf{s}_j'^p = \mathbf{0} \quad (3.15)$$

where

$$\mathbf{r}_{2D} = \begin{Bmatrix} x \\ y \end{Bmatrix}, \theta \text{ is a scalar} \quad \text{and} \quad \mathbf{r}_{3D} = \begin{Bmatrix} x \\ y \\ z \end{Bmatrix}, \quad \mathbf{p}_{3D} = \begin{Bmatrix} e_0 \\ e_1 \\ e_2 \\ e_3 \end{Bmatrix} \quad (3.16)$$



(a) Spherical joint: A rigid/constrained connection. The angle  $\theta$  is measured from global  $(x, y)$  to local reference of frame  $(\xi, \eta)$ .

(b) Force element: Joint is replaced by a force element (spring, damper or actuator). Forces  $\mathbf{F}_i$  and  $\mathbf{F}_j$  work at a distance of  $\mathbf{S}_i$  and  $\mathbf{S}_j$  from coordinate system centers.

Figure 3.2 Illustration of difference between a rigid and a flexible connection for bodies  $i$  and  $j$ . The forces and moments in the  $\mathbf{g}$ -vector always acts in the local reference of frame. The right figure shows forces  $\mathbf{F}_i$  and  $\mathbf{F}_j$  that are moved to the centre. The torque is:  $\mathbf{n} = \mathbf{s} \times \mathbf{F}$ .

Figure 3.2b shows two bodies being pulled against each other, but not using constraints. Instead force elements modify the RHS of Equation (3.12) and the equation system becomes smaller than if constraints were used. This is an example of a flexible connection of two rigid bodies, which the next chapter describes in more detail. This flexible connection is not to be confused with flexible multibody dynamics, where the bodies themselves can deform (like FEM models, see e.g. [12, 13]).

### 3.3 Rigid gear constraints

The traditional/simple multibody gear constraint in 2D for two external gears is

$$\Phi^{\text{gear}} \equiv \rho_i \dot{\theta}_i + \rho_j \dot{\theta}_j = 0 \quad (3.17)$$

where  $\rho$  is the radius and  $\dot{\theta}$  the angular velocity of either body. If one of the gears is internal, the radius is negative. In case any angular velocity is relative, e.g. a gear wheel attached to a planet carrier with angular velocity  $\dot{\theta}_c$ , the following gear constraint is used [2]

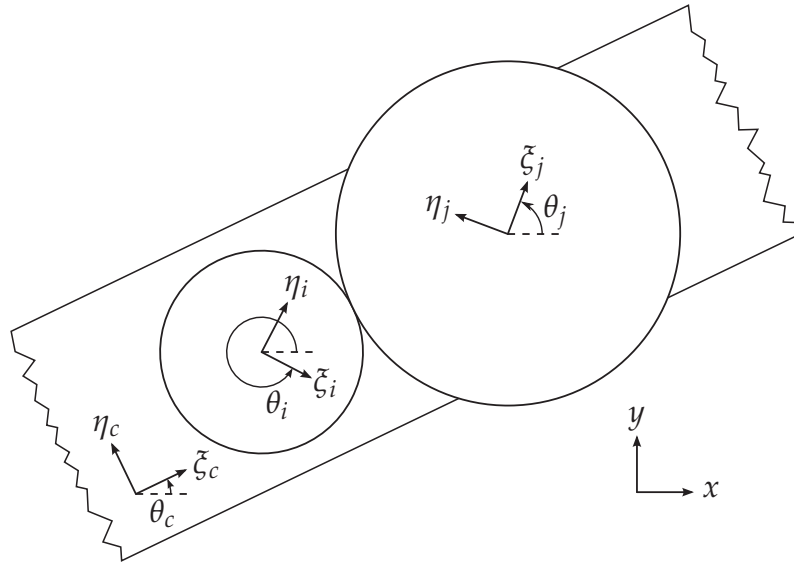


Figure 3.3 Spur gears  $i, j$  attached to moving body  $c$  (carrier).

$$\Phi^{\text{gear}} \equiv \rho_i (\dot{\theta}_i - \dot{\theta}_c) + \rho_j (\dot{\theta}_j - \dot{\theta}_c) = 0 \quad (3.18)$$

which is illustrated in Figure 3.3. This constraint can be used on a planetary gearbox as illustrated in Figure 3.4, using 4 gear constraints:

- $\Phi_1$  : Gear constraint:  $\rho_{\text{Pl}} (\omega_{\text{Pl},1} - \omega_c) + \rho_{\text{sun}} (\omega_{\text{sun}} - \omega_c) = 0$
- $\Phi_2$  : Gear constraint:  $\rho_r (\omega_r - \omega_c) - \rho_{\text{Pl}} (\omega_{\text{Pl},1} - \omega_c) = 0$
- $\Phi_3$  : Gear constraint:  $\rho_r (\omega_r - \omega_c) - \rho_{\text{Pl}} (\omega_{\text{Pl},2} - \omega_c) = 0$
- $\Phi_4$  : Gear constraint:  $\rho_r (\omega_r - \omega_c) - \rho_{\text{Pl}} (\omega_{\text{Pl},3} - \omega_c) = 0$

where subscript  $r$  means ring gear, subscript “ $c$ ” means (planet) carrier and “ $\text{Pl}.$ ” refers to the planet number ( $120^\circ$  apart if 3 planets are used, see Figure 3.4). Three of the constraints make the three planets turn and one additional constraint makes the sun gear turn.

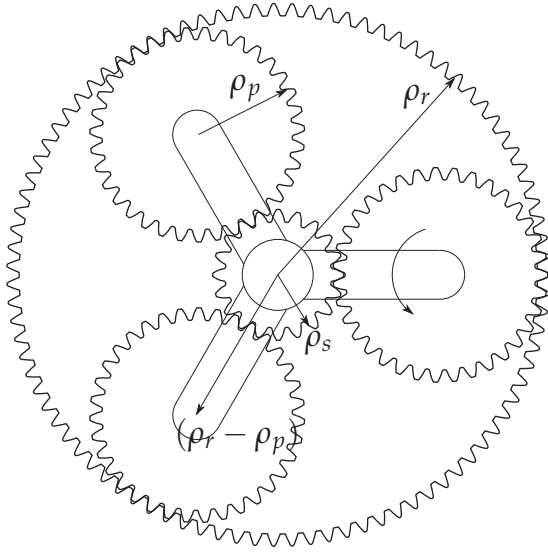


Figure 3.4 Planetary gearbox. Shown radius for sun ( $\rho_s$ ), planet ( $\rho_p$ ) and ring ( $\rho_r$ ) gears.

Gear forces:  $F_t$ : Tangential,  $F_n$ : Normal and  $F_r$ : Radial (horizontal) force directions ( $\alpha = 20^\circ$ , pressure angle).

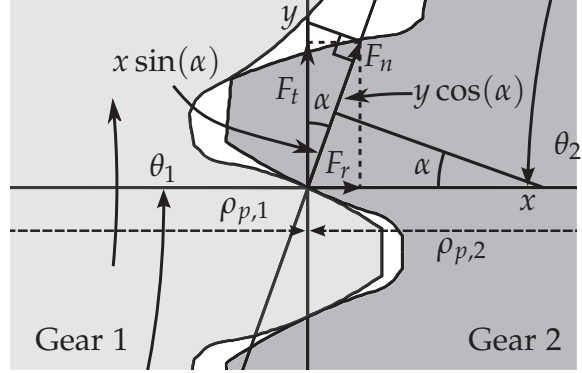


Figure 3.5 The contact point can move a distance along  $x$  or  $y$ , depending on either rotation or translation.

### 3.3.1 Improved gear constraint (no rotation/fixed)

An alternative rigid gear constraint can be explained from figure 3.5 by considering a projection of movement of the pitch/contact point into the gear tooth normal direction:

$$\begin{aligned}\Phi &= x_1 \sin \alpha + y_1 \cos \alpha + \theta_1(\rho_{p,1} \cos \alpha) = x_2 \sin \alpha + y_2 \cos \alpha - \theta_2(\rho_{p,2} \cos \alpha), \quad \text{or} \\ \ddot{\Phi} &= \ddot{x}_1 \sin \alpha + \ddot{y}_1 \cos \alpha + \dot{\omega}_1(\rho_{p,1} \cos \alpha) = \ddot{x}_2 \sin \alpha + \ddot{y}_2 \cos \alpha - \dot{\omega}_2(\rho_{p,2} \cos \alpha)\end{aligned}\quad (3.19)$$

where  $\rho_b = \rho_p \cos \alpha$  is the base circle radius [14]. The last term  $\theta(\rho_p \cos \alpha)$  is the one responsible for transferring the torque, i.e. if no translational forces exist then angular acceleration of either gears can still cause the pitch/contact point to move. The last term on the RHS is negative because for external gears, if one gear rotates in one direction then the other always rotates in the opposite direction.

For rigid gears, Equation (3.19) is an equilibrium that can be projected (from the tooth surface normal) into the tangential direction by dividing by  $\cos \alpha$  (see relationship between  $F_n$  and  $F_t$  on figure 3.5) and then the Jacobian for a 2-body 2D-system becomes:

$$\begin{bmatrix} \tan \alpha & 1 & \rho_{p,1} & -\tan \alpha & -1 & \rho_{p,2} \end{bmatrix} \begin{Bmatrix} \ddot{x}_1 \\ \ddot{y}_1 \\ \dot{\omega}_1 \\ \ddot{x}_2 \\ \ddot{y}_2 \\ \dot{\omega}_2 \end{Bmatrix} = 0 \quad (3.20)$$

using 3 generalised coordinates per body. The projection into the gear tooth normal ensures that the Lagrange multiplier  $\lambda$  for this particular constraint (see Equation (3.12)) is also a force in this direction. The improved gear constraint can also be used on a planetary gearbox using 4 rigid gear constraints again as with the simple gear constraint given by Equation (3.17). By using the simple gear constraint, the reaction forces  $R_{1x}$ ,  $R_{1y}$ ,  $R_{2x}$ ,  $R_{2y}$  on Figure 3.6 do not exist. This problem is solved using the improved gear constraint.

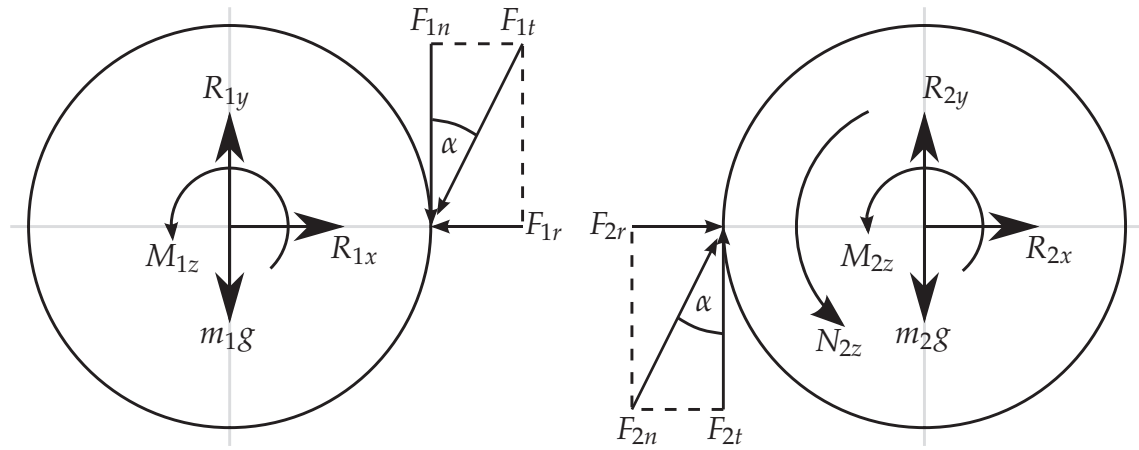


Figure 3.6 Free Body Diagram. An example would be to fix  $\theta_1 = 0$  radians (left gear) and apply torque on body 2 (right gear) and validate the obtained reaction forces.

### 3.3.2 Example of implementation – 2 bodies (no rotation/fixed)

A simple test problem can be programmed and illustrated by e.g. Figure 3.6, where the pressure angle  $\alpha$  is typically either  $20^\circ$  or  $25^\circ$ . The summarised details of a very simple multibody system are shown in Table 3.1 (details about equations and constraints are shown in the next section). The internal reaction forces are validated with results shown in Table 3.2 where the force of gravity from the masses is clearly seen in the  $y$ -direction.

The following identities can be checked numerically:



	Radius [m]	Mass [kg]	$F_x$ [N]	$F_y$ [N]	$N_z$ [Nm]
Gear 1	0.3	221.95	0	-2177.4	0
Gear 2	0.15	55.49	0	-544.3	75

Table 3.1 External forces and moments applied to the RHS of the equations of motion (values included the  $\mathbf{g}$ -vector in Equation (3.11) and (3.12)). These values are used with the example illustrated in Figure 3.6.

	$R_{1x}$ [N]	$R_{1y}$ [N]	$M_{1z}$ [Nm]	$R_{2x}$ [N]	$R_{2y}$ [N]	$M_{2z}$ [Nm]
$\Phi_{1+2}$	181.99	2677.36	0	0	0	0
$\Phi_3$	0	0	150	0	0	0
$\Phi_{4+5}$	0	0	0	-181.99	44.34	0
$\Phi_6$	-181.99	-500	-150	181.99	500	-75
$\Phi_{1 \rightarrow 6}$	0	2177.36	0	0	544.34	-75

Table 3.2 Reaction forces, when  $\theta_1 = 0$  rad (fixed) and input torque of 75 Nm is applied on gearwheel 2. Constraints  $\Phi_{1+2}$  and  $\Phi_{4+5}$  are revolute joints while  $\Phi_3$  fixes  $\theta_1$  and  $\Phi_6$  is the gear constraint which makes the force and moment equilibrium correct.

$$\left. \begin{array}{l} F_t = F_n \cos \alpha \\ F_r = F_n \sin \alpha \end{array} \right\} \Rightarrow \frac{F_t}{\cos \alpha} = \frac{F_r}{\sin \alpha} \Rightarrow F_r = F_t \tan \alpha \quad (3.21)$$

The radius on gear wheel 2 is 0.15 m so the vertical force in Figure 3.6 is  $F_{2t} = M_z/r = 75/0.15 = 500$  N, corresponding exactly to the output from the multibody program using this gear constraint (see results in Table 3.2). The radial force is also validated:

$$F_r = F_t \tan \alpha = 500 \tan(20^\circ) = 181.99 \text{ N} \quad (3.22)$$

The internal reaction forces will not appear using the gear constraint given by Equation (3.17) and the only problem with the improved gear constraint seems to be if things are rotating very quickly (e.g. rotating shafts and gears close to the generator in a wind turbine model with a gear ratio of e.g.  $>50$  from lowspeed side to highspeed side). In this case, increasing oscillations can make the solution unphysical and a smaller timestep has to be forced, but calculation time can be so slow that this solution is unpractical and unusable.

### 3.3.3 Example of implementation – 3 bodies (rotating)

A step towards modelling planetary gearboxes is to increase the number of bodies, so instead of having only 2 bodies (gears), a driver (planetary carrier) is

now added. The driver holds the planet in place, thereby simulating the situation where a planetary gear is rotating around the sun together with the carrier. The previously described problem is extended and now 8 constraints are used as shown in Table 3.3. The previous example used Equation (3.20) and with 6 DOFs this is a fully constrained multibody system. The new rotating multibody system has 9 DOFs (3 bodies) and 8 constraints and therefore one DOF is free and the planet can rotate. This changes the gear constraint equation slightly, i.e.  $\Phi_{1-5}$  is the same as previously.

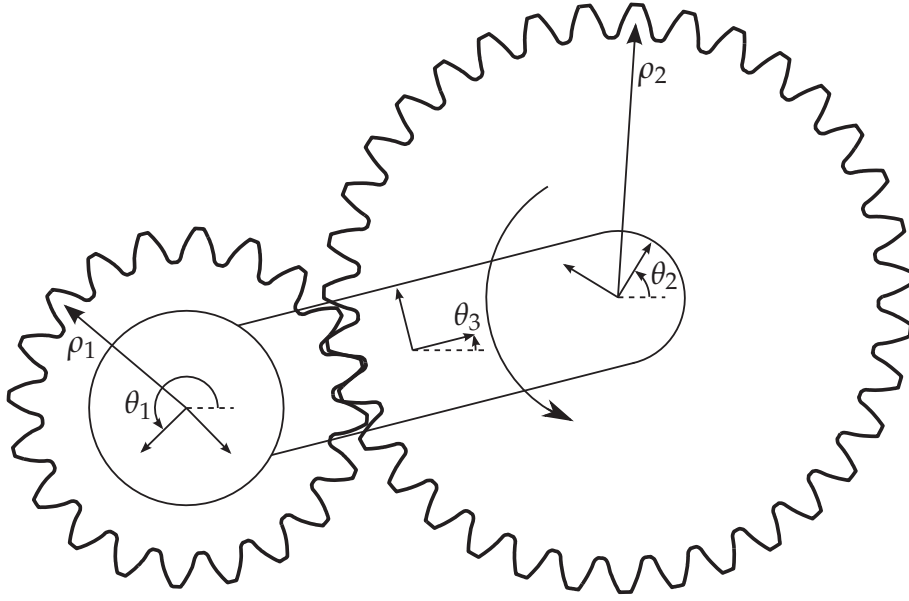


Figure 3.7 3-body gearbox illustration (sun, planet and carrier/driver).

Reformulation of Equation (3.19) and (3.20), for a simple planetary gearbox (for body  $i$  and  $j$ ):

$$\dot{\Phi} : (\mathbf{A}_n \cdot \mathbf{v}_r)^T \left[ \left( \begin{Bmatrix} \dot{x}_i \\ \dot{y}_i \end{Bmatrix} + \rho_i(\omega_i \hat{\mathbf{v}}_r) \right) - \left( \begin{Bmatrix} \dot{x}_j \\ \dot{y}_j \end{Bmatrix} - \rho_j(\omega_j \hat{\mathbf{v}}_r) \right) \right] = \begin{Bmatrix} 0 \\ 0 \end{Bmatrix} \quad (3.23)$$

using transformation matrix for the tooth surface normal direction ( $\theta = 90^\circ - \alpha$  so for  $\alpha = 20^\circ$ ,  $\theta = 70^\circ$ ):

$$\mathbf{A}_n = \begin{bmatrix} \cos \theta & -\sin \theta \\ \sin \theta & \cos \theta \end{bmatrix} \quad (3.24)$$

where  $\alpha$  is the pressure angle. The new gear-constraint (compared to the old one in equation (3.19)) is still a projection of movement/velocity/acceleration from the global coordinate system, into the gear tooth normal direction. But this time, it is necessary to measure the normal direction relative to a vector from the

---

$\Phi_{1-2}$  : B1: Sun gear attached to (0,0):

$$\mathbf{r}_1 = \{ 0 \ 0 \}^T$$

$\Phi_3$  : Sun gear doesn't rotate:

$$\theta_1 = 0$$


---

$\Phi_{4-5}$  : B2: Planet center attached to the planetary carrier:

$$\mathbf{r}_2 - (\mathbf{r}_3 + \mathbf{A}_3 \mathbf{s}'_3) = \{ 0 \ 0 \}^T$$

$$\text{where } \mathbf{s}'_3 = \{ \frac{1}{2}(\rho_1 + \rho_2) \ 0 \}^T$$


---

---

$\Phi_{6-7}$  : B3: Planetary carrier/driver attached to global coord. sys. (0,0):

$$\mathbf{r}_3 - \mathbf{A}_3 \mathbf{s}'_3 = \{ 0 \ 0 \}^T$$

$$\text{where } \mathbf{s}'_3 = \{ \frac{1}{2}(\rho_1 + \rho_2) \ 0 \}^T$$

$\Phi_8$  : Old gear constraint:

$$r_1 \cdot (\dot{\theta}_1 - \dot{\theta}_3) + r_2 \cdot (\dot{\theta}_2 - \dot{\theta}_3) = 0$$

$\Phi_8$  : New gear constraint:

(Eq. 3.23 and Figure 3.8)

---

*Table 3.3* All 8 constraints -  $\Phi_8$  shows both old and new gear constraint. Note that for comparison both gear constraints are expressed in velocities (the new gear constraint is non-holonomic, hence it cannot be integrated).

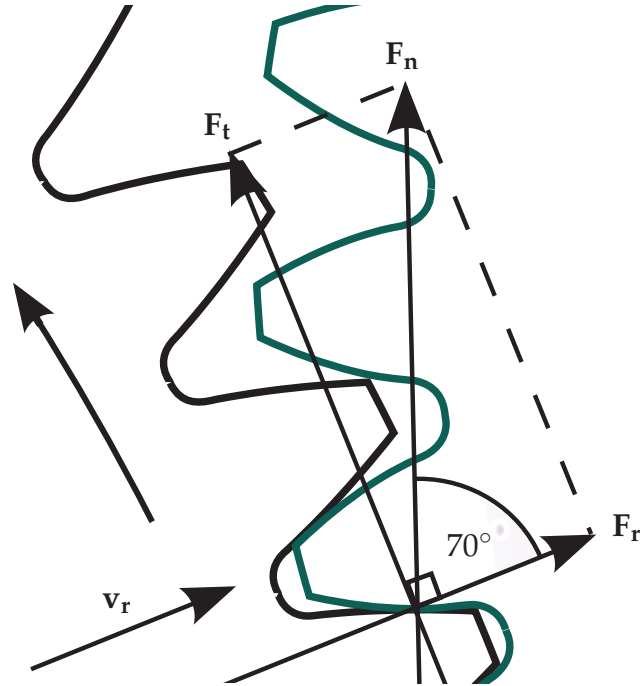


*Figure 3.8* Radial unit vector  $\mathbf{v}_r$  Gear tooth force directions:  $F_t$  (tangential),  $F_n$  (normal) and  $F_r$  (radial) directions.

centre of the sun to the centre of the planet and this unit vector is called  $\mathbf{v}_r$  (see Figure 3.8).

Figure 3.8 shows the planet centre and a line going to the centre of the sun. This is the radial direction and a projection of forces into this direction is  $\mathbf{F}_r$ . The  $\mathbf{F}_n$  direction is perpendicular to the teeth surface and in the normal direction. A projection of teeth forces perpendicular to the radial direction is the tangential force direction,  $\mathbf{F}_t$  shown in Figure 3.8. The constant  $2 \times 2$  transformation matrix  $\mathbf{A}_n$  is given by Equation (3.24) and the radial unit vector  $\mathbf{v}_r = \{\cos \theta_3 \ \sin \theta_3\}^T = (\mathbf{r}_2 - \mathbf{r}_1) / (\rho_1 + \rho_2)$  (normalised by pitch radii) is a unit vector in the direction of the vector going from the centre of the sun, to the planetary centre. The angle  $\theta_3$  is the orientation of the carrier (body 3) and this together with radii  $\rho_1$  and  $\rho_2$  is illustrated in Figure 3.7. If  $\mathbf{v}_r = \{x \ y\}^T$  is in the radial direction then the hat-vector  $\hat{\mathbf{v}}_r = \{-y \ x\}^T$  is in the tangential direction and perpendicular to  $\mathbf{v}_r$ .

Sometimes (it depends on CW/CCW rotation direction of the gears) the transformation matrix  $\mathbf{A}_n$  is either  $\mathbf{A}_{70}$  or  $\mathbf{A}_{110}$  (can also use  $\mathbf{A}_{-70}$  and  $\mathbf{A}_{-110}$ ). An “equilibrium analysis” of internal and external forces (and torque) as shown in Appendix A, can be made for this 3-body multibody model. Different cases can be tested, using either CW/CCW rotation and the 4 unit vector directions:  $\pm 70^\circ$ ,  $\pm 110^\circ$ . This “systematic approach” results in several pages of output reaction forces from all 8 constraints, although only the first page is included in the appendix. The sign of the internal reaction forces changes depending on the unit vector (although the gear constraint behaves correctly in any case with respect to acceleration and motion because the internal forces eliminate each other).

In order to model a planetary gearbox (e.g. see Figure 3.4 on page 24), extra bodies must be added. Gear wheels can be added in a similar way as described above, when going from two to three bodies. Typically a ring gear (with constraints similar to the sun gear) and two extra gears (planets) are added. The gear-constraint equations have been tested (internal gears, such as the ring gear, have negative radius) and the described procedure is used in all publications.

### 3.3.4 Differentiation of constraint equations

All constraints must be differentiated to form the Jacobian matrix. The following is an illustrative simple 3-body example in 2D, using the constraints from Table 3.3 on the preceding page:

$$\begin{bmatrix} & & \\ & & \\ & & \\ & & \end{bmatrix} \begin{Bmatrix} \ddot{x}_1 \\ \ddot{y}_1 \\ \dot{\omega}_1 \\ \ddot{x}_2 \\ \ddot{y}_2 \\ \dot{\omega}_2 \\ \ddot{x}_3 \\ \ddot{y}_3 \\ \dot{\omega}_3 \end{Bmatrix} = \begin{Bmatrix} \\ \\ \\ -\omega_3^2[A_3] \begin{Bmatrix} s'_{3,x} \\ s'_{3,y} \end{Bmatrix} \\ \\ -\omega_3^2[A_3] \begin{Bmatrix} s'_{3,x} \\ s'_{3,y} \end{Bmatrix} \\ z_1 \end{Bmatrix} \quad (3.25)$$

where (explained in section 3.3.5):

$$\begin{aligned} z_1 = & (\mathbf{A}_{70} \cdot \dot{\mathbf{v}}_{\mathbf{r}})^T [(-\dot{\mathbf{r}}_1 - \rho_1 \omega_1 \hat{\mathbf{v}}_{\mathbf{r}}) + (\dot{\mathbf{r}}_2 - \rho_2 \omega_2 \hat{\mathbf{v}}_{\mathbf{r}})] + \\ & (\mathbf{A}_{70} \cdot \mathbf{v}_{\mathbf{r}})^T (-\rho_1 \omega_1 \hat{\mathbf{v}}_{\mathbf{r}} - \rho_2 \omega_2 \hat{\mathbf{v}}_{\mathbf{r}}) \quad \text{RHS } (\gamma) \end{aligned}$$

The coefficients for the Jacobian matrix  $\Phi_{\mathbf{q}}$  multiplied with the accelerations of the generalised coordinates  $\ddot{\mathbf{q}}$  (DOFs) and the corresponding  $\gamma$ -values will be explained shortly. The Jacobian matrix  $\Phi_{\mathbf{q}}$  is

$$\begin{bmatrix} 1 & & & & & & \\ & 1 & & & & & \\ & & 1 & & & & \\ & & & 1 & & -1 & \\ & & & & 1 & -1 & -\mathbf{B}_3 \begin{Bmatrix} s'_{3,x} \\ s'_{3,y} \end{Bmatrix} \\ & & & & & 1 & -\mathbf{B}_3 \begin{Bmatrix} s'_{3,x} \\ s'_{3,y} \end{Bmatrix} \\ (\mathbf{A}_{70} \cdot \mathbf{v}_{\mathbf{r}})^T & z_2 & (-\mathbf{A}_{70} \cdot \mathbf{v}_{\mathbf{r}})^T & z_3 & 0 & 0 & 0 \end{bmatrix} \quad (3.26)$$

where  $\mathbf{B}$  is

$$\mathbf{B} = \begin{bmatrix} -\sin \theta & -\cos \theta \\ \cos \theta & -\sin \theta \end{bmatrix} \quad (3.27)$$

and  $z_2$  and  $z_3$  are given by:

$$\begin{aligned} z_2 &= (\mathbf{A}_{70} \cdot \mathbf{v}_{\mathbf{r}})^T (\rho_1 \cdot \hat{\mathbf{v}}_{\mathbf{r}}) & \text{Coeff. for } \dot{\omega}_1 \\ z_3 &= (\mathbf{A}_{70} \cdot \mathbf{v}_{\mathbf{r}})^T (\rho_2 \cdot \hat{\mathbf{v}}_{\mathbf{r}}) & \text{Coeff. for } \dot{\omega}_2 \end{aligned} \quad (3.28)$$

Equation (3.26) shows that constraints  $\Phi_{1-3}$  are trivial to differentiate. These constraints only involve the first 3 DOFs and the coefficients become 1. Constraints  $\Phi_{4-7}$  are a bit more complicated. An example illustrating the process of differentiation of constraints for  $\Phi_{4-5}$  is

$$\begin{aligned}
\Phi_{4-5} : \mathbf{r}_2 - (\mathbf{r}_3 + \mathbf{A}_3 \mathbf{s}_3') &= \{0 \ 0\}^T \Rightarrow \\
\dot{\Phi}_{4-5} : \dot{\mathbf{r}}_2 - (\dot{\mathbf{r}}_3 + \omega_3 \mathbf{B}_3 \mathbf{s}_3') &= \{0 \ 0\}^T \Rightarrow \\
\ddot{\Phi}_{4-5} : \underbrace{\ddot{\mathbf{r}}_2}_{LHS} - \underbrace{(\ddot{\mathbf{r}}_3 + \dot{\omega}_3 \mathbf{B}_3 \mathbf{s}_3')}_{LHS} - \underbrace{\omega_3^2 \mathbf{A}_3 \mathbf{s}_3'}_{RHS} &= \{0 \ 0\}^T
\end{aligned} \tag{3.29}$$

The last line in Equation 3.29 can be divided into LHS- and RHS-terms where LHS coefficients are inserted into the Jacobian matrix (see Equation (3.26)) and everything else is moved to the RHS (see Equation (3.25)). Constraints  $\ddot{\Phi}_{6-7}$  are found using the same method as above and generally coefficients in 2D and 3D for typically used constraints can be found in e.g. [2].

### 3.3.5 Differentiation of gear constraint equations

The improved gear-constraint is non-holonomic, meaning it is non-integrable from a velocity- to a position-level kinematic constraint. The system must be solved dynamically instead of kinematically (using Equations (3.11) and (3.12) and numerical time-integration). Using the same method of differentiation as before, with the non-holonomic velocity constraint given by Equation (3.23) yields

$$\begin{aligned}
\dot{\Phi}_8 : (\mathbf{A}_n \cdot \mathbf{v}_r)^T (\dot{\mathbf{r}}_1 + \rho_1 (\omega_1 \hat{\mathbf{v}}_r)) - (\mathbf{A}_n \cdot \mathbf{v}_r)^T (\dot{\mathbf{r}}_2 - \rho_2 (\omega_2 \hat{\mathbf{v}}_r)) &= 0 \Rightarrow \\
\ddot{\Phi}_8 : (\mathbf{A}_{70} \cdot \dot{\mathbf{v}}_r)^T (\dot{\mathbf{r}}_1 + \rho_1 \omega_1 \hat{\mathbf{v}}_r) + (\mathbf{A}_{70} \cdot \mathbf{v}_r)^T (\ddot{\mathbf{r}}_1 + \rho_1 \dot{\omega}_1 \hat{\mathbf{v}}_r + \rho_1 \omega_1 \dot{\hat{\mathbf{v}}}_r) \\
- (\mathbf{A}_{70} \cdot \dot{\mathbf{v}}_r)^T (\dot{\mathbf{r}}_2 - \rho_2 \omega_2 \hat{\mathbf{v}}_r) - (\mathbf{A}_{70} \cdot \mathbf{v}_r)^T (\ddot{\mathbf{r}}_2 - \rho_2 \dot{\omega}_2 \hat{\mathbf{v}}_r - \rho_2 \omega_2 \dot{\hat{\mathbf{v}}}_r) &= 0
\end{aligned} \tag{3.30}$$

By rearranging terms, one finds the result shown in Equation (3.28). For the sake of completeness, the following is provided for the same gear constraint in three dimensions:

$$\dot{\Phi}_{3D} : (\mathbf{A}_n \mathbf{v}_r)^T \left[ (\mathbf{r}_i + \rho_i \mathbf{A}_i \omega_i' \times \mathbf{v}_r) - (\mathbf{r}_j - \rho_j \mathbf{A}_j \omega_j' \times \mathbf{v}_r) \right] = 0 \tag{3.31}$$

$$\begin{aligned}
\ddot{\Phi}_{3D} : (\mathbf{A}_n \mathbf{v}_r)^T &\left( \ddot{\mathbf{r}}_i + \rho_i \left[ (\mathbf{A}_i \widetilde{\omega_i' \omega_i'}) \times \mathbf{v}_r + (\mathbf{A}_i \dot{\omega_i'}) \times \mathbf{v}_r + (\mathbf{A}_i \omega_i') \times \dot{\mathbf{v}}_r \right] \right) \\
- (\mathbf{A}_n \mathbf{v}_r)^T &\left( \ddot{\mathbf{r}}_j - \rho_j \left[ (\mathbf{A}_j \widetilde{\omega_j' \omega_j'}) \times \mathbf{v}_r + (\mathbf{A}_j \dot{\omega_j'}) \times \mathbf{v}_r + (\mathbf{A}_j \omega_j') \times \dot{\mathbf{v}}_r \right] \right) \\
+ (\mathbf{A}_n \dot{\mathbf{v}}_r)^T &(\dot{\mathbf{r}}_i + \rho_i (\mathbf{A}_i \omega_i') \times \mathbf{v}_r) - (\mathbf{A}_n \dot{\mathbf{v}}_r)^T (\dot{\mathbf{r}}_j - \rho_j (\mathbf{A}_j \omega_j') \times \mathbf{v}_r) = 0
\end{aligned} \tag{3.32}$$

The differentiation of a transformation matrix, vector and matrix algebra rules from section 3.1.3 on page 19 have been employed. Things become more

complicated because in 2D the angular velocity  $\omega$  is a scalar but in 3D it is a vector. For converting between notation with skew-symmetric matrices and cross-products, Equation (3.8) can be used.

### 3.3.6 Post-processing

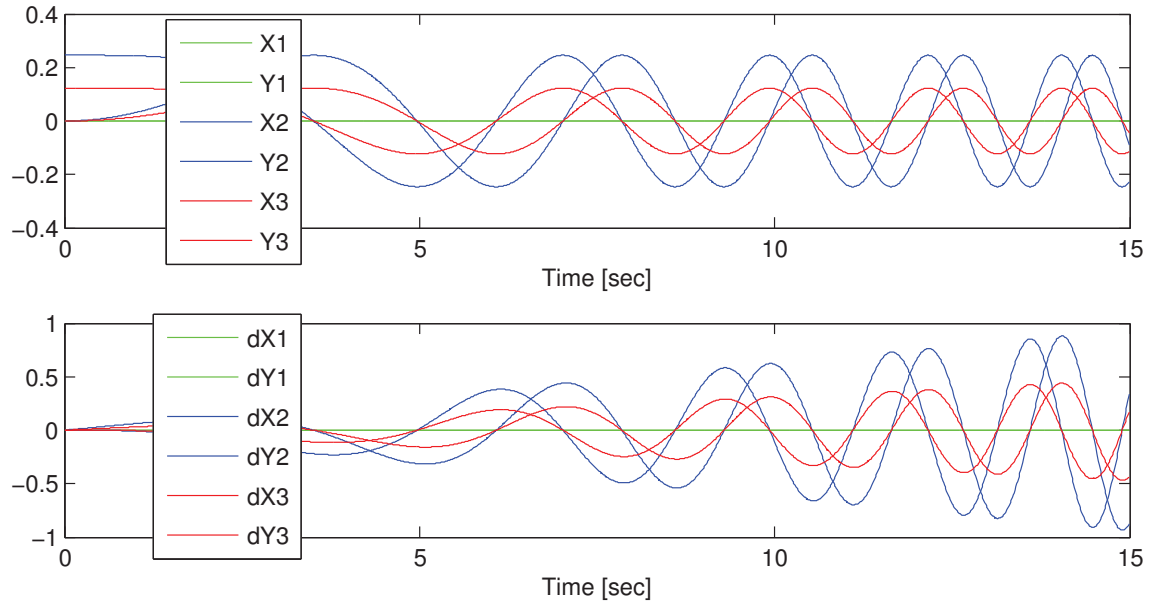


Figure 3.9 Position and velocity of accelerating 3-body model with rotating planet.

An example of post-processing the simple 3-body “gearbox” is shown in Figure 3.9, which illustrates the position and velocity of all three bodies, when starting from rest and accelerating the carrier using a constant external torque. It can be seen that the sun (body 1) is not moving but the planet (body 2) and carrier (body 3) accelerate.

This is the starting point for modelling a planetary gearbox. By using the same constraints as described above, the model can be extended with a ring gear and extra planets. A major issue with gear tooth reaction forces of all planets with a rigid multibody model will be solved using a flexible model in the next chapter.

## 3.4 Wind turbine model

Dimensions and measurements from a real 500 kW wind turbine (shown in the introduction in Figure 1.1 on page 2) at DTU Risø, Roskilde have been obtained. A 3D multibody model has been made using 8 rigid bodies (including a planetary gearbox) using the improved gear-constraint described above. The

programming task has been to implement code corresponding to the method illustrated in the previous example, described in section 3.3.3 and 3.3.4. The whole list of 8 bodies and 47 constraints is found in Appendix B. Both experimental data [15] and simulated data (using FLEX5) have been studied and a number of comparisons have been made. Some of these are published in [P1].

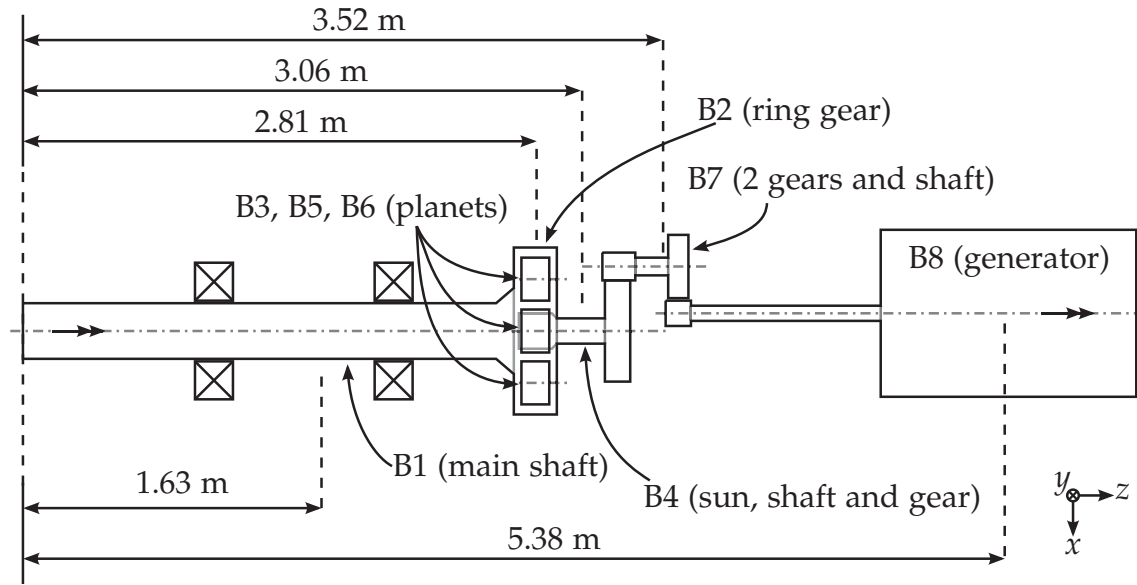


Figure 3.10 Simplified illustration of wind turbine model. All local coordinate systems are in the mass center for each body (resulting in a constant mass matrix).

Figure 3.10 shows the 8 bodies and the horizontal distance to the mass centres (local coordinate systems). Figure 3.11 shows an example of a snapshot from a Matlab animation with all local coordinate systems (coordinate axis  $\xi, \eta, \zeta$  uses red, green and blue colours respectively).

#### 3.4.1 Forces and moments

The output routine of FLEX5, allows for manually defining “sensors” which are data that should be stored at each timestep of the calculation. Some important sensors are: Rotor-position, wind speed, pitch angle, rotor/generator speed, power yield, blade deflection (edge and flap), tower/shaft torsion/bending, tilt angle, brake moment and axial force. The default FLEX5-program has 106 sensors defined in a textfile, as well as in the source code of the output routine of the program.

For postprocessing the data from these sensors, FLEX5 has a program that can plot stored sensor data. The output files from FLEX5 are in AFM/KSH-format described in [16]. Instead of using the old FPL0T32 DOS-program, a



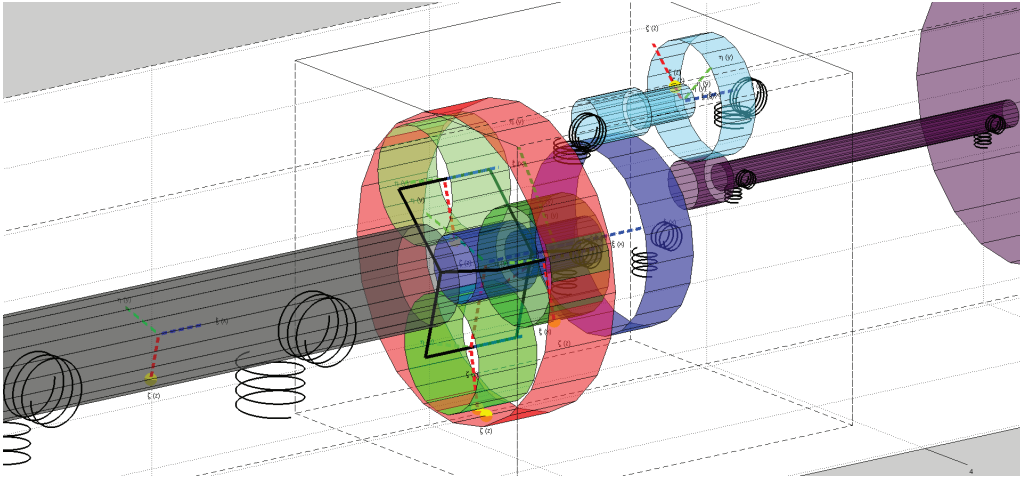


Figure 3.11 Matlab animation of wind turbine model with gearbox in the middle, low-speed side to the left and high-speed side to the right.

Matlab import program has been made. The FLEX5 sensor data is read into Matlab and saved to a Matlab-native file format so the full library of Matlab-functions can now be used (e.g. FFT-functions and signal processing toolboxes, etc.). An example of FLEX5-results using the Jacob Mann model [17, 18] for spatial and temporal fluctuations of the wind field (single point at hub height), is shown in Figure 3.12.

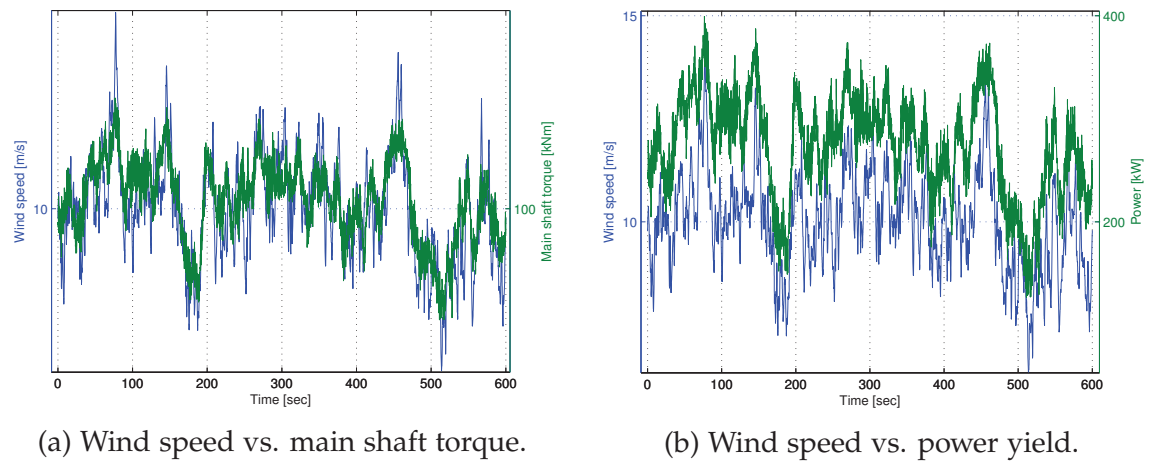


Figure 3.12 Illustration of wind speed (blue curve) in the same graph as main shaft torque and power yield, respectively (mean wind speed is approx. 10 m/s).

For gearbox simulations, the torque on the main shaft and generator is very important. With perfect bearings and a rigid nacelle, there will be no misalignment of gear teeth, which is considered here. One may argue that bearings and shafts as well as the tower and blades should be implemented as flexible bod-

ies in the multibody model, but these effects are not included. FLEX5 already includes these effects and it has not been easy to obtain stiffness and damping coefficients and generally all experimental/physical values are very difficult to obtain. The mass matrix was estimated using the masses of each body (either calculated using density for steel and approximate volume or using inspiration from FLEX5 input files and other various sources).

All 8 bodies feel the effect of gravity in the vertical direction ( $x$ , shown in Figure 3.10). In addition, the main shaft (body 1) and generator (body 8) are subject to additional external forces and torque. The blades and rotor mass contribute to a negative moment around a horizontal axis ( $y$ ) in the mass centre of body 1. The main shaft has huge blades affected by a fluctuating wind field and the generator which is subject to magnetic and electrical effects, e.g. the power grid. Generator torque is determined as slip which is a function of the angular velocity of the shaft minus the synchronous rotation speed, e.g. 1500 RPM. If the angular velocity of the generator is below the synchronous rotational speed, the generator acts like a motor. Only when above the synchronous rotational velocity does the generator produce power. With reference to Equation (3.12), the  $\mathbf{g}$ -vector on the RHS is defined by the following forces and moments ( $x$  is in the vertical direction, which is the same coordinate system definition used by FLEX5).

$$\mathbf{F}_1 = \begin{Bmatrix} F_x \\ F_y \\ F_z \end{Bmatrix}$$

$$\mathbf{M}'_1 = \mathbf{A}_1^T \left( \begin{Bmatrix} M_x \\ M_y \\ M_z \end{Bmatrix} + \begin{Bmatrix} 0 \\ 0 \\ -1.63 \text{ m} \end{Bmatrix} \times \begin{Bmatrix} F_x \\ F_y \\ F_z \end{Bmatrix} \right) \quad (3.33)$$

$$\mathbf{g} = \begin{Bmatrix} \mathbf{F}_1 \\ \mathbf{M}'_1 \\ \mathbf{F}_2 \\ \mathbf{M}'_2 \\ \vdots \\ \vdots \\ \mathbf{F}_7 \\ \mathbf{M}'_7 \\ \mathbf{F}_8 \\ \mathbf{M}'_8 \end{Bmatrix} \quad \text{where} \quad \begin{aligned} \mathbf{F}_{2-7} &= \begin{Bmatrix} m_{2-7} g \\ 0 \\ 0 \end{Bmatrix} \\ \mathbf{M}'_{2-7} &= \begin{Bmatrix} 0 \\ 0 \\ 0 \end{Bmatrix} \\ \mathbf{F}_8 &= \begin{Bmatrix} m_8 g \\ 0 \\ 0 \end{Bmatrix} \\ \mathbf{M}'_8 &= \begin{Bmatrix} 0 \\ 0 \\ -i M_z^* \end{Bmatrix} \end{aligned} \quad (3.34)$$

where  $i$  is the gear-ratio,  $m$  is mass,  $g$  is the gravitational constant and  $M_z^*$  is FLEX5 sensor 7 which is used as generator torque on body 8. The distance -1.63 m in Equation (3.33) is also shown in Figure 3.10 on page 33. It is the distance from the local coordinate system to the rotor.

A standard version of FLEX5 has a sensor-file with 106 “sensors” which are just output signals, e.g. wind speed at hub height, rotor position/speed, generator torque, deflection various places and forces and torque. In this case, signals 61-63 are used for extracting  $F_x$ ,  $F_y$  and  $F_z$  forces and signals 64-66 are used for extracting torque for  $M_x$ ,  $M_y$  and  $M_z$  and these forces and moments are applied to the rotor/main shaft (body 1) in the multibody program:

FLEX5 sensors 61-66 are used (on body 1), because they have force and torque in global coordinates. All values from FLEX5 are interpolated, for the time at the current time-step. The second term in Equation (3.33) is the torque from the wind at the centre of mass of body 1. The rule  $\mathbf{M} = \mathbf{r} \times \mathbf{F}$  to calculate the torque at a distance  $\mathbf{r}$  from the force  $\mathbf{F}$  has been employed [14]. The distance from the local coordinate system to the force (at the rotor) is -1.63 m. All mass centre distances from the rotor can be seen in Figure 3.10 on page 33.

The rotor and main shaft torque (body 1) from the aerodynamic code FLEX5 is mainly a function of wind speed and blade aerodynamic properties etc. The generator torque (body 8) is proportional with the slip (synchronous speed above rated speed, which is 1500 RPM).

The result of following this procedure can be visualised in a Matlab animation, e.g. see Figure 3.11. Publication [P1] was made using the method described above, a gear tooth profile generator program and Comsol Multiphysics. Examples that summarise the results of this chapter are shown in Figure 3.13 and 3.14.

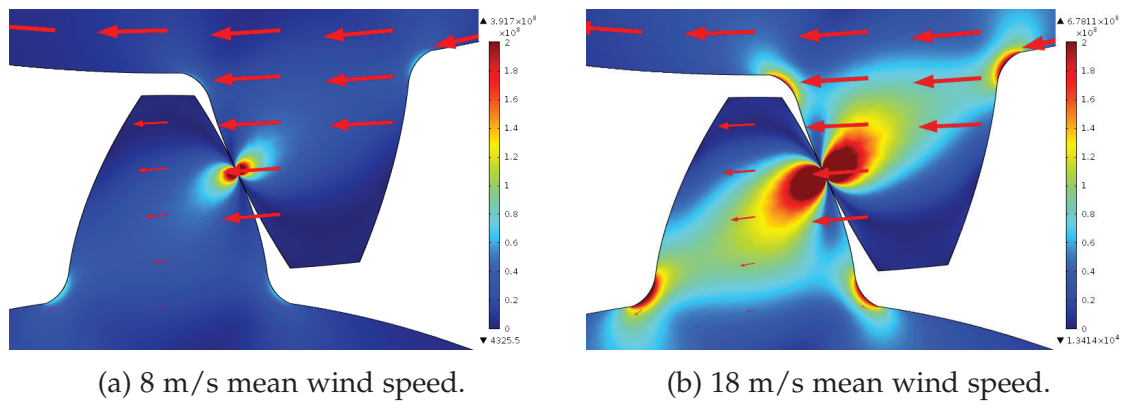


Figure 3.13 Sun/planet gear tooth stress (from [P1]).

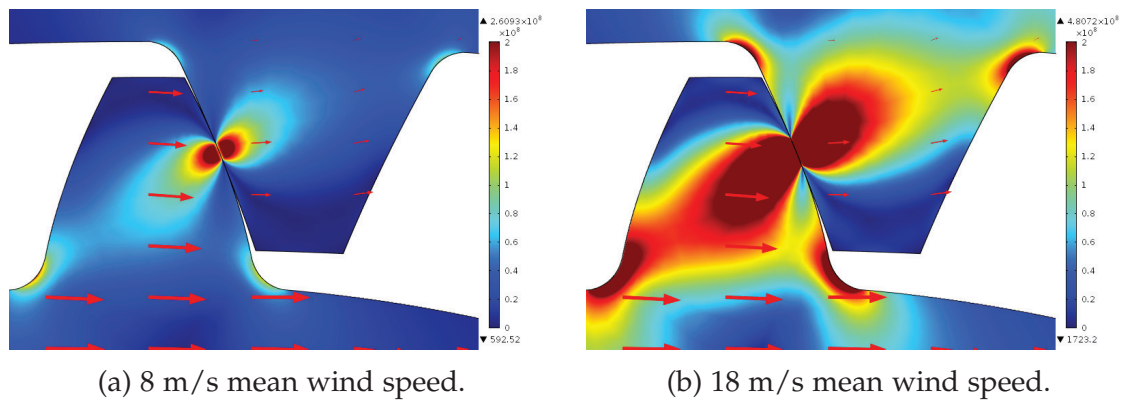


Figure 3.14 Planet/ring gear tooth stress (from [P1]).

## References

- [1] W. Schiehlen, "Multibody system dynamics: Roots and perspectives," *Multibody Systems Dynamics*, vol. 1, no. 2, pp. 149–188, 1997.
- [2] P. E. Nikravesh, *Computer-Aided Analysis of Mechanical Systems*, vol. 186. Prentice Hall, 1988.
- [3] E. J. Haug, *Computer Aided Kinematics and Dynamics of Mechanical Systems: Vol. I: Basic Methods*. Allyn and Bacon, 1989.
- [4] A. A. Shabana, *Dynamics of Multibody Systems*. Wiley & Sons, 1989.
- [5] A. A. Shabana, "Flexible multibody dynamics: Review of past and recent developments," *Multibody System Dynamics*, vol. 1, no. 2, pp. 189–222, 1997.
- [6] M. O. L. Hansen, *Aerodynamics of Wind Turbines*. Earthscan, 2nd ed, 2009.
- [7] N. L. Pedersen, *Analysis and synthesis of complex mechanical systems*. PhD thesis, 1998.
- [8] U. M. Ascher and L. R. Petzold, "Computer methods for ordinary differential equations and differential-algebraic equations," *Computer Methods for Ordinary Differential Equations and Differential-Algebraic Equations*, pp. 3–305, 1998.
- [9] J. G. d. Jalon, E. Bayo, and L. Y. Bahar, "Kinematic and dynamic simulation of multibody systems: The real time challenge," *Applied Mechanics Reviews - Including Supplement*, vol. 48, no. 1, p. B2, 1995.
- [10] C. Gear, "Simultaneous numerical solution of differential-algebraic equations," *Circuit Theory, IEEE Transactions on*, vol. 18, no. 1, pp. 89–95, 1971.
- [11] J. Baumgarte, "Stabilization of constraints and integrals of motion in dynamical systems," *Computer methods in applied mechanics and engineering*, vol. 1, no. 1, pp. 1–16, 1972.
- [12] M. Géradin and A. Cardona, *Flexible multibody dynamics: a finite element approach*. John Wiley, 2001.

- [13] F. M. L. Amirouche, *Fundamentals of multibody dynamics : theory and applications*. Birkhauser, 2004. Includes bibliographical references and index.
- [14] P. Klit, K. Casper, and N. L. Pedersen, *Machine Elements - Analysis and Design*. Polyteknisk Forlag, 2009.
- [15] K. S. Hansen and G. C. Larsen, "Database of wind characteristics: <http://www.winddata.com>," 1997-2011.
- [16] S. Øye, "Filstruktur for flex4-tidsseriefil," tech. rep., Technical University of Denmark, 1994.
- [17] J. Mann, "Wind field simulation," *Probabilistic Engineering Mechanics*, vol. 13, no. 4, pp. 269–282, 1998.
- [18] J. Mann, "The spatial structure of neutral atmospheric surface-layer turbulence," *J. Fluid Mech.*, vol. 273, pp. 141–168, 1994.

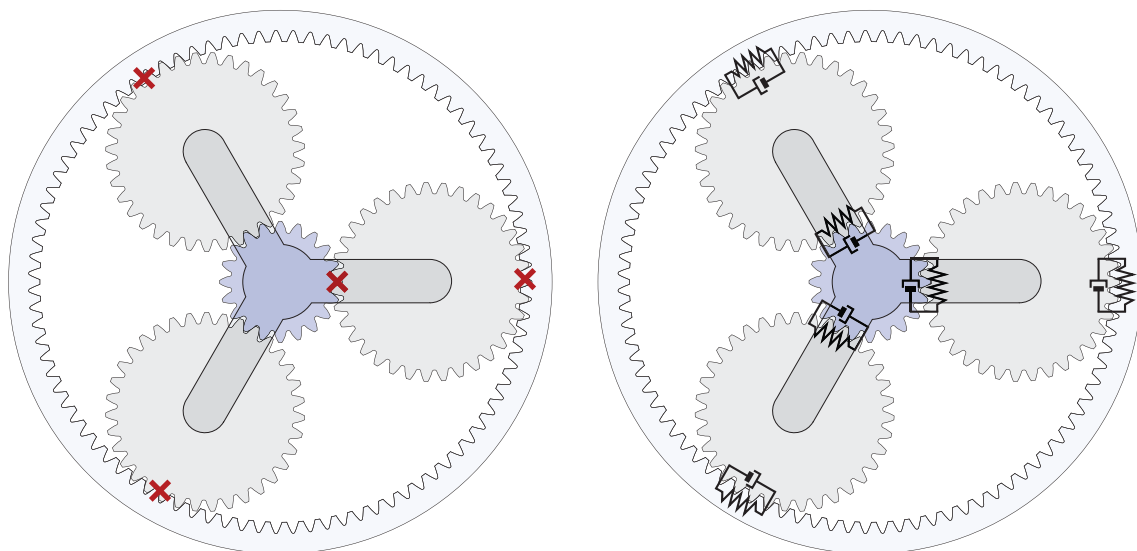
## Chapter 4

### Flexible gearbox model

The code made, using the procedure from the previous chapter, has strengths and weaknesses as shown in Table 4.1. Considerations about how to make the model more realistic include replacing rigid bodies like the main shaft, carrier and ground (bedplate) with flexible bodies.

Strengths	Weaknesses
Fast computation time (larger timesteps allowed)	Only 1 planet transfers the full torque
Reaction forces easily extracted	No elastic/load-sharing effects (no spring-damper effect)
Simple to code and implement (consistent with other rigid constraints)	Maybe slightly difficult to fully understand (e.g. CW/CCW, unit vector)

Table 4.1 Strengths and weaknesses of the rigid wind turbine model approach.



(a) Rigid planetary gearbox model.

(b) Flexible planetary gearbox model.

Figure 4.1 Rigid vs. flexible 6-body multibody planetary gearbox models.

As described in section 3.2.1, one possible approach is to replace constraints by force elements. It is clear that the blades and rotor are subject to fluctuations

in lateral, vertical and longitudinal forces which increase the stress on all components, e.g. the gearbox bearings. Together with shaft deflections, this can result in misaligned gear contact which is also an important problem. However, due to lack of experimental data, difficulties in obtaining good estimates for stiffness and damping coefficients for bearings, main shaft, carrier and bedplate and very long computation times, etc., it was decided to focus on the gear constraints and remove these using a 2D-program with no parallel gear stages (only 6 bodies are used). A spring and a damper are then added between gear teeth, implying that contacting gear teeth can penetrate each other. This new approach involves connecting bodies flexibly instead of rigidly as described in the previous chapter. It means that the RHS of the equations of motion in each timestep must be constantly updated to include these effects and therefore this approach requires more programming and book-keeping.

Figure 4.1 illustrates two approaches. Figure 4.1a is the approach described in the previous chapter and Figure 4.1b is the approach described in this chapter. Publication [P2] describes a method to evaluate gear tooth stiffness using FEM. Publication [P3] describes two multibody approaches to gearbox modelling and these are compared against each other (roughly the theory from the previous and this chapter).

## 4.1 Mass-damper-spring system

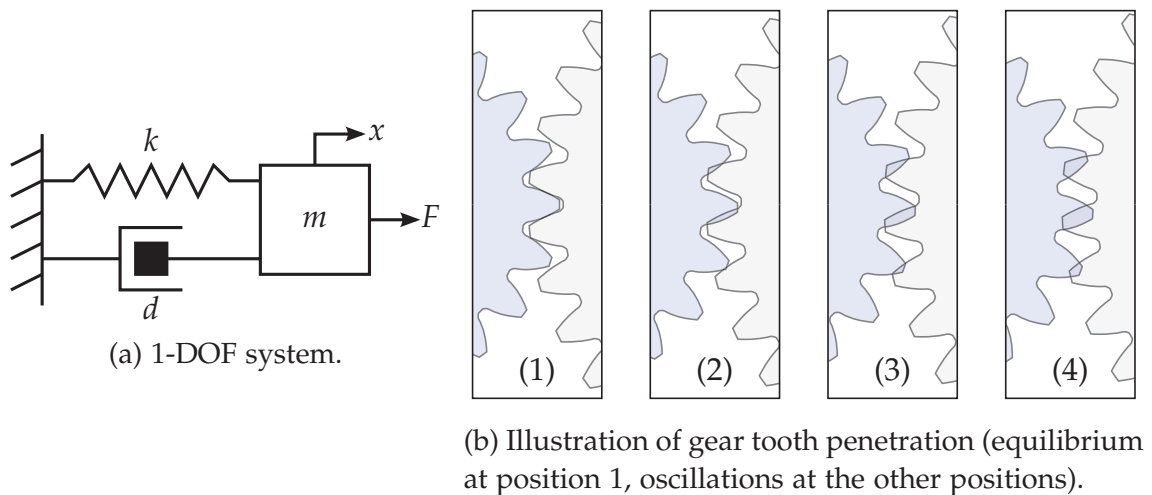


Figure 4.2 (a) Mass-damper-spring system related to (b) flexible gear tooth model.

The single DOF system, described by a single variable or coordinate, is the most basic mechanical mass-damper-spring system and illustrated in Figure



4.2a. The motion of the object with mass  $m$ , stiffness coefficient  $k$  and damping coefficient  $d$  subject to the force  $F$  is governed by a second order linear differential equation.

#### 4.1.1 No damping

In the simplest case all variables are constants, which together with  $d = 0$  is where many textbooks start when introducing undamped harmonic oscillations and free vibrations (see e.g. [1, 2]):

$$m\ddot{x}(t) + kx(t) = 0 \quad \Rightarrow \quad \ddot{x}(t) + \omega_n^2 x(t) = 0 \quad (4.1)$$

where  $\omega_n = \sqrt{k/m}$  is the natural frequency (a real constant). The period of oscillation is related to the natural frequency as  $T = (2\pi)/\omega_n$ . The solution to this equation with initial conditions  $x_0$  and  $\dot{x}_0$ , has the exponential form  $x(t) = Ae^{st}$ , which can be inserted into Equation (4.1) and dividing through by  $Ae^{st}$  yields the characteristic equation

$$s^2 + \omega_n^2 = 0 \quad (4.2)$$

which has two imaginary complex conjugate roots,  $\pm i\omega_n$ ,  $i = \sqrt{-1}$ . Inserting this into  $x(t) = Ae^{st}$  yields the general solution to Equation (4.1)

$$x(t) = A_1 e^{i\omega_n t} + A_2 e^{-i\omega_n t} \quad (4.3)$$

where  $A_1$  and  $A_2$  are complex constants of integration. The solution can also be written using the following real-valued constants  $A, \phi, A_1$  and  $A_2$

$$x(t) = A \sin(\omega_n t + \phi) = A_1 \cos \omega_n t + A_2 \sin \omega_n t \quad (4.4)$$

#### 4.1.2 Including damping

In the case where damping is included, a force in the opposite direction of the motion will decrease the amplitude of the response. The damping ratio  $\zeta$  determines the rate of decay of oscillations and is defined

$$\zeta = \frac{d}{2\sqrt{km}} = \frac{d}{2\omega_n m} \quad (4.5)$$

which can be inserted into Equation (4.1) with an extra damping term and external force

$$m\ddot{x}(t) + d\dot{x}(t) + kx(t) = F(t) \quad \Rightarrow \quad \ddot{x}(t) + 2\zeta\omega_n\dot{x}(t) + \omega_n^2 x(t) = \frac{F(t)}{m} \quad (4.6)$$

This has a solution similar to Equation (4.4)

$$x(t) = Ae^{-\zeta\omega_n t} \sin(\omega_d t + \phi) = e^{-\zeta\omega_n t} (A_1 \sin \omega_d t + A_2 \cos \omega_d t) \quad (4.7)$$

where  $A$ ,  $A_1$  and  $A_2$  are real-valued constants. The relationship between the undamped and damped natural eigenfrequency is

$$\omega_d = \omega_n \sqrt{1 - \zeta^2} \quad (4.8)$$

The damping force is proportional to velocity, i.e.  $F = d\dot{x}$ . Normal physical systems have positive mass, stiffness and damping coefficients and in these cases, a damped system can be characterised as underdamped ( $\zeta < 1$ ), overdamped ( $\zeta > 1$ ) or critically damped ( $\zeta = 1$ ) [1]. Critically and over-damped systems do not oscillate and critically damped systems converge to zero as fast as possible. It is therefore assumed that damping in gearboxes is underdamped, which also constitutes the most common case [1].

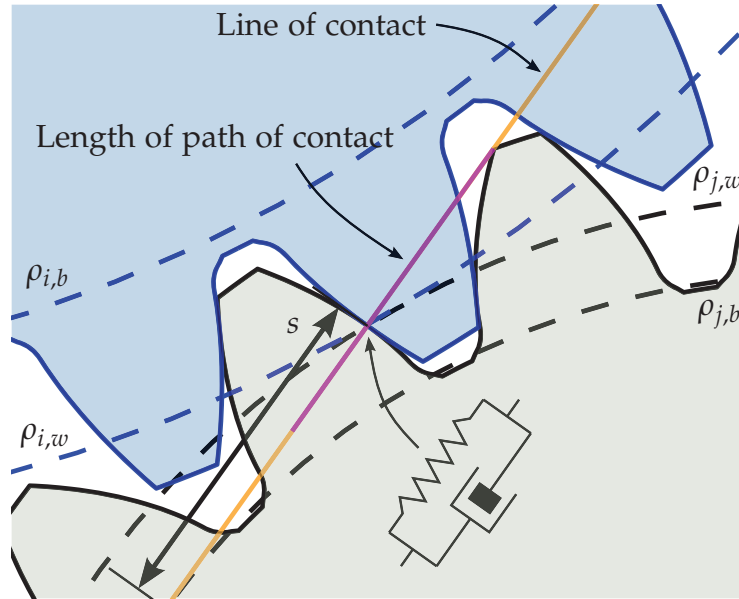
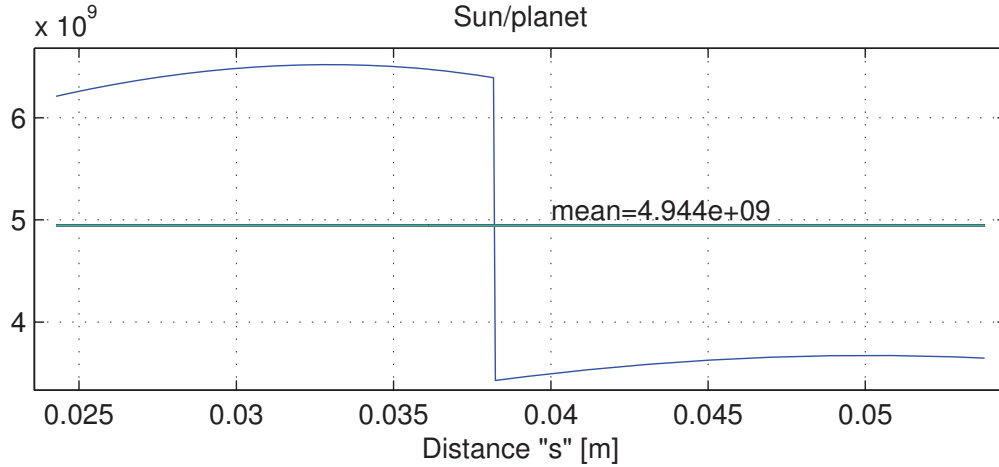


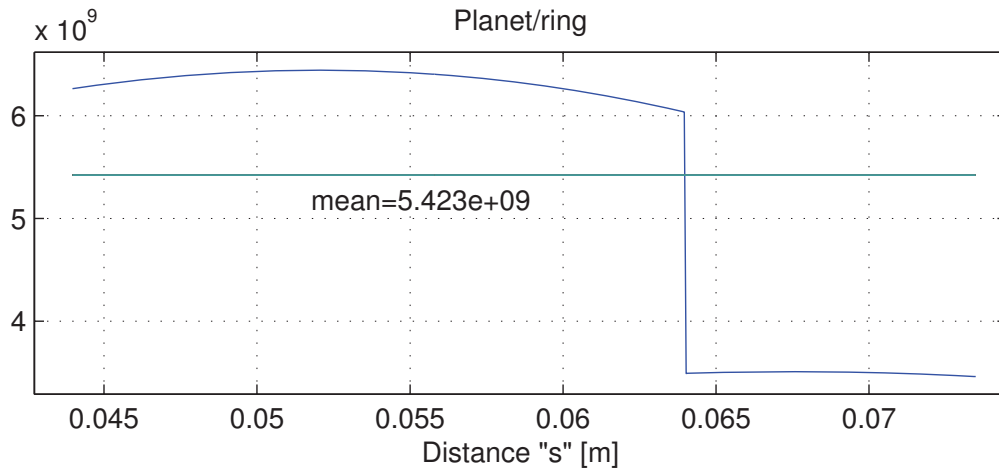
Figure 4.3 Base and working circles for gear  $i$  and  $j$  together with line of contact (tangent to base radii, yellow line) and length of path of contact (purple line). Also note the base circle arc length distance  $s$ , which is important when variable stiffness is used.

Figure 4.3 is an illustration of some important concepts in the equilibrium position (similar to the rigid case with no penetration). The line of contact is shown tangent to both base circles and the contact path illustrates where gear teeth are in contact. Equations of calculating base and working circles etc are given in e.g. [3, 4].

### 4.1.3 Gear tooth stiffness evaluation



(a) Sun/planet stiffness.



(b) Planet/ring stiffness.

Figure 4.4 Stiffness as a function of the base circle arc length  $s$ .

Stiffness coefficients for gear teeth for the 500 kW Nordtank wind turbine has been calculated using Comsol Multiphysics. The stiffness is a function of the base circle arc length  $s$  illustrated in Figure 4.3, i.e.  $s$  is measured as the distance from the base circle of the inner gear and measured along the line of contact. The “inner gear” is a matter of definition, e.g. the sun gear for sun/planet teeth in mesh and the planet gear for planet/ring gear in mesh.

The planetary gearbox in Figure 3.4 on page 24 has gear tooth profiles as shown in e.g. Figure 4.3. Figure 4.4a shows the sun/planet stiffness while Figure 4.4b shows the planet/ring stiffness. It is important to understand the problems arising from the switch from one to two gear teeth in mesh and vice-versa (the

stiffness is a function of the numerical solution and the contact point becomes harder to define). When two gear teeth are in mesh at the same time, the stiffness is high, but if only a single gear tooth is in mesh, the stiffness is low. This “shock” is seen to cause huge oscillations if insufficient damping is used. But implementating gear tooth stiffness like this seems realistic. Important gear tooth parameters including pictures of the wind turbine gearbox housing are found in Appendix C on page 70.

#### 4.1.4 Gear tooth damping

Gear tooth stiffness can be evaluated using FEM-programs (e.g. [5]), but gear tooth damping is more difficult to estimate and especially without any experimental data. If experimental data were available, one possible method of obtaining the damping ratio would be to look at the decay of the response signals. From Equation (4.8)  $\omega_n = \omega_d / \sqrt{1 - \zeta^2}$  which can be inserted into the amplitude part of Equation (4.7), i.e. only consider  $x(t) = Ae^{-\zeta\omega_n t}$  and imagine the last part,  $\sin(\dots) = 1$ , which yields

$$x(t) = A \exp \left( -\frac{\zeta}{\sqrt{1 - \zeta^2}} \omega_d t \right) \quad (4.9)$$

Consider the amplitude of the response at time  $t_0$  (initially) and  $t_N$  (after  $N$  periods) inserted into the above expression. This results in two equations that can be combined into (divide the  $x_0$  equation with the  $x_N$  equation and swap  $t_0$  and  $t_N$ )

$$\ln \frac{x_0}{x_N} = \exp \left( \frac{\zeta}{\sqrt{1 - \zeta^2}} \omega_d (t_N - t_0) \right) \quad (4.10)$$

which can further be reduced using  $(t_N - t_0) = \frac{2\pi}{\omega_d} N$

$$\begin{aligned} \ln \left( \frac{x_0}{x_N} \right) &= \frac{\zeta}{\sqrt{1 - \zeta^2}} 2\pi N \Rightarrow \\ (1 - \zeta^2) \left( \ln \left( \frac{x_0}{x_N} \right) \right)^2 &= \zeta^2 (2\pi N)^2 \Rightarrow \\ \zeta^2 \left( (2\pi N)^2 + \ln^2 \left( \frac{x_0}{x_N} \right) \right) &= \ln^2 \frac{x_0}{x_N} \end{aligned}$$

resulting in the following that can be used for estimating the damping ratio

$$\zeta = \frac{\frac{1}{2\pi N} \ln \left( \frac{x_0}{x_N} \right)}{\sqrt{1 + \left[ \frac{1}{2\pi N} \ln \left( \frac{x_0}{x_N} \right) \right]^2}} \quad (4.11)$$

## 4.2 Force element approach

The above-mentioned is the theoretical text-book approach, which should now be transferred into the multibody program. Based on the program code roughly described in the previous chapter, all gear constraint rows are removed from the Jacobian matrix. The result is a program where the main shaft and sun gear wheel can rotate. But nothing else rotates because there is nothing to connect the gears with any torque. The effect of bearings, i.e. axial and radial forces, is ignored, so it is assumed that the gear contact is perfectly aligned. Torque from FLEX5 for the rotor is put on the carrier body. Torque from FLEX5 for the generator is put on the sun gear. The RHS of equations of motion are modified in a similar way as described earlier (i.e. in section 3.4.1), however something more must be done. The total vector of external forces and moments for all bodies must be modified, i.e.

$$\mathbf{g} = \mathbf{g}^0 + \sum_k \mathbf{g}_{s/p} + \mathbf{g}_{p/r} \quad (4.12)$$

for  $k$  number of planets where index  $s/p$  is the force/torque contribution from sun/planet gear connection and index  $p/r$  is the force/torque contribution from the planet/ring gear. This method makes it easy to add/remove planetary gears.

The time-integrated solution from the multibody code yields  $\theta_i$  and  $\theta_j$  for the current rotation angle of the gears. It also provides  $\dot{\theta}_i = \omega_i$  and  $\dot{\theta}_j = \omega_j$  for the angular velocity of the two gear wheels. By using pitch radii  $\rho_i$  and  $\rho_j$  (or working circle radii if profile shift is used) and inspiration from the simplest gear constraint (Equation (3.17)), something that resembles the penetration depth could be formulated as:  $\theta_i \rho_i - \theta_j \rho_j$ . However, it is not that simple (publication [P3] describes all the details). From Hooke's law,  $F = -kx$ , it is clear that if the penetration depth  $x = 0$ , then there will be no spring forces. Take as an example the sun/planet gear connection: The gear tooth penetration depth  $l_p$  for a rotating planet is something multiplied by a transformation matrix for the driver/carrier ( $\mathbf{A}_d$ ) times a transformation matrix for the sun/planet ( $\mathbf{A}_{s/p}$ ) times a unit vector for the gear tooth normal direction just as in the previous chapter and the whole expression becomes

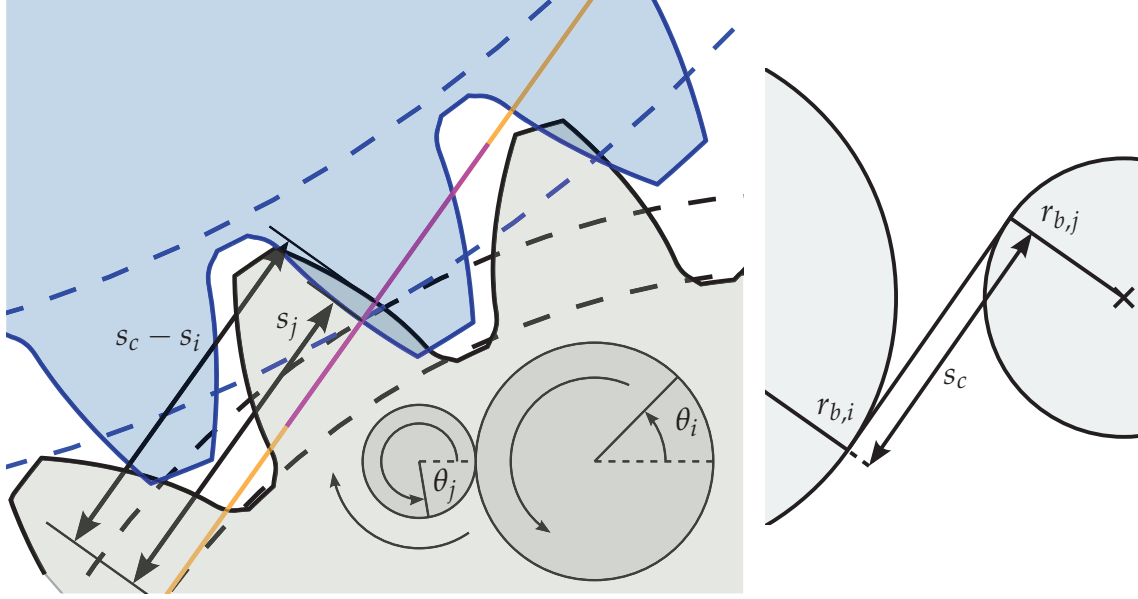
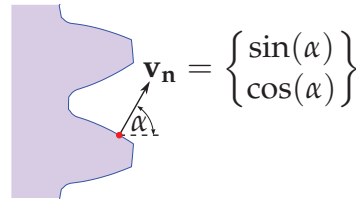


Figure 4.5 Tooth penetration, a little while after the snapshot in Figure 4.3 was taken. The base circle arc length is not easy to define. Total length between base radii is  $s_c$ .

$$\mathbf{l}_p = \mathbf{A}_d \mathbf{A}_{s/p} \mathbf{v}_n \left[ \rho_{b_i}(\theta_i - \theta_i^0 - \theta_d) + \rho_{b_j}(\theta_j - \theta_j^0 - \theta_d) \right], \quad (4.13)$$

where  $\rho_b$  is the base radius,  $\theta_d$  is the driver/carrier angle and  $\theta^0$  is the initial orientation of the gear at  $t = 0$  seconds. The unit tooth surface normal vector is implemented so it corresponds to the rigid gear constraint definition in the previous chapter:

$$\mathbf{v}_n = \begin{Bmatrix} \sin(\alpha) \\ \cos(\alpha) \end{Bmatrix} \quad (4.14)$$



Unit tooth surface normal vector.

Figure 4.6 Unit vector in gear tooth normal direction as a function of pressure angle  $\alpha$ .

Once the penetration depth is known, it can be multiplied with the stiffness (Hooke's law with the global vector  $\mathbf{l}_p$ :  $\mathbf{F}^k = k\mathbf{l}_p$ ) and Equation (4.12) can be employed.

The damping depends on the rate of change of the penetration depth, the velocity of penetration in the normal direction or the differentiated version of Equation (4.13)

$$\dot{\mathbf{l}}_{\mathbf{p}} = \mathbf{A}_{\mathbf{d}} \mathbf{A}_{\mathbf{s}/\mathbf{p}} \mathbf{v}_{\mathbf{n}} \left[ \rho_{b_i}(\omega_i - \omega_d) + \rho_{b_j}(\omega_j - \omega_d) \right] \quad (4.15)$$

In a cartesian coordinate system, the same approach as for stiffness is now used for damping so  $\mathbf{F}^{\mathbf{d}} = d\dot{\mathbf{l}}_{\mathbf{p}}$ . Reaction forces are opposite of each other for bodies  $i$  and  $j$ . Once again, the force contributions are added together using Equation (4.12). Publication [P3] includes additional details as well as examples that show the effect of implementing gear tooth flexibility using the approach described above.

#### 4.2.1 Realistic gear tooth stiffness

An important problem that had to be solved before stiffness curves from Figure 4.4 was implemented, is illustrated in Figure 4.5 on the preceding page. The figure shows that the distances to the tooth flanks in contact ( $s_j$  vs.  $s_c - s_i$ ) are not always the same when flexibility is implemented, even though both are measured from the same gear wheel base circle. It is important here to realise that, even though physically one or two gear teeth are in contact at the same time, numerically only one pair of teeth is in contact the whole time. And the numerical model updates the stiffness in each timestep, so it corresponds to where the gear tooth force acts at the current moment.

The current gear orientation is given by  $\theta_i$  and  $\theta_j$  as shown in Figure 4.5. It is defined that the base circle arc length is always measured from the inner gear (sun gear for s/p-connection and planet gear for p/r-connection). This means that the orientation of one of the gear wheels must be expressed as seen from the point of view of the inner gear (before it is possible to do gear tooth stiffness evaluation). It might help to think of the gears as rigid gears even though this is not the case anymore.

Example: Gear wheel  $i$  is the “inner gear” so the orientation of gear wheel  $j$  should be expressed as seen from gear wheel  $i$ . The orientation of gear  $j$  is  $\theta_j$  and if gear wheels are rigid it can be expressed as  $\theta_i^*$ . The average gear wheel orientation is then calculated as  $\bar{\theta}_i$ :

$$\bar{\theta}_i = \frac{\theta_i + \theta_i^*}{2}, \quad \text{where} \quad \theta_i^* = \frac{-\rho_{b_j}}{\rho_{b_i}} \theta_j \quad (4.16)$$

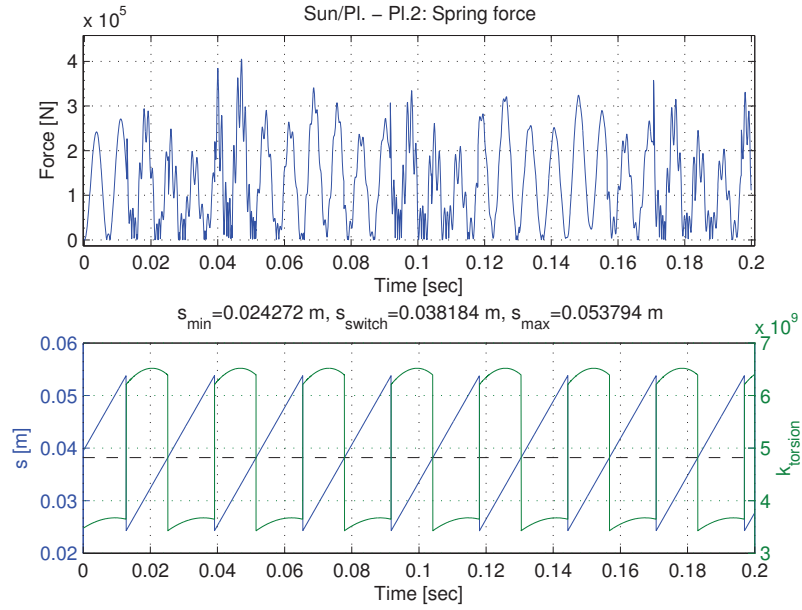
Due to the fact that the stiffness values shown in Figure 4.4 are repetitive, an important rule is now to ensure that the starting point of  $\bar{\theta}_i$  matches the starting point of the stiffness curve. Therefore, an offset is added – either relatively simple (without profile shift) or a bit more complicated (when profile shift is included). Finally, because the stiffness curve is repetitive and assuming the starting point and offset are correct, one may now wrap the average  $\bar{\theta}_i$ -angle

into the interval  $[0; 2\pi/z_i]$ , where  $z_i$  is the number of teeth on gear wheel  $i$ . The “equivalent” base circle arc length seen from gear  $i$  is then

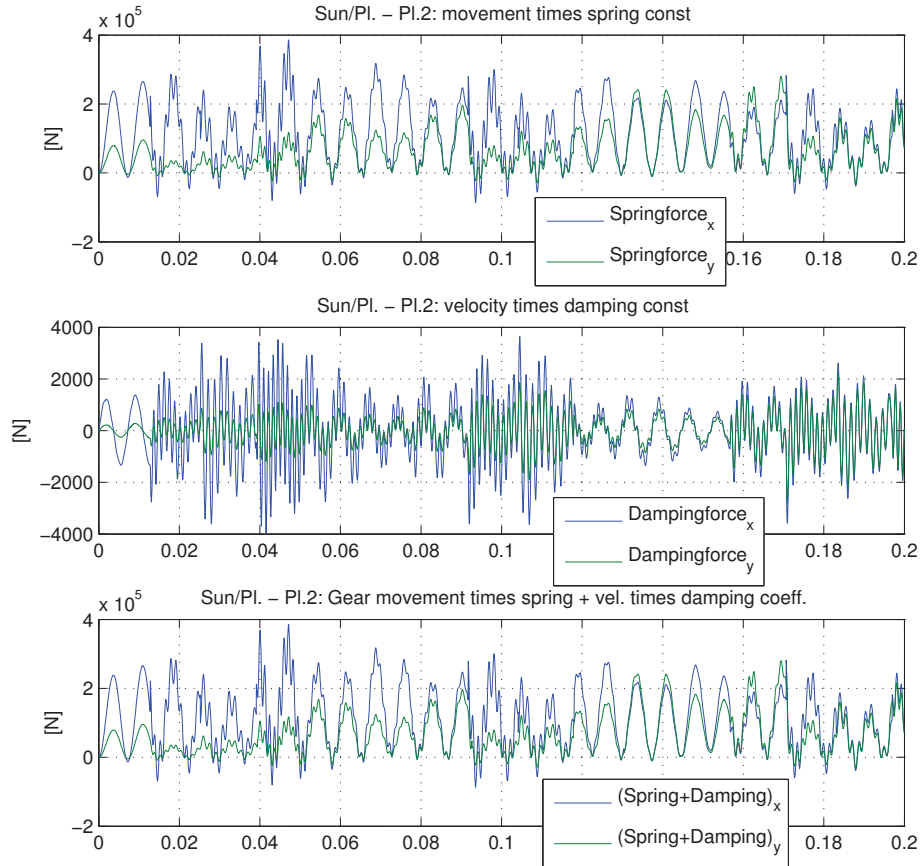
$$\bar{s}_i = \bar{\theta}_i \rho_b + s_{i,min} \quad (4.17)$$

which is the base circle arc length used to obtain the stiffness of the gears (Figure 4.4). The  $s_{i,min}$  is the minimum base circle arc length, because as Figure 4.5 shows, this value cannot be 0 (it has a minimum and a maximum value). Additional details are found in [P2] and [P3]. Figure 4.7 shows an example of gear tooth forces from the Matlab program.





(a) Norm of gear tooth forces and stiffness values as a function of the base circle arc length calculated using Equation (4.17).



(b) The  $x$ - and  $y$ -force components of each contribution of spring and damping forces together with the sum.

Figure 4.7 Realistic gear tooth forces (with constant damping ratio/coefficient).

## References

- [1] D. J. Inman, *Engineering Vibrations (3rd ed.)*. Prentice Hall, 2007.
- [2] L. Meirovitch, *Fundamentals of Vibrations*. McGraw-Hill, 2003.
- [3] P. Klit, K. Casper, and N. L. Pedersen, *Machine Elements - Analysis and Design*. Polyteknisk Forlag, 2009.
- [4] R. L. Norton, *Machine Design: An Integrated Approach, 2nd ed.* Prentice-Hall, 2000.
- [5] C. Multiphysics, “[www.comsol.se](http://www.comsol.se),” 1998-2012.

## Chapter 5

### Fatigue

Random (or stochastic) loads are important when dealing with models subjected to e.g. wind and wave forces. Fatigue is very important for wind turbines (and gearboxes) because high reliability and low maintenance improves the cost of energy. This becomes even more important for offshore installations, because repair costs are very expensive. Taking preventive precautions and being able to perform fatigue calculations is a necessary and important requirement that must be considered. A recommended method to estimate fatigue damage and thus the lifetime of a wind turbine is provided in [1].

This chapter describes a similar approach to this method, but applied to gear teeth fatigue related problems (gear tooth bending failure and surface stresses leading to pitting). A more detailed fatigue analysis involves calculating stresses using aeroelastic codes, possibly in combination with strain gauge measurements for model validation for measuring e.g. blade bending moment, yaw and tilt rotor moments, axial thrust, main shaft torque and tower bending and torsional moments [2].

#### 5.1 Fatigue damage calculation

Calculation of the cumulative fatigue damage for lifetime operation requires a rainflow counting program. If a stress/range simulation signal (timeseries) is unavailable for the whole lifetime, a series of representative smaller signals or timeseries are used. The calculated fatigue damage will then become multiplied by a factor such that e.g. the representative stress cycles for maybe 20 years of operation time have been assessed. For wind turbine fatigue calculations, it is important to know how often the wind speed is between e.g. 7–9 m/s, 9–11 m/s, 11–13 m/s etc. The Weibull cumulative distribution function [3] is given by

$$P(v < v_i) = P(v \geq 0) \left\{ 1 - \exp \left[ - \left( \frac{v_i}{A} \right)^k \right] \right\} \quad (5.1)$$

where  $P(v \geq 0)$  is the probability that the wind speed equals or exceeds zero, while  $P(v < v_i)$  is the probability that the wind speed is below  $v_i$ . A cumulative Weibull probability distribution function is shown in Figure 5.1a.

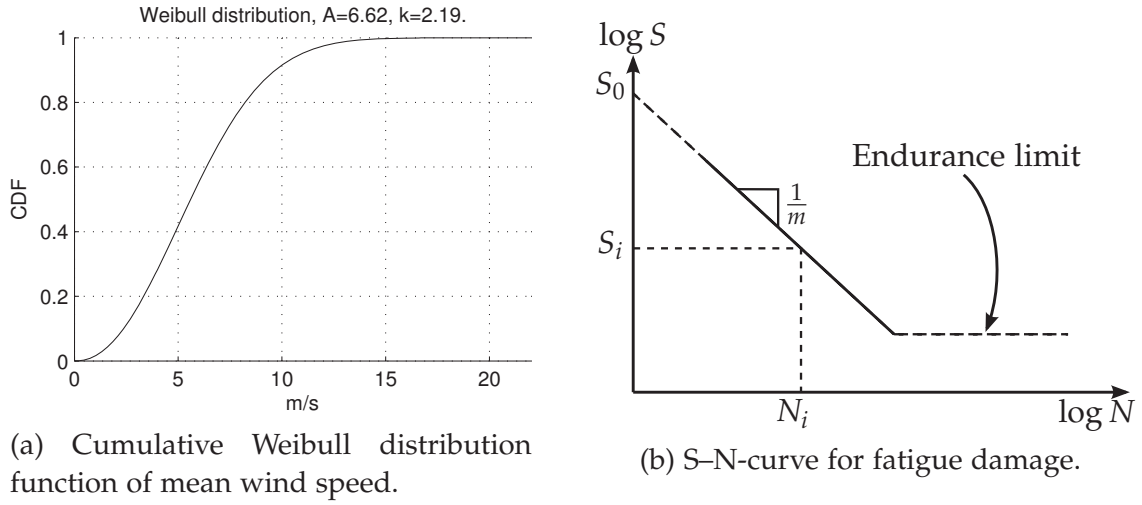


Figure 5.1 Cumulative Weibull distribution function and a Wöhler (S-N) curve.

For this project Weibull parameters  $A = 6.62$  and  $k = 2.19$  have been used (estimated using 5 years of measurement data). The figure shows that the probability of having a mean wind speed of less than or equal to 5 m/s is approximately 42%. The wind turbine is not in operation here because the main shaft torque is too low for efficient power production. The probability of having wind speeds below or equal to 13 m/s is almost 99%. By using these probabilities and based on the fact that there are 365 times 24 hours a year, the amount of hours in operation during a lifetime of e.g. 20 years can be calculated.

#### 5.1.1 Rainflow counting of stress cycles (linear damage hypothesis)

The rainflow counting (RFC) algorithm will be used on a time-series of measurements of simulation data. The number of counted cycles should be “upscaled” i.e. multiplied by a time-factor given by the number of hours in operation divided by the length of the time-series used for the rainflow-counting algorithm.

Figure 5.1b illustrates a Wöhler (S-N) curve. Stresses below the endurance limit do not contribute to fatigue damage even after infinite cycles. The curve itself is a curve-fit designed with a 50% failure likelihood and the uncertainty is therefore generally large [4]. The linear Palmgren-Miner rule, based on Palmgren [5] and Miner [6] states

$$D = \sum_{i=1}^j \frac{n_i}{N_i} = \sum_{i=1}^j n_i \frac{S_i^m}{S_0^m} \quad (5.2)$$

$$\log S_i = \log S_0 - \frac{1}{m} \log N_i \quad \Rightarrow \quad S_i = \frac{S_0}{N_i^{1/m}} \quad (5.3)$$

where  $i$  is a counter for all RFC-results,  $S$  is the stress range,  $n_i$  is the cycle count from the RFC-algorithm,  $N_i$  is the maximum number of stress cycles for the corresponding stress range  $S_i$ , the meaning of  $S_0$  and  $m$  is illustrated in Figure 5.1b ( $S_0$  is the stress range for intersection with the  $y$ -axis and  $1/m$  is the slope of the log-log curve,  $m$  is also known as the damage exponent). Typically 10-minutes time-series are used for the RFC-algorithm when experimental data is available (e.g. [7]). Due to high stiffness of gear teeth, long computation times and large amounts of collected data, only 30 seconds are simulated. The time-factor must be adjusted as explained in publication [P4] (the sun, planet and ring gears have different numbers of teeth).

## 5.2 Fatigue from gear tooth surface stresses (pitting)

Publication [P4] describes and investigates gear tooth fatigue using the flexible model previously described, in relation to:

- Gear tooth root bending
- Gear tooth surface contact (pitting)

From using the gear tooth forces from the previous chapter the gear tooth stresses can be calculated (either using FEM or Hertzian contact assumption, see e.g. [8]). It can be concluded that the stresses for gear tooth root bending using FEM-calculations are too low for causing fatigue. However, by using the Hertzian contact assumption at the surface [8], it can be concluded that the stress peaks sometimes contribute to fatigue under the assumption that the endurance limit for the sun gear is 800 MPa. The whole process of using e.g. Hertzian contact analysis and calculating timefactors is described in detail in [P4] and therefore the rest of this chapter is devoted to a discussion of some aspects and results that were not covered or included in [P4].

### 5.2.1 Tooth surface stress details

Figure 5.2 is an example consisting of 8 graphs for a single involved planet. Note that this graph is constructed using interpolated values, which is considered to be appropriate because the timestep is quite low due to high stiffness. The top 4 graphs are for the sun/planet and the lower 4 graphs are for the planet/ring. The three-dimensional graph in the upper left part of the figure is the most important and the other graphs to the right and below are simply derived using different viewpoints. The fourth graph in the lower right corner illustrates the average maximum von Mises contact stress as a function of the base circle arc

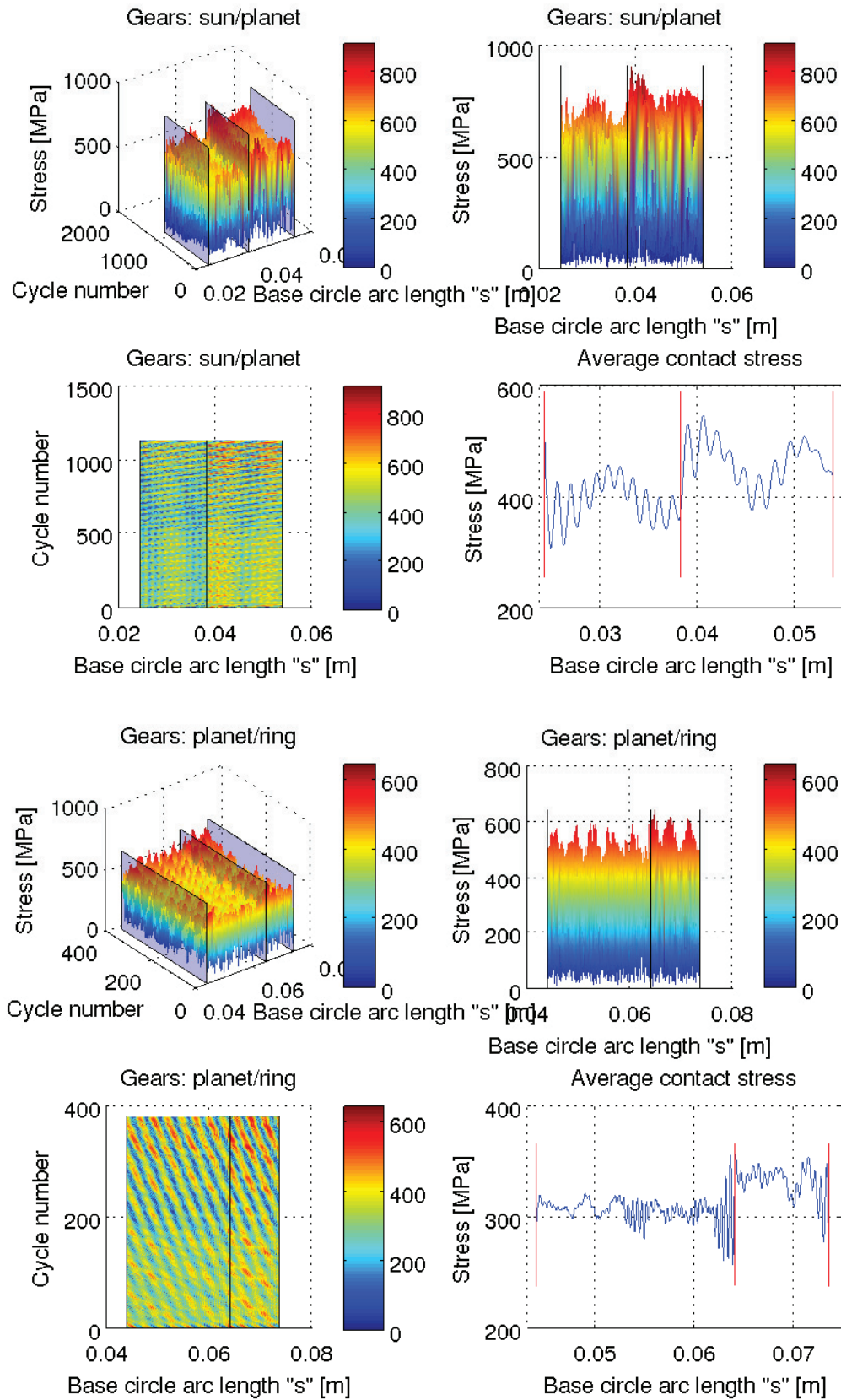


Figure 5.2 Hertzian contact stresses as a function of base circle arc length (and cycles).

length. This graph also shows that the stresses correctly are lower in the two-teeth region when compared with the stresses in the single-tooth region. It is observed that it seems like the maximum sun/planet stresses are larger than those for the planet/ring gear (seen from the maximum values of the color bars, i.e. 800 MPa vs. 600 MPa). Furthermore, generally it seems like the variation of the average sun/planet stresses is larger than that of the planet/ring (the two blue graphs entitled “Average contact stress”). These 8 graphs (4 sun/planet and 4 planet/ring) can be made for all 3 planets, although only one of them is shown here (with small deviations, they generally look the same as shown in the included graphs in Figure 5.2).

s [m]	0.0243	0.0382	0.0538
Teeth in contact	2	-	1

(a) Sun/planet

s [m]	0.044	0.064	0.0735
Teeth in contact	2	-	1

(b) Planet/ring

Table 5.1 Switch between single and multiple teeth in mesh (illustrated in Figure 4.4).

Table 5.1 shows the endpoints of the base circle arc length including the switch-point between two teeth and a single gear tooth in contact. This gives 3 interesting points to observe the stresses at, as a function of time. Additionally, a fourth point is interesting, namely the contact point of the working circles/pitch point (this point is illustrated in Figure 4.3 on page 43 as radius  $\rho_{i,w}$  and  $\rho_{j,w}$ ). The base circle arc length for the working circles/pitch point of the sun/planet gears in mesh is 0.0428 m. For the planet/ring gears in mesh, this value is 0.0668 m. Remember that base circle arc lengths are unless otherwise specified, measured from the “inner gear”, i.e. from the sun gear for the sun/planet gears in mesh and from the planet gear for planet/ring gears in mesh.

Figure 5.3 shows further data processing of the same results shown in Figure 5.2, which is required for doing a fatigue calculation. Specific points along the line of action (specified by the base circle arc length) are chosen and the corresponding stresses are picked out and plotted as a function of time (or cycle number, which is practically but not theoretically the same due to e.g. turbulent wind inflow and variations in rotor and generator torque etc). The specific points of interest are the ones from Table 5.1 with that modification that end-point values must be moved in, for the interpolation to have a sufficient number of data values to base an interpolation on. Additionally, the pitch point or the



location where the working circles meet is included, because this is often the location which serves as a “reference point” in other publications.

Figure 5.3 is interesting in relation to explaining the average maximum von Mises contact stress for all four points of interest. For the sun/planet gear teeth, it can be seen that the average stresses are approximately 390-470 MPa. For the planet/ring, the stress interval is 315-360 MPa and more narrow, which was also a conclusion observed from Figure 5.2. The rainflow count algorithm simply takes these “signals” (exactly the data plotted in Figure 5.3) and processes these into mean and amplitude/range bins. The damage is then calculated using Equation (5.2).

### 5.2.2 Results of accumulated fatigue damage

Publication [P4] only concerns fatigue in the pitch point, i.e. in the single-tooth region. Accurate results require longer simulations than 30 seconds, but due to the high stiffness of the gear teeth the simulation runs rather slow and consumes lots of memory. Remember, however, that due to the number of teeth these 30 seconds in reality correspond to 600, 1,050 and 2,730 seconds for the sun, planet and ring gears respectively (because the multibody program outputs tooth forces for all teeth the whole time, but in reality fatigue only happens for single gear teeth). The small timestep and high stiffness might be a problem and even though experiments have been done at other locations than the pitch point, it seems like the uncertainty of only using a simulation time of 30 seconds might be a problem, sometimes. It requires many long simulations to examine properly.

Figure 5.4a is a graphical representation of the values presented in Table 5.2, which is a result of the RFC-code. Figure 5.4b is then the accumulated total full cycles, taking the necessary timefactors (obtained using Weibull distribution and number of teeth) for 20 years of lifetime into account. The hypothesis behind [P4] is that this method is applicable for longer simulations and Figure 5.5 is the final result presented in [P4].

One possible conclusion from Figure 5.5 is that the sensitivity of fatigue as a function of turbulence intensity is very important for wind turbines in high turbulence regions. Generally it is said that offshore wind turbines are subject to relatively low turbulence and landbased wind turbines are subject to higher turbulence levels, which implies that phenomena such as wake-induced turbulence (turbulence generated in the wake of other wind turbines) is more important on land than at sea. It is a practical problem that the high stiffness leads to very small timesteps, but this could be a potential topic for improvement.



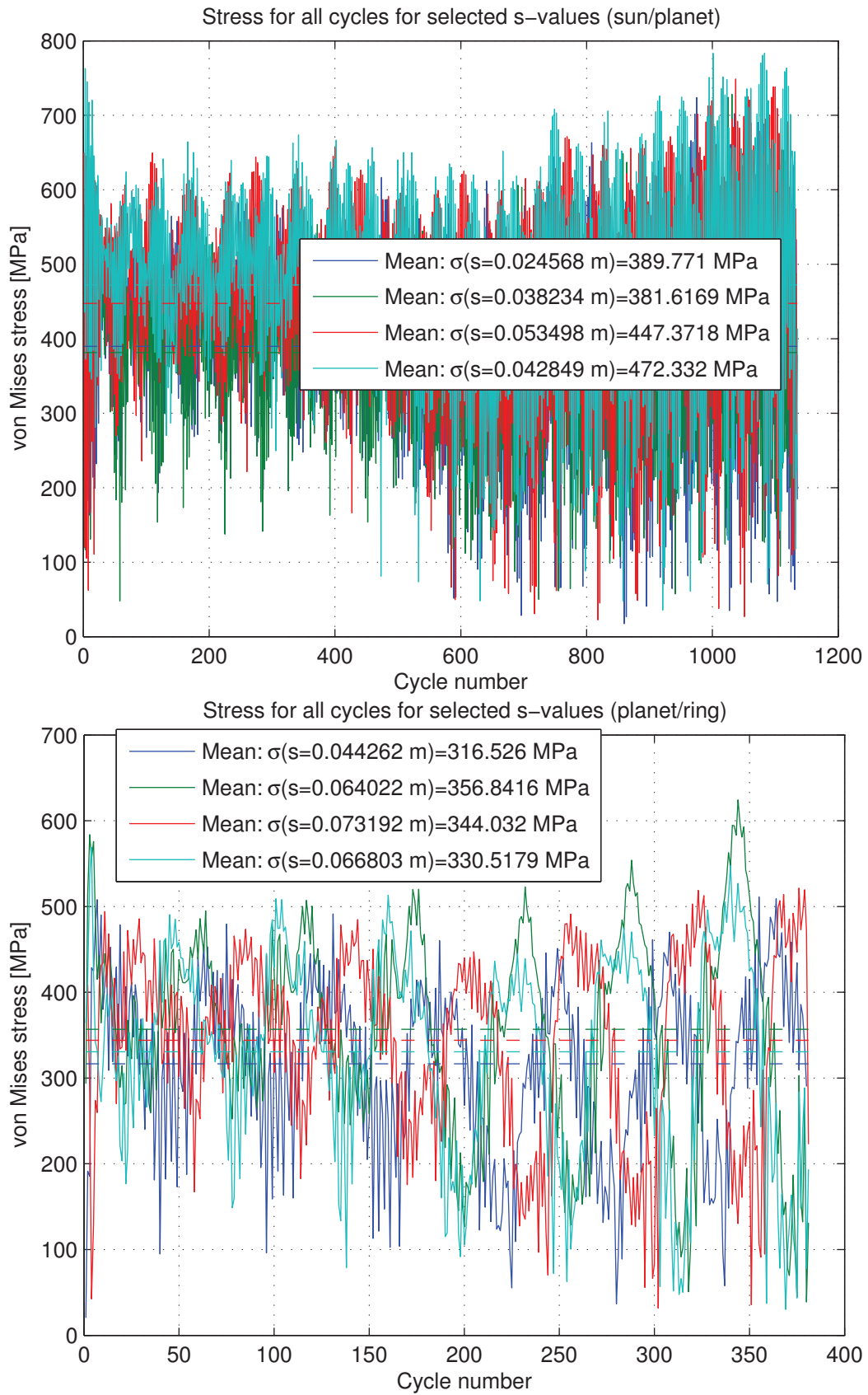
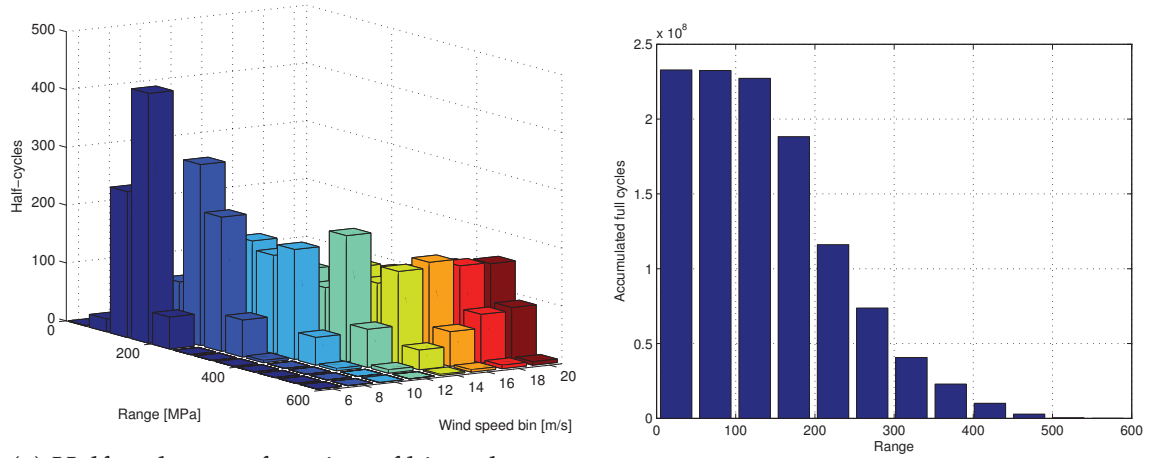


Figure 5.3 Interpolated maximum von Mises stresses at four specific points of interest.



(a) Half cycles as a function of binned mean wind speeds and von Mises range stress.

(b) Lifetime full cycle count.

Figure 5.4 Example of rain flow counting result using TI=8%.

Range [MPa]	6 m/s	8 m/s	10 m/s	12 m/s	14 m/s	16 m/s	18 m/s	20 m/s
25	1	1	1	3	3	1	3	5
74	22	16	6	16	24	16	16	12
124	252	30	28	14	16	20	12	12
173	432	100	50	55	43	42	40	42
223	55	313	78	44	36	36	36	32
272	0	232	185	78	54	57	63	67
322	0	64	170	140	108	102	88	86
371	0	4	190	118	148	134	130	132
421	0	0	48	218	130	116	122	118
471	0	0	4	66	160	170	158	156
520	0	0	0	6	34	60	84	90
570	0	0	0	0	2	4	6	6

Table 5.2 Rainflow count of half-cycles per time-series (see Figure 5.4a).

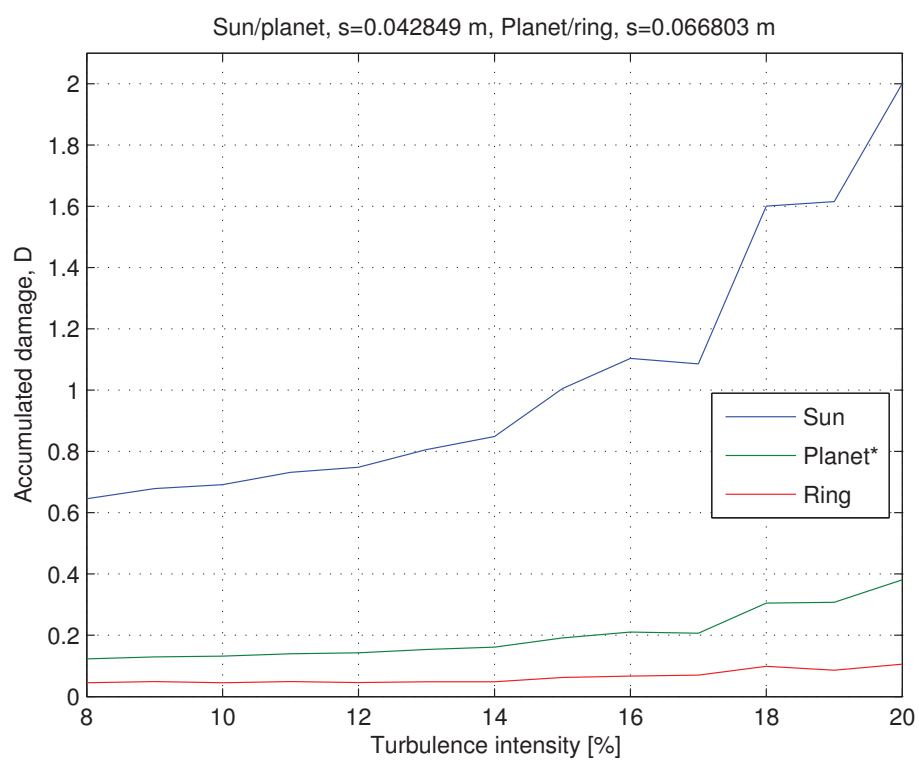


Figure 5.5 Accumulated damage as a function of increasing representative turbulence.

## References

- [1] P. Madsen, *Recommended practices for wind turbine testing and evaluation; 3. Fatigue Loads*, vol. 2. 1990.
- [2] M. O. L. Hansen, *Aerodynamics of Wind Turbines*. Earthscan, 2nd ed, 2009.
- [3] J. Seguro and T. Lambert, "Modern estimation of the parameters of the weibull wind speed distribution for wind energy analysis," *Journal of Wind Engineering and Industrial Aerodynamics*, vol. 85, no. 1, pp. 75 – 84, 2000.
- [4] P. Klit, K. Casper, and N. L. Pedersen, *Machine Elements - Analysis and Design*. Polyteknisk Forlag, 2009.
- [5] A. Palmgren, "Die lebensdauer von kugellagern," *Zeitschrift des Vereins Deutscher Ingenieure* 68.14, pp. 339–341, 1924.
- [6] M. A. Miner, "Cumulative damage in fatigue," *Journal of applied mechanics* 12, no. 3, pp. 159–164, 1945.
- [7] K. S. Hansen and G. C. Larsen, "Database of wind characteristics: <http://www.winddata.com>," 1997-2011.
- [8] R. L. Norton, *Machine Design: An Integrated Approach*, 2nd ed. Prentice-Hall, 2000.

## Chapter 6

### Conclusion

This thesis describes approaches for implementing multibody formulations of wind turbine drivetrains and gearboxes, using a realistic aerodynamic FLEX5 model, which to some extent has been validated using strain gauges and measurements<sup>1</sup>. The FLEX 5 model, data collection, validation and a multibody program is the framework of the project which focused specifically on gear teeth. The outcome of the project includes the present thesis and 4 research publications, with the main results that are shortly summarised:

- P1: The publication documented the efforts behind validation of the FLEX 5 model against experimental data and it introduced the concepts behind the 3D rigid wind turbine modelled using rigid gear constraints. The model was validated using the mean and variance values of mainly measured wind speeds, main shaft torques and power.
- P2: The publication introduces important concepts in relation to gear tooth elasticity, in order to obtain tooth loadsharing among all three planets in a planetary gearbox, which was a problem [P1] did not address. This publication describes the method of using elastic gear teeth, which is also used in the following publications.
- P3: Based on the two previous publications, this publication compares a rigid and a flexible approach. The effect of using discontinuous stiffness is evaluated in greater detail than is found in [P2], seen from a numerical perspective. Simple examples demonstrate the effect of parameter variation of both stiffness and damping and when compared with the rigid multibody model, it is concluded that the flexible model is useful and the hypothesis is that the flexible approach is more accurate than the rigid approach presented in [P1].
- P4: The publication focuses on using the flexible model, particularly in relation to investigating gear tooth fatigue issues. It can be concluded that it is a problem that the timescale with high stiffness of gear tooth is small and this might affect the accuracy of the results. However, the procedure is novel and useful.

---

<sup>1</sup><http://www.winddata.com>

For many purposes the rigid model is deemed fully usable, especially because it is much faster than the flexible model. Publication [P3] clearly shows that the flexible gear tooth forces are close to  $1/3$  of those of the rigid model for a gearbox with three planets, which was also expected. From a practical point of view, publication [P4] suggests that a small increase in turbulence in a high turbulence region (e.g. landbased wind farms) contributes relatively more to gear tooth fatigue damage when compared to a similar increase in low turbulence regions.

## Suggestions for future work

General suggestions for future work include adding more flexibility to the gearbox by removing additional constraints, e.g. to add mainshaft, carrier, bedplate or bearing (joint) flexibility. It could also involve obtaining additional experimental data and matching the numerical results more accurately. Another important challenge might involve optimisation of the described code and seeking better and faster methods for solving this problem. An objective could be to obtain faster computation times and/or in combination with lower memory consumption. Future research could also involve making the whole gear flexible instead of only the teeth. Alternatively, one could also try to fully couple an aerodynamic solver with the current (or an improved version of the) multibody code.

The results described in [P4] could be improved with longer simulation times or the rigid multibody method could be tested on the same procedure because it is faster and takes larger timesteps. 30 seconds for a fatigue simulation might be a bit low, even though the timestep is small and even though it should be multiplied by e.g. 20, 35 or 91 teeth. The problem is not as severe as it sounds because 30 seconds of gear tooth forces and stresses corresponds to running 600 seconds (10 minutes), 1,050 seconds (17.5 minutes) and 2,730 seconds (45.5 minutes) respectively. There is room for improving the code by e.g. not storing so many values.

Future work could also involve formulation of the flexible code in 3D and investigating the 3D effects of e.g. rattling and misalignment and/or in combination with helical gears. Finally, flexible bearing-related problems could also act as a source of failure that needs to be modelled and investigated further.



## Appendix A

### Example of equilibrium analysis

A figure of two gear wheels in mesh, is shown in Figure A.1. The sun center is fixed in the global coordinate system  $(0,0)$  and the planet center is fixed to the carrier. One end of the carrier is also fixed in  $(0,0)$  while the other end of the carrier is fixed to the center of the planet. The carrier angle is fixed to  $0^\circ$  (horizontal).

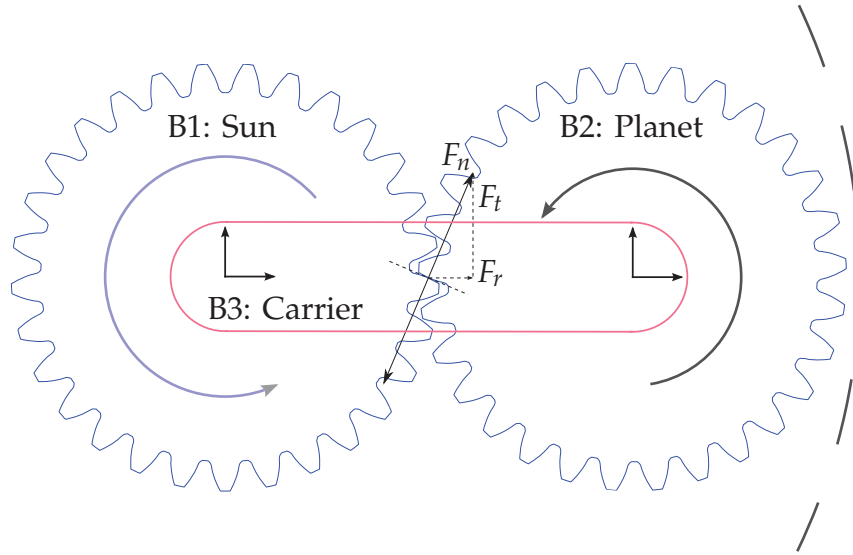
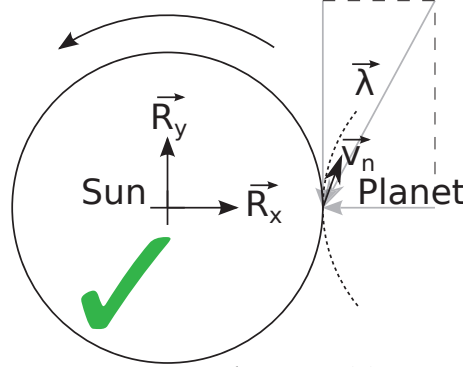


Figure A.1 Two gears in mesh connected by a carrier (in red). The ring gear is illustrated to the right. Torque can now be applied and reaction forces can be analyzed.

This 3-body multibody system can be programmed with 8 constraints as described in section 3.3.3 and 3.3.4 on page 29. If no gears are rotating, Newton's second law of motion describes that  $\mathbf{F} = \mathbf{ma} = \mathbf{0}$  and therefore the gear tooth reaction force(s) on the fixed gear are opposite of each other. 3 tables with reaction forces and moments are shown (rows are:  $Fx_1, Fy_1, Mz_1, Fx_2, Fy_2, Mz_2, Fx_3, Fy_3, Mz_3$ ):

1. Positive torque is applied to both gears (on the RHS), but nothing is moving because everything is static ( $\mathbf{F} = \mathbf{ma} = \mathbf{0}$ ).
2. Torque on gear 1 is increased slightly:  $M_1 = 0.09 + 0.01$ , meaning that both gears will rotate clockwise.
3. Torque on gear 1 is decreased slightly:  $M_1 = 0.09 - 0.01$ , meaning that both gears will rotate counter-clockwise.





Std:  $\mathbf{Ma} = \mathbf{F}_{\text{react}} + \mathbf{F}_{\text{ext}}$ , direction: CCW,  $v_n = A_{70}$ .

Std: $\mathbf{Ma}$	$\lambda_1^*$	$\lambda_2^*$	$\lambda_3^*$	$\lambda_4^*$	$\lambda_5^*$	$\lambda_6^*$	$\lambda_7^*$	$\lambda_8^*$	RHS	$\Sigma$
0.000	0.546	0.000	0.000	0.000	0.000	0.000	0.000	-0.546	0.000	0.000
0.000	0.000	1.500	0.000	0.000	0.000	0.000	0.000	-1.500	0.000	0.000
0.000	0.000	0.000	0.000	0.000	0.000	0.000	0.000	-0.090	0.090	0.000
0.000	0.000	0.000	0.000	-0.546	0.000	0.000	0.000	0.546	0.000	0.000
0.000	0.000	0.000	0.000	0.000	-1.500	0.000	0.000	1.500	0.000	0.000
0.000	0.000	0.000	0.000	0.000	0.000	0.000	0.000	-0.158	0.158	0.000
0.000	0.000	0.000	0.000	0.546	0.000	-0.546	0.000	0.000	0.000	0.000
0.000	0.000	0.000	0.000	0.000	1.500	0.000	-1.500	0.000	0.000	0.000
0.000	0.000	0.000	-0.247	0.000	0.124	0.000	0.124	0.000	0.000	0.000

M1+:  $\mathbf{Ma} = \mathbf{F}_{\text{react}} + \mathbf{F}_{\text{ext}}$ , direction: CCW,  $v_n = A_{70}$ .

M1+: $\mathbf{Ma}$	$\lambda_1^*$	$\lambda_2^*$	$\lambda_3^*$	$\lambda_4^*$	$\lambda_5^*$	$\lambda_6^*$	$\lambda_7^*$	$\lambda_8^*$	RHS	$\Sigma$
0.000	0.592	0.000	0.000	0.000	0.000	0.000	0.000	-0.592	0.000	0.000
0.000	0.000	1.626	0.000	0.000	0.000	0.000	0.000	-1.626	0.000	0.000
0.003	0.000	0.000	0.000	0.000	0.000	0.000	0.000	-0.098	0.100	0.000
0.000	0.000	0.000	0.000	-0.592	0.000	0.000	0.000	0.592	0.000	0.000
0.000	0.000	0.000	0.000	0.000	-1.626	0.000	0.000	1.626	0.000	0.000
-0.013	0.000	0.000	0.000	0.000	0.000	0.000	0.000	-0.171	0.158	0.000
0.000	0.000	0.000	0.000	0.592	0.000	-0.592	0.000	0.000	0.000	0.000
0.000	0.000	0.000	0.000	0.000	1.626	0.000	-1.626	0.000	0.000	0.000
0.000	0.000	0.000	-0.268	0.000	0.134	0.000	0.134	0.000	0.000	0.000

M1-:  $\mathbf{Ma} = \mathbf{F}_{\text{react}} + \mathbf{F}_{\text{ext}}$ , direction: CCW,  $v_n = A_{70}$ .

M1-: $\mathbf{Ma}$	$\lambda_1^*$	$\lambda_2^*$	$\lambda_3^*$	$\lambda_4^*$	$\lambda_5^*$	$\lambda_6^*$	$\lambda_7^*$	$\lambda_8^*$	RHS	$\Sigma$
0.000	0.500	0.000	0.000	0.000	0.000	0.000	0.000	-0.500	0.000	0.000
0.000	0.000	1.374	0.000	0.000	0.000	0.000	0.000	-1.374	0.000	0.000
-0.003	0.000	0.000	0.000	0.000	0.000	0.000	0.000	-0.083	0.080	0.000
0.000	0.000	0.000	0.000	-0.500	0.000	0.000	0.000	0.500	0.000	0.000
0.000	0.000	0.000	0.000	0.000	-1.374	0.000	0.000	1.374	0.000	0.000
0.013	0.000	0.000	0.000	0.000	0.000	0.000	0.000	-0.144	0.158	0.000
0.000	0.000	0.000	0.000	0.500	0.000	-0.500	0.000	0.000	0.000	0.000
0.000	0.000	0.000	0.000	0.000	1.374	0.000	-1.374	0.000	0.000	0.000
0.000	0.000	0.000	-0.227	0.000	0.113	0.000	0.113	0.000	0.000	0.000

Figure A.2 Gear tooth normal reaction force  $\lambda$  and unit vector  $v_r$  for  $[A_{+70}]$ . Reaction forces (70 deg).  $R_1, R_2$ : OK and opposite of vector  $\lambda$  (figure)!

## Appendix B

### Multibody gear constraints

Body	Description	Body	Description
1	MS + PC	5	Planet 2
2	Ring	6	Planet 3
3	Planet 1	7	Lower gearparts
4	Sun+shaft+gear 1	8	Generator+gearparts

Table B.1 Description of bodies. MS = main shaft. PC = planetary carrier.

Body	Description	LCS [ $\approx$ m]	Mass [kg]	$I_{zz}$ [kg·m <sup>2</sup> ]
1	MS + PC	1.62	1759	30.9 <sup>1</sup>
2	Ring	2.81	122	12.6
3	Planet 1	2.81	163	0.82
4	Sun+shaft+gear 1	3.12	145	3.58
5	Planet 2	2.81	163	0.82
6	Planet 3	2.81	163	0.82
7	Lower gearparts	3.54	31	0.41
8	Generator+gearparts	4.08	1180	118

Table B.2 Description of bodies. LCS = z-coordinate of local coordinates system, from global reference frame/system. MS = main shaft. PC = planetary carrier.

The following constraints / equations are used (only the simple gear-constraints are shown here even though implemented alternatively):

#### Body 1 (Main shaft + planetary carrier)

Main shaft is attached to two bearings, it has 3+2 constraint equations:

$\Phi_{1-3}$  : Main shaft, connected to first bearing (3 eqs) with a spherical joint:

$$\{r_1\} + [A_1]\{s'_{B1}\} - \{s''_{B1}\} = \{0 \ 0 \ 0\}^T$$

$\Phi_{4-5}$  : Main shaft, connected to second bearing (2 eqs) with a spherical joint:

$$\{r_1\} + [A_1]\{s'_{B2}\} - \{s''_{B2}\} = \{0 \ 0 \ 0\}^T$$

NB: Only the  $x$  and  $y$  equations are used from these 3 equations (last equation is ignored).

**Body 2 (Ring gear)**

$\Phi_{6-8}$  : Ring gear, connected with spherical joint to a fixed point (ground):

$$\{r_2\} - \{0 \ 0 \ 2.81\}^T = \{0 \ 0 \ 0\}^T$$

$\Phi_9$  : Parallel constraint:  $([A_2]\{\hat{Q}'_1\})^T\{r_{\text{rot}}\} = 0$ , NB: Parallel with bedplate

$\Phi_{10}$  : Parallel constraint:  $([A_2]\{\hat{Q}'_2\})^T\{r_{\text{rot}}\} = 0$

$\Phi_{11}$  : Fix rotation,  $\omega_{\zeta} = 0$

**Body 3 (Planet 1)**

$\Phi_{12-14}$  : Planetary carrier (body 1) connected to planet 1 (body 3):

$$\{r_1\} + [A_1]\{s'_{pl.1}\} - \{r_3\} = \{0 \ 0 \ 0\}^T, \text{ note } \{s'_{pl.1}\} = \{0.2775 \ 0 \ 0\}^T$$

$\Phi_{15}$  : Parallel constraint:  $([A_3]\{\hat{Q}'_1\})^T([A_1]\{r'_{\text{rot}}\}) = 0$

$\Phi_{16}$  : Parallel constraint:  $([A_3]\{\hat{Q}'_2\})^T([A_1]\{r'_{\text{rot}}\}) = 0$

$\Phi_{17}$  : Gear constraint:  $\rho_{\text{ring}}(\omega_{B2} - \omega_{B1}) - \rho_{\text{planet}}(\omega_{B3} - \omega_{B1}) = 0$

**Body 4 (Sun)**

$\Phi_{18-20}$  : Sun, connected to first bearing (3 eqs) with a spherical joint:

$$\{r_4\} + [A_4]\{s'_{B4}\} - \{s''_{B4}\} = \{0 \ 0 \ 0\}^T$$

$\Phi_{21-22}$  : Sun, connected to second bearing (2 eqs) with a spherical joint:

$$\{r_4\} + [A_4]\{s'_{B4}\} - \{s''_{B4}\} = \{0 \ 0 \ 0\}^T$$

NB: Only the  $x$  and  $y$  equations are used from these 3 equations (last equation is ignored).

$\Phi_{23}$  : Gear constraint:  $\rho_{\text{planet}}(\omega_{B3} - \omega_{B1}) + \rho_{\text{sun}}(\omega_{B4} + \omega_{B1}) = 0$

**Body 5 (Planet 2)**

$\Phi_{24-26}$  : Planetary carrier (body 1) connected to planet 2 (body 5):

$$\{r_1\} + [A_1]\{s'_{pl.2}\} - \{r_5\} = \{0 \ 0 \ 0\}^T, \text{ note } \{s'_{pl.2}\} = \{-0.1387 \ 0.2403 \ 0\}^T$$

$\Phi_{27}$  : Parallel constraint:  $([A_5]\{\hat{Q}'_1\})^T([A_1]\{r'_{\text{rot}}\}) = 0$

$\Phi_{28}$  : Parallel constraint:  $([A_5]\{\hat{Q}'_2\})^T([A_1]\{r'_{\text{rot}}\}) = 0$

$\Phi_{29}$  : Gear constraint:  $\rho_{\text{ring}}(\omega_{B2} - \omega_{B1}) - \rho_{\text{planet}}(\omega_{B5} - \omega_{B1}) = 0$

**Body 6 (Planet 3)**

$\Phi_{30-32}$  : Planetary carrier (body 1) connected to planet 3 (body 6):

$$\{r_1\} + [A_1]\{s'_{pl.3}\} - \{r_6\} = \{0 \ 0 \ 0\}^T, \text{ note } \{s'_{pl.3}\} = \{-0.1388 \ -0.2403 \ 0\}^T$$

$\Phi_{33}$  : Parallel constraint:  $([A_6]\{\hat{Q}'_1\})^T([A_1]\{r'_{\text{rot}}\}) = 0$

$\Phi_{34}$  : Parallel constraint:  $([A_6]\{\hat{Q}'_2\})^T([A_1]\{r'_{\text{rot}}\}) = 0$

$\Phi_{35}$  : Gear constraint:  $\rho_{\text{ring}}(\omega_{B2} - \omega_{B1}) - \rho_{\text{planet}}(\omega_{B6} - \omega_{B1}) = 0$

**Body 7 (Lower gear parts)**

Lower gear parts shaft is attached to two bearings, has 3+2 constraint equations:

$\Phi_{36-38}$  : Gear parts shaft, connected to first bearing (3 eqs) with a spherical joint:

$$\{r_7\} + [A_7]\{s'_{B1}\} - \{s''_{B1}\} = \{0 \ 0 \ 0\}^T$$

$\Phi_{39-40}$  : Gear parts shaft, connected to second bearing (2 eqs) w/ spherical joint:

$$\{r_7\} + [A_7]\{s'_{B2}\} - \{s''_{B2}\} = \{0 \ 0 \ 0\}^T$$

NB: Only the  $x$  and  $y$  equations are used from these 3 equations

(last equation is ignored).

$$\Phi_{41} : \text{Gear constraint: } (\rho_{\text{par.1}} \cdot \omega_{B4}) + (\rho_{\text{par.2}} \cdot \omega_{B7}) = 0$$

**Body 8 (Generator + gear parts)**

Generator + shaft is attached to the two bearings, has 3+2 constraint equations:

$\Phi_{42-44}$  : Generator + shaft, connected to first bearing (3 eqs) w/ spherical joint:

$$\{r_8\} + [A_8]\{s'_{B1}\} - \{s''_{B1}\} = \{0 \ 0 \ 0\}^T$$

$\Phi_{45-46}$  : Generator + shaft, connected to second bearing (2 eqs):

$$\{r_8\} + [A_8]\{s'_{B2}\} - \{s''_{B2}\} = \{0 \ 0 \ 0\}^T$$

NB: Only the  $x$  and  $y$  equations are used from these 3 equations

(last equation is ignored).

$$\Phi_{47} : \text{Gear constraint: } (\rho_{\text{par.3}} \cdot \omega_{B7}) + (\rho_{\text{par.4}} \cdot \omega_{B8}) = 0$$

## Appendix C

### Gearbox data

Figure C.1 is taken from inside the nacelle, which can open up for manual inspection and service. The gearbox manufacturer is Flender and basic gearbox data is provided in Table C.1.



(a) Gearbox (1 planetary gear stage and 2 parallel gear stages). (b) Slip rings on main shaft (gearbox front). (c) Gearbox (front) and generator (back).

Figure C.1 Selected gearbox pictures from the nacelle of the 500 kW wind turbine.

Gear location	Normal module, $M_n$	Teeth $z_1/z_2$	Ratio -	Face-width [mm]	Center distance [mm]
Planetary, outer	10	35/-91	2.6	210/238	-284
Planetary, inner	10	20/35	1.75	225/210	284
Parallel, 1st	7	20/81	4.05	185/165	370
Parallel, 2nd	5	29/72	2.48	130/120	265

Table C.1 Simplified gear details (ignoring helix angle and profile shift). Gear-radii is used in gear-constraints:  $\rho_{\text{ring}} = 455$  mm,  $\rho_{\text{planet}} = 177.5$  mm,  $\rho_{\text{sun}} = 100$  mm,  $\rho_{\text{par.1}} = 283.5$  mm,  $\rho_{\text{par.2}} = 70$  mm,  $\rho_{\text{par.3}} = 180$  mm,  $\rho_{\text{par.4}} = 72.5$  mm.

## **Appendix D**

### **Publications**

These publications (long titles are abbreviated) incl. page references follows:

- P1: (Rigid MATLAB drivetrain model of a 500 kW wind turbine), page 72.
- P2: On Gear Tooth Stiffness Evaluation, page 91.
- P3: (A Rigid and a Flexible Multibody gearbox model), page 112.
- P4: (Gear fatigue damage for increasing turbulence), page 136.

## Publication [P1]

Rigid MATLAB drivetrain model of a 500 kW wind turbine for predicting maximum gear tooth stresses in a planetary gearbox using multibody gear constraints

## RESEARCH ARTICLE

## Rigid MATLAB drivetrain model of a 500 kW wind turbine for predicting maximum gear tooth stresses in a planetary gearbox using multibody gear constraints

M. F. Jørgensen<sup>1</sup>, Niels L. Pedersen<sup>1</sup>, Jens N. Sørensen<sup>2</sup> and Uwe S. Paulsen<sup>2</sup>

<sup>1</sup> Department of Mechanical Engineering, Technical University of Denmark, Denmark

<sup>2</sup> Department of Wind Energy, Technical University of Denmark, Denmark

### ABSTRACT

The aeroelastic FLEX 5 code and a semi-advanced rigid multibody model has been utilized for simulating drivetrain forces and moments in a real 500 kW wind turbine. Experimental validation is carried out with results based on known physical properties of the blades, tower, hub, gearbox, shaft and nacelle, etc. The multibody model consists of eight bodies, from rotor to generator, where most joints are made using simple constraints. Semi-advanced gear constraints are used for obtaining (worst-case) gear tooth reaction forces in the first stage of the planetary gearbox. This constraint is useful for not only transferring torque but also for calculating the gear tooth and internal body reaction forces. The method is appropriate for predicting gear tooth stresses without considering all the complexity of gear tooth geometries. This means that, e.g. gear tooth load-sharing and load-distribution among multiple planetary gears are not taken into account. Finite Element Method (FEM) calculations show that when the wind turbine runs close to the maximum wind speed, the maximum gear tooth stress is in the range of 500–700 MPa, which is considered to be realistic using a “worst-case” method. The presented method is based on a comprehensive description of the aerodynamic input, including inflow turbulence and shear, as well as various modifications for yaw, dynamic stall and dynamic inflow. Forces and torque from the aeroelastic and industry-accepted code FLEX 5 are used as input to the multibody program, where the gear constraint is formulated such that the maximum tooth forces are included directly in the solution. Copyright © 2013 John Wiley & Sons, Ltd.

### KEYWORDS

drivetrain; multibody; planetary gearbox; tooth stresses; wind energy; FEM

### Correspondence

M. F. Jørgensen, Department of Mechanical Engineering, Technical University of Denmark, Denmark.

E-mail: mfjo@mek.dtu.dk

Received 19 December 2012; Revised 3 June 2013; Accepted 13 July 2013

## 1. INTRODUCTION

Wind turbine modeling software is constantly being improved or combined with other new codes and tools/models. The industry wants a better understanding that improves reliability and lower maintenance costs. An example of a challenge faced by industry is that wind turbines and main components are being upscaled to reduce energy costs, and this drives the development towards improving the existing wind turbine models. Upscaling is known to cause severe problems mainly because of an increase in weight and stresses.<sup>1</sup> Not many aeroelastic tools focus much on drivetrain loads which are very important—not to speak of the implications of changing a gearbox, which is typically a time-consuming and extremely costly exercise. It becomes critical to have accurate tools and models for predicting gear tooth stresses for all wind turbine sizes.

For predicting wind turbine loads, various aeroelastic modeling tools such as GH BLADED (Garrahd Hassan & Partners Limited, Bristol, UK), FAST (National Renewable Energy Laboratory, Golden, Colorado 80401-3393), ADAMS (MSC Software Corporation Santa Ana, California 92707), HAWC (DTU Risø, Roskilde, Denmark), HAWC2 (DTU Risø, Roskilde, Denmark), BHAWC (Siemens Wind Power A/S, Brande, Denmark) and different versions of FLEX (Stig Øye, Gentofte, Denmark) have been validated and used extensively by the wind turbine industry. An extensive code-comparison investigation<sup>2</sup>



was made within the International Energy Agency, known as the Offshore Code Comparison Collaboration. It was established as a wind turbine code-to-code verification forum, and a number of free publications<sup>3</sup> were made available to the public.

Globally installed wind power capacity has boomed in the last years, but the output from traditional wind turbine simulation tools provides little detailed insight into the dynamic behavior of drivetrains.<sup>4</sup> Forces and moments can be extracted from the aeroelastic tools and either the code can be coupled to a more advanced model, or the results can be post-processed using another program. There are a number of examples of this, and a number of those related to multibody/drivetrain/gearbox analysis are mentioned and discussed in the succeeding texts:

- As an example, GH BLADED provides an option to program a user-defined wind turbine controller that couples with the aeroelastic calculations. This dynamic link library (DLL)-interface enables the user to interact with a running simulation and for instance, to create a gearbox DLL.
- The HAWC2 aeroelastic code developed at Technical University of Denmark (DTU) Risø also addresses gearbox problems by interfacing with external DLLs, typically programmed in Fortran. As an example, Hansen, Rasmussen and Larsen (2011)<sup>5</sup> investigates “double contact” (tooth wedging) between gear wheels in a planetary gearbox, in an attempt to explain many gearbox failures occurring from 1995 to 2005. It is found that high planet carrier bearing clearance and low gear tooth backlash increase the risk of gear tooth “double contact”.
- In the study of Haastrup, Hansen and Ebbesen (2011),<sup>6</sup> the commercial multibody dynamics software ADAMS/VIEW (MSC Software Corporation Santa Ana, California 92707) was used to model the main shaft and gearbox (assumed to be without gears and high speed shaft to increase simulation speed) and different bushing models were investigated. Optimization was done in MATLAB (The MathWorks, Inc. Natick, Massachusetts 01760 USA) and ADAMS/VIEW was used for running simulations.
- In the study of Peeters, Vandepitte and Sas (2006),<sup>7</sup> different types of “torsional” multibody models of a wind turbine drivetrain (including the gearbox) were simulated using the LMS DADS (LMS International (a Siemens Business), 3001 Leuven, Belgium) multi-body software package. A step further was taken by using not only rigidly connected bodies but also by introducing a flexible multibody model where the bodies themselves can deform (as well as the couplings between bodies, which, e.g. could be the gear mesh or bearing stiffness). This gives more realistic dynamic results at the cost of making the problem more complicated because the additional degrees of freedom (DOF) are introduced by a finite element approach. Eigenfrequencies and modeshapes were shown, and the software package MSC/NASTRAN (MSC Software Corporation Santa Ana, California 92707) was used for calculation of finite element results.

The FLEX 5<sup>8</sup> code, developed at DTU Mechanical Engineering in the 1990, is commercially accepted as conforming to industry standards because of its long history in which it has been verified and tested (both in academia and in industry). For this reason, we employ this code to obtain loads for the described multibody drivetrain program in the present study. FLEX 5 is widely used in the industry and to a lesser extent in academia. Not many publications are made with FLEX 5 in relation to drivetrain/gearbox problems. A likely reason is that the original version is in Pascal, and interfacing with this is likely to be more problematic than saving the results and loading them into another program (not many Pascal libraries and developers exist today, and only a few people use this programming language today). An in-house developed Fortran version also exists. A FLEX 5 Pascal-demo capable of running simulations up to 5 min was used in preparing this article.

Using the multibody systems approach means that two or more rigid (or flexible) bodies are joined together by means of kinematic conditions (constraints). These bodies can undergo large rotations/displacements. Generally, there are two multibody disciplines: (1) kinematics, the study of position  $\{q\}$ , velocity  $\{\dot{q}\}$  and acceleration  $\{\ddot{q}\}$  without considering forces or moments and (2) kinetics/dynamics which take forces and moments into account. Several books deal with multibody dynamics, see, e.g. the studies of Nikravesh (1988)<sup>9</sup>, Haug (1989)<sup>10</sup> and Shabana (1989).<sup>11</sup> The present article describes a method to obtain drivetrain results including gear tooth stress, using a rigid multibody program and semi-advanced gear constraints using experimental data and FLEX 5 simulations.

Note that the convention used in this article for denoting a column vector is  $\{\cdots\}$ , and  $[\cdots]$  denotes a matrix.

## 2. METHOD DESCRIPTION

Figure 1 shows an outline of the method used in this paper for predicting gear tooth stresses. Using this approach, aeroelastic results from the FLEX 5 code are used as input, and the equations are formulated for a general constrained dynamic mechanical system using a rigid eight-body multibody program with semi-advanced gear constraints.

1. Wind turbine loads are calculated with FLEX 5 using a model based on the unsteady blade-element momentum (BEM) theory.<sup>12</sup> The dynamic system  $[M]\{\ddot{x}\} + [C]\{\dot{x}\} + [K]\{x\} = \{F_g\}$  with mass matrix  $[M]$ , stiffness matrix  $[K]$ , damping matrix  $[C]$  and a vector of generalized forces/external loads  $\{F_g\}$  is solved using a Runge–Kutta–Nyström scheme.

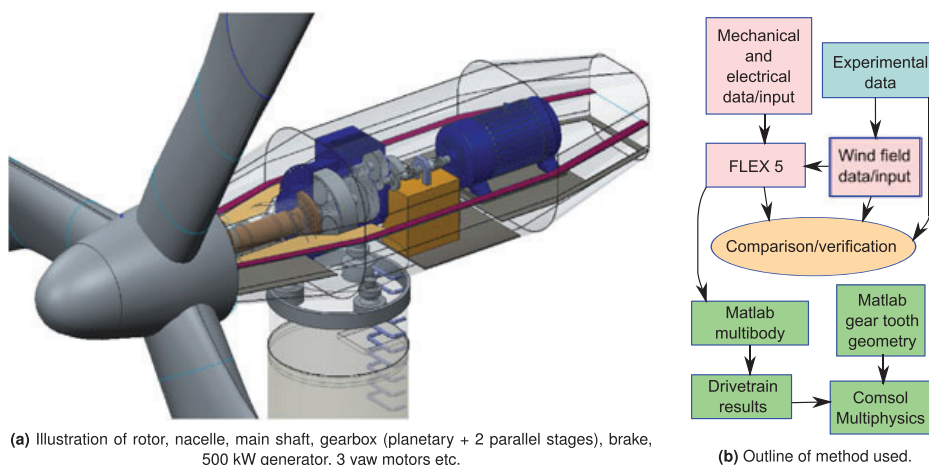


**Figure 1.** (a) Wind turbine/drivetrain illustration and (b) outline of method used.

- Verification was accomplished by comparing FLEX 5 results with experimental data, such as wind speed, power production, main shaft torque and bending moments. Experimental time series from Hansen and Larsen<sup>13</sup> were mainly selected, based on wind speed, wind direction and turbulence intensity. Only complete time series with full sensor data are used. In a few cases, time series are disregarded because the wind turbine is not in operation, down for maintenance; strain gauge measurements are not included or effects of signal drift, hysteresis or ambiguous calibration settings make the data obviously wrong. The measured power output and the measured main shaft torque were compared with values from simulated time series. The results correlate sufficiently well to argue that it is reasonable to use FLEX 5 for generating simulated time series for the further analysis.
- FLEX 5 forces and torque are used as input in the multibody drivetrain program. Equilibrium equations for force and moment are added with a set of constraints (Lagrange multipliers). The program makes it possible to extract reaction forces everywhere on the drivetrain although in this work, we focus on the gear tooth forces and stresses.
- Finally, gear tooth stresses on every gear wheel in the simulated wind turbine are calculated. The gear tooth profile pairs from the planetary gearbox for this specific 500 kW wind turbine were generated, rotated and meshed with MATLAB and the COMSOL MULTIPHYSICS (COMSOL AB SE-111 40 Stockholm SWEDEN) FEM package.

In this article, only the stresses on the gear wheels in the first stage of the gearbox are considered. The reason is mainly that the maximum torque is found on this side of the gearbox, and it is therefore assumed that the stresses are most critical here. If this is not the case, the whole procedure can be repeated for other gear wheels than those dealt with here. The numbering shown previously corresponds to the numbering of the following subsections that describe the procedure in more detail.

Instead of a dedicated commercial tool, a MATLAB program with semi-advanced gear constraints have been employed. One might argue that this model lacks insight into the dynamics of the model, but because of the fact that FLEX 5 already included the important overall dynamics of the whole system including tower, blade and mainshaft bending/torsion, the error by using a relatively simple multibody model is deemed acceptable. The maximum gear tooth stress problem can be described and made much more complicated than here but that also raises the number of unknowns to a higher level. By making our own code for obtaining maximum gear tooth forces, we have absolute control and understanding of what happens. It is not possible to modify this gearbox, and therefore, we cannot validate the final gear tooth stresses in this 500 kW wind turbine and gearbox. For the same reason, it is not possible to make conclusions on the accuracy (or lack of accuracy) using this method.

## 2.1. Aerodynamic and aeroelastic modeling

A list of mechanical properties and other important input data are shown in Figure 2. The wind field is specified in terms of mean wind speed and turbulence intensity. The force components  $\{F_x, F_y, F_z\}^T$  and moments  $\{M_x, M_y, M_z\}^T$  at the rotor are saved for use in the multibody program, which inputs them to the right hand side (RHS) of the equations of motion to be solved.

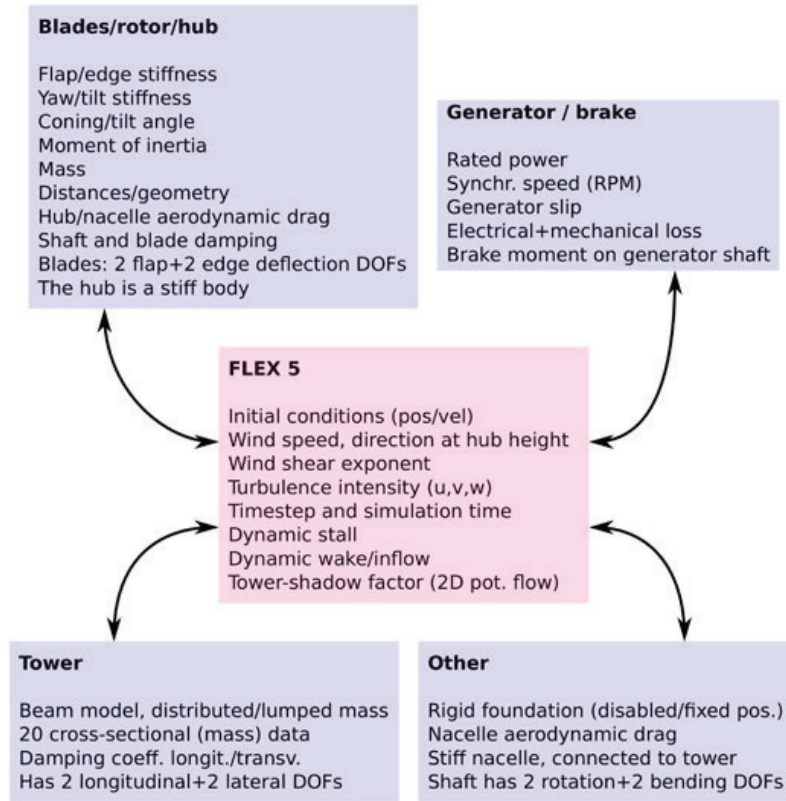


**Figure 2.** Aerodynamic input, model and a short outline of some important methods that illustrates how FLEX 5 works.<sup>8</sup>

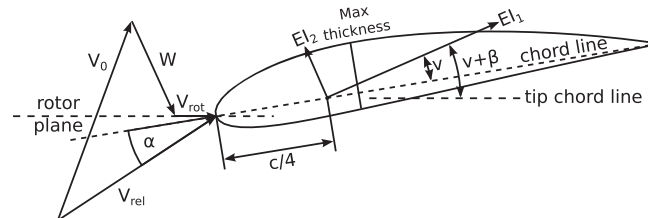


**Figure 3.** One blade section together with velocity triangle, inspired by Hansen (2009).<sup>12</sup> Note that the wind inflow here is shown for a yawed wind turbine which is seen because  $\{V_0\}$  is not perpendicular to the rotor plane. The chord length is  $c$ , and the reference point measured  $1/4$  chord length from the leading edge is illustrated.  $EI$  denotes the bending stiffness around first and second principal axes. Yaw error is neglected in the rest of this work.

FLEX 5<sup>8</sup> has DOF based on either rigid body motion or flexible mode shapes. The program uses six rigid foundation DOFs (translational+rotational), four tower bending modes/DOFs, two rotational DOFs for nacelle yaw and tilt. The shaft has four DOFs, i.e. rotation, a shaft torsion DOF/mode and two shaft bending DOFs/modes. Additionally, each of the three wind turbine blades has two flapwise and two edgewise modes/DOFs.<sup>8</sup> At each timestep, deflections described by the shape of the eigenmodes are calculated which again has an influence on, e.g. tower bending and the velocity triangle (Figure 3). The unsteady BEM method<sup>12</sup> gives the accelerations by solving equations of motion of a dynamic system. Time integration yields the position and velocities of all DOFs. Formally, the blades are discretized into 17 elements, with section data for bending stiffness, chord length, pitch angle, relative profile thickness and location of aerodynamic center.

Figure 3 shows the velocity diagram seen from the airfoil section [using the same conventions as in Hansen (2009)].<sup>12</sup> It illustrates that at some point in space given by  $\{r\} = \{x, y, z\}^T$ , the vector  $\{V_{rel}\}$  or the wind velocity seen locally from the point of view of the blade section is the sum of the three vector components:

- the turbulent wind inflow  $\{V_0\} = \{V_0(\{r\}, t)\}$ ;
- the induced velocity  $\{W\}$ , which is a vector field acting oppositely of the wind inflow. It is a thrust force caused by a pressure drop over the rotor, and the BEM method describes how to obtain this vector-field;
- and local velocity vector due to the rotation of the blade itself,  $\{V_{rot}\}$ .

From the left side of Figure 3, it can also be seen that the angle of attack  $\alpha$  is the angle between  $\{V_{rel}\}$  and the blade section chord line. The angle of attack  $\alpha$  is computed on the basis of the unsteady BEM method as described in Hansen (2009).<sup>12</sup> The blade lift  $C_l = C_l(\alpha)$  and drag coefficients  $C_d = C_d(\alpha)$  can then be found using table-lookup. These values are only representatives for standard aerodynamic profiles, not taking into account flow effects by vortex generators installed along the blade span, stall devices mounted on the leading edge or other roughness effects introduced by sand/dirt contamination on the blades. Blade lift  $L$  and drag  $D$  forces using density  $\rho$  and chord length (see chord line in Figure 3) are determined from the definition of  $C_l(\alpha)$  and  $C_d(\alpha)$ , and given by the equations

$$L(\alpha) = \frac{1}{2} \rho V_{rel}^2 c C_l(\alpha), \quad \text{and} \quad D(\alpha) = \frac{1}{2} \rho V_{rel}^2 c C_d(\alpha) \quad (1)$$

Forces for blade lift  $L(\alpha)$  and drag  $D(\alpha)$  are time dependent because the angle of attack  $\alpha$  for a given blade cross section is a function of the turbulent inflow, blade deflection velocity as well as pitch and yaw operations.

## 2.2. Validation of the aeroelastic model

Available experimental data<sup>13</sup> includes power yield, nacelle wind speed and direction, turbine yaw angle, rotor torque and bending moments from SG/strain gauge measurements. The wind data is taken from measurements at hub height, from a meteorological tower (met mast) at a distance of 2,5 rotor diameters from the wind turbine.

The inflow towards a wind turbine in terrain is highly complex.<sup>14</sup> It is impossible to exactly predict the turbulent wind field at all different locations on the blades. By using statistical tools, the behavior of the wind field as a function of radius can be estimated. Assumptions on values like wind shear exponent, cross-correlation/power spectral density/coherence and turbulence intensity, etc., is associated with large uncertainties when comparing different (short-term) time series with a real wind field. Values, e.g. wind shear exponent, can change during the day/months/years, depending on time series, but for practical reasons, only one approximate value (based on a large number of time series) is used.

For the experimental validation, the wind is required to come from an undisturbed direction in order to get the most idealized (and predictable) flow field. This condition reduces the number of time series to choose from. The red curve in Figure 4 shows the experimental turbulence intensity used in FLEX 5. The curve is an average of the available time series, which are shown as blue dots on the same graph. Not all time series on the figure are usable, but all the time series shown are from the specified “undisturbed” direction. There are only a few good experimental time series for wind speeds above  $16 \text{ m s}^{-1}$ .

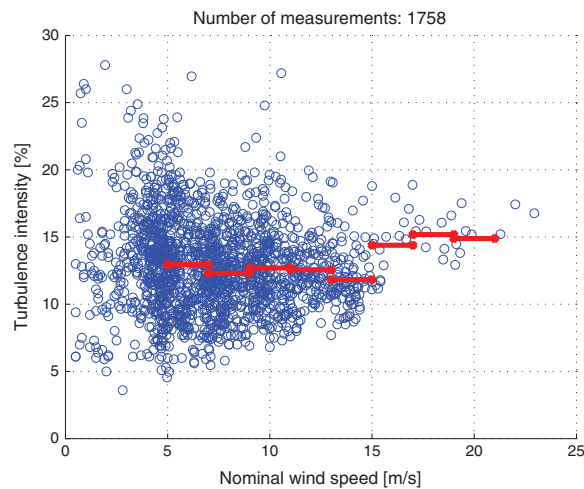


**Figure 4.** Turbulence intensity of experimental time series shown as 10 min averages (blue dots) and binned averages (red lines). The data is “filtered,” such that only time series from the undisturbed wind direction sector are shown.

**Table I.** Turbulence intensity used in FLEX 5 in the axial direction ( $\{u\}$ ), from experiments in Figure 4.

$\langle u \rangle$ (m s <sup>-1</sup> )	TI (%)	$\langle u \rangle$ (m s <sup>-1</sup> )	TI (%)
6	12.95	14	11.84
8	12.30	16	14.39
10	12.70	18	15.19
12	12.56	20	14.90

The aim is to simulate 8 different representative wind conditions (or bins) in the range of 6–20 m s<sup>-1</sup> with a bin size of 2 m s<sup>-1</sup>, as shown in Table I. This table also shows the average value for each bin, and the values are graphically depicted as the red curve on Figure 4.

It is generally assumed that the probability density function for atmospheric wind speed conforms to a Weibull distribution. The shape of this distribution indicates that higher wind speeds occur much less often than low wind speeds. The emphasis in this paper is therefore on comparing FLEX 5 and experimental values in the low wind speed region. However, wind speeds below 5 m s<sup>-1</sup> have too small impact to be interesting to analyse, and the wind rarely blows stronger than 20 m s<sup>-1</sup>. In addition, there are not enough good measured time series above 20 m s<sup>-1</sup>. It can directly be seen from Figure 4 that there are not many usable experimental time series above 18–20 m s<sup>-1</sup>. It was therefore decided that measurements between 5 and 7 m s<sup>-1</sup> are represented by a 6 m s<sup>-1</sup> FLEX 5 simulation and so on up to the 20 m s<sup>-1</sup> interval, giving eight representative intervals to investigate.

An assumption is made such that if both wind speeds, measured main shaft torque and power production, correlates well, then the FLEX 5 model is considered to be valid and usable for post-processing.

### 2.3. Multibody model of wind turbine drivetrain

For a general system with  $n$  generalized coordinates and  $m$  constraints, the number of DOF is  $n - m$ . For this model, eight bodies are used as shown in Figure 5. Each body has six cartesian coordinates (three translational and three rotational), so  $n = 48$ . Flexibility effects are ignored because it is assumed that they have little effect on the results, except in the planetary gearbox where more than one gear/pinion would transfer torque between sun and planet. This assumption means that the gear normal tooth forces arising from the sun to the planet(s) are incorrect, but for estimating maximum gear tooth forces, the proposed method works by using some simplified assumptions. See Figure 6(b) for an illustration of the problem with rigid gear constraints for planetary gearboxes. The correct torque and reaction forces will be transferred through one planet instead of being distributed through three planets, meaning that this can be seen as a “worst-case” study.

The following describes the multibody model and how a semi-advanced rigid gear-constraint that handles internal reaction forces correct is used. Despite the fact that this is a simplified approach to the real problem, this method will provide insight regarding maximum gear tooth forces inside the planetary gearbox. Future work would be to improve this methodology for increasing the accuracy, but that requires validation, and we did not have permission to make any “intrusive” modifications to this wind turbine or the gearbox in it. It does not matter which rigid gear constraint was used because Figure 6(b) shows that we have four equations for three planetary gears. Ideally, each gear is connected to the ring as well

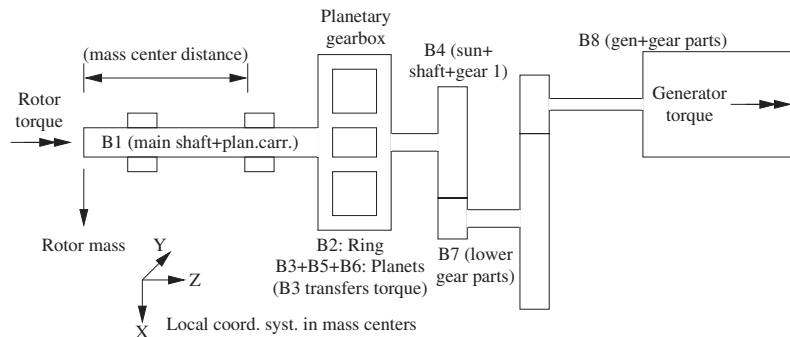


**Figure 5.** Illustration of wind turbine model. “B” followed by a number denotes “body number,” i.e. B3, B5 and B6 represents body 3, 5 and 6 (or planet 1, 2 and 3 respectively). Rotor torque (3 moments around x, y and z), generator torque (around z) and 3 force components acting on the rotor ( $F_x$ ,  $F_y$  and  $F_z$ ) are from FLEX 5. The coordinate system is the same as in FLEX 5 (z is axially etc).





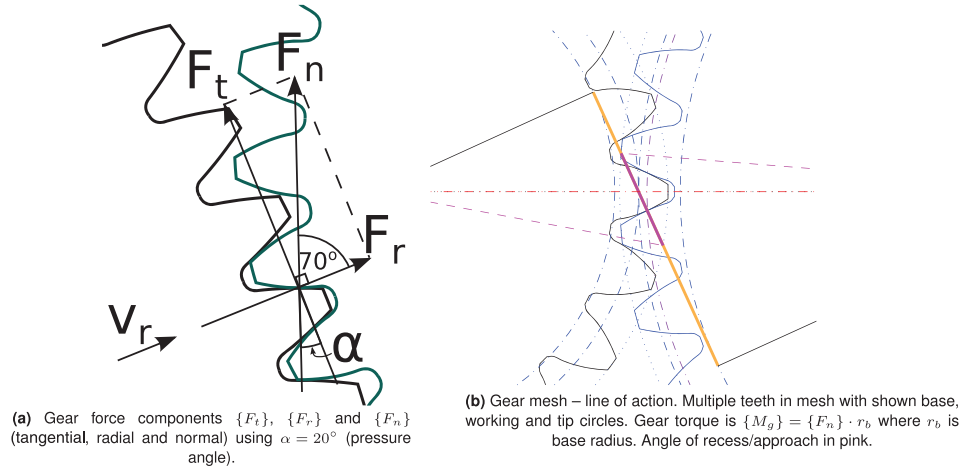


**Figure 7.** (a) Illustration 2D gear tooth force components. (b) Unit vector  $\{v_r(t)\}$  is in radial direction (center-to-center).

where  $\{\hat{Q}_1\}$  and  $\{\hat{Q}_2\}$  are two-column vectors from the skew-matrix (they are by definition guaranteed to be perpendicular to  $z$  or  $\zeta$  because they are basis vectors of the  $3 \times 3$  skew-matrix).

There is another way of forcing a body to be parallel with a given vector. For instance, the main shaft has a thrust bearing and a radial bearing. This can be expressed using 3 + 2 equations from equation (2). The spherical joint then acts like a thrust bearing that takes up axial forces (using equations for  $x$ ,  $y$  and  $z$  movement). The radial bearing uses two out of the three spherical joint equations, i.e. those equations take up forces using equations describing the  $x$  and  $y$  movement of the main shaft, simply because the main shaft is parallel with the  $z$  axis. In practice, the second “radial” bearing acts exactly like a spherical joint with one equation removed.

**Gear constraints:** The last type of constraint used is a gear constraint. The illustration in Figure 7(a) shows the gear tooth reaction forces, and we want to have a constraint that takes these forces into account. We use gear constraints in a simple and a semi-advanced version, and the simple version only transfers the torque, knowing nothing about the gear tooth forces. But the semi-advanced gear constraint knows about the forces shown in Figure 7(a), and therefore, the internal reaction forces can be calculated explicitly. We call it “semi-advanced” because of the fact that it is not advanced enough to know whether or not multiple teeth are in mesh at the same time (this is the case shown in Figure 7(b)). The following is a description of the simple gear constraint, followed by a description of the more advanced constraint:

**Simple** Requiring that the velocity at the point of contact along the line of action is the same for both body  $i$  and  $j$  yields<sup>9</sup>

$$v_i = v_j \Rightarrow \rho_i \dot{\phi}_i = -\rho_j \dot{\phi}_j \quad (4)$$

where  $\rho$  is the pitch radius, and  $\dot{\phi}$  is the angular velocity. Integration gives

$$\Phi = (\phi_i - \phi_i^0) \rho_i + (\phi_j - \phi_j^0) \rho_j = 0 \quad (5)$$

where the initial condition for rotation of each body is  $\phi^0$ , and  $\phi$  is the accumulated rotation angle. There is no coupling to any translational DOF, and therefore, the reaction forces in any translation direction is always 0 N. From Figure 7(a) one should expect gear tooth forces which are expected to produce internal reaction forces, but this doesn’t happen because the formulation is only depending on rotation, i.e.  $\phi$  (and  $\rho$  which is constant). This constraint however works well for transferring the torque even if the angular velocity is high.

**Semi – adv** Taking all DOFs into account (translational and rotational movement of body center positions), the velocity constraint becomes

$$([A_c] \{v_r\})^T (\{\dot{r}_i\} + \rho_{p,i} [A_i] \{\omega'_i\} \times \{v_r\}) - ([A_c] \{v_r\})^T (\{\dot{r}_j\} + \rho_{p,j} [A_j] \{\omega'_j\} \times \{v_r\}) = 0 \quad (6)$$

where  $[A_c]$  is a  $3 \times 3$  rotation matrix given by equation (8),  $\{v_r\}$  is a unit vector in the radial direction (Figure 7(a)),  $\{\dot{r}\}$  is the body center velocity,  $\rho_p$  is pitch circle radius,  $[A]$  is a coordinate transformation

matrix (from moving reference frame to the inertial frame) and  $\{\omega\}$  is the vector of angular velocities ( $3 \times 1$ ). This constraint gives the internal reaction forces automatically in the gear tooth surface normal direction (because that is the projection direction).

From equation (6), it can be seen that this constraint is a projection of generalized velocities of the two bodies  $i$  and  $j$ . The constraint equation is simply a dot product or a projection of a vector into the direction of another vector (the global velocity vector describing the relative movement of the pitch point). The direction ( $[A_c]\{v_r\}$ ) is the projected direction of the gear velocity constraint, and this direction is also the gear tooth surface normal direction. The gear tooth forces projected into the gear tooth surface normal direction yields the normal force which is shown as  $F_n$  on Figure 7(a). The radial unit vector is defined

$$\{v_r\} = \frac{\{r_j\} - \{r_i\}}{|\{r_j\} - \{r_i\}|} \quad (7)$$

and Figure 7(a) shows that  $\{v_r\}$  is constantly moving when the planets move, and therefore,  $\{v_r\} = \{v_r(t)\}$ . The gear tooth normal direction can be obtained by multiplying the constant rotation matrix  $[A_c]$  with the radial direction  $\{v_r\}$ , where  $[A_c]$  is

$$[A_c] = \begin{bmatrix} 1 & 0 & 0 \\ 0 & \cos(\beta) & -\sin(\beta) \\ 0 & \sin(\beta) & \cos(\beta) \end{bmatrix} \begin{bmatrix} \cos(\pi/2 - \alpha) & -\sin(\pi/2 - \alpha) & 0 \\ \sin(\pi/2 - \alpha) & \cos(\pi/2 - \alpha) & 0 \\ 0 & 0 & 1 \end{bmatrix} \quad (8)$$

The pressure angle  $\alpha$  is typically  $20^\circ$  or  $25^\circ$ . A helix angle  $\beta = 0^\circ$  for spur gears, and if this condition is not met, it is a helical gear. The  $[A_c]$  matrix is a constant time-independent transformation matrix consisting of two rotations. The rotation matrix  $[A_c]$  corresponds to

- i. First, a rotation around a vertical axis (around  $x$  in the global reference of frame—this coordinate system is shown graphically in Figure 5) and this rotation yields axial forces known to be caused by helical gears.
- ii. Secondly, a rotation of  $(\pi/2 - \alpha)$  radians in the counter-clockwise direction (around  $z$  in the new rotated coordinate system). The final rotation, in the  $xy$ -plane, transforms a unit vector  $\{v_r(t)\}$  into the tooth normal direction (the  $F_n$  direction in Figure 7(a)).

This constraint has proven itself valid for use with helical gears, where axial forces are a function of the helical angle  $\beta$ . Only the tangential gear tooth force  $F_t$  transfers torque. It can be seen that for a helical gear with helix angle  $\beta$ <sup>16</sup>

$$F_a = F_t \tan(\beta_w), \quad F_r = F_t \tan(\alpha_{tw}), \quad F_n = \frac{F_a}{\sin(\beta_w) \cos(\alpha_{nw})} \quad (9)$$

where  $F_a$  is the axial,  $F_r$  is the radial and  $F_n$  is the normal tooth force, whereas  $\alpha_{tw}$  and  $\alpha_{nw}$  are the working pressure angle in the tangential and normal plane, respectively. The subscript  $w$  for “working” refers to the fact that profile shift should be taken into account, if relevant. The relationships for  $F_a$ ,  $F_r$  and  $F_n$  can now be used in the multibody program.

The gear constraint is non-holonomic so it cannot (unlike the simple gear constraint) be integrated in time to form a position constraint. It is important to distinguish between constant and time-dependent vectors/matrices because equilibrium equations are described in terms of accelerations, and therefore, the constraints should be differentiated and also be expressed with acceleration coefficients. When time-dependent terms are differentiated, they introduce more terms that are moved to the RHS, but constant terms are straightforward to differentiate. We provide acceleration (and RHS) terms for the semi-advanced gear constraint in the section about solving the equations of motion (Section 2.3.3).

### 2.3.2. Implementation of multibody gear constraints into the MATLAB program.

Figure 5 illustrates how the eight bodies are connected to each other, except that the Figure 6(b) is required for understanding how the gear constraints are attaching each body (gear wheel) to each other. Most of the bodies remain fixed in space while they are rotating, but the planets are attached to the (rotating) planet carrier so they move up and down in the  $x/y$  coordinate system.

In total 47 constraints are used. The first five constraints are for body 1 (rotor and main shaft). The spherical joint is placed at the location of bearing 1 so the three constraint equations are given by equation (2). Then the two equations for the parallel constraint are added. After that six constraints are added for each of body 2 (ring gear), body 3 (planet 1), body 4 (sun), body 5 (planet 2), body 6 (planet 3), body 7 (lower gear parts) and body 8 (gear parts and generator). All bodies



**Table II.** List of the 47 constraints used for each of the eight bodies.

Body	Description	Constraints	Equations
1	Rotor, main shaft and planetary carrier	1 sph. + 2 par.	5
2	Ring gear	1 sph. + 2 par. + 1 fixed rotation	6
3	Planet 1	1 sph. + 2 par. + 1 semi-adv. gear constraint	6
4	Sun gear	1 sph. + 2 par. + 1 semi-adv. gear constraint	6
5	Planet 2	1 sph. + 2 par. + 1 semi-adv. gear constraint	6
6	Planet 3	1 sph. + 2 par. + 1 semi-adv. gear constraint	6
7	Lower gear parts	1 sph. + 2 par. + 1 simple gear constraint	6
8	Generator	1 sph. + 2 par. + 1 simple gear constraint	6

sph., spherical joints; par., parallel constraints.

have a gear constraint except for body 1. In other words, for each body 5 of the constraints fix the body in space. The sixth constraint is one of the described gear constraints that transfer the torque from rotor and generator into the gearbox. Table II illustrates how the 47 constraints are implemented.

The simple gear constraint is used for the generator body (body 8) as well as for body 7. The semi-advanced gear constraint is used in the planetary gearbox because this constraint is used for getting the maximum gear tooth normal forces.

### 2.3.3. Solving equations of motion using Lagrange multipliers.

The equations of motion to be solved<sup>9</sup> are given by

$$\begin{bmatrix} [M] & -[\Phi_q]^T \\ [\Phi_q] & [0] \end{bmatrix} \begin{Bmatrix} \{\ddot{q}\} \\ \{\lambda\} \end{Bmatrix} = \begin{Bmatrix} \{g\} \\ \{\gamma\} \end{Bmatrix} \quad (10)$$

where  $[M]$  is the mass matrix,  $[\Phi_q]$  is the Jacobian of constraint equations (holding coefficients to coordinate acceleration of every DOF),  $\{g\}$  is the vector of coordinates and  $\{\lambda\}$  is a vector of Lagrange multipliers. On the RHS,  $\{g\}$  is a vector of external forces (and torque from FLEX). Most of these constraint equations are straightforward to differentiate. For completeness, the derivative of the semi-advanced gear constraint given by equation (6) is reproduced here:

$$\begin{aligned} \ddot{\Phi} : ([A_c] \{v_r\})^T & \left( \{\ddot{r}_i\} + \rho_{p,i} \left[ ([A_i] \{\tilde{\omega}'_i\}) \times \{v_r\} + ([A_i] \{\dot{\omega}'_i\}) \times \{v_r\} + ([A_i] \{\omega'_i\}) \times \{\dot{v}_r\} \right] \right) \\ & - ([A_c] \{v_r\})^T \left( \{\ddot{r}_j\} - \rho_{p,j} \left[ ([A_j] \{\tilde{\omega}'_j\}) \times \{v_r\} + ([A_j] \{\dot{\omega}'_j\}) \times \{v_r\} + ([A_j] \{\omega'_j\}) \times \{\dot{v}_r\} \right] \right) \\ & + ([A_c] \{\dot{v}_r\})^T (\{\dot{r}_i\} + \rho_{p,i} ([A_i] \{\omega'_i\}) \times \{v_r\}) - ([A_c] \{\dot{v}_r\})^T (\{\dot{r}_j\} - \rho_{p,j} ([A_j] \{\omega'_j\}) \times \{v_r\}) = 0 \end{aligned} \quad (11)$$

All coefficients for the translational and rotational accelerations ( $\{\ddot{r}\}$  and  $\{\dot{\omega}'\}$ ) are collected in the Jacobian matrix  $[\Phi_q]$ , but most terms do not involve the coefficients and are therefore put on the RHS as  $\{\gamma\}$  terms in equation (10). The system of equations is time-integrated, using ODE45 in MATLAB, and this gives the positions and velocities.

The joint reaction forces can be found using the fact that mass times acceleration equals the sum of external forces and moments added together with reaction forces and moments:

$$[M] \{\ddot{q}\} = \{F_{ext}\} + \{F_{react}\} \Rightarrow [M] \{\ddot{q}\} - [\Phi_q^T] \{\lambda\} = \{F_{ext}\} \quad (12)$$

which is clear from equation (10). This means, e.g., that the main shaft bearing reaction forces can be calculated as  $(-[\Phi_q^T] \{\lambda\})$  using only the constraint(s)  $i$  and  $\{\lambda_i\}$  values from the joint(s) of interest. Not only are the main shaft reaction forces calculated in that way, but the gear tooth (reaction) normal forces corresponding to constraint(s)  $i$  are given by the Lagrange multiplier(s),  $\{\lambda_i\}$ . The reason is that the coefficients in the Jacobian matrix in each of the coordinate directions is a projection of the unit vector  $\{v_r\}$  (defined in relation to equation (6)) into the global coordinate system directions. Because the unit vector  $\{v_r\}$  already points into the gear tooth normal direction (Figure 7(a)), the joint reaction force in this case is simply the Lagrange multiplier  $\{\lambda\}$  associated with the corresponding gear-constraint number with no need for pre-multiplication of the Jacobian coefficients unless the tooth reaction forces should be projected into the global coordinate system directions.

Input torque (and forces) from FLEX 5 are known in advance, so in MATLAB a vector of external forces and moments is denoted  $\{g\} = \{F_x^1, F_y^1, F_z^1, M_{\xi}^1, M_{\eta}^1, M_{\zeta}^1, F_x^2, \dots, M_{\eta}^8, M_{\xi}^8, F_x^8\}^T$  where the force and torque from body 1 is inserted from the FLEX 5 calculation. It is also important to use the generator torque on body 8 and to check that the rotor speed is approximately in a steady state condition with acceptable acceleration levels.

### 2.3.4. Dealing with time-integration issues and oscillations.

It is known from the literature that some time-integration schemes are known to cause high-frequency problems, see e.g. the study of Krenk (2009).<sup>17</sup> When using the semi-advanced gear constraint on the high-speed shaft, it is observed that the rigid bodies that undergo the highest angular velocities are exerted to unphysical high-frequency oscillations, where the amplitude of oscillations increases with increasing angular velocity. The oscillations can be seen acting as rigid-body reaction forces, and hence, these affect the accelerations. They are not physical because if a constant torque is put on the rotor and generator sides, then one must expect that for a rigid multibody model, the surface gear tooth reaction forces are constant.

The gear ratio from the low-speed shaft to the high-speed shaft on the generator is approximately  $i = 55.8$ , meaning that with a standard-size ODE45 timestep from MATLAB, the number of timesteps per rotation is 55.8 times higher on the main (low speed) shaft than on the generator (high speed) shaft. The semi-advanced gear constraint is unusable at high speeds because the gear tooth normal force gradient changes speed too fast. A possible part of an explanation is given in the study of Krenk (2009),<sup>17</sup> which discriminates between two types of time-integration schemes: collocation and momentum-based methods. Collocation methods do not necessarily conserve such properties as momentum and energy, but momentum-based methods specifically conserve the physical properties of the underlying problems. Damping can also be added to remove oscillations, but with a gear ratio of  $i = 55.8$ , the oscillations on the high-speed shaft are too large.

One way of solving this problem is by using very small timesteps and demanding very high solver accuracy. Alternatively (the way the problem was solved for this work), the simple gear constraint from equation (4) is used in the final gearbox stage. This is where the oscillations are most pronounced due to a high-angular velocity. Small oscillations can safely be ignored because the effect of input torque from the turbulent wind is much more important. Combining both types of constraints in this model would appear to be a good way of obtaining the most relevant of the gear tooth normal forces and additionally of solving this oscillating time-integration phenomenon, causing physical impossible fluctuations in reaction forces and accelerations.

## 2.4. Finite element method model used to obtain gear tooth stresses

The FEM model was developed using COMSOL MULTIPHYSICS. For this particular 500 kW wind turbine, the gear tooth has a module of 10 and the helix angle  $\beta = 0^\circ$ . The number of teeth is 20, 35 and 91 respectively for the sun, planet and ring. Profile shift for the sun/planet is approximately 0.6 and 0.4, respectively. Profile shift for the planet/ring is approximately 0.4 and -0.8, respectively. Tip relief is used, and the full, exact planetary gear tooth geometry based on these values is shown in Figure 6(b) and 7(b). For spur gears, the working and base radius (shown in Figure 7(b)) is<sup>16</sup>

$$r_w = r_p \frac{\cos \alpha}{\cos \alpha_w} = \frac{r_b}{\cos \alpha_w} \quad (13)$$

where  $r_w$  is the working radius,  $r_p$  the pitch radii,  $r_b$  the base radius,  $\alpha$  is the pressure angle and  $\alpha_w$  is the transverse pressure angle, which is found by iteration using

$$x_1 + x_2 = (z_1 + z_2) \frac{\text{inv} \alpha_w - \text{inv} \alpha}{2 \tan \alpha}, \quad \text{furthermore: } \text{inv} \alpha = \tan \alpha - \alpha \quad (14)$$

where  $x_1$  and  $x_2$  are the addendum modification/profile shift, and  $z_1$  and  $z_2$  are the number of teeth. A few assumptions are required because of the complexity of using the aforementioned “semi-advanced” gear constraint with this eight-body rigid multibody model. They can be summarized as

- This gear constraint is a “worst-case” constraint in the sense that only the sun and planet 1 transfers torque due to insufficiently rigid model DOFs. By only considering this, one could expect that the real gear tooth stresses are in the range of 1/3 to the values we calculate in this paper.
- A FEM calculation is only made at the working circle where rolling occurs in order to reduce the number of load cases. This reduces the stresses, which are higher at the beginning of gear tooth contact (shown on Figure 7(b)).
- A 2D plane strain assumption is used, which also simplifies the problem. In addition, it reduces the maximum stresses because the normal force is distributed equally over the whole facewidth. This is only the case in an ideal world.

The described method is a simplified approach to solving a problem that is very complicated, especially considering the fact that in reality, the bedplate, shaft, planetary carrier and planets move, bend and twist. It is difficult to develop a good flexible gear constraint that takes tooth load-sharing into account, and it is also questionable whether or not the FEM model should assume that the gear teeth are in contact exactly at the rolling point of the working circles, or if the contact point should be moved. The underlying rationale for the approach described in this paper is to ignore problems that are too complicated (or time consuming) to model and instead develop a simplified physical model that considers both multibody gear constraints gear tooth stress modeling practices using FEM software (FEM modeling of gears are typically made as shown here, assuming that the contact point is where the pitch/working circles meet).

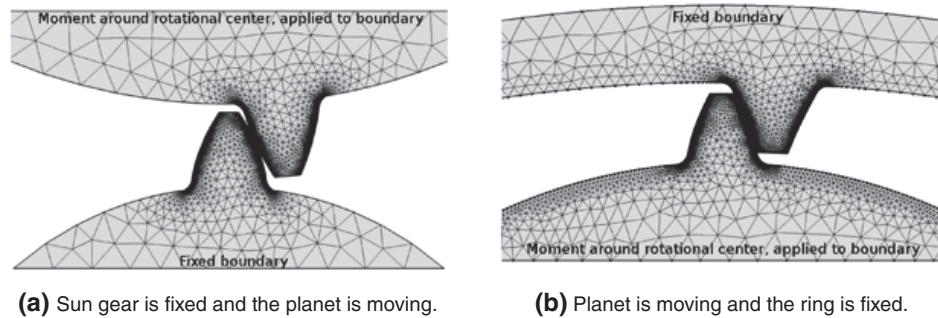


**Figure 8.** Finite element method mesh made using COMSOL MULTIPHYSICS. Between the two teeth, a contact boundary condition is made, having a static friction coefficient of  $\mu = 0.1$ . (a) Sun gear is fixed, and the planet is moving and (b) planet is moving, and the ring is fixed.

Figure 8 shows the Comsol FEM mesh and boundary conditions that were used. The torque is applied through the rotational center of one of the gears, whereas the other gear is fixed. In the figures showing the FEM results (Figures 13 and 14 in the next section), arrows indicate the displacement field due the applied torque.

## 2.5. Gearbox details

The investigated 500 kW wind turbine has been running at least since 1995 so the gear tooth stress levels should be in an “acceptable range”. The planetary stage itself has a gear ratio of 5.55, the first parallel gearbox stage has a gear ratio of 4.05 and the final parallel gearbox stage has a gear ratio of 2.48. The number of teeth is 20, 35 and 91 for the sun, planet and ring gears, respectively. The profile shift is  $x_s = 0.582$ ,  $x_p = 0.419$  and  $x_r = -0.840$ , respectively. For a description of how to use the aforementioned data for generating the tooth profile, see DIN 867 standard<sup>18</sup> and Pedersen and Jørgensen (2013).<sup>15</sup>

## 3. RESULTS

Important intermediate results are obtained (1) when comparing the output of the FLEX 5 model with measured values of wind speed, power and main shaft torque. The experimental and simulated bending moments (2) are compared against each other as another method of validation. The multibody program is then used for producing a full set of drivetrain reaction forces in all bearings holding the bodies in place. Finally, the gear tooth forces and stresses (3) from the planetary gearbox are evaluated.

### 3.1. Validation of wind speed, power and main shaft torque

Figure 9 shows an example of validation of the numerical results from FLEX 5. An undisturbed mean wind speed of  $10 \text{ m s}^{-1}$  with a representative turbulence intensity of 12.7% was compared with measurements for (a) wind speed [ $\text{m s}^{-1}$ ], (b) main shaft torsion [Nm] and (c) power production [kW]. Figure 10(a) and 10(b) show that the mean values of (a), (b) and (c) are acceptable whereas the standard deviation (SD) values are less well for high wind speeds compared to that for low wind speeds. However, this discrepancy is neglected because it has little practical impact.

In order to convey an impression of how well this wind turbine model performs at different wind speeds, mean and SD values were obtained and shown in Table III (assuming the data conforms to a normal/Gaussian probability density function). The yaw error, found as nacelle position minus the wind direction (both in degrees), is also shown in Table III from which it is apparent that the yaw error in most cases can be neglected. Considering all the many uncertainties with this kind of work, it was decided to completely neglect the yaw error on the basis of these numbers.

As shown in Figure 10, the experimental measured main shaft torque and produced power fits reasonable well with simulated FLEX 5 time series. It is important for the whole concept of using realistic simulation data in the design of a real wind turbine that the mean wind speed correlation with the main shaft torque and power production is good. This seems to be the case here.

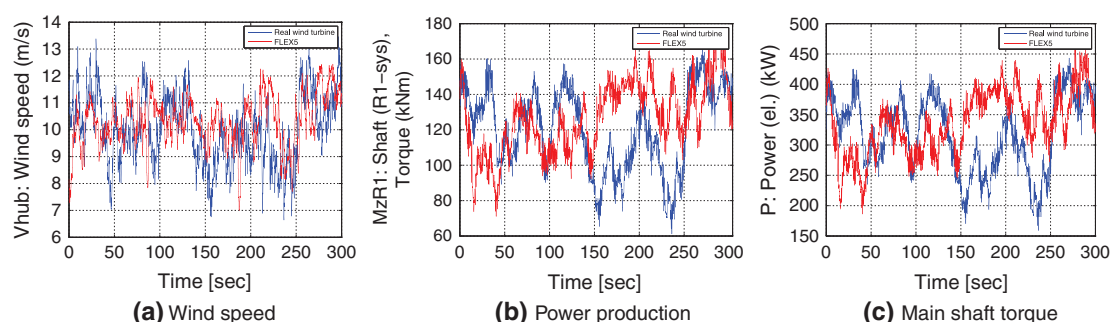


**Figure 9.** Example of validation of wind turbine model input (FLEX 5 vs. measurements) for (a) wind speed, (b) power production and (c) main shaft torque. Blue: Experimental values.<sup>13</sup> Red: Simulated values.

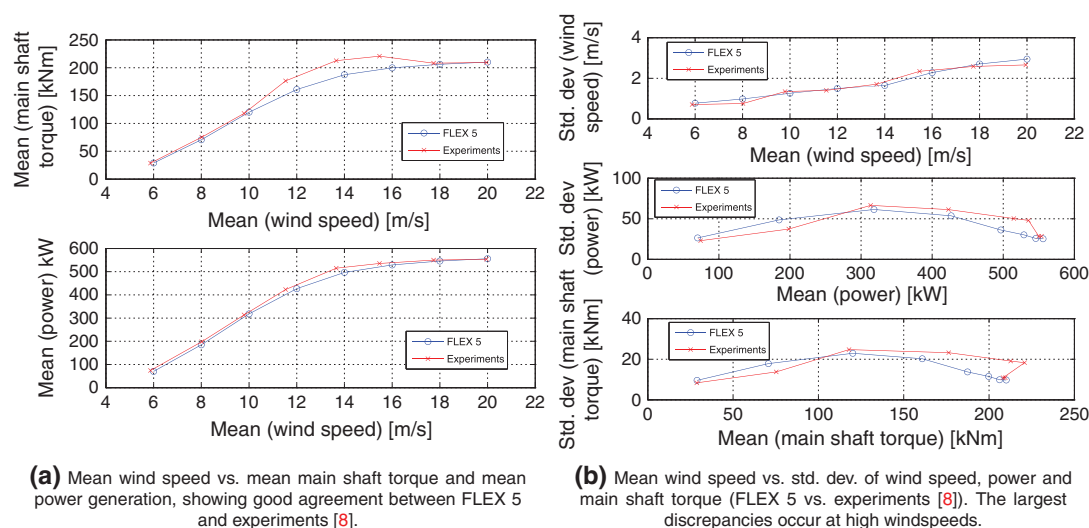


**Figure 10.** Statistical comparison of mean wind speed (a) mean power/main shaft torque and (b) standard deviation of wind speed/main shaft torque/power.

**Table III.** Wind speed ( $\text{m s}^{-1}$ )—statistics for FLEX 5 simulation data versus experimental data

n	FLEX 5 mean <u> ( $\text{m s}^{-1}$ )	Exp. mean <u> ( $\text{m s}^{-1}$ )	FLEX 5 SD $\sigma$ ( $\text{m s}^{-1}$ )	Exp. SD $\sigma$ ( $\text{m s}^{-1}$ )	Exp. mean Yaw error ( $^{\circ}$ )
1	6.00	5.87	0.77	0.71	-2.3
2	8.00	8.02	0.98	0.76	-2.0
3	10.00	9.79	1.26	1.35	1.9
4	12.00	11.53	1.50	1.40	-1.9
5	14.00	13.66	1.64	1.71	-2.6
6	16.00	15.47	2.28	2.34	-3.9
7	18.00	17.74	2.70	2.59	-0.3
8	20.00	19.95	2.95	2.66	0.4

SD, standard deviation.

### 3.2. Validation of bending moment

An illustration of important components for the investigated wind turbine is shown in Figure 11(a). For comparing bending moments obtained by using strain gauges at a particular location on the main shaft, dimensions from Figure 11(a) were

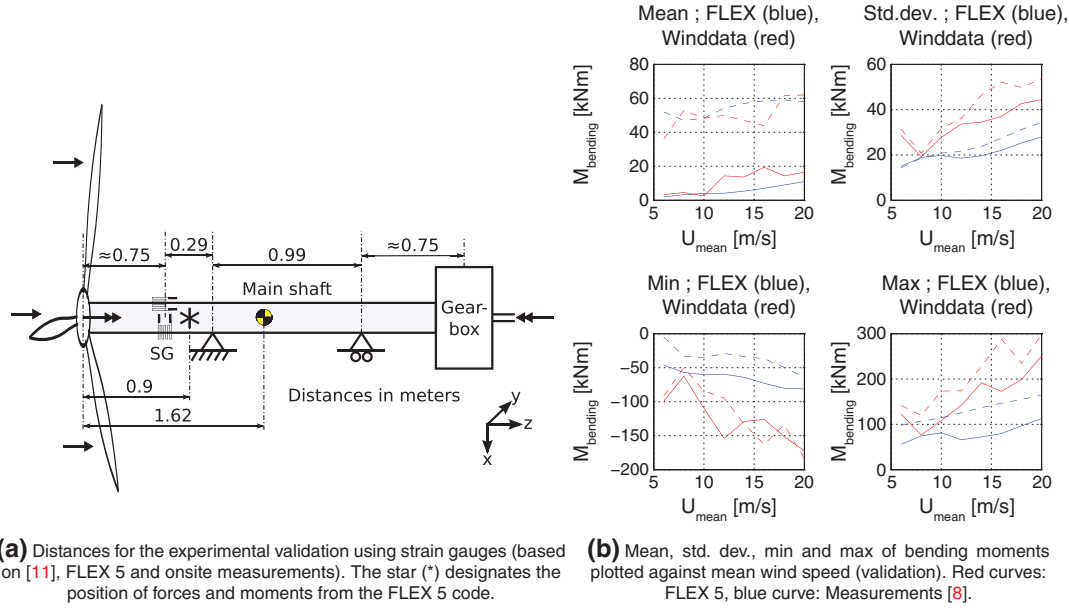


**Figure 11.** Experimental validation using strain gauges located 90° apart (this explains the difference between dotted and full lines). Results are transformed into a fixed (non-rotating) coordinate system so, the strain gauges measure the yaw and tilt moments. (a) Dimensions. (b) Results of the comparison. This result is acceptable considering the many uncertainties in the data.

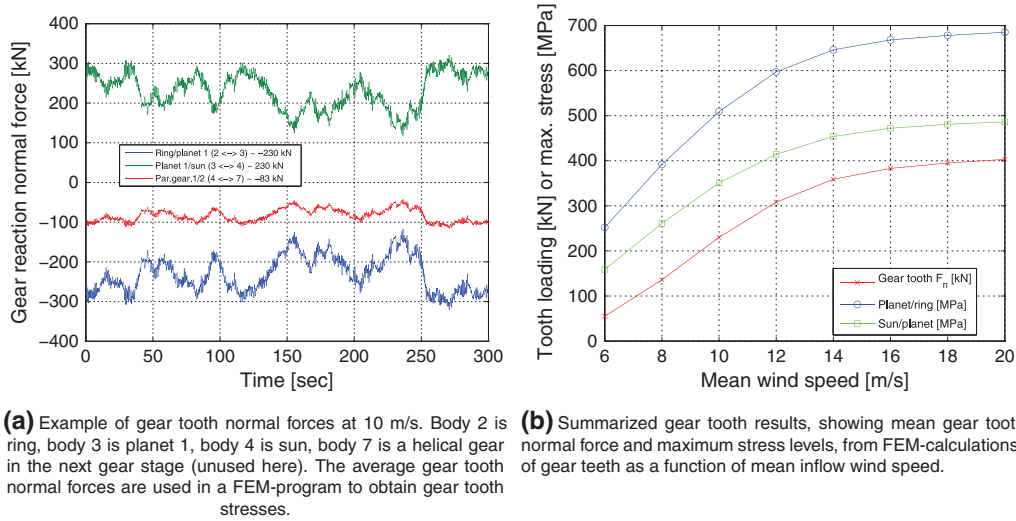


**Figure 12.** Gear tooth normal forces from the multibody program. (a) Example of gear tooth normal forces at 10 m s<sup>-1</sup> and (b) summarized gear tooth results.

used. The experimental strain gauge moment was taken from the study of Hansen and Larsen<sup>13</sup> at a distance 75 cm away from the rotor (as shown in the figure).

The calculated FLEX 5 strain gauge moment is determined as a moment from forces added with a moment from the aerodynamics. The moment from forces is calculated as  $\{M\} = \{s\} \times \{F\}$ , where the distance vector  $\{s\} = \{s_x, s_y, s_z\}^T$  only has a  $s_z$  component equal to  $(0.9-0.75) m = 0.15 m$ . The calculated strain-gauge moment acts at the star in Figure 11(a) so there is an offset error of 15 cm which requires some compensation. The total bending moment in the global reference frame is then given by

$$M_{SG,x}(\text{yaw}) = -0.15F_y + M_x, \quad \text{and} \quad M_{SG,y}(\text{tilt}) = 0.15F_x + M_y \quad (15)$$



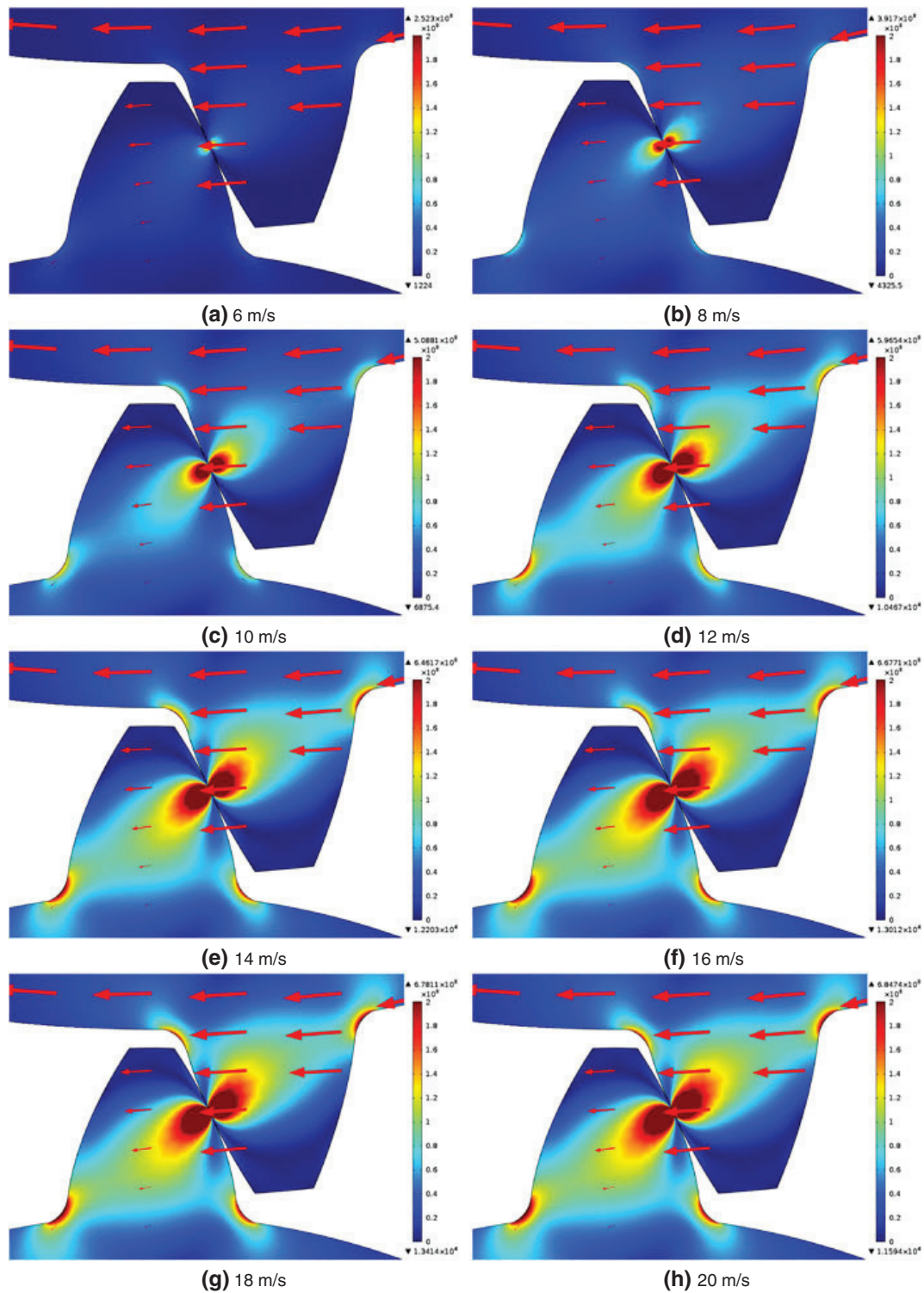


**Figure 13.** Sun/planet: Gear colors show the von Mises stress [ $\text{N m}^{-2}$ ] and arrows show the displacement field. (a) 6  $\text{m s}^{-1}$ , (b) 8  $\text{m s}^{-1}$ , (c) 10  $\text{m s}^{-1}$ , (d) 12  $\text{m s}^{-1}$ , (e) 14  $\text{m s}^{-1}$ , (f) 16  $\text{m s}^{-1}$ , (g) 18  $\text{m s}^{-1}$  and (h) 20  $\text{m s}^{-1}$ .

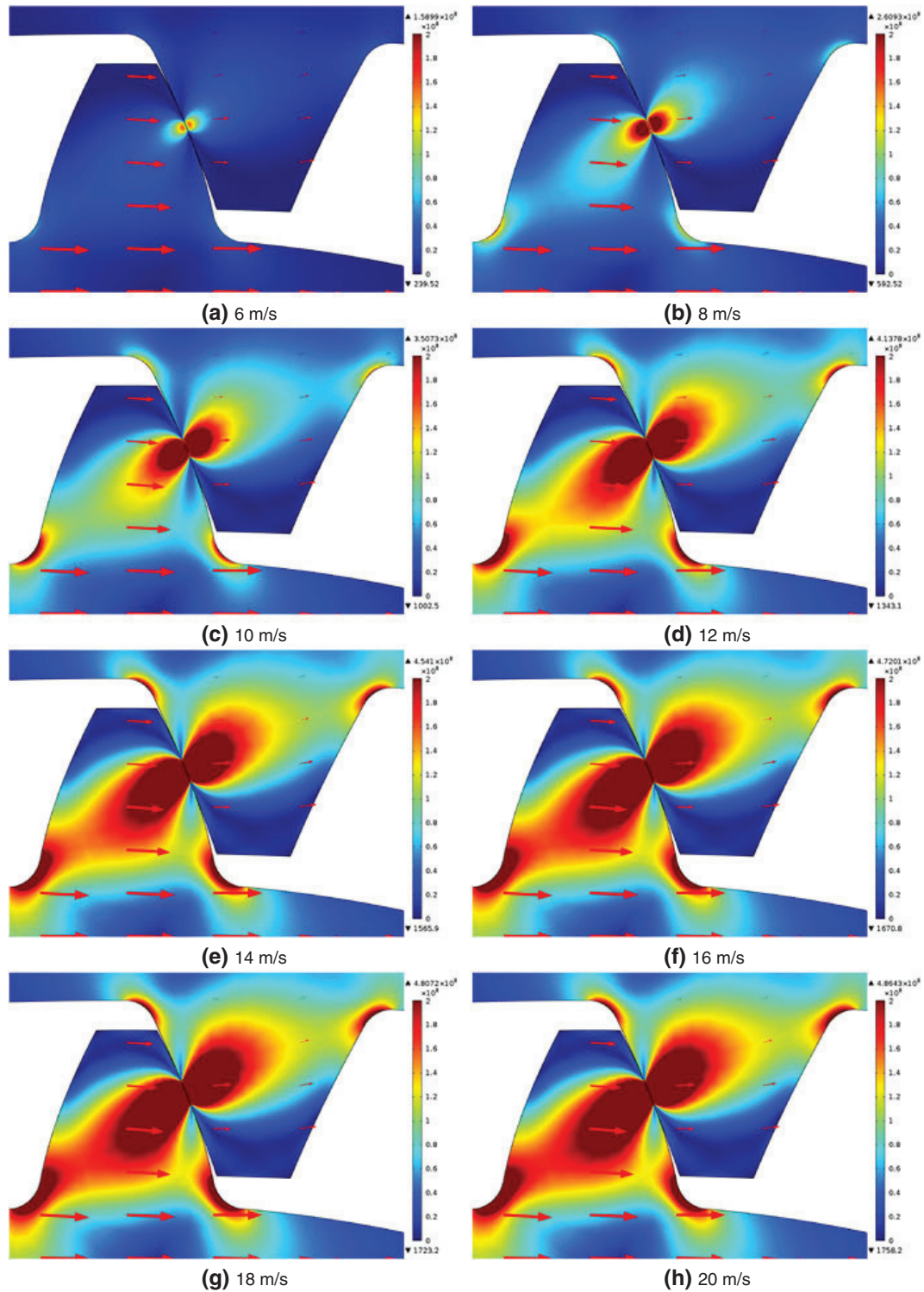


**Figure 14.** Planet/ring: Gear colors show the von Mises stress [N m<sup>-2</sup>]. Arrows show the displacement field. (a) 6 m s<sup>-1</sup>, (b) 8 m s<sup>-1</sup>, (c) 10 m s<sup>-1</sup>, (d) 12 m s<sup>-1</sup>, (e) 14 m s<sup>-1</sup>, (f) 16 m s<sup>-1</sup>, (g) 18 m s<sup>-1</sup> and (h) 20 m s<sup>-1</sup>.

From Table III, it can be seen that the yaw error is always less than 4% and is therefore assumed to be negligible.

The yaw and tilt moments, as a function of the mean wind speeds, are shown in Figure 11(b). The bending moments measured by strain gauges were multiplied by a coordinate transformation matrix associated with the moving local coordinate system, at all timesteps, in order to obtain the yaw and tilt bending moments in a fixed, non-rotating coordinate system. The strain gauge moment can also be shown in the local coordinate system instead of in the global system. In that case, the global moment-vector must be pre-multiplied by the transposed transformation matrix, which is a basic rule shown in many textbooks such as in the book of Nikravesh (1988).<sup>9</sup>

Figure 11(b) shows that the trends of the strain gauge measurements are correct. The most important graph is the first (in the top left corner), showing the average bending moment at the position of the strain gauges, plotted against mean wind speed. There are two signals for strain gauges rotated 90° apart (tilt and yaw directions). For many of the wind speed bins, the deviation is within 25%. The top right-hand figure shows the SD plotted against wind speed. The lower two graphs in Figure 11(b) show the minimum and maximum of the measured and simulated/calculated bending moments. It cannot be expected that all of these comparisons will always fit within  $\pm 10 - 20\%$ , but the figure illustrates the same tendencies in the simulations as in the experiments. In addition, the mean bending moments seem realistic.

Together with Figure 10, the FLEX 5 model is deemed to capture the effect of the measured experiments accurately enough for the purpose of feeding forces and torque into a multibody program.

### 3.3. Gear tooth forces and stresses

The multibody program makes it easy to extract reaction forces using equation (10), so for instance, the main shaft bearing reaction forces and planet carrier reaction forces are easily obtained. Gear tooth stresses at different wind speeds are relevant from a design perspective. An example of extracted gear tooth forces is seen in Figure 12(b), where the left-hand graph shows gear tooth normal forces in the planetary gear and in the subsequent normal external gear. The focus in this paper is to investigate the tooth forces where the loads are the highest. This occurs in the planetary gearbox, where the gear tooth normal forces are 230 kN, at an average turbulent wind speed of  $10 \text{ m s}^{-1}$ . The table to the right of Figure 12(b) shows the planetary gearbox tooth normal forces for the eight binned mean wind speeds, which has previously been described in terms of aeroelastic input for the FLEX 5 model.

By taking these gear tooth normal forces into COMSOL MULTIPHYSICS, the gear stresses when the gears are in contact at the working circle can be calculated. The results are divided into

- Figure 13 showing the gear tooth stresses between the sun and planet gear from  $6-20 \text{ m s}^{-1}$  and
- Figure 14 showing the gear tooth stresses between the planet and the ring gear from  $6-20 \text{ m s}^{-1}$ .

Figure 12(b) summarizes the results of the FEM calculations. It also shows the maximum gear tooth stress levels as a function of the mean wind speed. This seems to be clearly connected to the aerodynamics because it resembles the power curve of a wind turbine in the sense that the maximum stress curve rises steeply at  $6-10 \text{ m s}^{-1}$  and flattens out around  $16-20 \text{ m s}^{-1}$ . One of the most important results obtained is that the maximum stress never exceeds 700 MPa.

## 4. CONCLUSIONS

Comparisons of FLEX 5 with experimental data show that the aeroelastic model is accurate for producing usable and realistic input torque for the multibody code. This is the most important aspect of validation, and it is essential for the accurate prediction of the gear tooth normal forces. It is seen that the aerodynamic FLEX 5 model obtain the correct rotor/main shaft torque when comparing with measurements. However, in terms of predicting the bending moment, the model does not perform as well, which however is not an issue because the gear tooth stresses do not depend on these effects. By using the described multibody model, radial and axial rotor forces are absorbed by the main shaft bearings, and they have no influence on the gear tooth stresses.

The semi-advanced gear constraint presented in this paper would seem to be useful for predicting the gear tooth forces, even for helical gears. It is expected that this gear constraint can be further developed and used in a more advanced flexible gear-constraint model of a gearbox.

Using MATLAB and COMSOL MULTIPHYSICS together in order to predict gear tooth stresses yields good control over how to rotate the gears in order to investigate different load cases. Many different gear sizes can be tested using the method described in this paper, and the method can be extended and improved, if required. However, in the basic and simple version described here, it seems reasonable that the predicted von Mises stress level at a mean turbulent wind speed of  $6 \text{ m s}^{-1}$  was around 160–250 MPa, and when the wind turbine was loaded the most, at a full wind speed of  $20 \text{ m s}^{-1}$ , it was in the order of 490–690 MPa.

After surface hardening procedures, gear teeth can typically achieve a gear tooth bending strength and pitting resistance of something in the range of 1000–1500 MPa. The present results predict that there will be a sufficient safety factor for rare extreme loads during operation up to the investigated maximum turbulent wind input of  $20 \text{ m s}^{-1}$ .



However, it should be emphasized that the accuracy of this method, which in a way is described as a “worst-case” method and in other cases is too simple, is difficult to assess. The model does not capture for instance the effects of uneven gear loading, or that multiple teeth can be in mesh at the same time. It is an idealized method, which can be improved by, for instance, introducing a flexible gear constraint and by adding more advanced assumptions on some of the principles described. The accuracy could also be improved by using dedicated commercial software packages. This method is proposed as a way of obtaining some basic insights under simple assumptions, when there is no access to a full gear database or other expensive methods.

## ACKNOWLEDGEMENTS

Funding from DSF 09-071588 (Dynamic wind turbine model—from wind to grid) is highly appreciated. The authors are grateful for discussions about experimental measurements (winddata.com) with Kurt S. Hansen (DTU Wind Energy) and to Stig Øye (DTU Wind Energy) for discussion on using the aeroelastic FLEX 5 code. The authors are also grateful for discussions about multibody gear constraints and code implementation with Michael Rygaard Hansen and Morten Kjeld Ebbesen from University of Agder, Norway.

## REFERENCES

1. Sieros G, Chaviaropoulos P, Sorensen JD, Bulder BH, Jamieson P. Upscaling wind turbines: theoretical and practical aspects and their impact on the cost of energy. *Wind Energy* 2012; **15**: SI, 3–17, (English).
2. Jonkman J, Butterfield S, Passon P, Larsen T, Camp T, Nichols J, Azcona J, Martinez A. Offshore code comparison collaboration within IEA Wind Annex XXIII: phase II results regarding monopile foundation modeling, *European Offshore Wind Conference & Exhibition*, Berlin, Germany, 4–6 December 2007; 12.
3. Passon P, Kuehn M, Butterfield S, Jonkman J, Camp T, Larsen TJ. Oc3-benchmark exercise of aero-elastic offshore wind turbine codes - Art. No. 012071. *Science of Making Torque from Wind* 2007; **75**: 12071–12071.
4. Peeters JLM, Vandepitte D, Sas P. Structural analysis of a wind turbine and its drive train using the flexible multibody simulation technique. In *Proceedings of ISMA2006: International Conference on Noise and Vibration Engineering*, Vol. 1-8, Sas P, DeMunck M (eds). Katholieke Univ Leuven, Dept Mech Engn, 2006, International Conference on Noise and Vibration Engineering (ISMA2006): Louvain, Belgium, September 18–20, 2006; 3665–3679.
5. Hansen AM, Rasmussen F, Larsen TJ. Gearbox loads caused by double contact simulated with hawc2, *Proceedings*, Brussels in Belgium, 2011; 1–11.
6. Hastrup M, Hansen MR, Ebbesen MK. Modeling of wind turbine gearbox mounting. *Modeling, Identification and Control* 2011; **32**: 141–149.
7. Peeters JLM, Vandepitte D, Sas P. Analysis of internal drive train dynamics in a wind turbine. *Wind Energy* 2006; **9**: 141–161.
8. Øye S. Various flex 5 documentation, DTU Mechanical Engineering, 2001.
9. Nikravesh PE. *Computer-Aided Analysis of Mechanical Systems*, Vol. 186. Prentice Hall: Upper Saddle River, New Jersey 07458, 1988.
10. Haug EJ. *Computer Aided Kinematics and Dynamics of Mechanical Systems: Vol. I: Basic Methods*. Allyn and Bacon: Columbus, Ohio 43235, 1989.
11. Shabana AA. *Dynamics of Multibody Systems*. Wiley & Sons: Hoboken, New Jersey, 1989.
12. Hansen MOL. *Aerodynamics of Wind Turbines*, (2nd edn). Earthscan: London, UK, 2009.
13. Hansen KS, Larsen GC. Database of wind characteristics. [Online]. Available: <http://www.winddata.com>, 1997–2011 (Accessed on 15 November 2012).
14. Paulsen US, Wagner R. Imper: Characterization of the wind field over a large wind turbine rotor, DTU Wind Energy, Wind Energy Department, Technical University of Denmark, 2012. ISSN: 0106-2840.
15. Pedersen NL, Jørgensen MF. On gear teeth stiffness evaluation 2013. (submitted).
16. Klit P, Casper K, Pedersen NL. *Machine Elements—Analysis and Design*. Polyteknisk Forlag: Lyngby, Denmark, 2009.
17. Krenk S. *Non-Linear Modeling and Analysis of Solids and Structures*. Cambridge University Press: Cambridge, UK, 2009.
18. DIN 867 standard. Basic rack tooth profiles for involute teeth of cylindrical gears for general and heavy engineering, 1986.
19. Pedersen KOH, Hansen KS, Paulsen US, Sørensen P. Wind turbine measurement technique—an open laboratory for educational purposes. *Wind Energy* 2008; **11**: 281–295.

# Publication [P2]

On Gear Tooth Stiffness Evaluation

# On Gear Tooth Stiffness Evaluation

Niels Leergaard Pedersen & Martin Felix Jørgensen

Dept. of Mechanical Engineering, Solid Mechanics

Technical University of Denmark

Nils Koppels Allé, Building 404, DK-2800 Kgs. Lyngby, Denmark

email: nlp@mek.dtu.dk

**Abstract.** The estimation of gear stiffness is important for determining the load distribution between the gear teeth when two sets of teeth are in contact. Two factors have a major influence on the stiffness; firstly the boundary condition through the gear rim size included in the stiffness calculation and secondly the size of the contact. In the FE calculation the true gear tooth root profile is applied. The meshing stiffnesses of gears are highly non-linear, it is however found that the stiffness of an individual tooth can be expressed in a linear form assuming that the contact width is constant.

**Key words:** Gears, Stiffness, Spur, External/Internal, FE.

## 1 Introduction

To evaluate the forces in a multibody formulation of a planetary gearbox where multiple planet gears are in contact with the ring and sun gear an algebraic constraint formulation cannot be used if the forces on the individual teeth of the involved gears are of interest. We are forced to include in some way the gear contact and here include the flexibility, as discussed in i.e. [1, 2]. Including the flexibility through a full integration of a finite element (FE) formulation within the multibody simulation is not feasible due to the simulation time needed. Instead hybrid methods of lumping in some way the stiffness are needed. The present paper focuses on the estimation of gear teeth stiffnesses, these stiffnesses can then later be applied in a multibody modelling.

Gears are highly standardized and the most common gear design applied is controlled by the cutting tool or basic rack defined in [3], and seen in Figure 1. The gear load capacity can be evaluated using [4]. The basic contacting gear shape is the involute shape, due to the excellent properties of this shape. These properties includes that the contact forces act along a straight line and that a center distance error do not influence this. A change in center distance due to, e.g., loading will neither influence the gear ratio. The design variable that controls the involute shape is the pressure angle  $\alpha$ , see Figure 1. The commonly used value for the pressure angle is  $\alpha = \pi/9$ . The involute shape controls the gear part that is in contact with the other gear in the mesh. The gear root or bottom land that connects two neighbouring teeth is controlled by the cutting tool tip design, there is no contact between the teeth at the root. Different ways of modifying the root design and improving the stress concentrations can be found in [5, 6].

The contact between two involute gears follows the straight contact line (the dotted line in Figure 2) at all time during the contact. Seen from the individual tooth the contact load moves

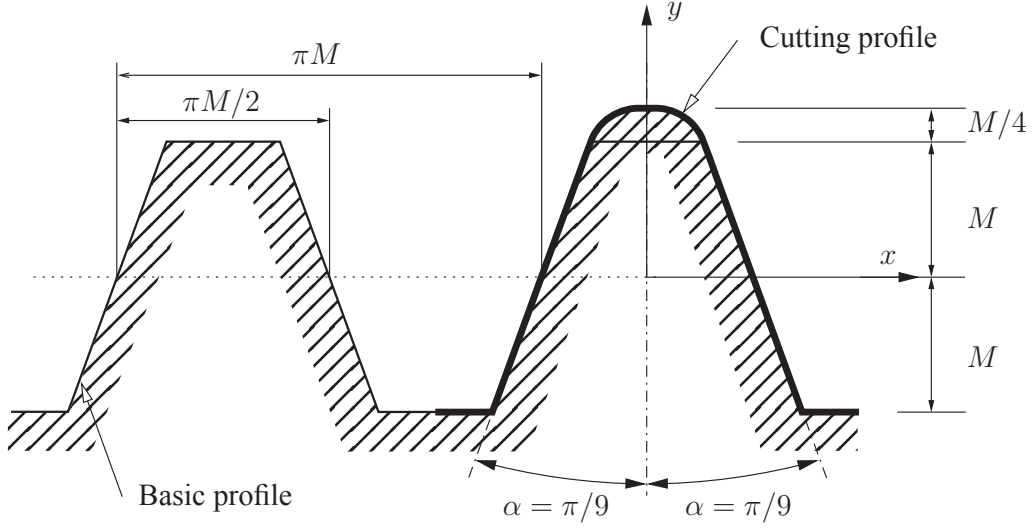


**Figure 1:** The cutting profile geometric definition and the basic profile based on the ISO profile.

along the involute shape. Due to the design of a tooth, see Figure 2, this results in an overall non-linear tooth stiffness along the contact line.

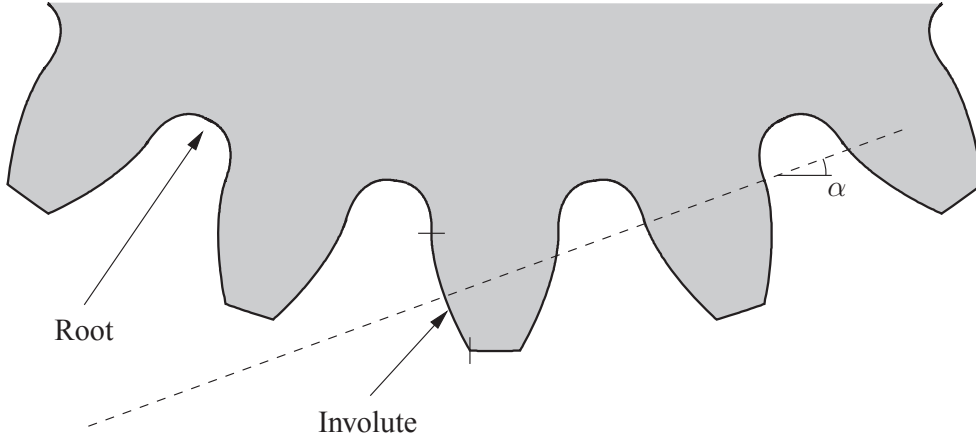


**Figure 2:** Part of a gear with 20 teeth and module  $M = 10\text{mm}$ . The line of contact is indicated by the dotted line, the angle is  $\alpha$  assuming that no profile shift have been applied to both gears in mesh.

The tooth stiffness is needed for multiple reasons. For gears in mesh we have different number of teeth in contact during the motion. For spur gears produced from a standard rack cutter with  $\alpha = \pi/9$  and a height of  $2M$ , i.e. two times the module (see [3] and Figure 1) we have that the maximum contact ratio is  $(\epsilon_\alpha)_{max} \approx 1.98$ . The contact ratio expresses the average number of teeth in contact during the motion. With more than two sets of teeth in contact we need the tooth stiffness for finding the load on the individual tooth. This is also the case for planetary gears where multiple planet gears are in contact with the sun gear and the ring gear. The nature of the gear mesh contact is discontinuous, for standard spur gears there are at some instance in time either one or two gear teeth sets in contact and this transition result in discontinuous mesh stiffness.

From a literature study it is obvious that many different approaches have been applied.

In [7] FE analysis was used for the tooth stiffness estimation. Here a model with only one tooth attached to a rim/ring with a given thickness of 2.5 times the tooth height was applied. The stiffness is calculated for two gears in contact, for one gear a torque is applied to the rim inner boundary and at the other gear the rim inner boundary is fixed. The tooth root is assumed circular. A principally different way of estimating the stiffness is to use the elastic energy. Using the elastic energy and the applied force for specifying the stiffness is clear and concise, the need for finding a deflection corresponding to the force is avoided. This way of establishing the stiffness is used in relation to bolt plate stiffness in [8–10] and is also the selected method in the present paper. In [11] the stiffness is found using an analytical estimation of the complementary elastic energy, several assumptions are applied in this work. Further stiffness evaluation of spur and helical gears can be found in, e.g., [12–17].

In the present paper two factors are found to have a major influence on the gear tooth stiffness, these are

- The gear rim size included in the stiffness calculation
- The contact zone size.

To the authors knowledge no thorough examination have been published in relation to these two factors, even for the simple case of spur gears. The bending strength calculations of most standards rely on the cantilever beam assumption (Timoshenko theory) and the tooth is clamped at the root. This is also the general choice for estimating the stiffness either by analytical method or numerical FE calculations. The present paper will focus on the definition of boundary conditions, and the influence from the contact zone width.

The paper presents an example where the found stiffnesses are used in the simulation of a planetary gearbox of a 500MW wind turbine. Modelling specifically related to planetary gearbox can be found in, e.g., [18] and in relation to wind turbine drive train see e.g. [19, 20]

The paper is organized as follows. Section 2 presents the geometric description and the tooth boundary parameterization. In Section 3 the individual tooth stiffness is given. The section includes a discussion on the important selection of boundary condition and contact width. The combined stiffness of two gear teeth in contact and the overall meshing stiffness are found. Section 4 presents an example where stiffnesses found using the proposed approach is used in a planetary gearbox of a wind turbine. Finally a generic gear tooth geometry determination in parametric form is presented in the appendix.

## 2 Parametric geometry description

The ISO profile gear geometry is controlled by the cutting tools outer profile design as presented in Figure 1. The standard profile is defined by connected curve segments (arc of circles and straight lines). A procedure for finding the curve segments can be found in [5, 6] and in the appendix of the present paper.

The gear tooth contact geometry is the envelope defined by rotating and simultaneously translating the straight side of the cutting tool. For this segment we know that the envelope corresponds to the involute shape, which for the curve given in Figure 3 is given as a function of  $s$  by

$$\begin{Bmatrix} x(s/r_b) \\ y(s/r_b) \end{Bmatrix} = \begin{bmatrix} \cos(s/r_b) & -\sin(s/r_b) \\ \sin(s/r_b) & \cos(s/r_b) \end{bmatrix} \begin{Bmatrix} r_b \\ -s \end{Bmatrix} \quad (1)$$

where  $r_b$  is the base circle radius, the parameter  $s$  is the base circle arc length which is directly related to the involute arc length. The base circle radius is given by

$$r_b = M \frac{z}{2} \cos(\alpha) \quad (2)$$

where  $z$  is the number of gear teeth.

We may use (1) as a specific alternative to the general parameterization presented in the appendix.

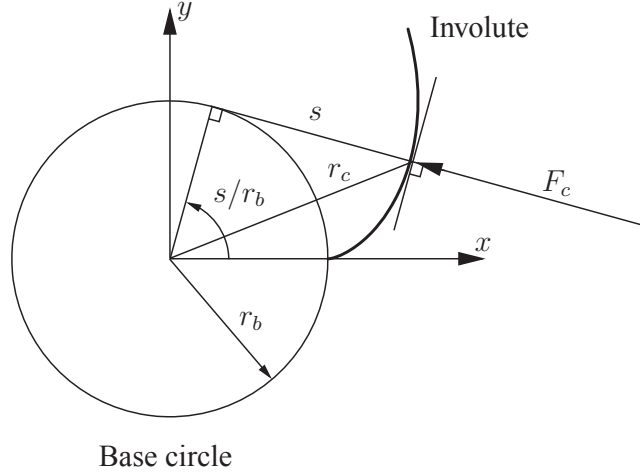


**Figure 3:** Base circle and involute geometry, the angle is defined by the base circle arc length  $s$ . An arbitrary contact load  $F_c$  is shown to be perpendicular to the involute shape.

The present papers primary objective is finding the tooth stiffness as a function of the loading point on the gear. In [11] the load position is defined by a profile parameter defined as

$$\xi = \frac{z}{2\pi} \sqrt{\frac{r_c^2}{r_b^2} - 1} \quad (3)$$

where  $r_c$  is the distance from the gear center to the contact point (see Figure 3). We directly see that

$$s = \sqrt{r_c^2 - r_b^2} \quad (4)$$

$$\xi = s \frac{z}{2\pi r_b} = \frac{s}{\pi M \cos(\alpha)} = \frac{s}{s_d} \quad (5)$$

here we have defined the contact pitch  $s_d = \pi M \cos(\alpha)$ , this distance is only a function of the pressure angle  $\alpha$  and the module.

The stiffness will in the present paper be given as a function of the base circle arc length  $s$ , from (16) and (5) follows that it can directly be scaled to be given as a function of  $r_c$  or  $\xi$ . The base circle arc length is directly related to the involute arc length. The involute arc length,  $L$ , measured from the base circle to the point defined by  $s$  is given by

$$L = \frac{s^2}{2r_b} \quad (6)$$

the squared  $s$  is therefore a direct involute arc length measure.

Assuming that the tooth involute is given then the stiffness also depends on the gear width but we may define a stiffness per width. The stiffness is however not only a function of the contact point position on the involute, the stiffness also depends on the remaining tooth part which is defined by the cutting tool top and the profile shift  $p_s$ . This is described in the following section.

### 3 Gear tooth stiffness

The stiffness of a structure related to a given load is usually in the linear case defined as the load  $F_c$  divided by the corresponding load displacement  $d_c$ .

$$K_g = \frac{F_c}{d_c} \quad (7)$$

The main problem with this definition is that in many cases the displacement does not have a clear and unique definition. To avoid this we will define the stiffness from the total elastic energy  $U$  (sum of strain energy  $U_\epsilon$  and stress energy  $U_\sigma$ ). Often the stress energy is referred to as the complementary elastic energy. For the linear case we have that  $U_\epsilon = U_\sigma = U/2$ . Assuming that we only have one set of loads, that scales proportional to the total load  $F_c$  the corresponding stiffness is given by

$$U = F_c d_c = F_c \frac{F_c}{K_g} \Rightarrow K_g = \frac{F_c^2}{U} \quad (8)$$

This way of establishing the stiffness is also used in relation to bolt plate stiffness in [8–10]. In [11] the elastic energy is also used as a direct stiffness measure. They assume the tooth to be equivalent to a cantilever beam clamped at the straight line that is perpendicular to the tooth center and at the same time tangent to the dedendum circle. They further assume that the tooth side is defined by the involute part, i.e., they neglect the root design, finally the load is moved to the tooth center line so that simplified formulas for the complementary elastic energy of a beam can be used. The elastic energy is found from an analytical expression of the elastic energy that includes the energy related to the shear force, i.e., there analysis corresponds to Timoshenko beam theory.

In the present paper 2D FE analysis is used for finding the elastic energy. The FE calculation is performed using the COMSOL program ([21]). Assuming linearity we can apply a unit load and the stiffness is then directly given as the inverse of the total elastic energy. In the FE calculation of the elastic energy plane strain is assumed.

#### 3.1 Stiffness of a single gear tooth

In the transmission of power there is always at least one set of teeth in contact and as such the combined stiffness of the two teeth is what we need for, e.g., multibody simulations of a

gearbox. Having found the stiffness of a single tooth as a function of the contact load position the combined stiffness can be established, as discussed in the next section.

The computations are performed with the same spur gear set as used in [11], the data used are

$$z_1 = 21, \quad z_2 = 49, \quad M = 4\text{mm}, \quad b = 20\text{mm}$$

i.e. no profile shift is used so that  $\alpha_w = \alpha = \pi/9$  (see (10)). The gear width is given by  $b$ , the width is not involved in the FE calculations but used for the specific stiffness values shown.

### Contact width

The first problem of defining a unique stiffness function for a tooth is that the stiffness is a function of the load size because the contact width changes as the load size change. To examine this effect we, in the initial case, clamp the tooth at the root as was also the case in [11]. In Figure 4 the pinion gear single tooth of the pinion ( $z_1 = 21$ ) and the wheel ( $z_2 = 49$ ) are shown, the difference in shape is clear.

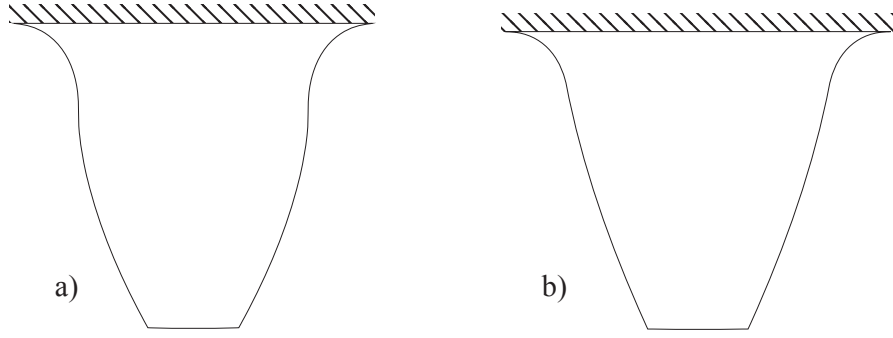


**Figure 4:** Single tooth clamped at the root for two different size gears ( $M = 4\text{mm}$ ). a) 21 teeth gear. b) 49 teeth gear.

It is a valid assumption that the contact stress acts as a Hertzian stress, and we know the radii of curvature; these are  $s_1$  and  $s_2$ , see Figure 5.

Idealized, the contact point of two gears follows the straight line of action. The line of action is the tangent to both base circles. The sum of the two arc length parameters  $s_1$  and  $s_2$  is therefore a constant  $s_c$ , see Figures 3 and 5.

$$s_c = s_1 + s_2 = (r_{b1} + r_{b2}) \tan(\alpha_w) \quad (9)$$

where  $r_{b1}$  and  $r_{b2}$  are the base circle radii of the two gears and  $\alpha_w$  is the transverse pressure angle found from the iterative solution of

$$p_{s1} + p_{s2} = (z_1 + z_2) \frac{\text{inv}(\alpha_w) - \text{inv}(\alpha)}{2 \tan(\alpha)} \quad (10)$$

with the involute angle defined as



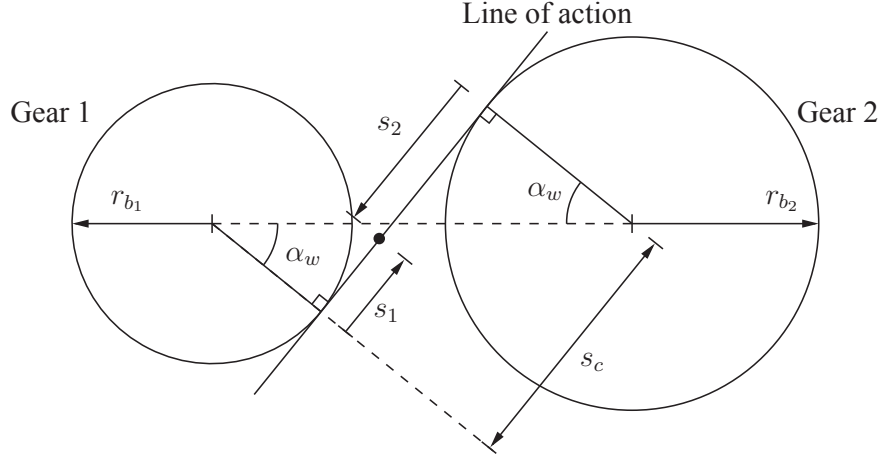


**Figure 5:** Basic gear geometry, the dot indicates a contact point.

$$\text{inv}(\theta) = \tan(\theta) - \theta \quad (11)$$

If there is no profile shift ( $p_{s1} + p_{s2} = 0$ ) then  $\alpha_w = \alpha$ .

Using Hertz theory the contact zone half width,  $a$ , is then given by

$$a \approx \sqrt{\frac{4}{\pi}(m_1 + m_2) \cdot \sqrt{F_c/b} \cdot \sqrt{s_1 - s_1^2/s_c}} = C \cdot \sqrt{F_c/b} \cdot \sqrt{s_1 - s_1^2/s_c} \quad (12)$$

$$m_1 = m_2 = \frac{1 - \nu^2}{E} \quad (13)$$

where  $C$  is a constant depending on the gear material ( $E$  is modulus of elasticity and  $\nu$  Poisson's ratio, here we assume the same material for both gears). Alternatively we can find the half width as a function of the maximum pressure in the contact.

$$a \approx 2(m_1 + m_2)(s_1 - s_1^2/s_c) \cdot p_{\max} \quad (14)$$

From (12) it is seen that the contact width change along the contact line due to the change in value of  $s_1$  and from (14) we see directly the dependence on the load size.

To exemplify the tooth in Figure 5a is used. The load is assumed to act at the pitch point ( $s_1 = s_{p1}$ ), this point is well defined when no profile shift is used.

$$s_{p1} = r_{b1} \tan \alpha \quad (15)$$

A gear with 21 teeth can usually mesh with gears from 17 to 147 teeth. With the material data  $E = 2.1 \cdot 10^5 \text{ N/mm}^2$  and  $\nu = 0.3$ , and setting the maximum pressure to  $p_{\max} = 1500 \text{ MPa}$  we find a contact half width range,  $a \in [167 \mu\text{m} : 326 \mu\text{m}]$ . In Figure 6 the tooth stiffness (from FE analysis) is shown as a function of the half width.

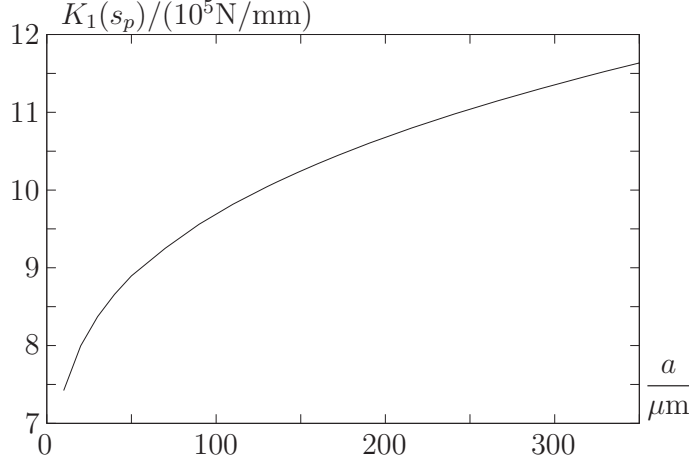


**Figure 6:** Stiffness of single tooth (Figure 5a) as a function of half the contact width. The load center is at the pitch point (assuming no profile shift).

In [11] the load size is defined as  $F_c = 1000\text{N}$ , with this load size we find  $a = 74.5\mu\text{m}$  corresponding to as stiffness of

$$K_1(s_{p1}) = 9.33 \cdot 10^5 \text{N/mm} \quad (16)$$

Although it is clear that the stiffness depends on the contact zone width in a non-negligible way the remaining part of the paper use  $a = 74.5\mu\text{m}$ . By doing this the influence from the contact width is neglected, i.e. an average contact width is assumed. The reason for using this assumption is that the width is a function of; the load size, the number of teeth on the gears in the mesh, the position on the line of action and a possible profile shift. This makes a generic stiffness function evaluation difficult.

In order to validate the result in (16) a rough estimate based on timoshenko beam theory is made, in [11] this was also the preferred method for calculating the elastic energy. With the load acting at the pitch point we can estimate the stiffness by a cantilever beam with dimension, length  $1.25M$ , height  $\pi M/2$  and width  $20\text{mm}$ . The stiffness found is  $9.7 \cdot 10^5 \text{N/mm}$ , which is in close correlation with the result in (16).

### Boundary condition

The second problem of defining a unique stiffness function for a tooth is the boundary condition applied. In the previous shown cases we clamped the tooth at the root which is a common assumption found in the literature. The stiffness is not only controlled by the tooth shape itself also the rim (or ring) thickness has a non-negligible influence. In [22] the rim is included in the stiffness evaluation of internal gears. In the present paper we estimate the influence from the rim thickness by using a model where the teeth are attached to a rim with thickness  $r_t$ . In Figure 7 part of a one tooth and a three teeth model is shown. In the figure the full rings that are used in the FE calculation are not shown. In the FE calculations results presented in Figure 8 the inside of the rim is clamped and the load is applied at the pitch point as done previously.

In Figure 7 the rim thickness is equal to the tooth module. By varying the rim thickness the stiffness presented in Figure 8 is found, the rim thickness is normalized by the tooth module. From the results it is clear that a one tooth model is sufficient for the stiffness estimation. That

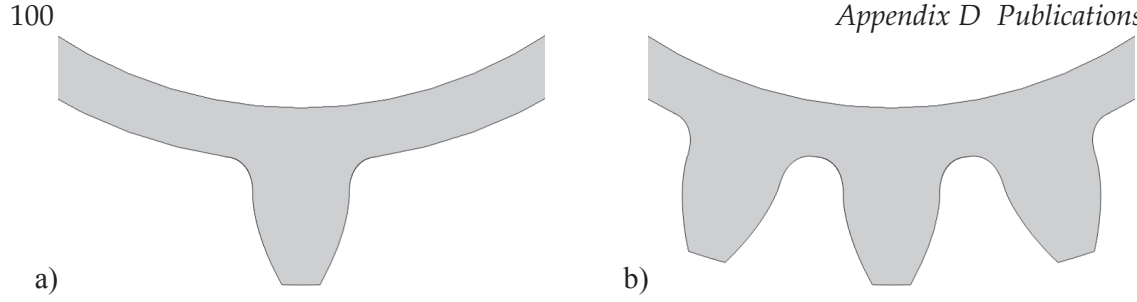


**Figure 7:** Part of geometry model here with a rim thickness  $r_t = M$ . 1) One tooth model. b) Three teeth model.

the rim can not be neglected from the calculation is also evident. A larger rim thickness gives larger distance to the clamped rim surface and therefore a smaller stiffness.

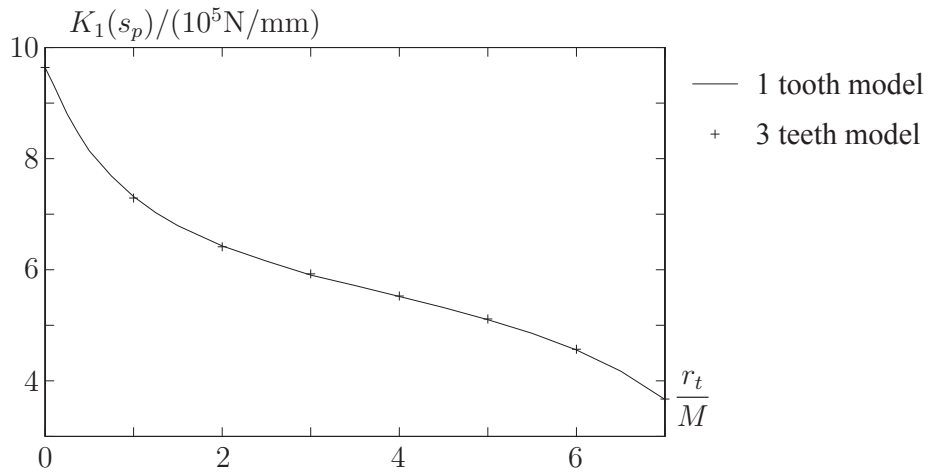


**Figure 8:** Stiffness of single tooth (Figure 5a) as a function of rim thickness. The load center is at the pitch point (assuming no profile shift).

For practical examples the actual gear rim thickness should be included in the calculation of stiffness. In Figure 8 it is seen that the stiffness is decreased significantly for large values of rim thickness, this is due to the relative small radius of the clamped boundary condition, which probably do not have a practical relevance.

In figure 9 a strain energy density colour and contour plot is given, indicating that the one tooth model is sufficient. From the figures it can also be concluded that the tooth stiffness is not influenced by a neighbouring tooth being engaged.

### Stiffness as a function of contact position

Before the stiffness as a function of contact point can be established a rim thickness must be defined. For the problem at hand with pinion (21 teeth) and wheel (49 teeth) we select to use input shaft diameter 50mm and output shaft diameter 65mm, these diameter values have been selected from [23]. Moving the load along the tooth involute the stiffnesses presented in Figures 10a and 10b are found. We notice the rather high actual stiffness variation, i.e. the difference in stiffness from lowest to highest value relative to the lowest value is over 100%.

The stiffness is seen to have an almost parabolic dependence on the base circle arc length  $s$ . The stiffnesses are in Figures 11 and 12 presented as a function of  $s^2$ .

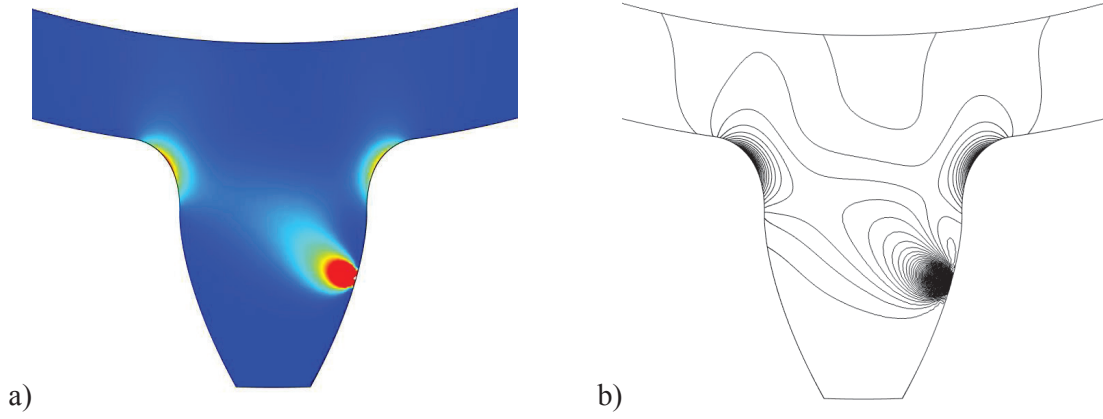


**Figure 9:** Illustration of the distribution of strain energy density. a) Colour plot. b) Contour plot.

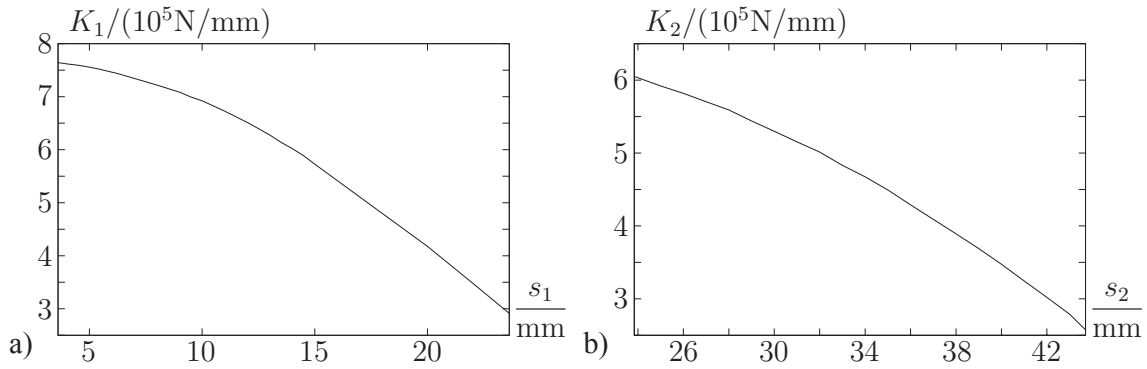


**Figure 10:** Stiffness of single tooth as a function of contact point position. a) 21 teeth gear (Figure 5a). b) 49 teeth gear (Figure 5b)

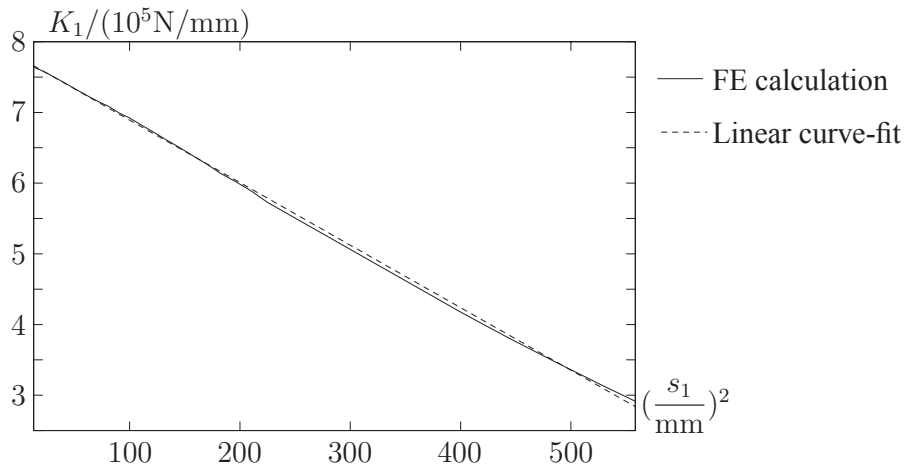


**Figure 11:** Stiffness of single tooth (Figure 5a) as a function of squared contact point position and linear curve-fit.

In the figures a linear curve-fit to the stiffness variation is also given. These linear curve-fits in the squared  $s_1$  and  $s_2$  parameters are

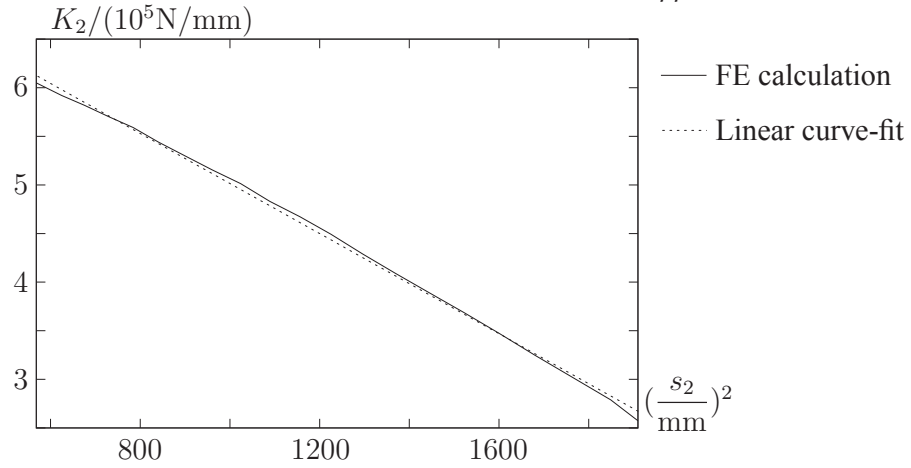


**Figure 12:** Stiffness of single tooth (Figure 5b) as a function of squared contact point position and linear curve-fit.

$$K_1(s_1) = (-8.844 \cdot 10^2 \cdot (s_1/\text{mm})^2 + 7.776 \cdot 10^5) \text{N/mm} \quad (17)$$

$$K_2(s_2) = (-2.574 \cdot 10^2 \cdot (s_2/\text{mm})^2 + 7.589 \cdot 10^5) \text{N/mm} \quad (18)$$

These two curve-fits are used in the following sections. In Figure 13 the loading of a tooth in the 49 teeth gear is shown for the case where the load acts very close to the tip.

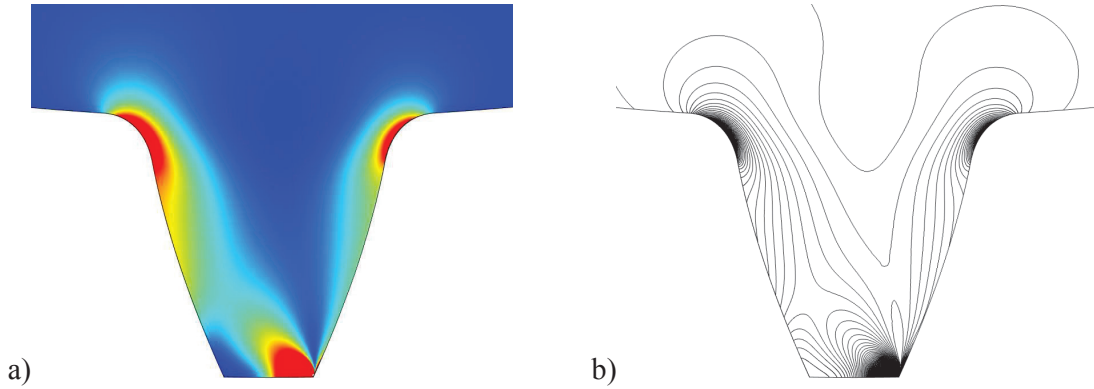


**Figure 13:** Illustration of the distribution of strain energy density of a tooth loaded close to the tip for the 49 teeth gear. a) Colour plot. b) Contour plot.

### 3.2 The combined stiffness of two gear teeth

The combined stiffness of two gear teeth,  $K_c$  directly follows the results from the previous section. The combined stiffness can be given as a function of either  $s_1$  or  $s_2$ , since the sum of  $s_1$  and  $s_2$  is known (9).

$$K_c(s_1) = \frac{1}{\frac{1}{K_1(s_1)} + \frac{1}{K_2(s_c - s_1)}}, \quad K_c(s_2) = \frac{1}{\frac{1}{K_1(s_c - s_2)} + \frac{1}{K_2(s_2)}} \quad (19)$$

The boundaries for one pair contact can be given relative to either the arc length  $s_1$  or  $s_2$ , here they are presented by the  $s_1$  parameter. The limits are

$$s_{1\min} = s_c - s_{2\max} = s_c - \sqrt{r_{a_2}^2 - r_{b_2}^2} \quad (20)$$

$$s_{1\max} = \sqrt{r_{a_1}^2 - r_{b_1}^2} \quad (21)$$

where  $r_{a_1}$  and  $r_{a_2}$  are the tip radii of the two gears. Using the present example we find

$$s_c = 0.14 \tan(\alpha), \quad s_{1\min} = 7.0986\text{mm}, \quad s_{1\max} = 23.629\text{mm}$$

Using (17) and (18) in (19) the stiffness of the two gears in contact is found. The combined stiffness is for this example seen to vary within 25%.

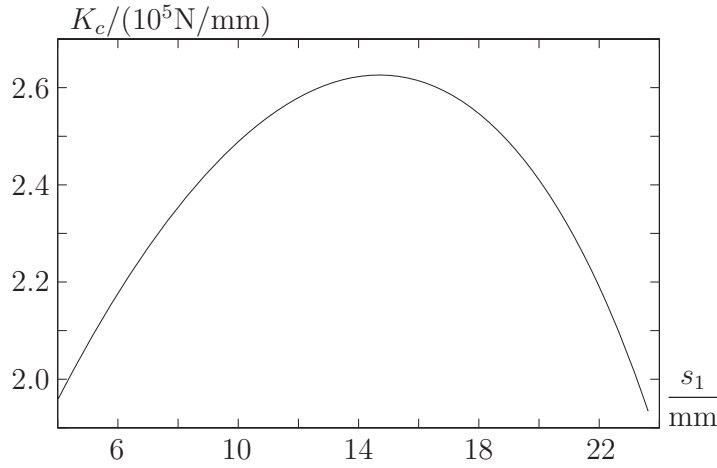


**Figure 14:** Combined stiffness of two gear teeth in contact.

### 3.3 Mesh stiffness

With two spur gears we typically have a contact ratio between 1 and 2, the contact ratio being the average number of teeth pairs in contact. It is therefore also possible to find the combined stiffness over the full contact region, i.e., with both one and two pairs of gear teeth in contact. Therefore we also directly can find the load sharing ratio. This is due to the fact that the contact point has a constant speed along the line of action, i.e. when two sets of teeth are in contact they act as two springs in parallel. The load sharing ratio is therefore directly given by the individual stiffness relative to the total stiffness, i.e. the load sharing ratio is the ratio of contact force on one gear tooth to the total contact force in the gear contact.

If one gear tooth pair is in contact we assume the stiffness to be  $K_{c_1}$  if two gear teeth pairs are in contact we have the stiffnesses  $K_{c_1}$  and  $K_{c_2}$ . The gear contact with two contact points is illustrated in Figure 15. The stiffnesses of the involved four teeth are  $K_1$  to  $K_4$  (all stiffnesses are functions of the position but for simplicity the indication is dropped in the subsequent equations). The stiffnesses  $K_1$  and  $K_3$  are associated with Gear 1 and stiffnesses  $K_2$  and  $K_4$  with Gear 2.

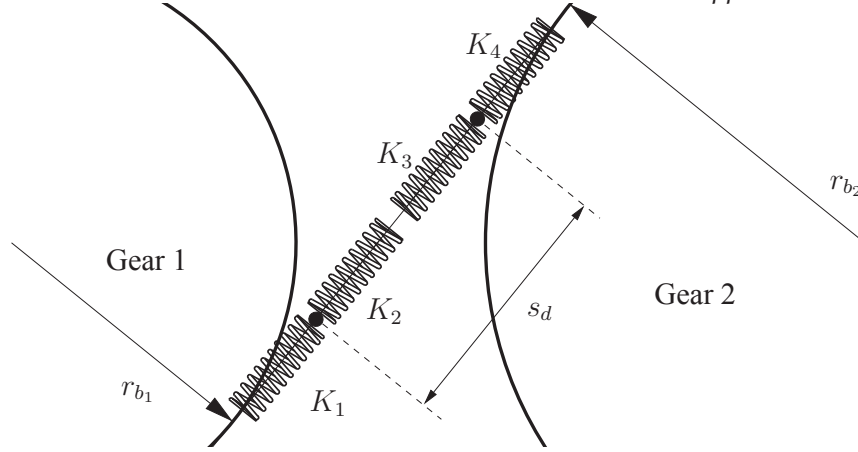


**Figure 15:** Illustration of two gear teeth pair contact, the two dots are the contact points. The stiffnesses  $K_1$  and  $K_3$  are associated with Gear 1 and stiffnesses  $K_2$  and  $K_4$  with Gear 2.

The contact point stiffnesses are

$$K_{c1} = \frac{1}{\frac{1}{K_1} + \frac{1}{K_2}}, \quad K_{c2} = \frac{1}{\frac{1}{K_3} + \frac{1}{K_4}} \quad (22)$$

The total mesh stiffness is  $K_g = K_{c1} + K_{c2}$  and the load sharing ratio's are

$$R_1 = K_{c1}/K_g, \quad R_2 = K_{c2}/K_g \quad (23)$$

The transition point from one to two pair contact is controlled by the distance between the contact points  $s_d$  (the contact pitch).

The boundaries for one or two pair contact are given in (20) and (21). The contact regions are therefore defined by

$$\begin{aligned} s_{1\min} \leq s_1 \leq s_{1\max} - s_d &\Rightarrow \text{Two pair contact} &\Rightarrow R_1 = K_{c1}/K_g \\ s_{1\max} - s_d \leq s_1 \leq s_{1\min} + s_d &\Rightarrow \text{One pair contact} &\Rightarrow R_1 = 1 \\ s_{1\min} + s_d \leq s_1 \leq s_{1\max} &\Rightarrow \text{Two pair contact} &\Rightarrow R_1 = K_{c1}/K_g \end{aligned}$$

From the previous eq. the contact ratio is given by

$$\epsilon_\alpha = \frac{s_{1\max} - s_{1\min}}{s_d} \quad (24)$$

The mesh stiffness for the two gears (21 teeth and 49 teeth) can now be found. The result is presented in Figure 16.

Finally in Figure 17 the load share ratio for the gear mesh is shown.

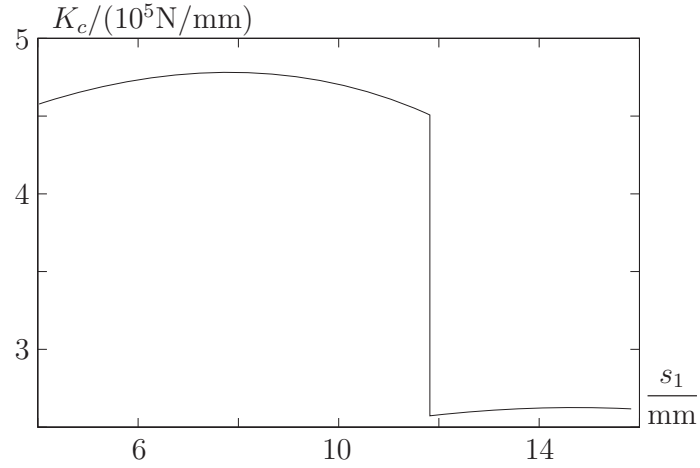


**Figure 16:** Mesh stiffness of two gears, which shows the discontinuity due to number of teeth in contact.

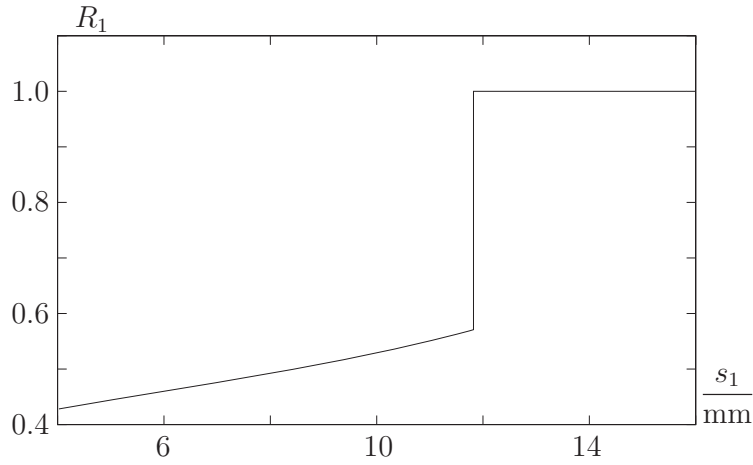


**Figure 17:** The load share ratio.

## 4 Wind turbine example

A wind turbine planetary gearbox is illustrated in Figure 18. The relevant data for the gear teeth are

$$z_s = 21, \quad z_p = 36, \quad z_r = 93, \quad M = 10\text{mm}, \quad b = 210\text{mm}$$

the subscripts correspond to; sun gear, planet gear and ring gear.

With the planet carrier as the input and the sun as output (the ring fixed) we have a gear ratio of 5.43. With the selected number of teeth on the planet and ring we have avoided the possibility of involute, trochoid and trimming interference. The input shaft diameter is 300mm and the output shaft with the sun gear mounted has a diameter 170mm. The ring gear rim thickness is 50mm. The sun gear tooth stiffness is found as presented in previous section, and this also holds for the ring gear with the exception that here the teeth are on the inside and the clamped boundary is on the outside. For the planet gears we have a slightly different situation



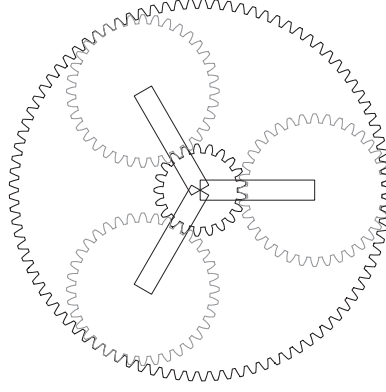


**Figure 18:** Illustration of planetary gear, with three planet gear connected to the carrier.

since they function as idle gears. However this will not change their stiffness significantly so the stiffness is found as for the sun gear, the planet gears center hole diameter is 200mm.

The individual teeth stiffnesses found are

$$K_s = (-1.752 \cdot 10^3 \cdot (s_s/\text{mm})^2 + 9.607 \cdot 10^6) \text{N/mm} \quad (25)$$

$$K_p = (-7.437 \cdot 10^2 \cdot (s_p/\text{mm})^2 + 8.441 \cdot 10^6) \text{N/mm} \quad (26)$$

$$K_r = (3.930 \cdot 10^2 \cdot (s_r/\text{mm})^2 - 2.909 \cdot 10^6) \text{N/mm} \quad (27)$$

The mesh stiffness estimation follows the description from the previous section with some minor differences. For the contact between the internal gear (ring) and the external gear (planet) the constant parameter  $s_c$  is defined by

$$s_c = s_r - s_p = (r_{b2} - r_{b1}) \tan(\alpha_w) \quad (28)$$

and the minimum and maximum values are

$$s_{1\min} = s_{2\min} - s_c = \sqrt{r_{a2}^2 - r_{b2}^2} - s_c \quad (29)$$

$$s_{1\max} = \sqrt{r_{a1}^2 - r_{b1}^2} \quad (30)$$

The meshing stiffness for the sun/planet and planet/ring contact is given in Figures 19a and 19b. The difference in the contact ratio is directly seen. The contact ratio's are

$$\epsilon_{\alpha_{\text{sun/planet}}} = 1.631, \quad \epsilon_{\alpha_{\text{planet/ring}}} = 1.936$$

In the simulation the following mass moments of inertia are used

$$I_s = 1173 \text{Kg}\text{m}^2, \quad I_p = 12.6 \text{Kg}\text{m}^2, \quad I_{\text{carrier}} = 3000 \text{Kg}\text{m}^2$$

the relative high value for the carrier is due to the added inertia from blades and rotor, the high value for the sun is due to the secondary gear steps and the generator. The simulation is initiated from constant speed and with a constant input and output torque, i.e. initially no teeth are loaded. One simulation is performed with assumed constant stiffness of the

sun/planet and planet/ring contact, the used values are  $K_c(\text{sun/planet}) = 4.719 \cdot 10^6 \text{ N/mm}$  and  $K_c(\text{planet/ring}) = 5.529 \cdot 10^6 \text{ N/mm}$ , i.e. the stiffnesses corresponds to the real stiffnesses mean values. In the second simulation we let the stiffnesses vary as shown in Figure 19. A viscous damper is added to each spring, the damping coefficient used is  $c = 10^2 \text{ Ns/mm}$ . To illustrate the influence from the discontinuous nature of the stiffness we in Figure 19c plot the angular speed of a planet gear.

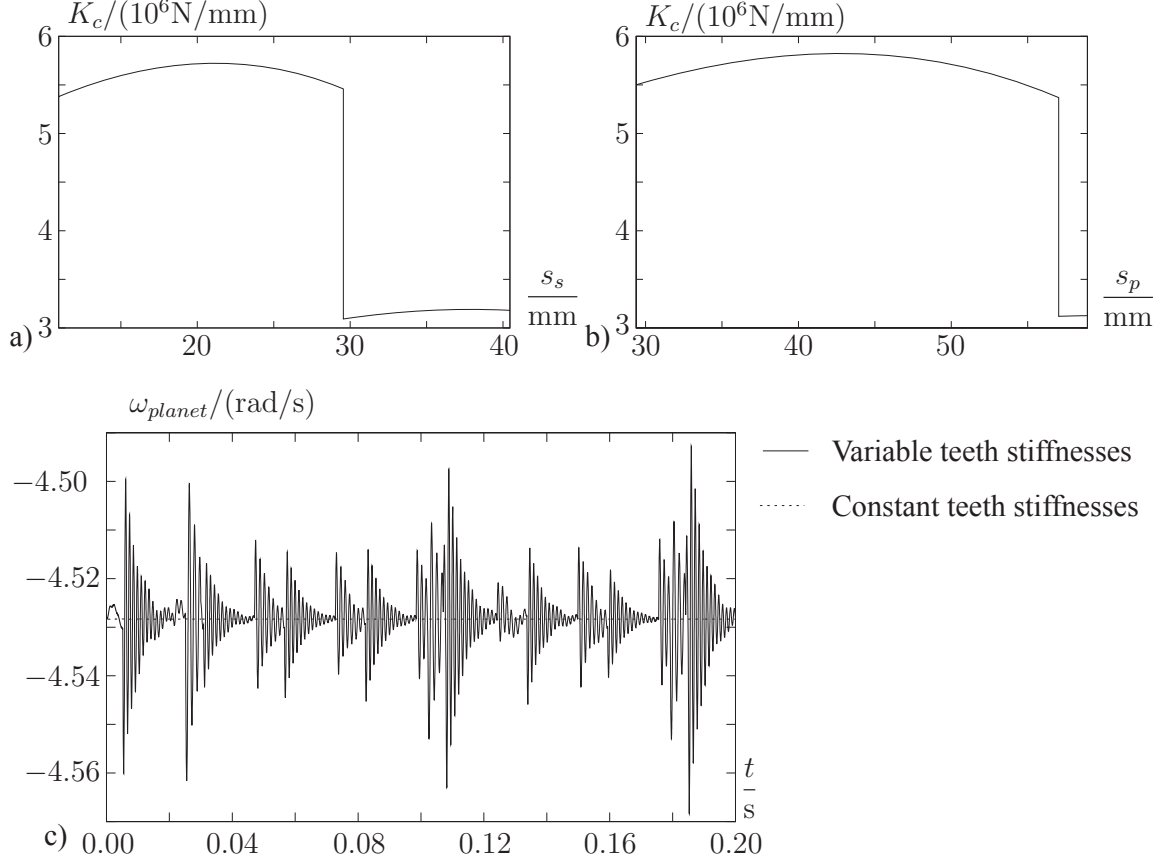


**Figure 19:** a) Mesh stiffness of the sun/planet gear contact. b) Mesh stiffness of the planet/ring gear contact. c) Angular speed of planet gear when applying constant meshing stiffness and when using the stiffnesses shown in a) and b). A zoom of the angular speed variation using constant stiffness is shown in Figure 20.

In Figure 20 the result for constant meshing stiffness is shown alone. The influence from the true stiffness compared to a constant stiffness is seen directly. From the figures we see that the variation in the angular speed is damped out if constant stiffness is used whereas for the real stiffness variation we see abrupt changes each time there is a discontinuity in the meshing stiffness, i.e. the jump in the stiffness of each gear contact is the source for the transient response seen in Figure 19c.

## 5 Conclusion

The paper presents a method for estimating the stiffness of individual gear teeth as a function of the contact point position. The stiffness evaluation is performed using FE analysis, and the stiffness is evaluated using the elastic energy and the applied load. By using the elastic energy

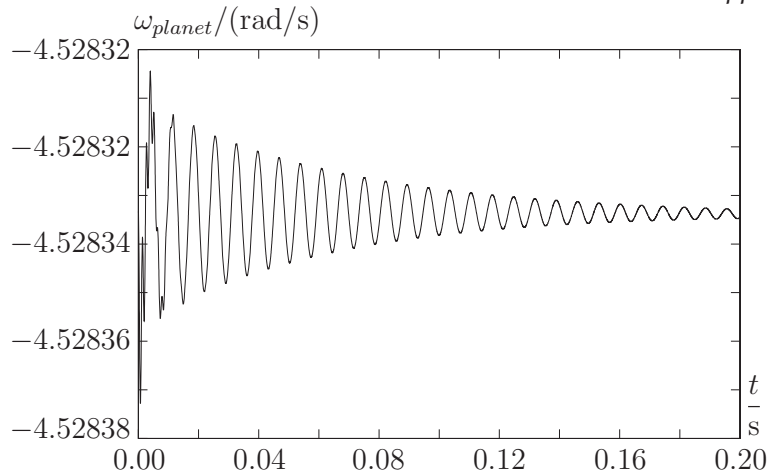


**Figure 20:** Angular speed of planet gear with constant gear teeth stiffnesses.

a consistent stiffness evaluation is possible without the use of displacement. Two factors are found to have a major influence on the stiffness value. The gear rim thickness must be included for estimating the teeth stiffnesses. The load size should also be included because the load size influences the contact length (Hertzian theory), and the contact length has a direct influence on the stiffness. With an increased rim thickness the stiffness is reduced while an increased contact length increases the stiffness. In the present paper we have selected a given value for the contact length and hereby neglected the non-linear effect coming from the load size.

The full gear tooth geometries are used in the FE calculations, and a parametric tooth shape derivation is presented. The FE analysis shows that a model including the gear rim and a single tooth attached to the rim is sufficiently accurate for finding the tooth stiffness.

With the individual teeth stiffnesses in a gear mesh found the overall meshing stiffness can be found. The individual teeth stiffnesses are found in all cases to be almost linear when expressed in the involute arc length of the teeth. This leads to rather simple expressions for the meshing stiffness. The paper ends with a multibody simulation example of a wind turbine planetary gearbox. The meshing stiffness discontinuous nature is found to have a non-negligible influence on the simulations.

### Acknowledgment

For discussions and suggestions we wish to thank Prof. Peder Klit and Prof. Pauli Pedersen. The funding for Martin F. Jørgensen through DSF-09-071588 (Dynamic wind turbine model - from wind to grid) is highly appreciated.

### References

- [1] P. Ziegler, P. Eberhard, and B. Schweizer. Simulation of impacts in geartrains using different approaches. *Archive of Applied Mechanics*, 76(9-10):537–548, 2006.
- [2] S. Ebrahimi and P. Eberhard. Rigid-elastic modeling of meshing gear wheels in multibody systems. *Multibody System Dynamics*, 16(1):55–71, 2006.
- [3] DIN 867. Basic rack tooth profiles for involute teeth of cylindrical gears for general engineering and heavy engineering (German standard). 1986.

- [4] ISO 6336-1. Calculation of load capacity of spur and helical gear - part1: Basic principles, introduction and general influence factors (International standard). 1996.
- [5] N. L. Pedersen. Reducing bending stress in external spur gears by redesign of the standard cutting tool. *Structural and Multidisciplinary Optimization*, 38(3):215–227, 2009.
- [6] N. L. Pedersen. Improving bending stress in spur gears using asymmetric gears and shape optimization. *Mechanism and Machine Theory*, 45(11):1707–1720, 2010.
- [7] M. H. Arafa and M. M. Megahed. Evaluation of spur gear mesh compliance using the finite element method. *Proceedings of the Institution of Mechanical Engineers Part K-Journal of Mechanical Engineering Science*, 213(6):569–579, 1999.
- [8] N. L. Pedersen and P. Pedersen. On prestress stiffness analysis of bolt-plate contact assemblies. *Archive of Applied Mechanics*, 78(2):75–88, 2008.
- [9] N. L. Pedersen and P. Pedersen. Stiffness analysis and improvement of bolt-plate contact assemblies. *Mechanics Based Design of Structures and Machines*, 36(1):47–66, 2008.
- [10] N. L. Pedersen and P. Pedersen. Bolt-plate contact assemblies with prestress and external loads: Solved with super element technique. *Computers & Structures*, 87(21-22):1374–1383, 2009.
- [11] J. I. Pedrero, M. Pleguezuelos, M. Artés, and J. A. Antona. Load distribution model along the line of contact for involute external gears. *Mechanism and Machine Theory*, 45(5):780–794, 2010.
- [12] C. Tsay. Helical gears with involute shaped teeth: geometry, computer simulation, tooth contact analysis, and stress analysis. *Journal of Mechanisms, Transmissions, and Automation in Design*, 110(4):482–491, 1988.
- [13] C. R. M. Rao and G. Muthuveerappan. Finite element modelling and stress analysis of helical gear teeth. *Computers & structures*, 49(6):1095–1106, 1993.
- [14] F. L. Litvin, J. S. Chen, J. Lu, and R. F. Handschuh. Application of finite element analysis for determination of load share, real contact ratio, precision of motion, and stress analysis. *Journal of Mechanical Design, Transactions of the ASME*, 118, number =, 1996.
- [15] Y. Zhang and Z. Fang. Analysis of tooth contact and load distribution of helical gears with crossed axes. *Mechanism and Machine Theory*, 34(1):41–57, 1999.
- [16] J. Hedlund and A. Lehtovaara. A parameterized numerical model for the evaluation of gear mesh stiffness variation of a helical gear pair. *Proceedings of the Institution of Mechanical Engineers, Part C: Journal of Mechanical Engineering Science*, 222(7):1321–1327, 2008.
- [17] S. Li. Effect of addendum on contact strength, bending strength and basic performance parameters of a pair of spur gears. *Mechanism and Machine Theory*, 43, number =, 2008.
- [18] A. Al-Shyyab and A. Kahraman. A non-linear dynamic model for planetary gear sets. *Proceedings of the Institution of Mechanical Engineers, Part K (Journal of Multi-Body Dynamics)*, 221(4):567–576, 2007.

- [19] M. Haastrup, M. R. Hansen, M. K. Ebbesen, and O. Ø. Mouritsen. Modeling and parameter identification of deflections in planetary stage of wind turbine gearbox. *Modeling, Identification and Control*, 33(1):1–11, 2012.
- [20] M. F. Jørgensen, N. L. Pedersen, J. N. Sørensen, and U. S. Paulsen. Multibody drivetrain model of a 500 kW wind turbine for predicting gear tooth stresses in a planetary gearbox. *Wind Energy*, 2013. online.
- [21] COMSOL AB. Stockholm, www.comsol.se, 1998-2009.
- [22] M. R. Letaief, F. Chaari, and M. Haddar. Influence of internal gears rim thickness and design on gearmesh stiffness. *International Review of Mechanical Engineering*, 1(1):62–67, 2008.
- [23] DIN 748 Blatt 1. Zylindrische wellenenden (German standard). 1970.

## Appendix

As shown in [5, 6] for any curve defined in parametric form as

$$x = M \cdot f(t) \quad (31)$$

$$y = M \cdot g(t) \quad (32)$$

where  $M$  is the tooth module, we may find the corresponding resulting shape on the gear. The derivation is repeated here for completeness. The  $x$  and  $y$  coordinates refers to the coordinate system of Figure 1.

The resulting gear form can be found from the envelope of these curve segments. Rotating and translating the curve segments around the gear blank gives the parameterization

$$\begin{Bmatrix} x(t, \theta) \\ y(t, \theta) \end{Bmatrix} = M \begin{bmatrix} \cos(\theta) & -\sin(\theta) \\ \sin(\theta) & \cos(\theta) \end{bmatrix} \begin{Bmatrix} f(t) - \theta \cdot z/2 \\ g(t) - z/2 - p_s \end{Bmatrix} \quad (33)$$

where  $z$  is the number of teeth and  $p_s$  is a possible profile shift factor, the boundaries for  $t$  depends on the curve segment. The parameterization (33) is a set of curves controlled by two parameters,  $t$  which describes the position along the curve and  $\theta$  that describes the curve translation and rotation. The envelope of (33) is determined by differentiating (33) with respect to  $t$  and  $\theta$  and demanding that these two vectors are aligned, i.e., that

$$\frac{dx(t, \theta)}{d\theta} \frac{dy(t, \theta)}{dt} - \frac{dy(t, \theta)}{d\theta} \frac{dx(t, \theta)}{dt} = 0 \quad (34)$$

By solving (34),  $\theta(t)$  is determined as a function of  $t$ . We find

$$\theta(t) = \frac{2}{z} \left( \frac{g'(t)}{f'(t)} (g(t) - p_s) + f(t) \right) \quad (35)$$

where  $g'(t)$  and  $f'(t)$  are the derivative with respect to  $t$ . This function can then be put back into (33) to describe the envelope analytically in parametric form.

For a straight cutting tool segment that lies between the two points  $(x_1M, y_1M)$  and  $(x_2M, y_2M)$  we have

$$f(t) = (1-t)x_1 + tx_2, \quad f'(t) = x_2 - x_1, \quad t \in [0 : 1] \quad (36)$$

$$g(t) = (1-t)y_1 + ty_2, \quad g'(t) = y_2 - y_1, \quad t \in [0 : 1] \quad (37)$$

this gives

$$\theta(t) = \frac{2}{z} \left( \frac{y_2 - y_1}{x_2 - x_1} ((1-t)y_1 + ty_2 - p_s) + (1-t)x_1 + tx_2 \right), \quad t \in [0 : 1] \quad (38)$$

The remaining cutting tool segments are the arc of a circle and singular points. For an arc segment with a radius  $r_A$  and a center  $(x_{AC}, y_{AC})$  we have

$$f(t) = x_{AC} + r_A \cos(t), \quad f'(t) = -r_A \sin(t), \quad t \in [\alpha_s, \alpha_e] \quad (39)$$

$$g(t) = y_{AC} + r_A \sin(t), \quad g'(t) = r_A \cos(t), \quad t \in [\alpha_s, \alpha_e] \quad (40)$$

this gives

$$\theta(t) = \frac{2}{z} (-\cot(t)(y_{AC} - p_s) + x_{AC})), \quad t \in [\alpha_s, \alpha_e] \quad (41)$$

For a point  $(x_p, y_p)$  we directly have

$$\begin{Bmatrix} x(t) \\ y(t) \end{Bmatrix} = M \begin{bmatrix} \cos(t) & -\sin(t) \\ \sin(t) & \cos(t) \end{bmatrix} \begin{Bmatrix} x_p - t \cdot z/2 \\ y_p - z/2 - p_s \end{Bmatrix} \quad (42)$$

The entire gear contour is now determined from the different envelopes of the curve cutting tool curve segments. The presented gear boundary derivation in analytical form can be applied to any tool design; if the segments are given by analytical functions, i.e.  $f(t)$  and  $g(t)$ , then the gear boundary is also given analytically by the use of (33) and (35).

## Publication [P3]

Comparison and implementation of a Rigid and a Flexible Multibody Planetary Gearbox Model

# Comparison and implementation of a Rigid and a Flexible Multibody Planetary Gearbox Model

Jørgensen, M. F. Dep. of Mech. Eng. Solid Mechanics Lyngby, 2800 Denmark	Pedersen, N. L. Dep. of Mech. Eng. Solid Mechanics Lyngby, 2800 Denmark	Sørensen, J. N. Dep. of Wind Energy Fluid Mechanics Lyngby, 2800 Denmark
--	---	--

## Abstract

*We propose algorithms for developing (1) a rigid (constrained) and (2) a flexible planetary gearbox model. The two methods are compared against each other and advantages/disadvantages of each method are being discussed. The rigid model (1) has gear tooth reaction forces expressed by Lagrange multipliers. The flexible approach (2) is being compared with the gear tooth forces from the rigid approach, first without damping and second the influence of damping is examined. Finally, variable stiffness as a function of base circle arc length is implemented in the flexible approach such that it handles the realistic switch between one and two gear teeth in mesh. This improvement is then tested on a realistic planetary gearbox in a 500 kW wind turbine [15] with profile shift. It can be concluded that both approaches are fully usable.*

## 1 Introduction

Many researchers/engineers consider not only the gearbox itself but also the system it is part of. Of particular increasing interest are wind turbine gearboxes, because new wind turbines are large and gearboxes are one of the most expensive and critical components. By analysing the whole drivetrain as a system, it is possible to simulate the dynamics of bearings, gear wheels, shafts and generators, i.e. stators and rotors. In [21] three types of multibody wind turbine drivetrain models have been implemented using the multibody software package DADS. It is found that adding bearing flexibility is important for an accurate prediction of the eigenfrequencies.

The disadvantage of modelling a large system, i.e. the whole drivetrain or even the dynamics of the whole windturbine, is that the complexity increases. Modelling large systems should not be an issue, when using most commercial multibody software tools. The commercial multibody software package Adams/View (MSC software) is used in [8] to investigate best practices for gearbox bushings in wind turbine drive-trains. Other people combine their own gear programs into commercial tools. This approach is made in [22, 10] where an aeroelastic tool is used to model a bigger system, i.e. a whole wind turbine including flexibility of the blades and tower with turbulent inflow.

In this article we present algorithms that are implemented in Matlab and can therefore serve as inspiration to others. Focus is on the planetary gearbox without modelling the system it is part of, i.e. how the gearbox is connected to motors/generators etc. The models are presented with results using simplified and realistic loads. For the latter, we look at a planetary gearbox of a 500 kW wind turbine and use loads calculated by the aeroelastic and industry-accepted tool FLEX5 [28]. For additional details of the experimental validation of this particular 500 kW gearbox, including the rigid multibody approach, see [15].

### 1.1 Multibody modelling

Introductions to the field of planar and spatial multibody dynamics are given in [18, 23, 11, 7, 1]. A mechanical system is defined in [18] as a collection of bodies or links, which relate one body to



the other. Bodies in these systems are connected by joints and/or force elements like actuators, springs and dampers. Mechanics is defined as the branch of analysis which involves the study of motion, time and forces on objects. The classical approach to solving the equations of motion for a constrained mechanical system is to solve equations for an index 3 Differential Algebraic Equation (DAE) system (see e.g. [9]). The  $n$  differential equations coupled with  $m$  algebraic equations is written

$$\begin{cases} \mathbf{M}\ddot{\mathbf{q}} - \Phi_{\mathbf{q}}^T \boldsymbol{\lambda} = \mathbf{g}, & \Phi_{\mathbf{q}} = \frac{\partial \Phi}{\partial \mathbf{q}} \\ \Phi(\mathbf{q}, t) = \mathbf{0} \end{cases} \quad (1)$$

Where  $\mathbf{M} \in \mathbb{R}^{n \times n}$  is the mass/inertia matrix,  $\mathbf{q} \in \mathbb{R}^n$  is a vector of cartesian coordinates,  $\Phi_{\mathbf{q}} \in \mathbb{R}^{m \times n}$  is the Jacobian of the  $\Phi(\mathbf{q}, t) \in \mathbb{R}^m$  kinematic constraint equations,  $\boldsymbol{\lambda} \in \mathbb{R}^m$  are the Lagrange multipliers and  $\mathbf{g} \in \mathbb{R}^n$  are the external body forces applied in the global reference system, affecting the origin of the local coordinate system of corresponding bodies.

The local coordinate system is usually located in the center of mass, because this is a straightforward way to ensure a time-independent constant inertia/mass matrix. The vector  $\Phi(\mathbf{q}, t)$  is a symbol of general rheonomous constraints because at least one of the constraints is explicitly time-dependent. Geometrical constraints are used to fix the gears of the planetary gearbox, hence  $\Phi(\mathbf{q}) = \mathbf{0}$ , which are scleronomous or time-independent. An example of a gear constraint for external gears is

$$\Phi^{\text{gear}} \equiv \rho_i \dot{\theta}_i + \rho_j \dot{\theta}_j = 0 \quad (2)$$

where the radii for gear wheel pairs  $i$  and  $j$  is given by  $\rho$  and  $\dot{\theta}$  denotes the angular velocity of both gear wheels [18]. However, this constraint does not provide any realistic reaction forces because there's no coupling to translational degrees-of-freedom (DOF). Both methods described in this article provide a realistic coupling between rotational (for transforming the torque between bodies) and translational DOFs.

In case of position constraint violations, different techniques have been proposed in the litterature, e.g. [18, 26, 12]. One method is to use general coordinates classification / coordinate partitioning methods (manual/automatic) [25]. The numerical error is reduced by only performing numerical integration for the independent coordinates. After this step, the dependent coordinates are solved using e.g. Newton-Raphson. This is generally very slow. Another method is to use an extension of feedback control theory which modifies open-loop system equations such as  $\ddot{\mathbf{y}} = \mathbf{0}$  to closed-loop system equations such as  $\ddot{\mathbf{y}} + 2\alpha\dot{\mathbf{y}} + \beta^2\mathbf{y} = \mathbf{0}$  where  $\alpha$  and  $\beta$  are positive constants [4]. This approach is known as Baumgarte stabilization. The method is not perfect, but solves the problem to a certain extent and is relatively easy to implement.

Various techniques for solving (1) were developed and are described by many authors in e.g. [18, 2, 14, 6]. Constraints are expressed at acceleration level, to form equations of motion from the DAE-system (1) into an ODE in the form given by [18]:

$$\begin{bmatrix} \mathbf{M} & -\Phi_{\mathbf{q}}^T \\ \Phi_{\mathbf{q}} & \mathbf{0} \end{bmatrix} \begin{Bmatrix} \ddot{\mathbf{q}} \\ \boldsymbol{\lambda} \end{Bmatrix} = \begin{Bmatrix} \mathbf{g} \\ \gamma - 2\alpha\dot{\Phi} - \beta^2\Phi \end{Bmatrix} \quad (3)$$

The Baumgarte stabilization terms  $\alpha$  and  $\beta$  are included, but can be ignored if there are negligible constraint violations. In this work  $\alpha = \beta = 0$ . By a proper selection of initial position, velocity ( $\mathbf{q}, \dot{\mathbf{q}}$ ), constraints ( $\Phi$ ) and forces and moments on the right-hand-side (RHS), the equation system (3) can be solved for the accelerations  $\ddot{\mathbf{q}}$ . A time-integration scheme such as e.g. Runge-Kutta can then yield the velocity- and position- vector of coordinates ( $\mathbf{q}, \dot{\mathbf{q}}$ ) for all timesteps.

## 2 Methods

Both rigid and flexible multibody dynamics are specifically concerned with analysis of bodies undergoing large displacements (both rigid body motion and elastic deformations). For general formulations of flexible multibody systems see [24, 7] and references therein.

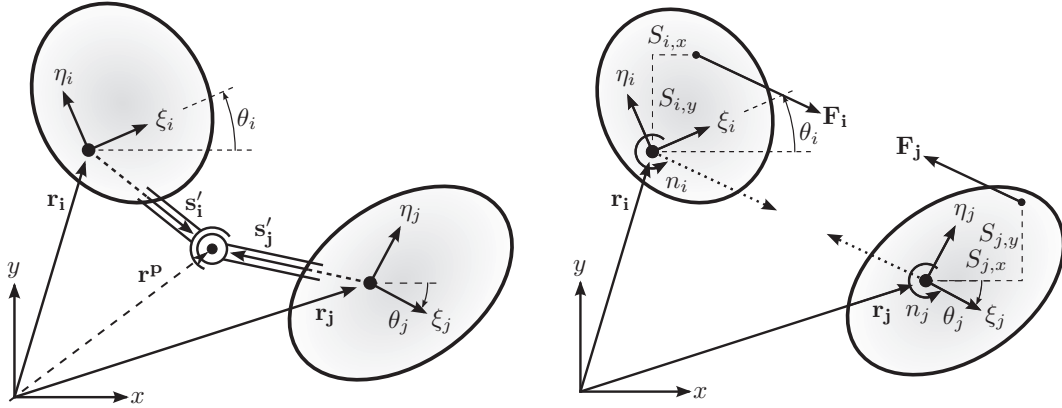
The following illustrates how to calculate the length between points from two different objects/-bodies, using two different local coordinate systems  $i$  and  $j$ :

$$\mathbf{l} = \mathbf{r}_j + \mathbf{A}_j \mathbf{s}'_j - \mathbf{r}_i - \mathbf{A}_i \mathbf{s}'_i \quad \mathbf{A}_{2D} = \begin{bmatrix} \cos \theta & -\sin \theta \\ \sin \theta & \cos \theta \end{bmatrix} \quad \mathbf{A}_{3D} = [\mathbf{x} \quad \mathbf{y} \quad \mathbf{z}] \quad (4)$$

where  $\mathbf{r}$  is a vector in the global system to the local coordinate system,  $\mathbf{A}$  is a transformation matrix from local to global coordinates and  $\mathbf{s}'$  is a vector in the local coordinate system. The primed vectors are all in the local coordinate system, e.g.  $\boldsymbol{\omega}'$  and vectors without a prime, e.g.  $\boldsymbol{\omega}$ ,  $\mathbf{r}$  or  $\mathbf{s}$  are defined in the global coordinate system. The full transformation matrix in 2D is explicitly shown due to its simplicity. In 3D the expression for obtaining the coordinates of the matrix  $\mathbf{A}_{3D}$ , depends on the parameterization used, e.g. Euler parameters (quaternions), Euler angles or Bryant angles etc. Only the orthogonal unit vectors  $(\mathbf{x}, \mathbf{y}, \mathbf{z})$  are shown in the 3D transformation matrix and these unit vectors can be obtained with different algorithms, see e.g. [18].

## 2.1 Connecting bodies, rigidly and flexibly

With a kinematical description of a joint, i.e. using a constraint formulation, no flexibility exists in the joint and the joint acts as a rigid connection. But if the constraint (Figure 1a) is removed and replaced by a force pair (Figure 1b) then the effect of how e.g. springs and dampers affect the two connecting bodies can be programmed. The mathematically most simple joint between bodies  $i$  and  $j$  is a spherical joint, which is illustrated in Figure 1a and described as  $\Phi^s : \mathbf{r}_i + \mathbf{A}_i \mathbf{s}'_i - \mathbf{r}_j - \mathbf{A}_j \mathbf{s}'_j = \mathbf{0}$ . The constraint equations ensures that two points measured from body  $i$  and  $j$  coordinate systems coincide because  $\mathbf{l} = \mathbf{0}$ . From optimization theory, Farkas lemma guarantees the existence of Lagrange multipliers  $\boldsymbol{\lambda}$  [3] which can also be interpreted as fictive forces or moments. The spherical joint can be transformed into a flexible connection by removing the joint and replacing it with a force element.



(a) Spherical joint: A rigid/constrained connection. At the joint,  $\mathbf{l} = \mathbf{0}$ , see equation (4). The angle  $\theta$  is measured from global  $(x, y)$  to local reference of frame  $(\xi, \eta)$ .

(b) Joint removed and added a force element (spring, damper or actuator). Bodies  $i$  and  $j$  are pulled towards each other by the forces  $\mathbf{F}_i$  and  $\mathbf{F}_j$ , acting at a distance of  $\mathbf{s}_i$  and  $\mathbf{s}_j$ .

Figure 1: Illustration of difference between a rigid and a flexible connection for bodies  $i$  and  $j$ .

When a rigid multibody model is changed into a model where some of the constraints are formulated by use of force elements (springs/dampers/actuators), the idea is to remove constraints from  $\Phi$  and instead formulate equations that explicitly describe the forces or moments acting on the affected bodies. This reduces the number of rows in  $\Phi_q$  and  $\boldsymbol{\lambda}$ . Replacing constraints with force element contributions means that the  $\mathbf{g}$ -vector in (3) is modified. For instance body  $i$  could have an external force vector of  $\mathbf{g}_i = [f_x, f_y, n]^T_i$  where  $f_x$  and  $f_y$  is the sum of horizontal and vertical external body forces, while  $n$  is the sum of moments. A force element as shown in Figure 1b can be inserted by changing the external force vector, e.g.  $\mathbf{g}_i = [f_x + F_{i,x}, f_y + F_{i,y}, n - s_{i,y}F_{i,x} + s_{i,x}F_{i,y}]^T_i$ , which could be illustrated by either inserting a translational actuator, a spring or a damper. The forces  $\mathbf{F}_i$

and  $\mathbf{F}_j$  are in that way moved to the center of the local reference of frame together with the torque which is calculated as:  $\mathbf{n} = \mathbf{s} \times \mathbf{F}$ . Extending the formulation to include element/body flexibility is described in e.g. [20, 23]. Another description of flexibility effects in multibody systems is given in e.g. [13], which describe approaches for connecting rigid bodies for elastic straight and taper segments subject to extension, torsion and bending.

### 2.1.1 Implementation details of using force pairs

If a spring is inserted between the two bodies, the corresponding joint constraint should obviously be removed. The individual extra RHS force contribution to the  $\mathbf{g}$ -vector in (3) becomes the scalar value of  $\Delta\mathbf{F} = k(\mathbf{l} - \mathbf{l}_0)$ , where  $\mathbf{l}$  is the deformed spring length cf. Equation (4),  $\mathbf{l}_0$  is the undeformed spring length and  $k$  is the spring stiffness. Body  $i$  and  $j$  would sense the opposite force of each other as shown in Figure 1. Rigid spherical or revolute joint connections between bodies can be transformed into flexible damper/spring connections using the approach described above. The damping force is  $\Delta\mathbf{F} = d\dot{\mathbf{l}}$  where  $d$  is the scalar damping coefficient and the derivative of the length calculated from Equation (4) is

$$\begin{aligned}\dot{\mathbf{l}}_{2D} &= \dot{\mathbf{r}}_j + \dot{\theta}_j \mathbf{B}_j \mathbf{s}'_j - \dot{\mathbf{r}}_i - \dot{\theta}_i \mathbf{B}_i \mathbf{s}'_i & \text{where: } \mathbf{B} &= \begin{bmatrix} -\sin \theta & -\cos \theta \\ \cos \theta & -\sin \theta \end{bmatrix} \\ \dot{\mathbf{l}}_{3D} &= \dot{\mathbf{r}}_j + \tilde{\omega}_j \mathbf{A}_j \mathbf{s}'_j - \dot{\mathbf{r}}_i - \tilde{\omega}_i \mathbf{A}_i \mathbf{s}'_i & \text{where: } \omega &= \mathbf{A} \omega' = \mathbf{A} \{\omega_\xi \ \omega_\eta \ \omega_\zeta\}^T\end{aligned}\quad (5)$$

The skew-symmetric matrix of a vector is a  $3 \times 3$ -matrix and for  $\omega$  it is  $\tilde{\omega}$ . A useful method of calculating the cross product between two vectors is to multiply the skew-symmetric matrix of the first vector with the second vector, e.g.  $\tilde{\omega} \mathbf{s} = \omega \times \mathbf{s}$ . The skew-symmetric matrix for e.g. the vector of local angular velocities  $\omega'$  is

$$\tilde{\omega}' = \begin{bmatrix} 0 & -\omega_\zeta & \omega_\eta \\ \omega_\zeta & 0 & -\omega_\xi \\ -\omega_\eta & \omega_\xi & 0 \end{bmatrix} \quad (6)$$

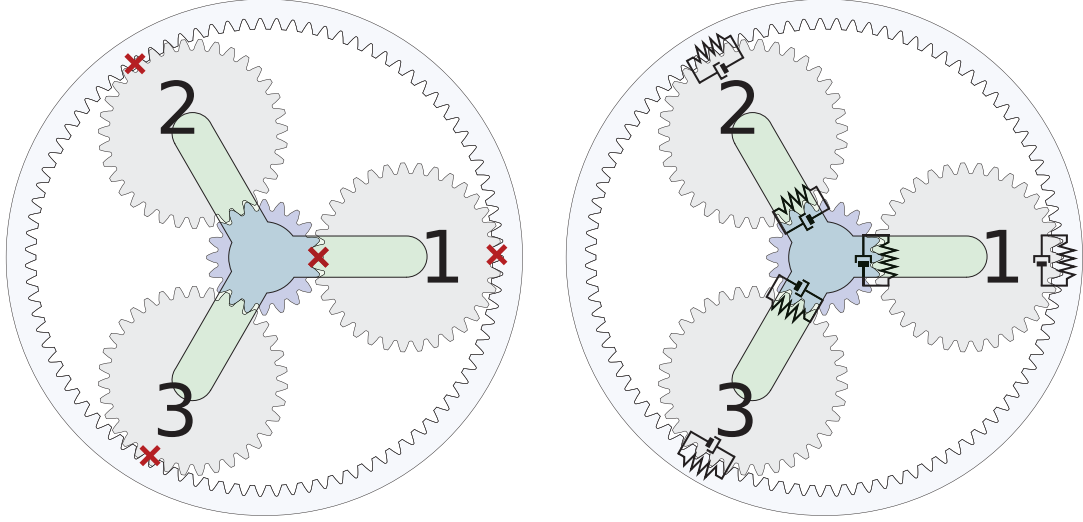
### 2.1.2 Constraints used for both models

Consider Figure 2 which shows the two fundamentally different approaches in this article for constructing a multibody planetary gearbox model with realistic reaction forces. The rigid approach works using Lagrange multipliers (i.e. constraints) and the flexible approach works by using linear springs and dampers with details described in section 2.3. Linear in the sense that the gear tooth penetration depth is measured along a line acting normal to the tooth surface.

The constraints which constitute the kinematic/geometric/algebraic equations of the model must rigidly connect bodies and ensure that: The center of most bodies is fixed to either the ground, i.e. sun, ring and carrier or to another body i.e. the planets. The planetary carrier connects ground with other objects such as the planets themselves. When more than two planets are used, the center of the planetary carrier is also the center of mass of the sun or the ring gear (these mass centers are coinciding). For only a single planet, the carrier is modelled simply as a bar with one end fixed to the global coordinate system origin while the other end is fixed to the planet. The mass center for a carrier connecting only a single planet will be in the middle of the endpoints of the carrier. Gear constraints make the wheels in the planetary gearbox rotate correctly. Focus in this article is on comparing the two different approaches for modelling a planetary gearbox.

## 2.2 Rigid model

Figure 2 shows two versions of a 6-body multibody model, i.e. consisting of sun, ring, 3 planetary gears and a planetary carrier. With 3 coordinates per body (2D) there are 18 DOF and with 6 coordinates per body (3D) there are 36 DOF. All 6 bodies are fixed at their mass center to either ground or to the planetary carrier. In 2D this require 12 equations and in 3D it require 30 constraint equations. In addition the ring gear cannot rotate. Left is 5 DOFs but with 4 gear constraints it means that once torque is applied to either body, all bodies will behave appropriately.



(a) Rigid planetary gearbox model with 4 gear constraints and 1 rotational DOF. Planet 1 transfers torque to/from the sun gear. Planets 2 and 3 can only have 1 gear constraint (either to sun or to ring gear) to prevent an over-constrained system.

(b) Flexible planetary gearbox model – all planets are “active”. For illustrative purposes, the spring and damper is shown in the tangential direction. This is merely a projection of the real spring tooth forces which work in the tooth normal direction.

Figure 2: Difference between rigid and flexible 6-body multibody planetary gearbox model.

The gear tooth normal, radial and tangential forces are shown in Figure 3a, which also shows the path of contact as the tangent between two base circles (the green line). When two gear teeth mesh the distance from gear centers to anywhere on the contact line, varies along the yellow line. The gear loads depend on the transmitted torque and base radius.

Both illustrations in Figure 3 show that as the contact point (red dot in the illustrations) moves, the radii to the contact point continuously change. Despite that the radii of the contact point change, a fundamental property of involute gears is that the normal gear tooth force is always the torque divided by the base gear radius  $\rho_b$ , i.e.  $F_n = M/\rho_b$ .

The effect of vibrations, size of teeth, material errors, lubrication, number of teeth in mesh at the same time etc [16] have no influence in this model. One could also argue that contact ratio should be implemented as a factor that reduces the gear tooth loads, because the contact ratio is defined as the average number of teeth in mesh at the same time. But this has not been the focus area here.

### 2.2.1 Description of rigid gear constraint

The problem when modelling a planetary gearbox with the simple gear constraint (2) is that only the torque is transferred through the rotational coordinates. There is lack of gear tooth forces, thus no physical reaction force contribution exists in  $\lambda$ , only torque. By considering an idealized gear, the constraint (2) is changed into the following non-holonomic gear constraint

$$(\mathbf{A}_n \mathbf{v}_r)^T [(\dot{\mathbf{r}}_i + \rho_i \mathbf{A}_i \tilde{\omega}_i' \mathbf{v}_r) - (\dot{\mathbf{r}}_j - \rho_j \mathbf{A}_j \tilde{\omega}_j' \mathbf{v}_r)] = 0 \quad (7)$$

where  $\mathbf{v}_r$  is a unit vector between the center of both gears (see Figure 3b),  $\mathbf{A}_n$  is a transformation matrix (see (4)) that depends on direction of rotation (CW/CCW) such that the matrix product  $(\mathbf{A}_n \mathbf{v}_r)$  becomes a unit vector in the tooth surface normal direction as shown in Figure 3b. The gear constraint (7) is a dot product between a projection direction vector and a velocity vector of the red tooth contact point shown in Figure 3. This constraint equation gives a reaction force contribution because it includes all translational and rotational coordinates of involved bodies. It also has a physical meaning in the tooth surface normal direction. The constraint equation (7) is written completely out for 2D:

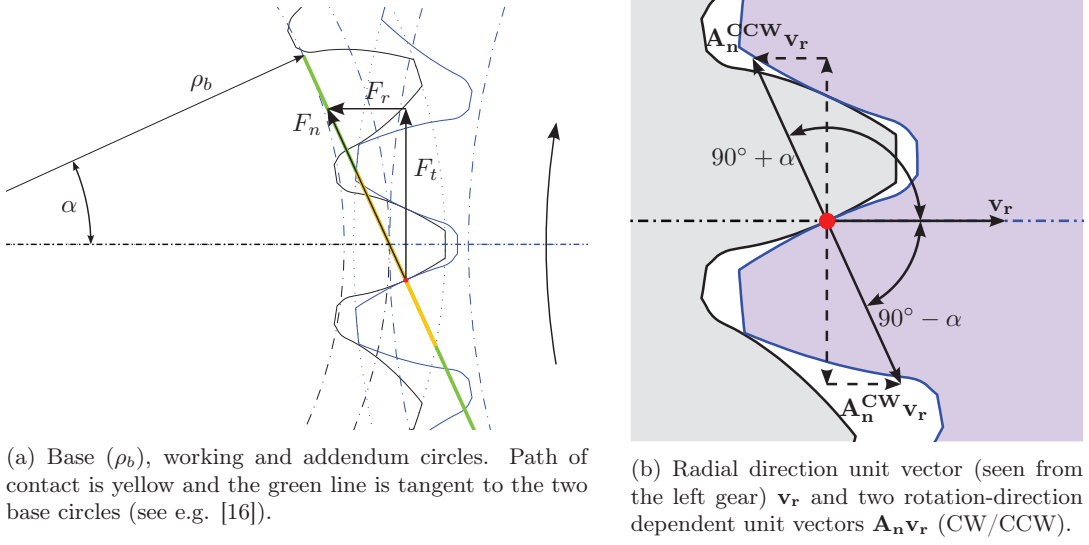


Figure 3: Illustration of gear tooth force components  $F_n$ ,  $F_r$  and  $F_t$ , pressure angle  $\alpha$  etc.

$$\dot{\Phi}_{2D} : (\mathbf{A}_n \cdot \mathbf{v}_r)^T \left[ \left( \begin{Bmatrix} \dot{x}_i \\ \dot{y}_i \end{Bmatrix} + \rho_i (\omega_i \hat{\mathbf{v}}_r) \right) - \left( \begin{Bmatrix} \dot{x}_j \\ \dot{y}_j \end{Bmatrix} - \rho_j (\omega_j \hat{\mathbf{v}}_r) \right) \right] = 0 \quad (8)$$

where the unknown translational coordinates are  $x, y$  and the rotational coordinate is  $\omega$  while  $\hat{\mathbf{v}}_r$  is a rotated tangential unit vector. If the tangential unit vector  $\mathbf{v}_r = \{v_x, v_y\}^T$  is rotated  $90^\circ$  it becomes  $\hat{\mathbf{v}}_r = \{-v_y, v_x\}^T$ . In 3D we have

$$\dot{\Phi}_{3D} : (\mathbf{A}_n \mathbf{v}_r)^T \left[ \left( \begin{Bmatrix} \dot{x}_i \\ \dot{y}_i \\ \dot{z}_i \end{Bmatrix} + \rho_i \mathbf{A}_i \begin{Bmatrix} \omega_\xi^i \\ \omega_\eta^i \\ \omega_\zeta^i \end{Bmatrix} \times \mathbf{v}_r \right) - \left( \begin{Bmatrix} \dot{x}_j \\ \dot{y}_j \\ \dot{z}_j \end{Bmatrix} - \rho_j \mathbf{A}_j \begin{Bmatrix} \omega_\xi^j \\ \omega_\eta^j \\ \omega_\zeta^j \end{Bmatrix} \times \mathbf{v}_r \right) \right] = 0 \quad (9)$$

It is easy to see that both for a 2D case with DOF for  $(\dot{x}, \dot{y}, \omega)$  as well as for a 3D case with DOF for  $(\dot{x}, \dot{y}, \dot{z}, \omega_\xi, \omega_\eta, \omega_\zeta)$ , all DOF's are involved.

### 2.2.2 Equations of motion

Equation (3) is solved for the accelerations  $\ddot{\mathbf{q}}$  in each timestep and it is seen that  $\Phi_q \ddot{\mathbf{q}} = \gamma$ . The Jacobian submatrix  $\Phi_q$  holds coefficients for the acceleration terms. It is therefore necessary to collect coefficients for  $\ddot{\mathbf{q}}$  into the Jacobian ( $\Phi_q$ ). By using  $\dot{\mathbf{v}} = \boldsymbol{\omega} \times \mathbf{v}$ , Equation (8) differentiated becomes

$$\begin{aligned} \ddot{\Phi}_{2D} : (\mathbf{A}_n \dot{\mathbf{v}}_r)^T (\dot{\mathbf{r}}_i + \rho_i \dot{\omega}_i \hat{\mathbf{v}}_r) + (\mathbf{A}_n \mathbf{v}_r)^T (\dot{\mathbf{r}}_i + \rho_i \dot{\omega}_i \hat{\mathbf{v}}_r + \rho_i \omega_i \hat{\dot{\mathbf{v}}}_r) \\ - (\mathbf{A}_n \dot{\mathbf{v}}_r)^T (\dot{\mathbf{r}}_j - \rho_j \dot{\omega}_j \hat{\mathbf{v}}_r) - (\mathbf{A}_n \mathbf{v}_r)^T (\dot{\mathbf{r}}_j - \rho_j \dot{\omega}_j \hat{\mathbf{v}}_r - \rho_j \omega_j \hat{\dot{\mathbf{v}}}_r) = 0 \end{aligned} \quad (10)$$

Equation (9) differentiated is (maximum 1 skewmatrix above symbols is used for cross products)

$$\begin{aligned} \ddot{\Phi}_{3D} : (\mathbf{A}_n \mathbf{v}_r)^T (\dot{\mathbf{r}}_i + \rho_i [(\mathbf{A}_i \widetilde{\omega'_i} \omega'_i) \times \mathbf{v}_r + (\mathbf{A}_i \omega'_i) \times \mathbf{v}_r + (\mathbf{A}_i \omega'_i) \times \dot{\mathbf{v}}_r]) \\ - (\mathbf{A}_n \mathbf{v}_r)^T (\dot{\mathbf{r}}_j - \rho_j [(\mathbf{A}_j \widetilde{\omega'_j} \omega'_j) \times \mathbf{v}_r + (\mathbf{A}_j \omega'_j) \times \mathbf{v}_r + (\mathbf{A}_j \omega'_j) \times \dot{\mathbf{v}}_r]) \\ + (\mathbf{A}_n \dot{\mathbf{v}}_r)^T (\dot{\mathbf{r}}_i + \rho_i (\mathbf{A}_i \omega'_i) \times \mathbf{v}_r) - (\mathbf{A}_n \dot{\mathbf{v}}_r)^T (\dot{\mathbf{r}}_j - \rho_j (\mathbf{A}_j \omega'_j) \times \mathbf{v}_r) = 0 \end{aligned} \quad (11)$$

From these equations, LHS coefficients to the Jacobian matrix and RHS contributions to  $\gamma$  can be found.

### 2.3 Flexible model

All the rigid model constraints are kept in the flexible version of the multibody code except for the gear constraints that are removed. Body centers still need to be centered and fixed to each other correctly. This means that e.g. the planetary carrier is still fixed to planet gear wheel centers and sun/ring gear wheel centers are still fixed to the ground. All gear constraints are removed and replaced by force elements, as depicted in Figure 1. A linear spring and damper element is implemented as shown in Figure 4 and the objective is to find an algorithm that calculates  $\Delta F$  or the tangential projection of it, which multiplied by the radius  $\rho$  is the torque.

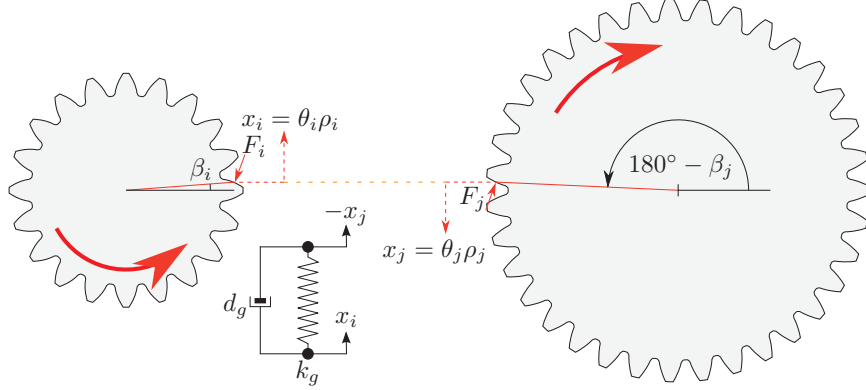


Figure 4: Illustration of spring  $k_g$  and damper  $d_g$  between two gears for a simplified spring/damper system. Gear tooth force is perpendicular to teeth surface.

#### 2.3.1 Description of force element algorithm in the flexible model

For every planet in a planetary gearbox (e.g. see Figure 2),  $\mathbf{g}_{s/p}$  contain the sun/planet gear tooth forces and moments and  $\mathbf{g}_{p/r}$  holds the planet/ring gear tooth forces and moments. Every pair of sun/planet and planet/ring forces and moments consists of spring and damper forces/moments such that  $\mathbf{g} = \mathbf{g}^0 + \mathbf{g}^k + \mathbf{g}^d$  where  $\mathbf{g}^0$  is the initial body forces and torque,  $\mathbf{g}^k$  is the forces and torque from springs and  $\mathbf{g}^d$  is the force and torque from dampers (in the global reference of frame). The total vector of external forces and moments for all bodies is modified such that  $\mathbf{g} = \mathbf{g}^0 + \sum_k \mathbf{g}_{s/p} + \mathbf{g}_{p/r}$  for  $k$  number of planets. This approach makes it easy to add/remove planets in a systematic way because the algorithm is generic and modular.

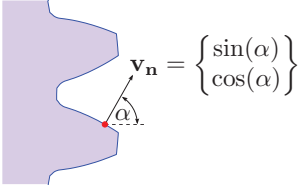
From Figure 4 it is seen that for a 1D spring and damper, forces are proportional to either a tangential distance interpreted as the penetration depth measured from the equilibrium position or to an angular velocity difference (the time derivative difference in rotation speeds). These equations have to be changed a bit, in order to calculate the forces in higher dimensions, i.e. a transformation matrix is added. A 2D model is sufficient to illustrate the concept as this can easily be implemented in a 3D model. First the tangential tooth penetration depth is found, then the time derivative difference is found and finally the spring and damping coefficients are multiplied and the force contributions are added together.

#### 2.3.2 Calculation of forces and moments

The driver/carrier angle  $\theta_d$  is the angle from the global  $x$ -axis to the local  $x$ -axis of the coordinate system for the first planet. This angle has a corresponding rotation matrix  $\mathbf{A}_d$ . Similarly,  $\mathbf{A}_{s/p}(\phi)$  is a transformation matrix for the angle from the center of the sun to the center of the current planet in mesh. Example: For the planetary gearbox in Figure 2, every sun/planet angle  $\phi$  in  $\mathbf{A}_{s/p}(\phi)$  is:  $\phi_1 = 0^\circ$ ,  $\phi_2 = 120^\circ$  and  $\phi_3 = 240^\circ$  (insert the angles in (4) to obtain each of the transformation matrices). There will be a loop that sums up all force contributions for all involved planets. The gear tooth penetration depth  $\mathbf{l}_p$  is now given by the projection

$$\mathbf{l}_p = \mathbf{A}_d \mathbf{A}_{s/p} \mathbf{v}_n [\rho_{b_i}(\theta_i - \theta_i^0 - \theta_d) + \rho_{b_j}(\theta_j - \theta_j^0 - \theta_d)], \quad (12)$$

where the unit tooth surface normal vector is:

$$\mathbf{v}_n = \begin{Bmatrix} \sin(\alpha) \\ \cos(\alpha) \end{Bmatrix} \quad (13)$$


Unit tooth surface normal vector.

Figure 5: Unit vector in the penetration direction as a function of gear tooth pressure angle  $\alpha$ .

In equation (12),  $\theta^0$  is the initial angle at  $t = 0$  seconds. Normally  $\theta^0 = 0^\circ$  and if this is not the case it means that the gear will start rotated in a position that is not the equilibrium position. Additionally,  $\rho_b$  is the base circle radius for the involved body. The penetration depth is associated with the stiffness properties (constant/linear/non-linear etc) of the gear(s). The “velocity difference” is associated with the damping properties of the gear(s) and can be written

$$\dot{\mathbf{l}}_p = \mathbf{A}_d \mathbf{A}_{s/p} \mathbf{v}_n [\rho_{b_i}(\omega_i - \omega_d) + \rho_{b_j}(\omega_j - \omega_d)] \quad (14)$$

The absolute forces in cartesian coordinates are proportional to the spring/damping coefficients so  $\mathbf{F}^k = k\mathbf{l}_p$  and  $\mathbf{F}^d = d\dot{\mathbf{l}}_p$ . Reaction forces are opposite of each other for bodies  $i$  and  $j$ .

**Torque** If  $\mathbf{v} = \begin{Bmatrix} x \\ y \end{Bmatrix}$  then  $\hat{\mathbf{v}} = \begin{Bmatrix} -y \\ x \end{Bmatrix}$  is the same vector rotated  $90^\circ$  CCW and the tangential direction is expressed as a function of the radial unit vector:  $\mathbf{v}_t = \hat{\mathbf{v}}_r$ . Therefore the scalar tangential gear tooth force is the dot product:  $F_t^{k+d} = \hat{\mathbf{v}}_r^T(\mathbf{F}^k + \mathbf{F}^d)$  and the absolute torque is  $M = \rho_w F_t$  where  $\rho_w$  is the working circle radii. For gear wheels  $i$  and  $j$  the change on the RHS,  $\mathbf{g}^{\text{Flex}} = \mathbf{g}^k + \mathbf{g}^d$  becomes

$$\mathbf{g}_i^{\text{Flex}} = \begin{Bmatrix} -k\mathbf{l}_p - d\dot{\mathbf{l}}_p \\ -\rho_{w_i} F_t^{k+d} \end{Bmatrix}, \quad \mathbf{g}_j^{\text{Flex}} = \begin{Bmatrix} k\mathbf{l}_p + d\dot{\mathbf{l}}_p \\ -\rho_{w_j} F_t^{k+d} \end{Bmatrix} \quad (15)$$

The equations (15) are calculated twice as many times as there are planets, i.e. both for the sun/planet and for the planet/ring connections and all the force contributions are added together.

## 2.4 Stiffness model with variable (multiple) teeth in mesh

The above assumptions rely on a simplification, where the multibody code knows nothing of the current number of gears in mesh since the stiffness is given as a constant. Improved realism and accuracy of the flexibly-connected model can be obtained by letting the stiffness be a function of the rotation angles of the gears. The stiffness coefficients of gear teeth are generally non-linear and a function of the point of contact and the size of the contact load, see e.g. [19]. The meshing stiffness is the combined stiffness of two gears in contact. The number of gear teeth pairs in contact is also changing, usually between one or two pairs in contact. This leads to discontinuities in the meshing stiffness. The point of contact on a gear tooth can be given as a function of the base circle arc length as shown in [19]. The base circle arc length  $s_1$  is also shown in Figure 6.

In the present paper we use the same method as described in [19] for extracting the stiffness as a function of the base circle arc length  $s_1$ . The FEM package Comsol Multiphysics [17] is used for obtaining the stiffness coefficients. Other methods for including tooth stiffness are found in [5, 27]. Figure 7a and 7b show respectively the sun/planet and planet/ring stiffness. As soon as two teeth are in mesh at the same time, the stiffness almost increases to the double. The figures can also be used to calculate the contact ratio, i.e. the average number of teeth in mesh at the same time. It can thus directly be seen that the planet/ring contact ratio is higher than the sun/planet contact ratio. Introducing this kind of stiffness into the multibody program causes small “shock impulses” which can decay fast or slow, depending on the amount of damping added.



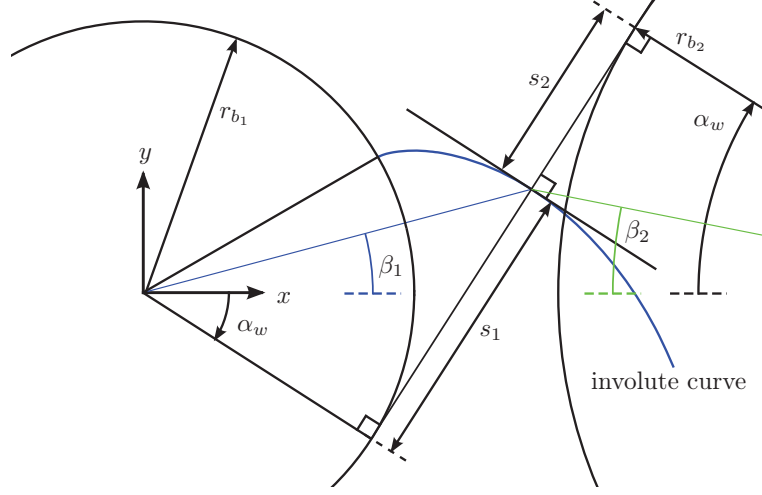


Figure 6: Base circle arc length,  $s_1$  and  $s_2$  with involute curve shown on gear 1. The load from gear 2 acts along the line of action. Base circle radii are denoted  $r_b$  and working pressure angle is  $\alpha_w$ . Angle from center to contact points are denoted  $\beta$ .

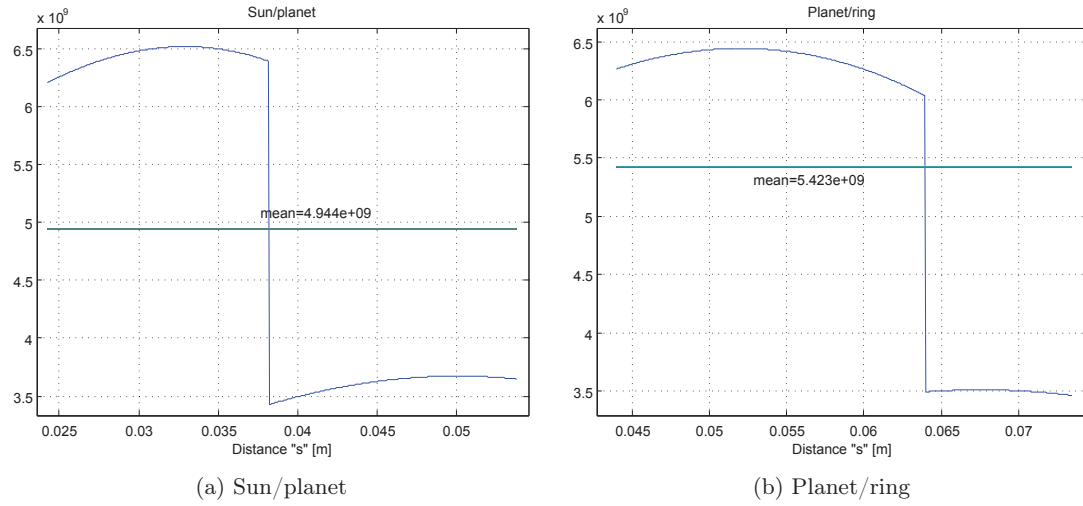


Figure 7: Stiffness as a function of the base circle arc length  $s$  (cyclic dependence).



In order to obtain stiffness expressions we need to relate the rotation of the involved gears to the defined stiffness variations. The gear rotations are defined by the variables  $\theta_1$  and  $\theta_2$ . Since these two rotations are unconstrained we define a mean value. The stiffness is defined relative to the base circle arc length of gear number one, i.e. a mean value  $\bar{\theta}_1$  is defined as the mean value of the actual  $\theta_1$  and the value  $\theta_1^*$  (the latter being the value that  $\theta_1$  would have relative to the  $\theta_2$  value if a gear constraint was used instead):

$$\bar{\theta}_1 = \frac{\theta_1 + \theta_1^*}{2}, \quad \theta_1^* = \frac{-r_{b_2}}{r_{b_1}} \theta_2 \quad (16)$$

We also need to relate the change in angle  $\Delta\theta_1$  to the change in base circle arc length  $\Delta s_1$  of the contact point, using the simple linear relation

$$\Delta s_1 = r_{b_1} \Delta\theta_1 \quad (17)$$

An offset-adjustment  $\Delta\theta^a$  is the relationship between the mean angle and the stiffness lookup-values. The final relationship between gear angle and base circle arc length is

$$\theta_s = \bar{\theta}_1 + \Delta\theta^a - N \frac{2\pi}{Z_1}, \quad \theta_s \in \left[0 ; \frac{2\pi}{Z_1}\right] \quad (18)$$

$$s_1 = \theta_s r_{b_1} + s_{1_{min}} \quad (19)$$

where  $s_{1_{min}}$  is the minimum value of the arc length for the specific set of gears.

#### 2.4.1 Without profile shift

For the given configuration used here the offset of the angles is the same for all planets. The offset-adjustment for the sun/planet is:

$$\Delta\theta^a = \frac{-\pi}{2Z_s} + \tan(\alpha_{w_{s/p}}) - \alpha_{w_{s/p}} + \arctan\left(\frac{s_{1_{min}}}{\rho_{b_s}}\right) \quad (20)$$

The offset-adjustment for the planet/ring is:

$$\Delta\theta^a = \frac{\pi}{2Z_p} + \tan(\alpha_{w_{p/r}}) - \alpha_{w_{p/r}} + \arctan\left(\frac{s_{1_{min}}}{\rho_{b_p}}\right) \quad (21)$$

#### 2.4.2 Including profile shift

Inclusion of profile shift,  $x_1$ , means that all planets interacts with the sun and the ring at different places, i.e. the discontinuity in the stiffness does not happen at the same time for all three planets (see Figure 12a). An individual offset for all gear contacts is:

- Sun/planet:

$$\Delta\theta_{s/p}^a = \frac{1}{Z_s} \left( \frac{\pi}{2} - 2x_{1_{s/p}} \tan(\alpha_{w_{s/p}}) \right) - \tan(\alpha_{w_{s/p}}) + \alpha_{w_{s/p}} + \frac{s_{1,min}}{\rho_{b_s}} - \arctan \frac{s_{1,min}}{\rho_{b_s}} \quad (22)$$

$$\text{Pl.1: } \Delta\theta^a = \Delta\theta_{s/p}^a$$

$$\text{Pl.2: } \Delta\theta^a = \Delta\theta_{s/p}^a + \frac{2\pi}{3}$$

$$\text{Pl.3: } \Delta\theta^a = \Delta\theta_{s/p}^a - \frac{2\pi}{3}$$

- Planet/ring:

$$\Delta\theta_{p/r}^a = \frac{1}{Z_p} \left( \frac{\pi}{2} - 2x_{1_{p/r}} \tan(\alpha_{w_{p/r}}) \right) - \tan(\alpha_{w_{p/r}}) + \alpha_{w_{p/r}} + \frac{s_{1,min}}{\rho_{b_p}} - \arctan \frac{s_{1,min}}{\rho_{b_p}} \quad (23)$$

$$\text{Pl.1: } \Delta\theta^a = \Delta\theta_{p/r}^a$$

$$\text{Pl.2: } \Delta\theta^a = \Delta\theta_{p/r}^a - \frac{2\pi}{3}$$

$$\text{Pl.3: } \Delta\theta^a = \Delta\theta_{p/r}^a + \frac{2\pi}{3}$$

### 3 Results

Some simple test cases have been made using a fictive planetary gearbox with 20 teeth on the sun gear, 40 teeth on each of the planet gears and  $(20 + 2 \cdot 40) = 100$  teeth on the ring gear. No profile shift is used. This teeth combination is specifically suitable for running simulations with parameter variations based on the number of planets. For the teeth to mesh properly, the absolute number of teeth on the sun and ring gears should be added together and also be a multiple of the number of planets. The sum of 120 teeth therefore means that parameter variations can be made for 1, 2, 3 and 4 planets and the angle between all planets are equally distributed, i.e.  $360^\circ$  divided by the number of planets. This can be seen in Figure 8. The results section is concluded with results for a real planetary gearbox operating in a 500 kW wind turbine.

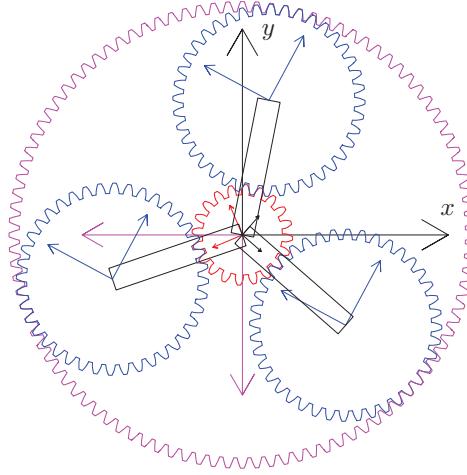


Figure 8: Matlab implementation of the rigid and the flexible planetary gearbox models.

#### 3.1 Gearbox with 1-4 planets

The two types of models described above are implemented and compared against each other. A set of input parameters are made for constructing low eigenfrequencies with large amplitudes, which can easily be seen in a Matlab animation. We choose to have low eigenfrequencies with large amplitudes because we want to visually look at the gear tooth animation and inspect if the tooth penetration looks correct, before using realistic values into to model. The mass moments of inertia therefore has to be very low. The number of bodies is equal to the number of planets plus the planetary carrier and sun and ring gears.

Figure 8 is shown with 3 planets although there is space for 4 planets. Input torque is put on the planetary carrier i.e. the driver. The carrier angle  $\theta_d$  is measured from the global  $x$ -axis to the local  $x$ -axis of the carrier. This local carrier  $x$ -axis is aligned in the direction of the center of the first planet. The first planet always starts at  $0^\circ$ , then the next planet is located at  $360^\circ/p$  for  $p$  number of planets and subsequent planets are placed evenly distributed in the CCW direction. The initial position of the carrier is  $0^\circ$  so  $\theta_d(t = 0) = 0^\circ$  and a number of 5 second simulations are carried out with driver input torque as shown in Table 1a. The mass moments of inertia of all bodies are shown in Table 1b. Additional planets are added by repeating mass properties of body 2. The input torque is negative so the carrier will move in the CW direction and end up in the position as shown in Table 1c. Without damping and with a constant stiffness coefficient of 500 [N/m], the deviation between the rigid and the flexible model is less than 1%, which is deemed acceptable. The visual inspection of the tooth penetration phenomenon from the Matlab animation shows that the model works as expected, with a cyclic harmonic motion. This is impossible to see with realistic tooth stiffness.

Time [s]	Torque [Nm]
0-2	-4
2-5	0

(a) Carrier torque for simple example with  $k = 1000$  N/m and  $d = 0$  Ns/m.

Body	$I_{zz}$	Desc.
1	0.123	Sun
2	1.97	Planet
3	77.1	Ring
4	0.15	Carrier

(b) The mass/inertia matrix [kg·m<sup>2</sup>].

Planets	Gearbox model		$\epsilon$ [%]
	Rigid	Flexible	
1	-100.92°	-100.25°	0.66
2	-58.73°	-58.40°	0.56
3	-41.17°	-40.96°	0.51
4	-31.69°	-31.54°	0.47

(c) The final carrier angle  $\theta_d$  ( $t = 5$  sec) and relative difference  $\epsilon$  in % between the two models.

Table 1: Matlab input parameters, description of bodies and results.

### 3.1.1 Gear tooth forces - rigid vs flexibly-connected model (1-4 planets)

For the rigid gear constraint, the reaction forces are already in the gear tooth surface normal direction. For a dynamic system

$$\mathbf{M}\ddot{\mathbf{q}} = \mathbf{g}_{\text{ext}} + \mathbf{g}_{\text{react}} \Rightarrow \mathbf{M}\ddot{\mathbf{q}} - \Phi_{\mathbf{q}}^T \boldsymbol{\lambda} = \mathbf{g}_{\text{ext}} \quad (24)$$

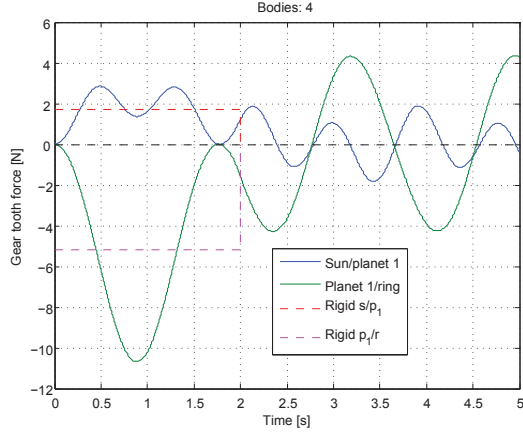
the term  $-\Phi_{\mathbf{q}}^T \boldsymbol{\lambda}$  yields the reaction forces but only the gear tooth reaction forces are interesting. The flexibly connected method doesn't have Lagrange multipliers for the gear tooth reaction forces and therefore it is necessary to implement some book-keeping that tracks the penetration depth and penetration velocity if damping is included.

Figures 9a– 9d show the gear tooth forces, for producing the same results as provided in Table 1c. The gear tooth force from the rigid model is compared with the flexible gear tooth forces, given by the expression  $\hat{\mathbf{v}}_{\mathbf{r}}^T (\mathbf{F}^k + \mathbf{F}^d)$ . To visually be able to clearly inspect the results in a Matlab-animation, the frequencies are chosen to be low. This can be done by using low stiffness values. Damping is not included initially.

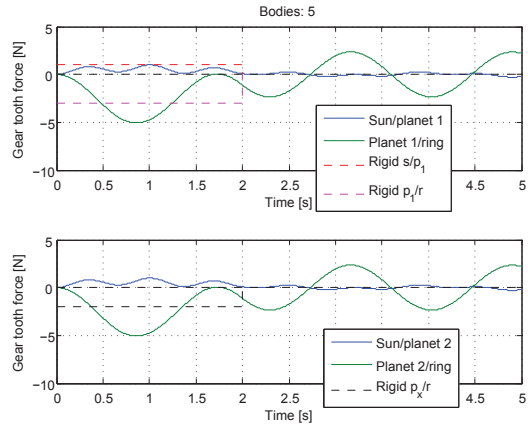
The effect of using only a single planet is easy to understand (see Figure 9a). It can easily be seen that after 2 seconds the carrier torque is removed and left is only a simple harmonic motion which without damping will continue forever (this infinite harmonic behaviour will become even more clear when the stiffness is increased by a factor 10 in the following section). By using numerical integration in Matlab from 0–5 seconds, it can be seen that the area under the rigid/flexible sun/planet curves deviates around 5%. The area under the planet/ring curves deviate approx 1%. In other words, the antiderivative of the gear tooth force curve is approximately the same in either case.

When using 2 or more planets (figures 9b- 9d), it is more difficult to assess the influence of how the rigid gear constraint behaves in comparison with the flexible gear connection. In the rigid case, the first planet behaves differently from the other planets while in the flexible case all planets behave equally. This is true as long as no profile shift is used and as long as the initial rotation error is inexistent. Planets 2-4 have 1 gear constraint on the sun gear as well as on the ring gear, causing a single gear tooth reaction force two places. The flexible model yields gear forces everywhere but they're the same when no profile shift is used and with the same perfectly aligned initial conditions. For this reason two subplots are shown for the simulation with 2-4 planets because the subplot for planet 2 is the same for all following planets.

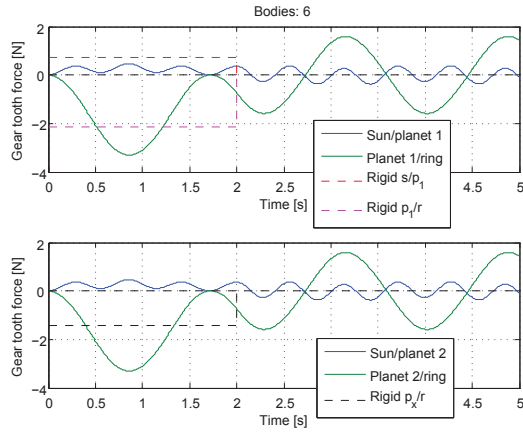
When 2 or more planets are used, it is easy to realize that the flexible gear connection is highly recommended in favor of the rigid gear constraint. Physically the flexible method is more correct when comparing with the rigid method. However, the latter is easier to implement, it is faster if the stiffness is high and realistic and it doesn't require any book-keeping at all.



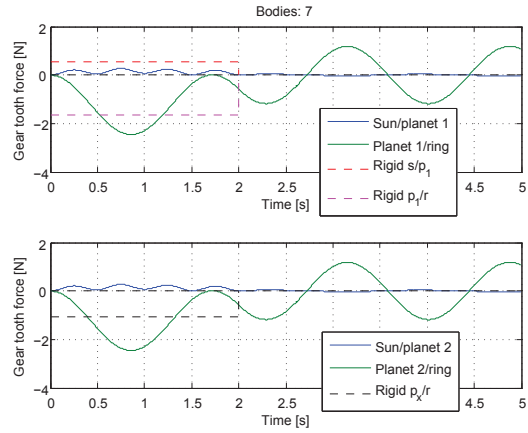
(a) 1 planet rigid/flexible comparison. The rigid gear constraint provides a good “average” for gear tooth force.



(b) 2 planet rigid/flexible comparison. As shown in Figure 2, only planet 1 has both gear constraints at sun/planet and planet/ring.



(c) 3 planet rigid/flexible comparison. The gear tooth forces for planets 2 and 3 are the same, when profile shift  $x = 0$ .



(d) 4 planet rigid/flexible comparison. It can be seen that the rigid gear constraint is a rough inaccurate estimate of the flexible gear tooth forces.

Figure 9: Gear tooth forces for the rigid vs. flexibly-connected artificial planetary multibody gearbox model with 1-4 planets.

### 3.1.2 The effect of damping

The stiffness is now increased by a factor 10 so  $k = 5000$  N/m and the number of planets is chosen to be 3 which is deemed to be a typical case. Different damping coefficients are added but profile shift is not used and perfect initial rotation angles as described in the previous section are used again.

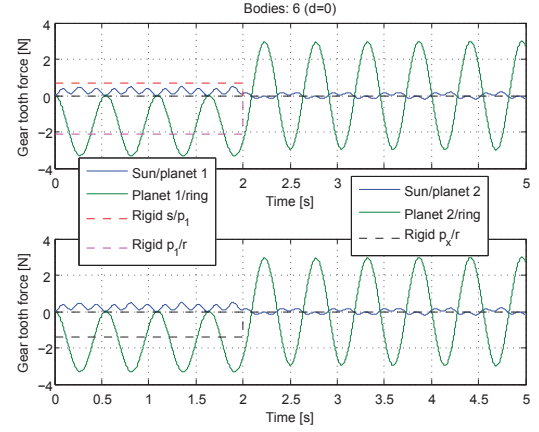
Table 10a in comparison with Table 1c shows that as the stiffness is increased the relative difference between the two approaches decreases and in addition the amount of damping has little influence on the relative movement of the carrier angle after 5 seconds. From basic theory of vibrations it is known that for a 1-DOF spring-mass system, the natural frequency is

$$\omega = \sqrt{\frac{k}{m}}, \quad k \text{ is stiffness, } m \text{ is mass.} \quad (25)$$

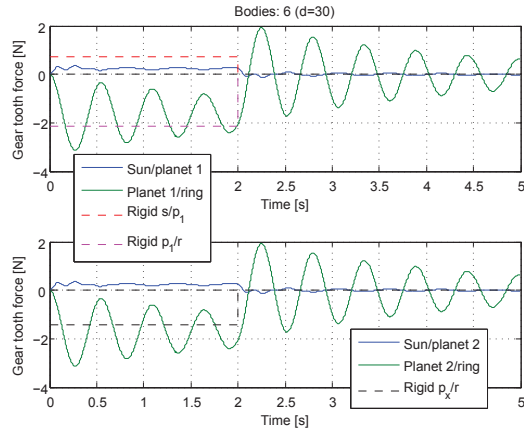
If the mass is constant and the stiffness increases by a factor 10 the natural frequency is expected to increase by a factor of  $\sqrt{10} = 3.16$  which also seems to be the case. We can estimate the half period length with  $k = 500$  N/m from Figure 9a- 9d and it is approximately 1.75 seconds. From figures 10b- 10d the half period length is approx 0.55 seconds. The ratio between the two is very close to 3.16, so the theoretical decrease in period length is confirmed as we increase the stiffness by a factor of 10.

Gearbox model (3 pl, rigid $\theta_d = -41.17^\circ$ )		
Damping	Flexible $\theta_d$	$\epsilon$ [%]
0	$-41.127^\circ$	0.104
10	$-41.143^\circ$	0.067
20	$-41.152^\circ$	0.044
30	$-41.157^\circ$	0.031
40	$-41.160^\circ$	0.023
50	$-41.162^\circ$	0.019
60	$-41.164^\circ$	0.015

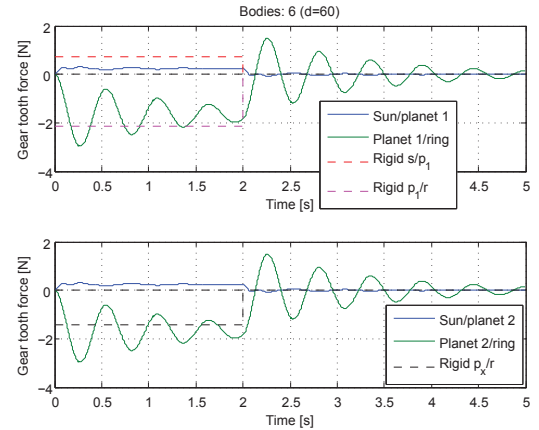
(a) The final carrier angle  $\theta_d$  and relative difference  $\epsilon$  in % between the two models, when adding damping.



(b) Using damping coefficient,  $d = 0$  Ns/m.



(c) Using damping coefficient,  $d = 30$  Ns/m.



(d) Using damping coefficient,  $d = 60$  Ns/m.

Figure 10: Gear tooth forces for the rigid vs. flexibly-connected artificial planetary multibody gearbox model for different damping coefficients.

After 2 seconds, Figure 10b shows the infinite harmonic motion of the gear teeth penetrating each other. As long as no damping is included, the gear tooth forces are oscillating to an amplitude

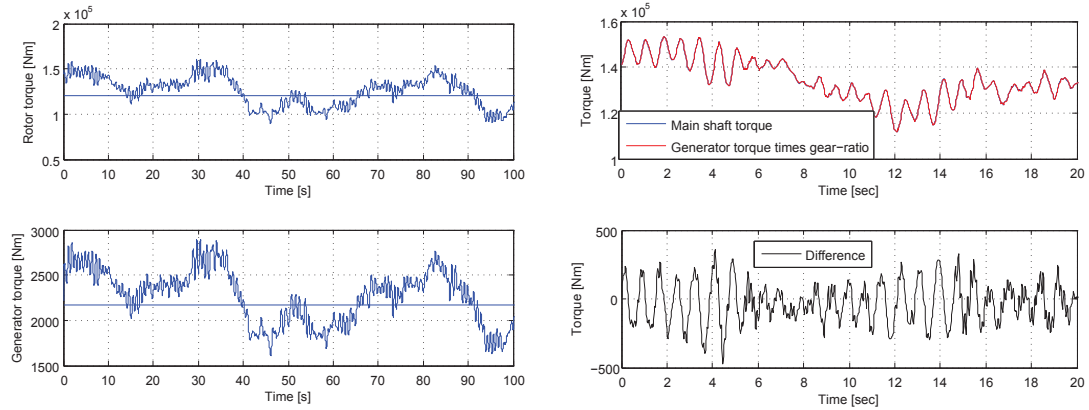
given by the penetration depth at  $t = 2$  seconds, which is the moment where all external forces and moments are removed. Only the inertia of the system keeps the planetary carrier rotating and since no damping is involved, the energy of the system is preserved which can be seen by the regular periodic oscillations.

Figure 10d illustrates the equilibrium condition where the stiffness and damping forces “locks up” the gear teeth so after a while, the gears will end up moving in a steady and similar way as the rigid model. This is something that is seen very clearly in e.g. a Matlab animation. With damping gear teeth can rotate while penetrating each other (otherwise the spring forces would be 0). By analyzing the forces in the program, it can be seen that at exactly 2 seconds the gear teeth penetration depth is not large, but due to inertia, the spring forces are at a maximum around 2.2 seconds. The damping forces are almost constant but decrease slightly from 2.2 to 5 seconds. The result is that the sun/planet and planet/ring gear tooth forces end up at around  $\pm 2.3$  N while the planetary gearbox rotates as steady as in the rigid model with small (or no) acceleration jumps. Equilibrium with no external forces mean that if the sun/planet force is 2.3 N then the planet/ring force should be -2.3 N and if this is not the case, the planet will rotate in a non-ideal way which is seen as a kind of rotation, which the rigid model would never do.

This behaviour of using damping coefficients was fully expected. The bigger the damping coefficients is, the more the flexibly-connected planetary gearbox will behave like a rigid model and this is something that must be taken into account for real practical examples like those described in the following section.

### 3.2 Analysis of the planetary gearbox in a 500 kW wind turbine

A real planetary gearbox has much higher stiffness and damping values than those analyzed in the previous section, which on the other hand provides low-frequency results that look good for realtime Matlab animations for visual inspection of the penetration depth phenomenon. For the sake of modelling a real planetary gearbox, it is not realistic to model the gear tooth stiffness as a constant value. The gear tooth stiffness from Figure 7a (sun/planet) and Figure 7b (planet/ring) is used in the following, for modelling a planetary gearbox with 20, 35 and 91 teeth for respectively the sun, planet and ring gears. The profile shift is  $x_s = 0.582$ ,  $x_p = 0.419$  and  $x_r = -0.840$ , respectively and for input, realistic loads from [15] are used. The rotor torque is used on the planetary carrier and the generator torque is used on the sun gear, i.e. their values are inserted to the RHS of Equation (3).



(a) Rotor/main shaft torque in a real 500 kW wind turbine in a wind field with a mean speed of 10 m/s.

(b) Main shaft torque vs. generator torque times gear ratio causes small acceleration changes.

Figure 11: Realistic input torque for the realistic multibody planetary gearbox model .

Figure 11 shows some realistic input loads that to some extent have been verified by using the aerodynamic FLEX5 software tool [28] and comparing with experimental data [15].

Because the stiffness for this model is much higher than before, the timestep has to be much smaller, which increases computation time and consequently the total simulation time is rather short. It

must however be long enough to be able to remove the first part of the simulation results due to turbulent (wind) inflow, giving the model time to find something that can be regarded quasi-steady. In other words, it takes a while before inertia forces and accelerations are in a semi-equilibrium state.

### 3.2.1 Results from the 500 kW planetary gearbox model

In order to save computation time the initial velocity of the planetary carrier, connected directly to the rotor, is set to 2.86 rad/s or 27.3 RPM which can be seen from FLEX5 simulation results. The torque on the carrier and sun is then interpolated using Figure 11 and in the beginning of each timestep the  $\mathbf{g}$ -vector (1) on the RHS of the equations of motion is updated accordingly, causing some acceleration fluctuations due to turbulence.

Body	$I_{xx} = I_{yy}$	$I_{zz}$	Desc.
1	145	1173	Sun
2	122	12.6	Planet 1
3	163	0.8	Ring
4	1759	3000	Carrier
5	122	12.6	Planet 2
6	122	12.6	Planet 3

Table 2: More realistic mass/inertia matrix [kg·m<sup>2</sup>].

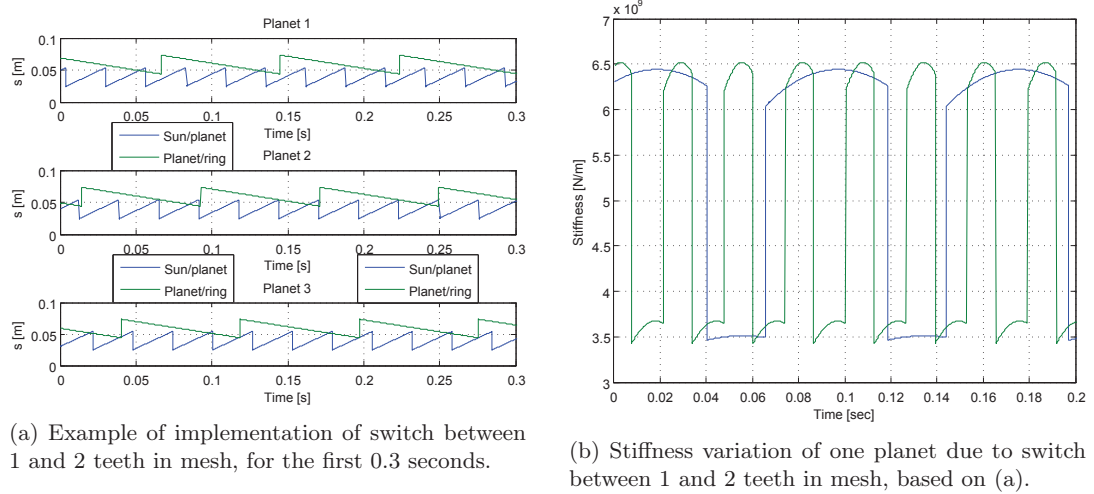


Figure 12: 6-body multibody model and demonstration of realistic stiffness model using profile shift. If the base circle arc length is below a threshold value, 2 teeth are in mesh and otherwise only a single teeth is in mesh.

Table 2 is the mass matrix for our realistic 500 kW wind turbine. As the gears rotate, the base circle arc length changes and because profile shift is used, the switch between 1 and 2 gears in mesh will happen at different times for all individual planets. The base circle arc length from Equation (19) as a function of time is shown in Figure 12a, which also shows that the sun rotates faster than the planets. Figure 12b shows the actual corresponding stiffness values of the planetary gearbox, based on Figure 7 for one of the planets. Figure 13 shows the linear spring and damping forces together with the sum of these.

Figure 14 shows a comparison of the rigid vs. the flexible approach for this particular planetary gearbox using two different damping coefficients. It is interesting to note that the mean values are almost identical and approximately 1/3 of the rigid gear tooth forces. This corresponds fully to the fact that Figure 2 only shows 1 sun/planet gear constraint with the rigid model (because no

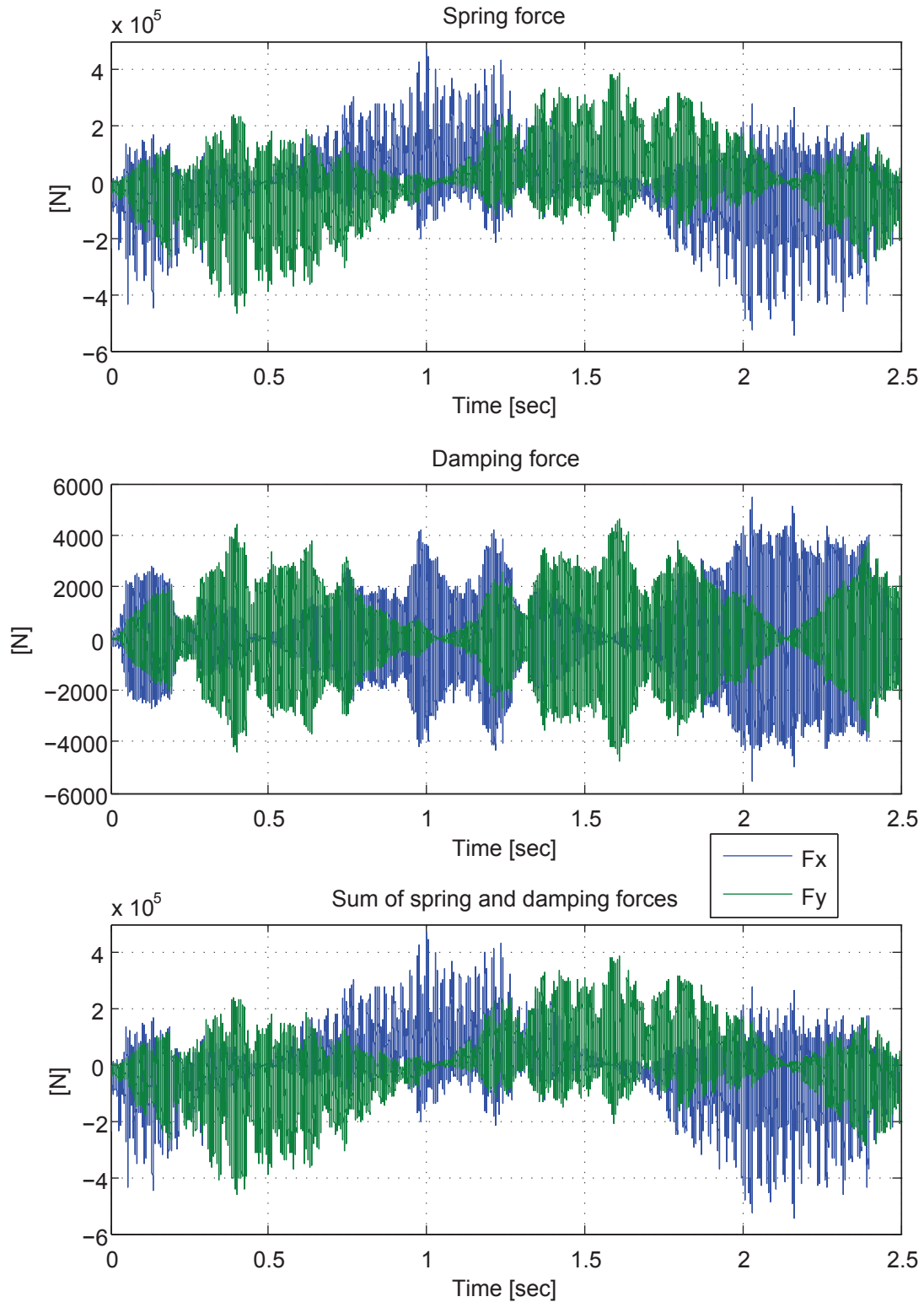


Figure 13: The damping force is direction-dependent as the spring forces are (blue color for  $x$ , green color for  $y$ ). Damping forces increase as the spring forces increase and vice versa ( $d = 20 \cdot 10^3$  Ns/m was used). It can be seen that spring forces are dominant – single planet forces are shown.

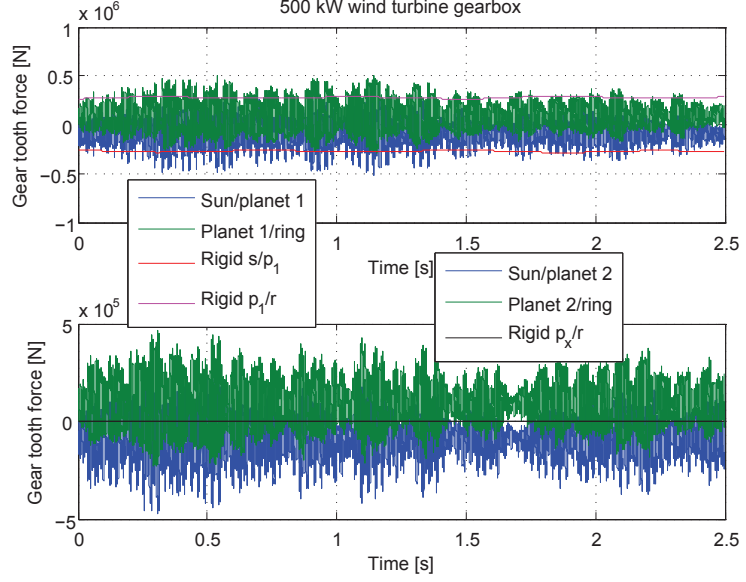


more constraints can be added). By experimenting it can be seen that higher damping decreases the amplitude of the gear tooth forces, because then gear teeth are not allowed to penetrate each other to the same extent.

Finally it becomes interesting to look at the torque from accelerations and moment of inertia of e.g. the sun, shown in Figure 15. It can be seen that the standard deviation of the torque becomes small the closer we get to the “rigid” case, which is equivalent to increasing the damping. In other words, damping prevents gear tooth penetration.

Desc.	F [kN]
Rigid $p_1/r$	277
Rigid $s/p_1$	-272
Flex. $p_1/r$	93
Flex. $s/p_1$	-91

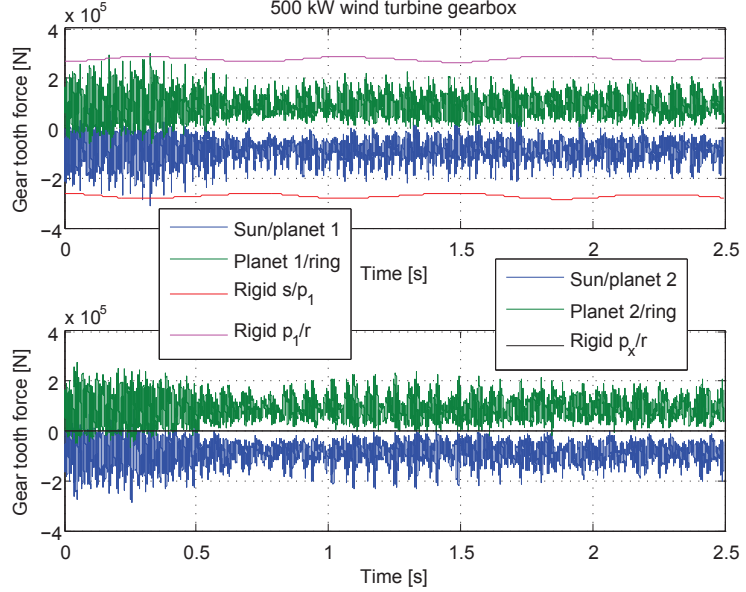
(a) Average gear tooth forces. Final carrier angle is  $409.636^\circ$  using the flexible approach.



(b) Gear tooth forces using  $d = 2 \cdot 10^4$  Ns/m.

Desc.	F [kN]
Rigid $p_1/r$	277
Rigid $s/p_1$	-272
Flex. $p_1/r$	93
Flex. $s/p_1$	-91

(c) Average gear tooth forces. Final carrier angle is  $409.637^\circ$  using the flexible approach.



(d) Gear tooth forces using  $d = 4 \cdot 10^4$  Ns/m.

Figure 14: Gear tooth forces using rigid/flexibly connected bodies for modelling a real planetary gearbox using profile shift and realistic stiffness/damping parameters. Final carrier angle is  $409.622^\circ$  by using the rigid approach, meaning that the difference is negligible.

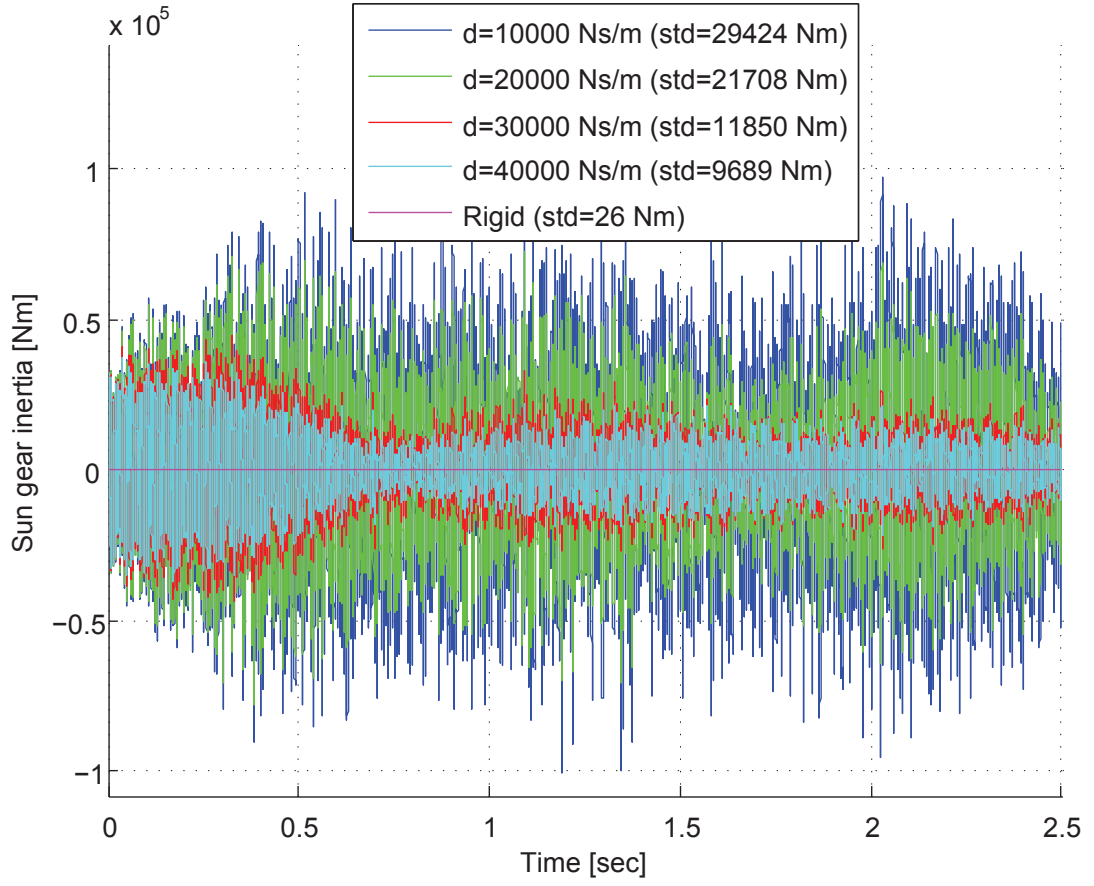


Figure 15: Inertia term for the sun gear ( $M_{sun} = I_{zz} \ddot{\theta}$ ) using different damping coefficients, for the realistic planetary gearbox in a 500 kW wind turbine.

## 4 Conclusions

Two fundamentally different approaches for modelling multibody planetary gearboxes have been described and implemented in Matlab. The first approach is a completely rigid model, where bodies are connected through a rigid gear constraint that allows reaction forces easily to be extracted, from the vector of Lagrangian multipliers.

The second approach also uses rigid bodies, but the bodies are connected through springs and dampers. Comparing the two approaches shows that gear tooth reaction forces must be in good agreement between each other because when running a simple example with 1-4 planets and no damping, the total angular movement of the carrier seems to be the same for all cases. The deviation of the position of the final carrier angle after 5 seconds is found to be less than 1 %. These results could probably also be obtained by using a simpler rigid gear constraint such as  $\phi_i \dot{\theta}_i = -\rho_j \dot{\theta}_j$  from [18], but then it would not be straightforward to obtain the gear tooth reaction forces, which is the scope of the present paper.

As we increase the stiffness, the natural frequency behaves well accordingly to the theory of harmonic motion for springs. By adding more and more damping, the gears in the planetary gearbox clearly rotates more and more like they would do, if implemented using a rigid gear constraint. The results and the comparison we provide results for in this article, are interesting because each method has its advantages and disadvantages:

- The rigid gear constraint is generally very fast, but experiments with 1-4 planets show that the gear tooth forces are only a “rough” estimate of the real planetary gear tooth forces. A major drawback with this method is that only one of the planets can have a gear connection to both the sun and the ring, meaning that not all planets will feel the same gear tooth forces when operating under the same ideal initial conditions. Also fatigue calculations are inaccurate because the force variations are too small.
- The flexibly-connected method is deemed much more realistic and should therefore be used for accurate calculations. However, a major drawback is that by using realistic stiffness and damping parameters the time-step decreases significantly and therefore the simulation time becomes much longer than by using the rigid approach. The method is suitable for fatigue as well as other detailed calculations.

For the flexible method we describe a method which implements gear tooth stiffness depending on the rotation angles of the two gears in mesh. This method is also capable of taking profile shift into account, for making more realistic simulations. Intuitively it makes sense, that the mesh stiffness is higher when 2 teeth are in mesh compared to when only a single tooth is in mesh. Simulations show that with no profile shift and “perfect” initial conditions, such as initial gear body rotation angles, all planets experience the shift between 1 and 2 gears in mesh at the same time. But with profile shift, the tooth clash when switching between 1 and 2 teeth in mesh, is shifted such that it happens at different times for different planets.

Finally, we present simulations for a model of a real planetary gearbox in a 500 kW wind turbine. For the planetary gearbox with 3 planets in the 500 kW wind turbine, the gear tooth forces using the flexible model are close to 1/3 of those by using the rigid model. We demonstrate that the standard deviation of the moment from accelerations and moment of inertia becomes smaller the higher damping we use. Our two fundamentally different approaches are theoretically validated and usable for planetary gearbox modelling with any number of planets, using multibody dynamics.

## Acknowledgements

This research was supported by DSF (Danish Council for Strategic Research) grant 09-071588. The rigid multibody model have been developed with help from discussions with Michael Rygaard Hansen and Morten Kjeld Ebbesen from University of Agder, Norway. Their support is gratefully acknowledged.

## References

- [1] Farid M. L. Amirouche, *Fundamentals of multibody dynamics : theory and applications*, Birkhauser, 2004, Includes bibliographical references and index.
- [2] Uri M. Ascher and Linda R. Petzold, *Computer methods for ordinary differential equations and differential-algebraic equations*, Computer Methods for Ordinary Differential Equations and Differential-Algebraic Equations (1998), 3–305.
- [3] Ds Bae and Ej Haug, *A recursive formulation for constrained mechanical system dynamics – 2. closed-loop systems*, Mechanics of structures and machines **15** (1988), no. 4, 481–506.
- [4] J Baumgarte, *Stabilization of constraints and integrals of motion in dynamical systems*, Computer methods in applied mechanics and engineering **1** (1972), no. 1, 1–16.
- [5] Saeed Ebrahimi and Peter Eberhard, *Rigid-elastic modeling of meshing gear wheels in multi-body systems*, Multibody System Dynamics **16** (2006), no. 1, 55–71.
- [6] C Gear, *Simultaneous numerical solution of differential-algebraic equations*, Circuit Theory, IEEE Transactions on **18** (1971), no. 1, 89–95.
- [7] Michel Géradin and Alberto Cardona, *Flexible multibody dynamics: a finite element approach*, John Wiley, 2001.
- [8] Morten Haastrup, Michael R. Hansen, and Morten K. Ebbesen, *Modeling of wind turbine gearbox mounting*, Modeling, Identification and Control **32** (2011), no. 4, 141–149.
- [9] E. Hairer and G. Wanner, *Solving ordinary differential equations ii: Stiff and differential-algebraic problems second revised edition with 137 figures*, Springer Series in Computational Mathematics **14/2** (1996).
- [10] Anders Melchior Hansen, Flemming Rasmussen, and Torben J. Larsen, *Gearbox loads caused by double contact simulated with hawc2*, Proceedings of EWEA Annual Event from Brussels, Belgium (2011), 11.
- [11] Edward J. Haug, *Computer aided kinematics and dynamics of mechanical systems: Vol. i: Basic methods*, Allyn and Bacon, 1989.
- [12] E.J. Haug and J. Yen, *Implicit numerical integration of constrained equations of motion via generalized coordinate partitioning*, American Society of Mechanical Engineers, Design Engineering Division (Publication) DE **19-3** (1989), no. pt 3, 117–123.
- [13] R L Huston and Y Wang, *Flexibility effects in multibody systems*, NATO ASI Series E Applied Sciences - Advanced Study Institute **268** (1994), 351.
- [14] J G de Jalon, E Bayo, and L Y Bahar, *Kinematic and dynamic simulation of multibody systems: The real time challenge*, Applied Mechanics Reviews - Including Supplement **48** (1995), no. 1, B2.
- [15] M. F. Jørgensen, N. L. Pedersen, J. N. Sørensen, and U. S. Paulsen, *Rigid matlab drivetrain model of a 500 kw wind turbine for predicting maximum gear tooth stresses in a planetary gearbox using multibody gear constraints*, Wind Energy (2013).
- [16] Peder Klit, Knud Casper, and Niels L. Pedersen, *Machine elements - analysis and design*, Polyteknisk Forlag, 2009.
- [17] COMSOL Multiphysics, [www.comsol.se](http://www.comsol.se), 1998-2012.
- [18] Parviz E. Nikravesh, *Computer-aided analysis of mechanical systems*, vol. 186, Prentice Hall, 1988.
- [19] N. L. Pedersen and M. F. Jørgensen, *On gear teeth stiffness evaluation*, (submitted) (2013).

- [20] N. L. Pedersen and M. L. Pedersen, *A direct derivation of the equations of motion for 3D-flexible mechanical systems*, International Journal for Numerical Methods in Engineering **41** (1998), no. 4, 697–719.
- [21] Joris L. M. Peeters, Dirk Vandepitte, and Paul Sas, *Analysis of internal drive train dynamics in a wind turbine*, Wind Energy **9** (2006), no. 1-2, 141–161.
- [22] Flemming Rasmussen, Anders Melchior Hansen, and Torben J. Larsen, *Can transient loads occur internally in a planetary gearbox?*, Proceedings of EWEA 2012 - European Wind Energy Conference & Exhibition (2012).
- [23] Ahmed A. Shabana, *Dynamics of multibody systems*, Wiley & Sons, 1989.
- [24] Ahmed A. Shabana, *Flexible multibody dynamics: Review of past and recent developments*, Multibody System Dynamics **1** (1997), no. 2, 189–222.
- [25] R. A. Wehage and E. J. Haug, *Generalized coordinate partitioning for dimension reduction in analysis of constrained dynamic-systems*, Journal of Mechanical Design-Transactions of the ASME **104** (1982), no. 1, 247–255.
- [26] Ding-Xuan Zhao, Yu-Xin Cui, Tao Ni, Ying Zhao, and Chao-Fei Wang, *A new method for solving the constraint multibody system dynamic equation*, Advanced Materials Research **345** (2012), 361–364.
- [27] P. Ziegler, P. Eberhard, and B. Schweizer, *Simulation of impacts in geartrains using different approaches*, Archive of Applied Mechanics **76** (2006), no. 9-10, 537–548.
- [28] Stig Øye, *Various flex 5 documentation*, DTU Mechanical Engineering, 2001.

## Publication [P4]

Gear fatigue damage for a 500 kW wind turbine exposed to increasing turbulence using a flexible multi-body model

# Gear fatigue damage for a 500 kW wind turbine exposed to increasing turbulence using a flexible multibody model

Jørgensen, M. F. Dep. of Mech. Eng. Solid Mechanics Lyngby, 2800 Denmark	Pedersen, N. L. Dep. of Mech. Eng. Solid Mechanics Lyngby, 2800 Denmark	Sørensen, J. N. Dep. of Wind Energy Fluid Mechanics Lyngby, 2800 Denmark
--	---	--

## Abstract

*This paper investigates gear tooth fatigue damage in a 500 kW wind turbine using FLEX5 and own multibody code. FLEX5 provides the physical wind field, rotor and generator torque and the multibody code is used for obtaining gear tooth reaction forces in the planetary gearbox. Different turbulence levels are considered and the accumulated fatigue damage levels are compared. An example where the turbulence/fatigue sensitivity could be important, is in the middle of a big wind farm. Interior wind turbines in large wind farms will always operate in the wake of other wind turbines, causing increased turbulence and therefore increased fatigue damage levels. This article contributes to a better understanding of gear fatigue damage when turbulence is increased (e.g. in the center of large wind farms or at places where turbulence is pronounced).*

## 1 Introduction

Gearbox failures and emergency stops caused by drivetrain problems are very expensive for the wind turbine industry. Drivetrain components are critical for operation, they're typically large, heavy and expensive to repair or replace. Costs for operation and maintenance (O&M) increase by the time wind turbines are non-producing. Component lifetime reliability is important. A key parameter to designing drivetrain components is calculation (estimation) of accumulated fatigue damage. Related problems during the lifetime of a wind turbine are issues with corrosion, wear and leading edge blade erosion, which can reduce the performance.

The efficiency of wind turbines is continuously being improved in order to decrease the total cost of energy and therefore it is important to be able to investigate the fatigue damage under different circumstances. One way of dealing with fatigue problems is mechanical: Changing the design, increasing safety factors, dimensions etc. which could increase the weight and price. Another method is by developing or improving wind turbine controller mechanisms. Today, wind turbines are complicated machines with a lot of electrical equipment such as controllers for automatic adjustment of e.g. pitch/yaw regulation. In [15] an indirect torque control (ITC) technique has been investigated and the idea is that electromagnetic torque transients caused by grid faults and disturbances results in significant gearbox fatigue. As demonstrated in [23] there is also a lot of development going on in the field of "condition monitoring" which include recording huge amounts of data using sensors for e.g. oil temperature, wind/rotor/generator speed, vibration/accelerometers, current and power output etc., which is then processed for early diagnosis of problems.

Fatigue loads for rotor and main gearbox bearings are calculated in [8] using a method that couples non-linear Finite Element Method (FEM) and super element technique with a multibody approach (see e.g. [7, 5]). An approach to predicting wind turbine gearbox reliability for three generic gearbox configurations, based on assumptions of estimated failure rates, is given in [26]

The most common cause of gearbox failure is surface contact fatigue (see [4] which also presents examples and describes rolling contact fatigue, sliding-rolling contact fatigue and spalling). Recently, researchers from National Renewable Energy Laboratory (NREL) in the US initiated the Gearbox



Reliability Collaborative (GRC) and guarantee privacy of commercially sensitive information, see [17] in order to investigate gearbox problems and seek solutions that will lead to higher gearbox reliability.

A description of four stages of fatigue damage from initial crack to failure is given in [28], which also provides an overview of the topic from a historical perspective together with a description of definitions and suggestions for the concept of fatigue damage control.

A typical procedure for fatigue load data analysis for wind turbine gearboxes is given in [18]. In this article we will use the commercial software package FLEX5 [29] for obtaining wind turbine loads (forces and torque) and we focus on investigating gear tooth fatigue, using a multibody dynamics program developed in Matlab.

In this work, gear tooth stresses are found using either Comsol Multiphysics [16] or empirical calculated Hertzian contact stresses. A Matlab rainflow counting program (RFC) is used for determining the fatigue damage, based on an estimated Wöhler-curve (stress vs. number of cycles to failure). The gear teeth are modeled as flexible and the discontinuous nature of the stiffness is included.

### 1.1 Proposed Method

Figure 1 demonstrates the concept of this article, which is to calculate gear tooth fatigue based on turbulent wind input.

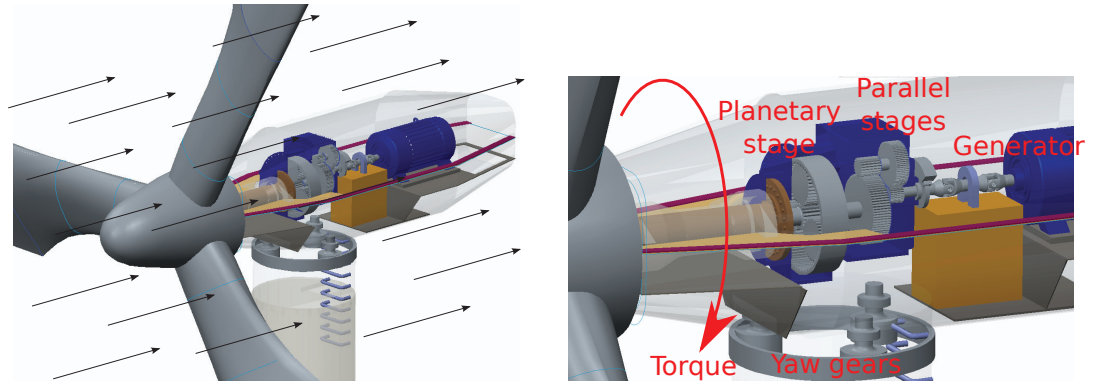


Figure 1: Wind turbine subject to a given wind field with illustration of main shaft torque, driving the carrier and planets in the gearbox, for generating power through the generator.

Accumulated fatigue damage for a wind turbine producing power using wind speed from 6-20 m/s and a bin size of 2 m/s will be investigated (the 6 m/s bin contains wind speeds from 5-7 m/s etc.). Based on [11] the turbulence intensity (TI) is set to around 10-20% throughout the whole interval. For this particular site the Weibull parameters based on 5 years of wind data from [6] are calculated. The parameters have been extrapolated to hub height at 36 m and [24] provides a description of how to perform this using the (1) maximum likelihood method, (2) a modified maximum likelihood method and (3) a graphical method. The Weibull cumulative distribution function [24] is given by

$$P(v < v_i) = P(v \geq 0) \left\{ 1 - \exp \left[ - \left( \frac{v_i}{A} \right)^k \right] \right\} \quad (1)$$

where  $P(v \geq 0)$  is the probability that the wind speed equals or exceeds zero while  $P(v < v_i)$  is the probability that the wind speed is below  $v_i$ . Weibull parameters for this site is estimated to  $A = 6.62$  and  $k = 2.19$  using 5 years of measurement data. The rated lifetime is 20 years or approximately  $(20 \cdot 365 \cdot 24) = 175200$  hours but the wind turbine does not run all the time as seen in Table 1 (approximately 60% of the time).

The aerodynamic tool FLEX5 and a multibody program is used for obtaining the gear tooth loads under representative and realistic conditions, however these simulations are rather short compared to the timescales in Table 1. Therefore it is important to ensure the statistical behavior of the

Wind speed [m/s]	6	8	10	12	14	16	18	20
In operation [hours]	45418	31900	16320	6189	1751	370	58	7

Table 1: Hours of operation at different wind speeds (binned). Total operation is 102013 hours.

simulation input and output as simulation results will be extrapolated to a lifetime operation of 20 years.

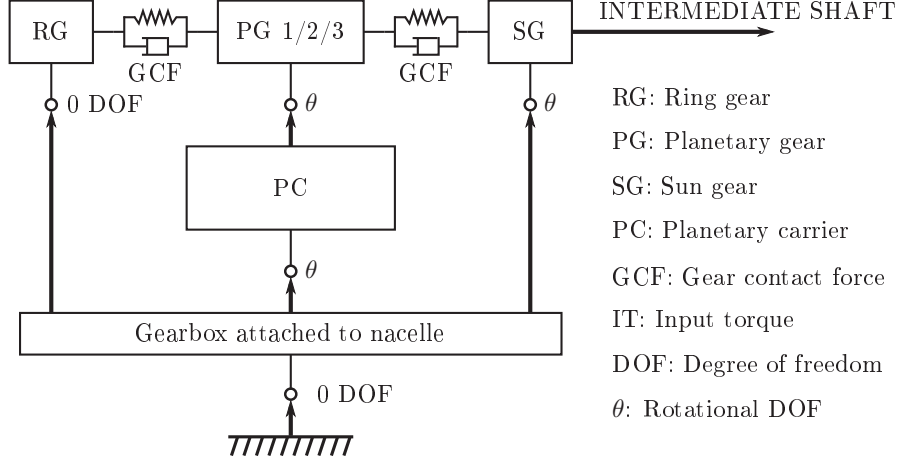


Figure 2: Topology diagram of the Matlab multibody gearbox model (as illustrated in [3]).

For the multibody program, a similar procedure as in [3] with topology diagram shown in Figure 2 will be employed. But instead of using data from the NREL (GRC) 750 kW wind turbine [17], data from a 500 kW planetary gearbox will be used. For aerodynamics FLEX5 instead of FAST is used, own multibody code instead of SIMPACK is used, rainflow counting and Palmgren-Miner summation instead of an expression for crack propagation is used.

## 1.2 Wake effects and turbulence in wind farms

The explanations to what happens to the turbulence for specific wind turbines in wind farms are complicated because it is difficult to measure a 3D-wind field and time-consuming to make Computational Fluid Dynamics (CFD)-calculations covering all possible situations and possibly also different wind directions. Figure 3a illustrates a relatively uniform mean wind field hitting the first row of wind turbines, but the wind field the second and third row of wind turbines will face is not the same as the first row due to “wake effects” (see e.g. images of “Horns Rev 1 wake effects”, found many places).

Figure 3b illustrates that the interior wind turbines in a wind farm will always be subject to wake-induced turbulence no matter which direction the wind comes from. A thorough discussion about the science behind wake effects is comprehensive and impossible to cover here. In this work, the wind field has homogenous turbulence (all statistical moments are equal) but in reality things are much more complicated. Typically the turbulence or fatigue loads on the second row of wind turbines (Figure 3a) are higher than that of the first row due to wake effects. This is clearly supported by experimental data from e.g. the Vindeby wind farm (south of Denmark) and described in [27], which shows that the standard deviation of the turbulence and wind load (flap-wise bending moment) increases for wind turbine 4W and 5E in [27, see Fig. 1.2, 1.3] when these wind turbines appear in the wake of other wind turbines. An equivalent load graph as a function of the wind direction clearly shows peaks due to wake effects and for this reason it is obvious to link turbulence level and fatigue loadings. A general assumption could be that the turbulence for interior wind turbines is always larger than that of the first row of wind turbines. This assumption is however vague and we have not found scientific evidence whether e.g. turbulence levels on the second row of wind turbines are larger than e.g. the third, fourth, fifth row etc. The question

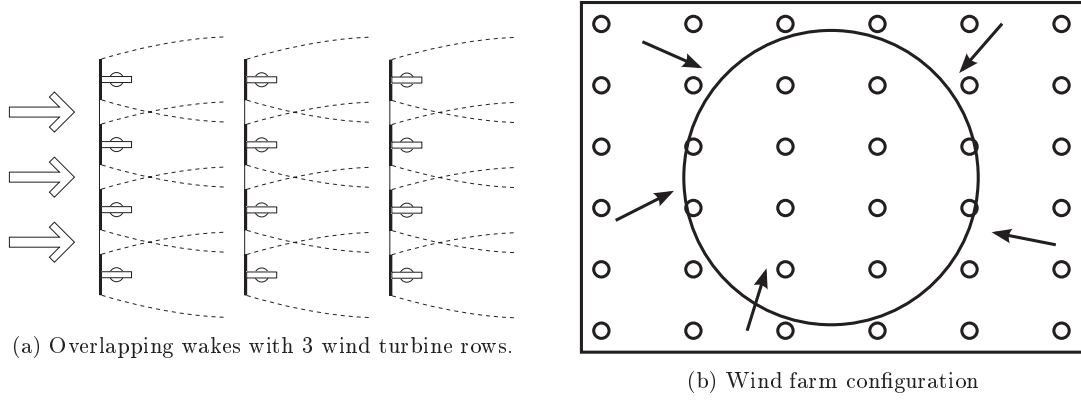


Figure 3: Wake effects in wind farms (arrows indicate possible wind directions).

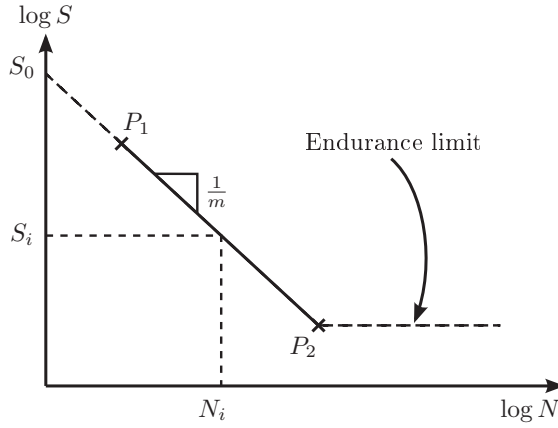


Figure 4: S-N-curve for fatigue damage.

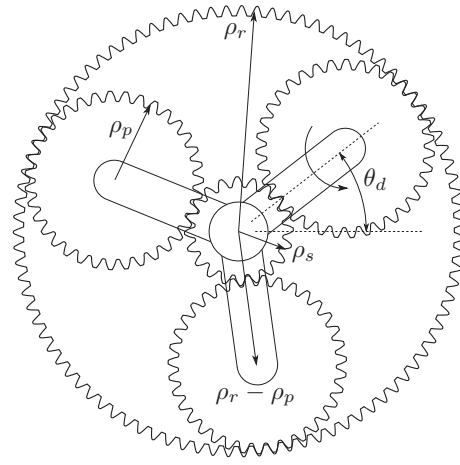


Figure 5: Planetary gearbox with radii for sun  $\rho_s$ , planet ( $\rho_p$ ) and ring ( $\rho_r$ ) gears. Planetary carrier (driver) angle is  $\theta_d$ .

about how turbulence affects individual wind turbines, has a tremendous effect on the relevance of this work for gearboxes in a wind farm.

### 1.3 Fatigue damage

Employing S-N or Wöhler curves is a suitable approach that is generally accepted for fatigue lifetime estimation. The idea of the chosen method is to use a rainflow counting algorithm on the gear tooth stress time-series. The result is a measure of cycle amplitudes or ranges which can be counted in bins and collected in a rainflow matrix, which is a function of mean values and ranges. See e.g. [13] for a description of the rainflow counting algorithm, which together with the linear Palmgren-Miner rule, based on Palmgren [21] and Miner [14] forms the following important relationships

$$D = \sum_{i=1}^j \frac{n_i}{N_i} = \sum_{i=1}^j n_i \frac{S_i^m}{S_0^m}, \quad (2)$$

$$\log S_i = \log S_0 - \frac{1}{m} \log N_i \Rightarrow S_i = \frac{S_0}{N_i^{1/m}} \quad (3)$$

Equation (2) states the accumulated fatigue damage, also known as the linear damage hypothesis. Generally the material/component will fail when the sum  $D \geq 1$ . At stress level number  $i$ , the

number of counted cycles  $n_i$  is a result of the rainflow counting algorithm evaluated on the time series. The algorithm returns the range (or amplitude) of all stresses for the  $i^{\text{th}}$  case, i.e.  $(n_i, s_i)$ . Capital  $N_i$  is the maximum number of cycles to failure and also shown in Figure 4.

Equation (3) describes the curve in Figure 4 and  $1/m$  is the slope in the loglog-plot. The  $m$  is the damage exponent, describing the rate of change in maximum allowed stress as the cycle count changes. This exponent is typically 3-3.5 for steel, 7 for cast iron and 10-20 for glass- and carbon-fiber component materials.

Lifetime predictions cannot alone be based on this, because the S-N-curve is typically based on statistical data based on small-scale experiments and the S-N-curve itself is associated with large uncertainties where the safety factor would be based on empirical values. Accurate information about the S-N-curve for huge wind turbine components like the gears described in the present article, is assumed to be known although in reality this is difficult to obtain. The gear root bending stresses are obtained using Finite Element Modelling (FEM) using Comsol Multiphysics [16]. Surface stresses are considered as well and calculated using Hertzian contact stresses [20].

## 2 Planetary gearbox model

The following section describes planetary gearbox details (tooth data and facewidth etc.) followed by a description of the implemented multibody code for obtaining gear tooth forces and stresses. The number of teeth in the first (planetary) gearbox stage is 20, 35 and 91 for respectively the sun, planet and ring gears. The profile shift is  $x_s = 0.582$ ,  $x_p = 0.419$  and  $x_r = -0.840$ , respectively. Minimum contact facewidth for sun/planet and planet/ring is 210 mm. It is assumed that bearings and wind turbine model components are rigid such that the gear tooth forces depend on axial rotor and generator torque, regardless of transverse forces and torque (a 2D model). A real wind turbine and gearbox which has been running since 1995 is considered. It is therefore expected that the calculated accumulated fatigue,  $D$  in Equation (2), for 20 years of operation should be acceptable.

### 2.1 Multibody program code

Multibody dynamics software is used to couple or link mechanical rigid or elastic bodies with each other. General introductions to the field are given in e.g. [19, 25, 5]. Equations of motion are expressed using the following  $n$  differential equations coupled with  $m$  algebraic equations

$$\begin{cases} \mathbf{M}\ddot{\mathbf{q}} - \Phi_{\mathbf{q}}^T \boldsymbol{\lambda} = \mathbf{g}, & \Phi_{\mathbf{q}} = \frac{\partial \Phi}{\partial \mathbf{q}} \\ \Phi(\mathbf{q}, t) = 0 \end{cases} \quad (4)$$

where  $\mathbf{M} \in \mathbb{R}^{n \times n}$  is the mass/inertia matrix,  $\mathbf{q} \in \mathbb{R}^n$  is a vector of cartesian coordinates,  $\Phi_{\mathbf{q}} \in \mathbb{R}^{m \times n}$  is the Jacobian of the  $\Phi(\mathbf{q}, t) \in \mathbb{R}^m$  kinematic constraint equations,  $\boldsymbol{\lambda} \in \mathbb{R}^m$  are the Lagrange multipliers and  $\mathbf{g} \in \mathbb{R}^n$  are the external body forces applied in the global reference system. Constraint equations in the  $\Phi(\mathbf{q}, t)$ -vector are expressed at acceleration level, to form equations of motion from the DAE-system (4) into an ODE in the form given by [19]:

$$\begin{bmatrix} \mathbf{M} & -\Phi_{\mathbf{q}}^T \\ \Phi_{\mathbf{q}} & \mathbf{0} \end{bmatrix} \begin{Bmatrix} \ddot{\mathbf{q}} \\ \boldsymbol{\lambda} \end{Bmatrix} = \begin{Bmatrix} \mathbf{g} \\ \boldsymbol{\gamma} \end{Bmatrix} \quad (5)$$

Force elements (springs and dampers) are used to model the connecting flexibility between rigid gears, instead of using (rigid) gear constraints. A full description of the applied force element algorithms as illustrated by Figure 2 is presented in [10], where it is compared to a method using a constraint formulation instead.

The force element algorithm requires knowledge of the total gear tooth force, i.e. the sum of the gear tooth forces on either one or two teeth. Fatigue is a local phenomenon in single points so knowledge of the force, i.e. magnitude and direction and where it is acting on a single tooth is required. The main specific points of interest are either at the gear root or at the tooth surface contact point. The difference between obtaining and storing the force acting on a single tooth instead of the total gear force, can be regarded as a matter of calculating a mesh stiffness ratio and

then internally store the mesh stiffness of a single tooth. As an example, if two teeth are in mesh and their stiffnesses are the same, the mesh stiffness ratio is 50%. Then the single tooth force is the half of that used by the multibody dynamics code. This method is described in details in [10] (see also Figure 8 on page 8). The force acting on a single tooth is found by using Hooke's law:  $\mathbf{F} = k\mathbf{x}$  where  $\mathbf{x}$  is the tooth penetration depth from the multibody code and  $k$  is the stiffness.

## 2.2 Gear tooth flexibility

A flexible 2D multibody program has been made, which unlike a rigid model has gear tooth penetration as illustrated in Figure 7a. The details of this code is described in [10] and shortly summarized here. A transformation matrix is defined as

$$\mathbf{A}(\theta) = \begin{bmatrix} \cos \theta & -\sin \theta \\ \sin \theta & \cos \theta \end{bmatrix}, \quad (6)$$

and the penetration depth  $\mathbf{l}_p$  along the line of action for gear bodies  $i$  and  $j$  is

$$\mathbf{l}_p = \mathbf{A}_d \mathbf{A}_{s/p} \mathbf{v}_n [\rho_{b_i}(\theta_i - \theta_i^0 - \theta_d) + \rho_{b_j}(\theta_j - \theta_j^0 - \theta_d)], \quad (7)$$

where  $\mathbf{A}_d$  is a driver/carrier transformation matrix (using  $\theta_d$  shown in Figure 5),  $\mathbf{A}_{s/p}$  is a transformation matrix from the direction shown using  $\theta_d$  (Figure 5) to one of the three planets, e.g.  $0^\circ$ ,  $120^\circ$  or  $240^\circ$ . The unit tooth surface normal vector  $\mathbf{v}_n$  is a function of the pressure angle (typically  $\alpha = 20^\circ$  or  $\alpha = 25^\circ$ ), illustrated in Figure 6 and defined as

$$\mathbf{v}_n = \begin{Bmatrix} \sin(\alpha) \\ \cos(\alpha) \end{Bmatrix} \quad (8)$$

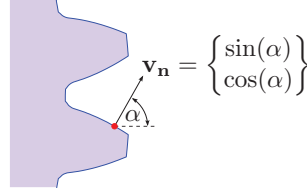


Figure 6: Unit tooth surface normal vector in the penetration direction as a function of gear tooth pressure angle  $\alpha$ .

Gear tooth penetration is illustrated in Figure 7a. The time-differentiated penetration depth  $\dot{\mathbf{l}}_p$  is associated with damping and is calculated using

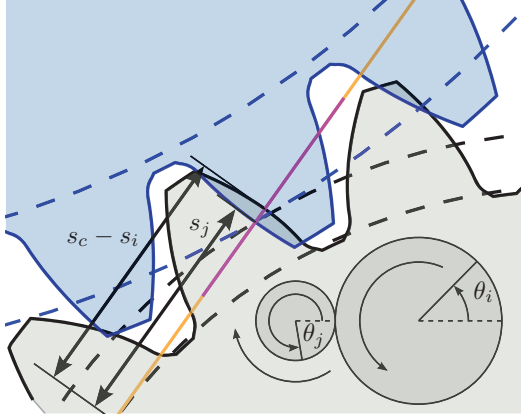
$$\dot{\mathbf{l}}_p = \mathbf{A}_d \mathbf{A}_{s/p} \mathbf{v}_n [\rho_{b_i}(\omega_i - \omega_d) + \rho_{b_j}(\omega_j - \omega_d)] \quad (9)$$

With stiffness coefficient  $k$  and damping coefficient  $d$ , gear tooth stiffness and damping forces are calculated using  $\mathbf{F}^k = k\mathbf{l}_p$  and  $\mathbf{F}^d = d\dot{\mathbf{l}}_p$  respectively. Reaction forces are opposite of each other for bodies  $i$  and  $j$  and the force is applied to the  $\mathbf{g}$ -vector on the right hand side (RHS) of Equation (5). Additionally, these forces contribute to additional torque. A radial unit vector from center of sun to center of planet gear  $\mathbf{v}_r$  is introduced. This radial unit vector  $\mathbf{v}_r$  can be rotated  $90^\circ$  using the hat vector

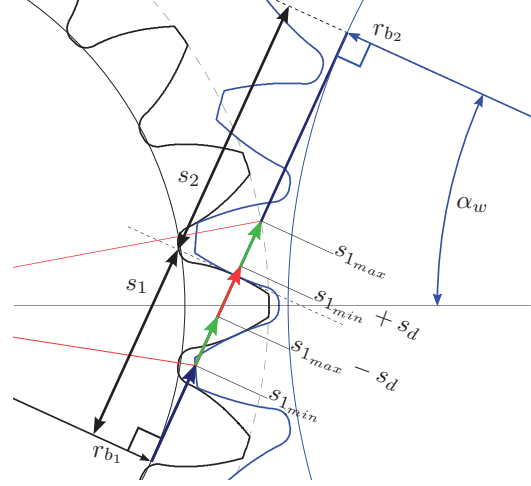
$$\mathbf{v} = \begin{Bmatrix} x \\ y \end{Bmatrix}, \quad \Rightarrow \quad \hat{\mathbf{v}} = \begin{Bmatrix} -y \\ x \end{Bmatrix} \quad (10)$$

and the tangential gear tooth force is the spring and damping force sum projected into the tangential direction using the dot product  $F_t^{k+d} = \hat{\mathbf{v}}_r^T (\mathbf{F}^k + \mathbf{F}^d)$ . Hence, the torque is  $M = \rho_w F_t^{k+d}$  where  $\rho_w$  is working circle radius [12]. The total force and torque vector on the RHS of Equation (5) becomes

$$\mathbf{g}_i^{\text{Flex}} = \begin{Bmatrix} -k\mathbf{l}_p - d\dot{\mathbf{l}}_p \\ -\rho_{w_i} F_t^{k+d} \end{Bmatrix}, \quad \mathbf{g}_j^{\text{Flex}} = \begin{Bmatrix} k\mathbf{l}_p + d\dot{\mathbf{l}}_p \\ -\rho_{w_j} F_t^{k+d} \end{Bmatrix} \quad (11)$$



(a) Gear tooth model using flexible model. The result of the multibody program yields the angles  $\theta_i$  and  $\theta_j$ . From this, the base circle arc lengths  $s_i$  and  $s_j$  are calculated. A FEM-program ([16]) was used for obtaining stiffnesses, see details in [10].



(b) Base circle arc length,  $s_1$  and  $s_2$  with line of action seen from the point of view of gear 1. Base circle radii are denoted  $r_b$  and working pressure angle is  $\alpha_w$ . Green arrows indicate 2 teeth in contact (high stiffness) and the red arrow indicates 1 tooth in contact with the other gear.

Figure 7: Tooth penetration and estimation of equivalent stiffness from flexible multibody model. The sum of distances  $s_1 + s_2 = s_c$  is a constant, see additional details in [22].

### 2.3 Gear tooth stiffness, base circle arc length and gear tooth forces

Figure 7 illustrate some important concepts in relation to gear geometry and the base circle arc lengths  $s_1$  and  $s_2$ . With flexible connected bodies both gear wheels can penetrate each other. The gear tooth stiffness has been calculated using a Finite Element Method (FEM) package [16] and expressed as a function of an “average” angle or base circle arc length. Figure 7a show gear tooth penetration (strongly exaggerated for illustrative purposes) and the average of  $s_i$  and  $s_j$  is made equal to  $s_1$  in Figure 7b. This figure illustrates the FEM-model contact point as a function of  $s_1$  and it is based on  $s_1$  the gear tooth stiffness is calculated from. This method is suggested as a good way to implement additional realism, see [10] for additional details.

Figure 7b show that the base circle arc length represents the current rotation of both gear wheels as well as the gear tooth penetration depth of each gear tooth into the other gear(s) in mesh. The sum of  $s_1$  and  $s_2$  is constant, but both distances change as a realistic dynamic model of the gear teeth requires this. By means of the gear tooth penetration depth, the “average” base circle arc length and the gear tooth stiffness, the total gear tooth force for all teeth is calculated and plotted in Figure 8. This figure show both total gear tooth forces (used on the RHS of Equation (5)) as well as a fictive “single tooth force”, including corresponding (lower graph) base circle arc length and tooth stiffness as a function of time.

A “fictive” single gear tooth force is required for fatigue analysis. The reason is that is necessary to only look at one gear tooth at the time, even though sometimes the load is shared among two gear teeth. The problem is extensively described in [22], but shortly explained the single gear tooth force is calculated as  $F_t k_1 / k_t$ , where  $F_t$  is the total gear tooth force (sum of spring and damping forces),  $k_1$  is the single gear tooth stiffness and  $k_t$  is the total gear tooth stiffness.

Figure 8 shows 0.2 seconds of simulation time and it shows whether 1 or 2 teeth are in mesh at a given time period (high stiffness is when two gear teeth are in mesh and low stiffness of around  $3.5 \cdot 10^9$  N/m is when only one gear tooth is in mesh). The figure shows that most of the time 2 gear teeth are in mesh, except in the interval [0.145; 0.17] seconds.

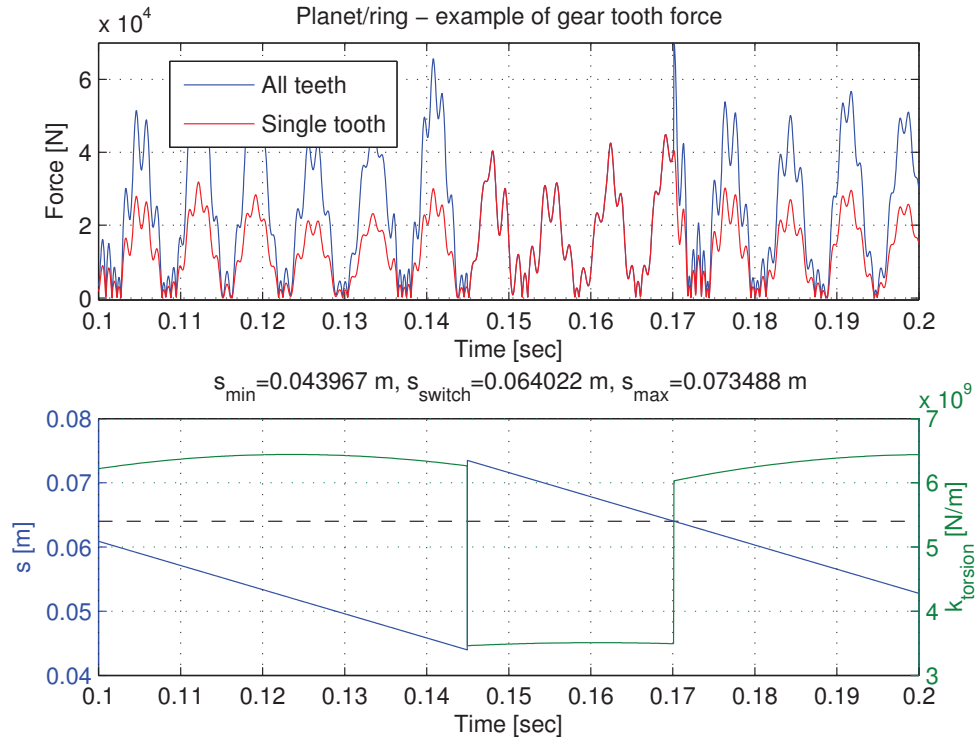


Figure 8: Top graph: The total gear tooth force is shown in blue, while the gear tooth force from a single gear (due to lower stiffness) is shown in red. When only one pair of teeth is in mesh, the red and blue curves are coinciding. The multibody program uses the blue curve, but for the fatigue analysis we use the red (single-tooth contact) curve. Lower graph: The base circle arc length of the inner gear ( $s_1$  on Figure 7b) and corresponding FEM-stiffness.

## 2.4 Gear tooth stresses in relation to fatigue analysis

The gear tooth stiffness properties is the same as in [10] and the damping coefficient is estimated to  $d = 40 \cdot 10^3$  Ns/m. The following two stress situations has been examined

1. Gear tooth bending failure: A FEM-program has been used for obtaining stresses in the situation where a unit force is applied to different contact points (defined as the base circle arc length).
2. Gear tooth surface failure: Hertzian stress assumption is applied and pure rolling contact of sphere-on-sphere is assumed. The maximum stress a little below the surface is calculated.

The details of the two approaches are elaborated below and the 8 cases illustrated in Table 1 are considered using increasing turbulence intensity (TI).

### 2.4.1 Gear tooth root bending failure

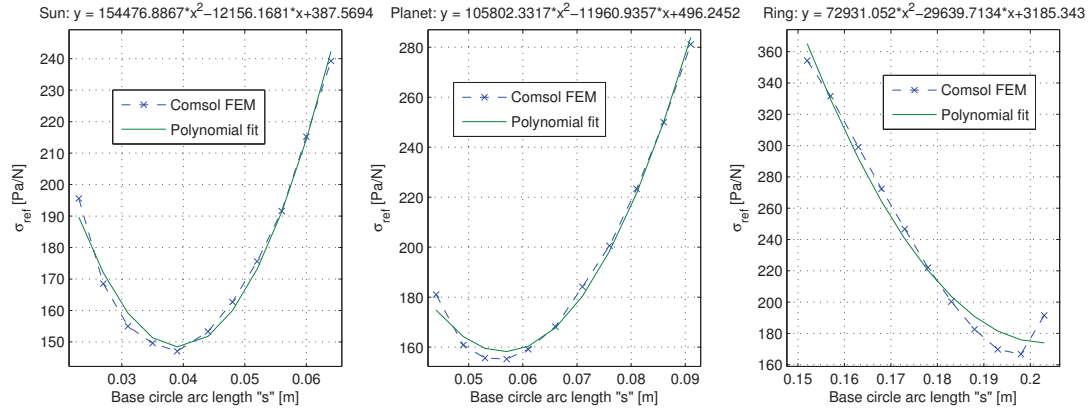


Figure 9: Maximum von Mises stress at gear tooth for a unit force (1 N) applied at a given base circle arc length distance “s”. A second order polynomial fit approximates the FEM-results well, for the base circle arc length intervals of interest.

The gear tooth stresses are assumed to be linearly dependent on the magnitude of the gear tooth force obtained from the multibody program (from Figure 8). In other words, the gear tooth stresses are assumed to be the normal single gear tooth force multiplied by the polynomial function describing the relationship between stresses and base circle arc length (see Figure 9). Furthermore it is assumed that the maximum stress appears at the same point in the tooth root although this is not completely true, i.e. the point of maximum stress moves slightly.

### 2.4.2 Gear tooth surface stresses - pitting

Contact surface stresses are calculated as if two cylinders with radii equal to the base circle arc lengths are in contact. The cylinder length is the minimum gear facewidth, resulting in an ellipsoidal-prism pressure distribution as described in [20]. Gear teeth are not only exerted to pure rolling but also to significant sliding which change the stress state. This quickly becomes a complicated problem and therefore the complexity is significantly reduced by estimating the maximum von Mises stress using a simple average between a static and a dynamic loading coefficient from [20]. This can be justified because the averaging stress coefficient is deemed not important to calculate exactly, since it is the same for all simulation results and because the objective is to study the relative change in fatigue damage in cases of increasing turbulence.

A cylindrical geometry constant  $B$  is defined as

$$B = \frac{1}{2} \left( \frac{1}{\rho_1} + \frac{1}{\rho_2} \right) \quad (12)$$



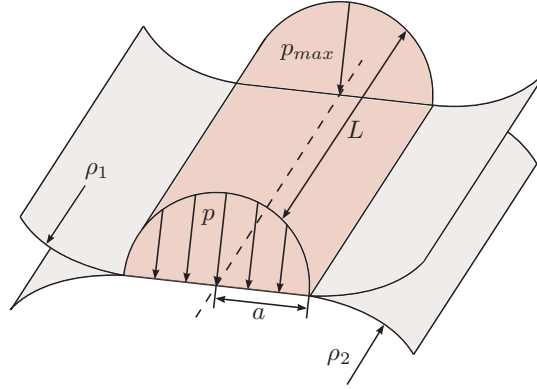


Figure 10: Hertzian pressure distribution with cylindrical contact using radii  $\rho_1$  and  $\rho_2$ .

where  $\rho_1$  and  $\rho_2$  are the base circle arc lengths of the two gears in mesh (also illustrated in Figure 10, i.e. corresponding to the values of  $s_1$  and  $s_2$ ). The contact-patch half-width  $a$  is illustrated in Figure 10 and can be calculated as

$$a = \sqrt{\frac{2}{\pi} \frac{m_1 + m_2}{B} \frac{F}{L}} \quad (13)$$

using material constants  $m_1 = m_2 = \frac{1-\nu^2}{E}$  where  $\nu = 0.3$  is the Poisson ratio and  $E = 210$  GPa is the Young's modulus. The maximum pressure/stress is

$$P_{max} = \frac{2F}{\pi a L} \quad (14)$$

The estimated Von Mises stress is taken as an average of a static and a dynamic coefficient (from [20]) and it is estimated to  $\sigma = P_{max} \left( \frac{0.57+0.73}{2} \right) = 0.65 P_{max}$ . Because the relative fatigue damage is important, it is deemed that it is not that important whether 0.6, 0.65 or 0.7 is used but 0.65 can be justified, at least to illustrate the proposed method. The maximum von Mises stress is found subsurface [20] leading to fatigue micro-cracks and development of pitting. The von Mises stress is used together with a rainflow-counting program that has been verified against a similar tool that is part of FLEX 5.

### 3 Implementation details

Necessary to describe in greater details are:

- Time-factors for rainflow counting algorithm for matching operational hours from Weibull-distribution.
- S-N (Wöhler) curve considerations, i.e. material fatigue characteristics.

#### 3.1 Adjusting time-factors due to different gear teeth in contact

Simulation time is 30 seconds (computation time is 10-15 hours per run). For fatigue-calculations the simulation time must be “upscaled” to the real number of operational hours given by the Weibull distribution for this particular site. Table 2 shows a simple time-factor calculation, i.e. when using the rainflow-counting algorithm, the number of cycles must be multiplied by this number to get an idea of the accumulated fatigue damage over the lifetime. The time-factor is calculated as the operational hours times 3600 seconds, divided by the simulation time in seconds. It is assumed that everything within those 30 seconds of simulation time is representative for the whole lifetime. Due to the high stiffness of the gear teeth the timestep is rather small and the simulation time limit depends on computation time and memory.

Wind speed [m/s]	6	8	10	12	14	16	18	20
In operation [hours]	45418	31900	16320	6189	1751	370	58	7
Time-factor (TF)	5450160	3828000	1958400	742680	210120	44400	6960	840

Table 2: Time scaling for 30 seconds simulation time.

The sun has 20 teeth, the planets have 35 teeth and the ring 91 teeth. In other words “on average” those 30 seconds of simulation time and corresponding von Mises stresses, correspond to 600 simulation seconds for one specific sun gear, 1050 simulation seconds for one specific planet gear and 2730 seconds for one specific ring gear. The time-factor will simply be reduced by the number of gear teeth. Another important thing to consider is that every full rotation of a tooth on the sun gear, is met by teeth from the three planet gears (see Figure 5). Therefore the fatigue from the calculated stresses for teeth in contact must be added together. Instead of having three 30-second simulations this situation corresponds to making a fatigue calculation on a longer 90-second simulation. The same idea for the sun gear can also be used for a full ring gear cycle, which “sees” 3 planet planet/ring gear connections. One rotation of the planet gear however corresponds to “only” a 60-second simulation because one gear tooth will see another tooth from the ring and from the sun gear at all times. Tooth-adjusted time-factors are summarized in Table 3.

Wind speed [m/s]	6	8	10	12	14	16	18	20
In operation [hours]	45418	31900	16320	6189	1751	370	58	7
TF <sub>s</sub> (×20, 90 sec)	272508	191400	97920	37134	10506	2220	348	42
TF <sub>p</sub> (×35, 60 sec)	155719	109371	55954	21219	6003	1269	199	24
TF <sub>r</sub> (×91, 90 sec)	59892	42066	21521	8161	2309	488	76	9

Table 3: Adjusted time scaling for teeth on different gears. Last three rows is the fatigue time-factor for a sun, planet or a ring gear tooth. Because the stresses (and gear tooth forces) are comparable, a fatigue calculation doesn’t need to be done on all individual planets.

### 3.2 S–N-curve details

Realistic S–N-curves for these particular gear teeth are difficult to obtain and therefore the endurance limit as well as the slope must be estimated. The surface treatment procedure as well as heat treatment is unknown. No useful information is available about whether e.g. shot peening or case hardening procedures have been used. Another pitfall is that e.g. in [2] the surface fatigue limit is higher than the internal fatigue limit, i.e. for microcrack growth and fish-eye formation. It is known from [20] that the maximum von Mises stress is slightly below the surface which is therefore expected to decrease the endurance limit. We will estimate S–N-parameters (see Figure 4) based on [9, 1] using the two points in Table 4 and obtain the expression (see Figure 4)

$$s(N) = s_0 N^{\frac{-1}{m}} \quad (15)$$

where  $s_0 = 28.9$  GPa and  $m = 3.4$ , while  $\sigma_e$  is the endurance limit in MPa. A large uncertainty is involved when choosing material and S–N parameters, however for illustrative purposes we choose the endurance limits in Table 5. The endurance limit works as a threshold which effectively can neglect fatigue problems if raised just slightly to e.g. 850-1000 MPa. Table 5 shows that the sun and planet gears have the same, relatively high, endurance limit. It makes sense if the workshop uses the same material and heat/surface treating/hardening procedure for the most critical gear wheels with an estimated endurance limit of 800 MPa. With 91 teeth on the ring gear, this can be manufactured cheaper and in this case the endurance limit is estimated to only 500 MPa which results indicate is sufficient.

Adjusting the S–N curve and endurance limits makes a great difference in the results. If all parameters are the same (e.g. endurance limit of 550 MPa), results clearly illustrate that the sun gear is most exposed to fatigue. A plausible explanation is that three planet gear teeth are acting on the sun and the sun gear has only 20 teeth. Results also clearly show that the ring gear is the least subjected to fatigue. Although it is constantly exposed to contact from three planet teeth, it has a total of 91 teeth and hence the lowest timefactor.

	$N$ [cycles]	$\sigma$ [MPa]
$P_1$	$3 \cdot 10^4$	1400
$P_2$	$1 \cdot 10^6$	500

Table 4: S–N curve parameters using two points ( $P_1$  and  $P_2$  can be seen in Figure 4).

	$\sigma_e$ [MPa]
Sun gear	800
Planet gear	800
Ring gear	550

Table 5: Endurance limits for S–N curve.

## 4 Results

Results are divided into a section dealing with root bending failure and surface stresses (pitting).

### 4.1 Root bending failure

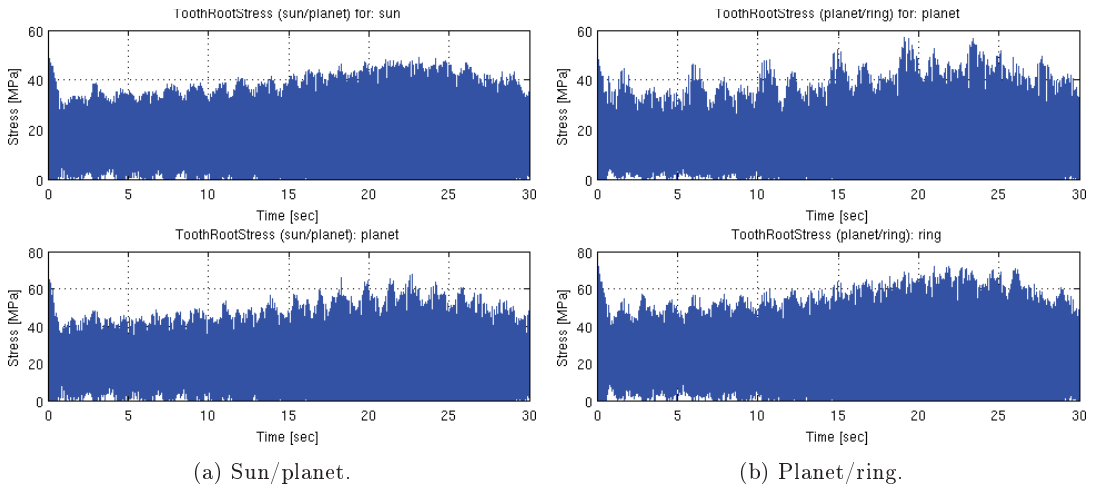


Figure 11: Gear tooth root stresses using TI=10% and mean wind speed  $\bar{U} = 20$  m/s.

The maximum gear tooth stresses are expected using a mean wind speed of 20 m/s. However the results in Figure 11 using TI=10% indicate that the maximum stresses at the gear root is approximately 60 MPa, which is clearly below the endurance (or fatigue) limit. Even though the maximum stress would be higher for increasing turbulence intensities, it is still not considered a problem. It can be concluded that for these particular gear teeth, no fatigue damage will happen at the root.

### 4.2 Surface stresses / pitting

The maximum von Mises stress using  $\bar{U} = 20$  m/s and TI=10% is found to be 6-700 MPa which will contribute to fatigue damage. Figure 12 is an example of the planet/ring stress level for a 30-second simulation. The idea is to select a specific location on a gear tooth (i.e. choose a corresponding  $s$ -value, see Figure 7) and draw a vertical line using the results from Figure 12b and process the von Mises stress using a rainflow-counting algorithm and the S–N-curve data from Table 4.

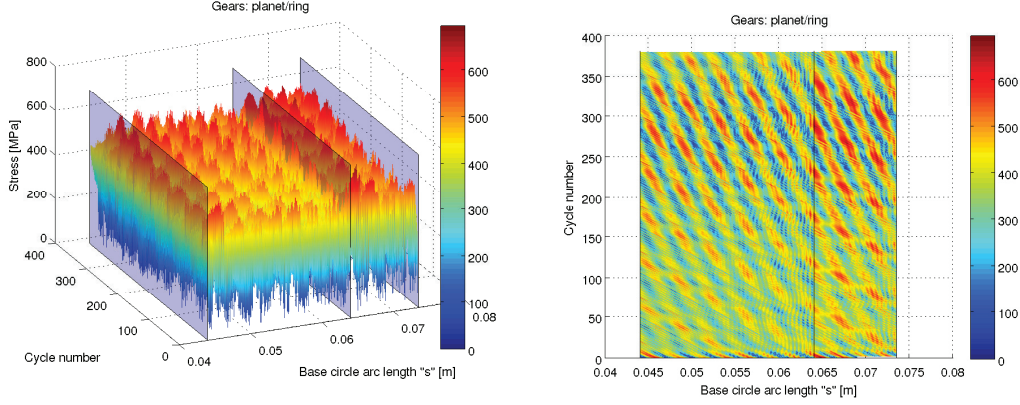
$s$ [m]	0.0243	0.0382	0.0538
Teeth in contact	2	-	1

(a) Sun/planet

$s$ [m]	0.044	0.064	0.0735
Teeth in contact	2	-	1

(b) Planet/ring

Table 6: Switch between single and multiple teeth in mesh (the planet/ring delimiters are also shown in Figure 12, making it easier to see whether one or two teeth are in mesh).



(a) 3 transparent plates are inserted, left region shows two-teeth contact and right region shows single-tooth contact. (b) 2D plot of (a) including both regions (black vertical lines). Mean wind speed is 20 m/s, TI=10%.

Figure 12: Estimated von Mises stress for 30 second simulation time, as a function of base circle arc length “s”. For this to be plotted properly, interpolated von Mises stress values are used.

#### 4.2.1 Average von Mises stress

Figure 7a illustrates how the base circle arc length  $s$  is measured and Table 6 indicates important base circle arc lengths (the middle value for  $s$  is the interface/switch-point between a single and two teeth in mesh). In relation to sun/planet and planet/ring gear tooth contact, it is defined to measure the base circle arc length from the “inner gear”. In other words, for sun/planet gear tooth contact,  $s$  is measured relative from the sun base circle and for planet/ring gear tooth contact  $s$  is measured relative from the planet base circle (remember that one could also express the same base circle arc length measured from the other gear, so this is a matter of choice or definition). A consequence of this choice is that low  $s$ -values means tooth contact is close to the “inner gear” and vice versa. In addition low  $s$ -values implies high stiffness because two gear teeth is in mesh and vice versa for high  $s$ -values where only a single tooth is in mesh.

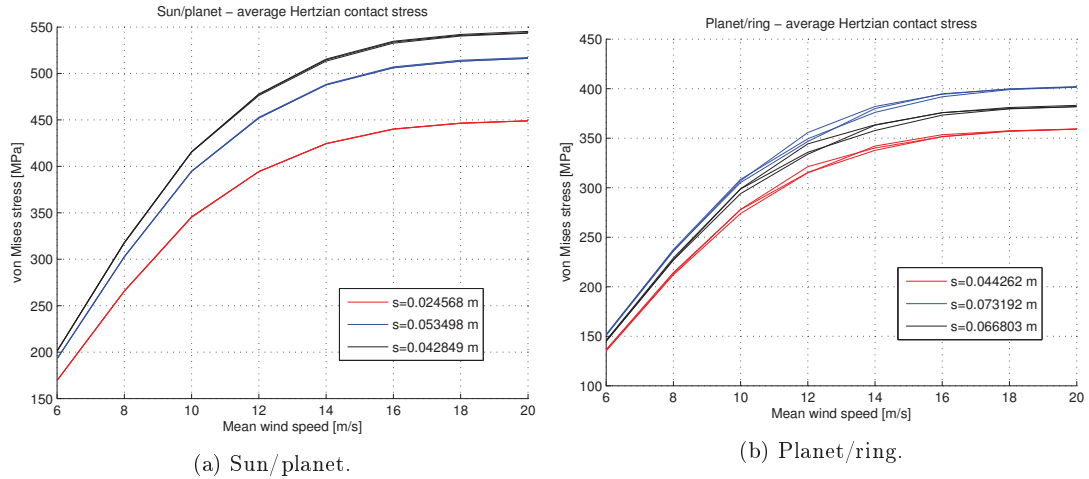


Figure 13: Average von Mises contact stress for TI=10%.

Figure 12 shows an example of the stresses calculated for a simulation with indication of 3 different base circle arc length locations. The multibody program only calculates the gear tooth forces as a function of the dynamics of the whole system and that system does not guarantee to store the results at exactly any given point (which is necessary for a fatigue calculation). For that reason,

interpolation has been used and because the stiffness is very high, the timestep is low causing long computation times. Simulations each require around 5-10 GB of memory for only 30 seconds. With high stiffness and low timestep it is deemed that interpolation of gear tooth forces is a good solution for calculating the stresses at specific locations. The pattern in Figure 12 indicates that the interpolated stresses are not “random”. The pattern indicates that regions of high and low stresses are a repetitive and cyclic phenomena, as a result of using realistic non-linear stiffness. Because interpolation is used, the endpoints of the base circle arc length distances are not applicable for interpolation. There are too few stress results here, i.e. only seldom the multibody program calculates the solution exactly at the endpoints. Two of the base circle arc lengths in Figure 12 are close to the endpoint values in Table 6 but not completely the same. This also applies to Figure 13. The location indicating a switch from one to two gears in mesh from Table 6 ( $s=0.0382$  m and  $s=0.064$  m) is excluded because such an interpolation yields unpredictable and unusable stresses. On one side of the interpolation, two teeth are in mesh and on the other side, only a single tooth is in mesh with the other gear.

From Figure 13 it can be concluded that the average stresses are lowest for low values of  $s$  (the two red curves). This is a region with high stiffness due to the fact that two teeth are in mesh at the same time. Additionally, a black curve is added to both graphs in Figure 13. This line indicates the contact point of the two working circles, i.e. the pitch point where only rolling appears (everywhere else sliding takes place). At this point only a single tooth is in mesh and that explains the higher stresses. Figure 12 shows that the stresses are not the same everywhere, i.e. it is ambiguously which value of  $s$  yields the maximum average stresses for both sun/planet and planet/ring results. Figure 13 resembles a behavior similar to those found using a rigid multibody model in [11]. It assumed that multiple flexible planets on one hand decrease the gear tooth force because additional planets share the load. On the other hand, the gear tooth force is probably increased because not all springs and dampers are aligned equally (especially not when addendum modification is used). In other words, if one of the planets tries to rotate in one direction, one of the other planets could try to rotate in another direction due to the spring/damper force. With high stiffness these spring and damper forces are not negligible and cause the three planets to act against each other while trying to rotate the sun and ring gears at the same time.

#### 4.2.2 Accumulated rainflow counting results

Figure 14 is an example of processing the 30 seconds sun/planet von Mises stress calculation results through the RFC-code. Figure 14a shows the stress range for each of the 6-20 m/s mean wind speed bins. It can be seen that the change from 6-8 and 8-10 m/s is huge in comparison with the change from e.g. 16-18 or 18-20 m/s. Figure 14b is the cumulative number of full cycles, using the time factor for the sun gear ( $TF_s$  from Table 3). Both figures illustrate that if the endurance limit exceeds around 850-1000 MPa, then fatigue and surface pitting of the sun gear is not a problem. Similar observations can be made for the planet and ring gears.

#### 4.2.3 Cumulative fatigue damage due to increased turbulence

The IEC 61400-1 standard about design requirements for wind turbines specifically operate with 3 classes for turbulence intensity: 12%, 14% and 16%. Turbulence intensity depends on e.g. surface roughness i.e. how many disturbances are present from e.g. trees/buildings etc and also hub height. In other words, the turbulence intensity is generally lower for offshore wind turbines (undisturbed) when compared to that of landbased wind turbines. With increasing altitude, the flow is generally also less disturbed leading to less “average” turbulence.

	6 m/s	8 m/s	10 m/s	12 m/s	14 m/s	16 m/s	18 m/s	20 m/s	$\Sigma$
Sun	0	0	0	0	0.2185	0.3727	0.0869	0.0132	0.69
Planet*	0	0	0	0	0.0416	0.0710	0.0166	0.0025	0.13
Ring	0	0	0	0.0116	0.0177	0.0125	0.0028	0.0004	0.05

Table 7: Example of accumulated fatigue damage using  $TI=10\%$  (\* means average of 3 planets).

Table 7 shows the contribution of fatigue damage at different mean wind speeds and the total

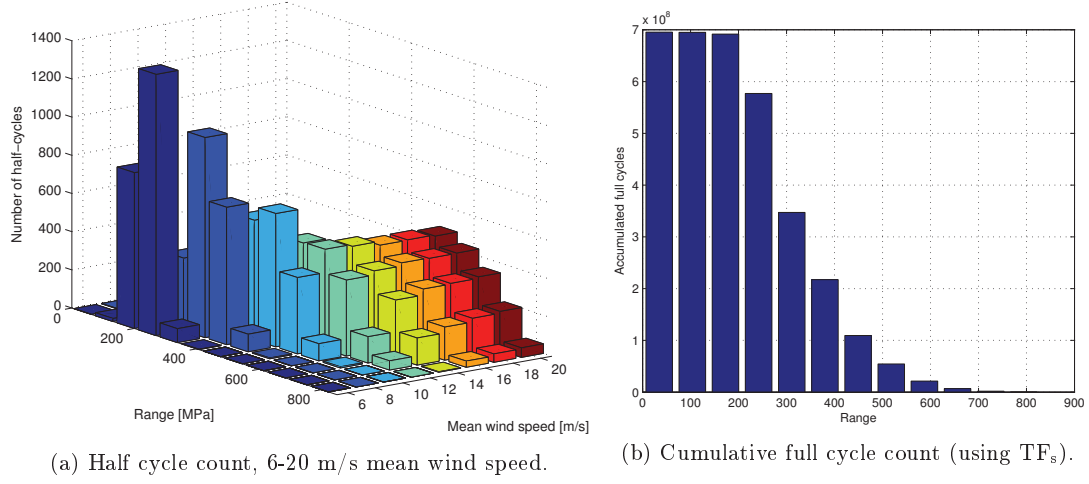


Figure 14: Example of rain flow counting result using TI=10%.

fatigue damage on each gear wheel. The star after the planet denotes average fatigue damage on each of the three planets. It can be concluded that generally wind speeds of 14-16 m/s contribute the most to fatigue. The explanation is that even though the stress range count is higher at higher wind speeds, the wind rarely blows above 16 m/s.

	8%	10%	12%	14%	16%	18%	20%
Sun	0.65	0.69	0.75	0.85	1.10	1.60	2.00
Planet*	0.12	0.13	0.14	0.16	0.21	0.30	0.38
Ring	0.05	0.05	0.05	0.05	0.07	0.10	0.11

Table 8: Total fatigue damage as a function of increasing turbulence.

Table 8 shows total cumulative damage as a function of increasing turbulence. Assuming that the material data and S-N-curve data are realistic, gear tooth surface pitting at the sun gear is expected if the average turbulence exceeds 14-16%. The ring gear with an endurance limit of only 550 MPa is still not exposed to as much fatigue damage as the planet gear with 800 MPa endurance limit. With 91 teeth, the ring gear is the most durable to pitting caused by surface fatigue but with lowered endurance limit, this result was not obvious. However, with 500 MPa endurance limit for the ring gear, the planet gear becomes least subject to fatigue damage. Figure 15 graphically summarizes the lifetime fatigue calculation results, using the flexible multibody model and Hertzian contact stress assumption. This gearbox is only deemed usable if the representative turbulence level is below 15%. Accumulated damage increases quickly for increasing turbulence intensity above approximately 16-17%. Results suggest that the sun gear with few teeth, will be the most important to protect by ensuring correct maintenance and regular inspections. Possibly extra care of the sun gear must also be taken under manufacturing. The results finally demonstrate the importance of specifying a material and surface/heat treatment process leading to a high endurance limit, for the sun gear.

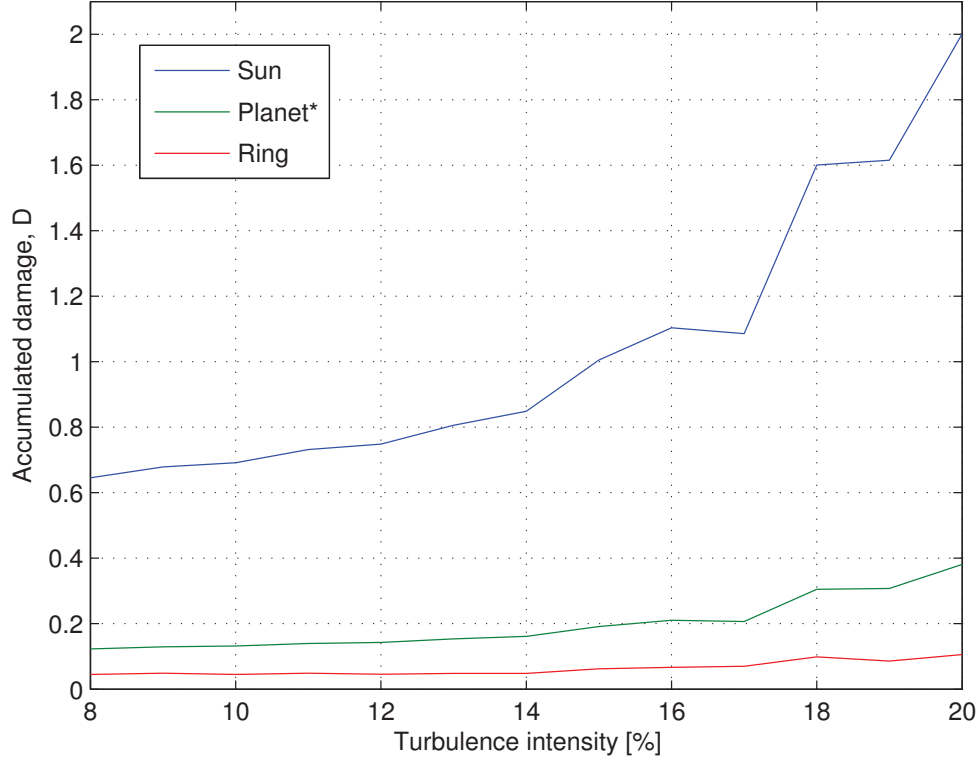


Figure 15: Accumulated fatigue on sun, planet and ring gears for lifetime operation (20 years).

## 5 Conclusions

This paper focuses on investigating fatigue problems in relation to gear teeth in a planetary gearbox. The Weibull cumulative distribution function and Palmgren-Miner linear damage hypothesis is used together with

1. A method for estimating gear root stresses.
2. A method involving Hertzian contact stress assumption.

It is found that the investigated 500 kW windturbine gearbox has no fatigue-problems related to gear tooth root bending. The Hertzian contact stress assumption implies calculating the maximum von Mises stresses slightly under the gear tooth surface. Fatigue damage occurs under the assumption of using an endurance limit of 800 MPa for the sun and the planet gear wheels. The interpretation of this result is that fatigue just below the gear tooth surface can lead to gear tooth surface pitting, which eventually increases the risk of gearbox failure. Furthermore it can be concluded that:

- The average von Mises stress flattens out in the high mean wind speed region, i.e. in the interval of mean wind speeds approximately between 15-20 m/s, the stresses are not much higher than at 15 m/s. This behavior resembles that of a typical power-curve for a wind turbine and it also resembles a similar result published in [11].
- The stresses at specific locations have been calculated using interpolation and it can clearly be seen that the von Mises stress on a single gear tooth in the region where two gear teeth are in mesh (low base circle arc lengths), are lower than in the region where only a single tooth is in mesh. Specifically it can be concluded that the stresses at the working circle/pitch point and for higher base circle arc lengths are higher, than at points specified by low base circle arc lengths. The gear tooth stresses on a specific place on the tooth are lower in the

region where two gear teeth share the load, when compared to the case where only a single gear tooth must take the whole load.

- When estimating the effect of turbulence on gear tooth surface pitting, a marginal increase in turbulence in the high turbulence region relatively contributes much more to accumulated fatigue damage, than the same increase in low turbulence regions.

For low turbulence intensities, wake effects (turbulence generated from other wind turbines in a wind farm) are not deemed important as a cause of gearbox failure due to pitting caused by subsurface cracks. Generally it can be assumed that the turbulence intensity for offshore wind turbines is generally lower than that of similar landbased wind turbines, because these are located near obstacles such as trees, buildings, uneven terrain etc which increase the turbulence. Therefore particular attention to pitting as a cause of gearbox failure, should be taken when making wind turbine layouts of wind farms in regions with high turbulence. A vague practical conclusion is that results suggests that wake effects as a cause of pitting fatigue leading to gearbox failures for e.g. landbased wind turbines (higher turbulence) could be more important than similar wake effects for offshore wind turbines (generally lower turbulence regions, the flow is more undisturbed).

### **Acknowledgements**

This research was supported by DSF (Danish Council for Strategic Research) grant 09-071588.



## References

- [1] Howard E Boyer, *Atlas of fatigue curves*, ASM International, 1986.
- [2] N Bretl, Stefan Schurer, Thomas Tobie, and Karsten Stahl, *Investigations on tooth root bending strength of case hardened gears in the range of high cycle fatigue*, (2013).
- [3] Wenbin Dong, Yihan Xing, Torgeir Moan, and Zhen Gao, *Time domain-based gear contact fatigue analysis of a wind turbine drivetrain under dynamic conditions*, International Journal of Fatigue (2012).
- [4] P.J.L. Fernandes and C McDuling, *Surface contact fatigue failures in gears*, Engineering Failure Analysis **4** (1997), no. 2, 99–107.
- [5] Michel Géradin and Alberto Cardona, *Flexible multibody dynamics: a finite element approach*, John Wiley, 2001.
- [6] Kurt S. Hansen and Gunner C. Larsen, *Database of wind characteristics*: <http://www.winddata.com>, 1997-2011.
- [7] Edward J. Haug, *Computer aided kinematics and dynamics of mechanical systems: Vol. i: Basic methods*, Allyn and Bacon, 1989.
- [8] Andreas Heege, Jaume Betran, and Yvan Radoveic, *Fatigue load computation of wind turbine gearboxes by coupled finite element, multi-body system and aerodynamic analysis*, Wind Energy **10** (2007), no. 5, 395–413.
- [9] Th Hirsch, H Wohlfahrt, and E Macherauch, *Fatigue strength of case hardened and shot peened gears.(retroactive coverage)*, Shot Peening: Science, Technology (1987), 547–560.
- [10] M. F. Jørgensen, N. L. Pedersen, and J. N. Sørensen, *Comparison and implementation of a rigid and a flexible multibody planetary gearbox model*, (submitted) (2013).
- [11] M. F. Jørgensen, N. L. Pedersen, J. N. Sørensen, and U. S. Paulsen, *Rigid matlab drivetrain model of a 500 kw wind turbine for predicting maximum gear tooth stresses in a planetary gearbox using multibody gear constraints*, Wind Energy (2013).
- [12] Peder Klit, Knud Casper, and Niels L. Pedersen, *Machine elements - analysis and design*, Polyteknisk Forlag, 2009.
- [13] P Madsen, *Recommended practices for wind turbine testing and evaluation; 3. fatigue loads*, vol. 2, 1990.
- [14] Milton A. Miner, *Cumulative damage in fatigue*, Journal of applied mechanics **12**, no. 3 (1945), 159–164.
- [15] Marta Molinas, Jon Are Suul, and Tore Undeland, *Extending the Life of Gear Box in Wind Generators by Smoothing Transient Torque With STATCOM*, IEEE Transactions on Industrial Electronics **57** (2010), no. 2, 476–484 (English).
- [16] COMSOL Multiphysics, [www.comsol.se](http://www.comsol.se), 1998-2012.
- [17] Walt Musial, Sandy Butterfield, and Brian McNiff, *Improving wind turbine gearbox reliability*, Proceedings of the European Wind Energy Conference, 2007.
- [18] Bernd Niederstucke, Andreas Anders, Peter Dalhoff, and Rainer Grzybowski, *Load data analysis for wind turbine gearboxes*, Final Report of Enhanced Life Analysis of Wind Power Systems (2003).
- [19] Parviz E. Nikravesh, *Computer-aided analysis of mechanical systems*, vol. 186, Prentice Hall, 1988.
- [20] Robert L Norton, *Machine design: An integrated approach, 2nd ed.*, Prentice-Hall, 2000.

- [21] Arvid Palmgren, *Die lebensdauer von kugellagern*, Zeitschrift des Vereins Deutscher Ingenieure 68.14 (1924), 339–341.
- [22] N. L. Pedersen and M. F. Jørgensen, *On gear teeth stiffness evaluation*, (submitted) (2013).
- [23] Meik Schlechtingen, Ilmar Santos, and Sofiane Achiche, *Wind turbine condition monitoring based on scada data using normal behavior models*, Applied Soft Computing **13** (2013), 259–270.
- [24] J.V. Seguro and T.W. Lambert, *Modern estimation of the parameters of the weibull wind speed distribution for wind energy analysis*, Journal of Wind Engineering and Industrial Aerodynamics **85** (2000), no. 1, 75 – 84.
- [25] Ahmed A. Shabana, *Dynamics of multibody systems*, Wiley & Sons, 1989.
- [26] K Smolders, H Long, Y Feng, and PJ Tavner, *Reliability analysis and prediction of wind turbine gearboxes*, European Wind Energy Conference, 2010.
- [27] Sten. Tronæs Frandsen and Risø National Laboratory., *Turbulence and turbulence-generated structural loading in wind turbine clusters*, Risø National Laboratory, 2007.
- [28] A. K. Vasudevan, K. Sadananda, and G. Glinka, *Critical parameters for fatigue damage*, International Journal of Fatigue **23** (2001), no. SUPP/1, 39–53.
- [29] Stig Øye, *Various flex 5 documentation*, DTU Mechanical Engineering, 2001.





**DTU Mechanical Engineering**  
**Section of Solid Mechanics**  
Technical University of Denmark

Nils Koppels Allé, Bld. 404  
DK- 2800 Kgs. Lyngby  
Denmark  
Phone (+45) 4525 4250  
Fax (+45) 4593 1475  
[www.mek.dtu.dk](http://www.mek.dtu.dk)  
ISBN: 978-87-7475-370-4

**DCAMM**  
**Danish Center for Applied Mathematics and Mechanics**

Nils Koppels Allé, Bld. 404  
DK-2800 Kgs. Lyngby  
Denmark  
Phone (+45) 4525 4250  
Fax (+45) 4593 1475  
[www.dcam.dk](http://www.dcam.dk)  
ISSN: 0903-1685